UNIVERSITY OF LEEDS

Preparation and Performance of Novel CaO-Based Sorbents for High-Temperature CO_2 Removal

March 2019

Sergio Ramirez Solis

Submitted in accordance with the requirements for the degree of

Doctor of Philosophy

The University of Leeds

Energy Research Institute

School of Chemical and Process Engineering (SCAPE)

The candidate confirms that the work submitted is his own, except where work which has formed part of jointly-authored publications has been included. The contribution of the candidate and the other authors to this work has been explicitly indicated below. The candidate confirms that appropriate credit has been given within the thesis where reference has been made to the work of others.

Results exhibited in Chapter 4 and 5 are based on research work that has produced a jointly-authored publication:

Sergio Ramirez-Solis*, Valerie Dupont, Steven J. Milne. Preparation and Evaluation of CaO-based CO_2 Sorbents Deposited on Saffil Fibre Supports. Energy & Fuel, 2018.

The experimental work, data collection and processing, and paper writing up are ascribed to the candidate. Dr. Valerie Dupont and Dr. Steven Milne contributed to the analysis of results and discussion. In addition, a significant input in terms of comments, edits, and proofreading were provided by them.

Acknowledgements

To the greatest extent, I would like to acknowledge the guidance and support provided by my supervisors Dr Valerie Dupont and Dr Steven Milne all along the way, which started a few years ago like a dream and has now become a reality. Thank you for trusting and giving me the valuable opportunity to perform my PhD under your supervision. Although challenges emerged periodically, I would like to remark that without your assistance and experience, it would have been difficult to get ahead and show positive results in each stage of the PhD. In addition, I want to thank for the availability showed for sorting out issues concerning not only the research work performed in this thesis but also in circumstances beyond the PhD project.

My most sincere thanks also to all those others who contributed directly or indirectly to the accomplishment of this thesis. Karine Alves Thorne, Stuart Micklethwaite, Simon Lloyd, and Dr Adrian Cunliffe deserve gratefulness for the technical support and training provided on the different characterization techniques used to perform each analysis. Jonathan Cross and Adam Kelsall at Unifrax are acknowledged as industrial collaborators for supplying Saffil fibres.

I am grateful to my friends and colleagues Syed Z. Abbas, Hussein Alshamary, Zainab Ibrahim S G Adiya, Hafizah Yun, and all those that I forget at this moment, for sharing valuable moments. Thanks guys for your support at hard times and cultural knowledge transmitted throughout the long conversations after weary days. All my gratefulness to my sponsor the National Council of Science and Technology (CONACYT) for award me with a Scholarship to conduct my PhD at England. Without your support, my dreams would never have become true.

Finally, I would like to express my gratitude and love to my parents (Sergio-Gloria), siblings (Cynthia-Christopher), nieces (Nahomy-Hannah) and fiancée (Frida W.R.M) for accompanying and encourage me to achieve my goals. Special thanks to my aunt Magdalena for her valuable economic and moral support not only during my studies but also along my entire life. Although my grandmother (Consuelo) and godfather (Francisco) are no longer with us, this trophy (PhD) is in their memory. I apologize for all unmentioned persons in this brief acknowledgements section, many thanks for their contribution no matter how small or substantial it was.

Sergio Ramirez Solis, March 2019

Abstract

Sorption-Enhanced Steam Reforming process (SESR) is an auspicious technology for hydrogen (H_2) production with simultaneous capture of carbon dioxide (CO_2) derived from design modifications performed on the conventional Steam Reforming Process (SRP). Enhancing the reforming reaction in terms of kinetics, yield and purity through capturing in situ CO_2 using high temperature solid sorbents brings advantages including reduction in energy requirements and lower investment capital. Even though SESR is a cost-effective route for energy generation based on organic volatile and gaseous feedstock including natural gas, its implementation implies overcoming challenges. Diminishing the sintering in CaO-based CO_2 sorbents has become one of these challenges since the reactivity of these captors decreases significantly as the number of carbonation/calcination cycles proceeds.

This research work centres its efforts in the development of novel sintering resistant CaO-based CO_2 sorbents enhanced by means of the incorporation of a refractory, high surface area, polycrystalline fibrous support (Saffil), with high-Al_2O_3 content, acting as structural stabilizer of CaO. Four families of CaO-based CO_2 sorbents were prepared using wet impregnation and precipitation methods. Different variants such as CaO precursor, precipitant agents, pH, stirring, aging time, etc. were tested to optimize the synthesis parameters. The best preparation conditions were aimed at achieving a homogeneous deposition of CaO over the Saffil support as well as a morphology in CaO that might improve the durability of CO_2 acceptors. In particular, the formation of nanoflakes, and particles with an octahedral shape were found to be two of the most promising morphologies.

Upon the determination of optimal synthesis parameters, the as-prepared CO_2 sorbents were characterized in order to determine their physicochemical properties such as textural features (surface area and pore size distribution – N_2 physisorption), real CaO content (XRF), dispersion of CaO over Saffil supports (SEM-EDX), phase identification (XRD), etc.

Carrying capacities and durability of CaO-based CO_2 sorbents were assessed through multicycle carbonation/decarbonation tests under controlled conditions such as temperature and atmosphere. The dynamic/isothermal experiments

conducted in a TGA system confirm an enhancement in reactivity when CaO grows over the periphery of the Saffil support. In addition to the use of a support, achieving a ‘clamping effect’ (to diminish lateral mobility of CaO, thus avoiding particle densification), in conjunction with the morphology adopted by CaO, is shown to provide thermal stability. SEM-EDX techniques applied on used CaO-based sorbents (30 carbonation-calcination cycles) corroborate that the enhancement in durability is due to the outstanding sintering resistance exhibited when CaO adopted the nanoflake or octahedral structure.

The viability of the as-prepared sorbents was also confirmed through a kinetic study in which kinetic parameters and mechanisms associated with both carbonation and calcination reactions were estimated. Concerning the CO_2 uptake kinetics, the isothermal method was used to collect mass change data whilst model-based equations were employed to elucidate the kinetic triplet. For the calcination reaction, the kinetic study was performed using both isothermal and non-isothermal methods. Activation energies assessed for the carbonation and calcination reactions were compared among them and also in relation with other CaO-based sorbents available in the literature for reliability purposes.

Table of Contents

List of Tables

List of Figures

Nomenclature

	Definition
CO_2	Carbon Dioxide
N_2O	Nitrous oxide
H_2	Hydrogen
N_2	Nitrogen
CO	Carbon monoxide
CH_4	Methane
SO_3	Sulphur oxide
NO_X	Nitrogen oxides
NiO	Nickel oxide
NiO/Al_2O_3	Nickel oxide supported on alumina
Fe_3O_4/Cr_2O_3	Iron/chromium-based catalyst
$Cu/ZnO/Al_2O_3$	Copper/zinc oxide/alumina-based catalysts
Ppm, ppb	Parts per million or billion
S	Steam
C	Carbon
NH_3	Ammonia
$CaMg(CO_3)_2$	Dolomite
K_2CO_3	Potassium carbonate
S/C	Steam-to-carbon ratio
CaO/C	Sorbent-to-carbon ratio
O_2	Oxygen
H_2O	Water (Steam)
HT	Hydrotalcites
E_r	Overall energy for a molecule at distance *r* from the surface
E_D	Interaction energies due to dispersion forces
E_P	Electronic field caused by polarity of the surface.
$E_{F\mu}$	Electric dipole of the molecule
E_{FQ}	Quadrupole Interaction of the molecule with the surface field gradient
E_R	Short-term repulsion forces
i	Specie
MOFs	Metal organic frameworks
MO	Metal oxide
BeO	Beryllium oxide
MCO_3	Metal carbonate
CaO	Calcium oxide

$CaCO_3$	Calcium Carbonate
$Ca(OH)_2$	Calcium Hydroxide
Li, Na, K	Alkali metals
Li_2ZrO_3	Lithium Zirconate
Li_4SiO_4	Lithium Orthosilicate
Na_2ZrO_3	Sodium Zirconate
Li_2O	Lithium oxide
Y_2O_3	Yttrium (III) oxide
Li/K,Li/Zr	Lithium/potassium or Zirconium ratio
$Ca(C_2H_3O_2)_2 \cdot xH_2O$, *CaAc*	Calcium acetate hydrate
$[CH_3CH(OH)COO]_2Ca\ xH_2O$	Calcium l-lactate hydrate
$C_{12}H_{22}CaO_{14}\ H_2O$	Calcium d-gluconate monohydrate
$O_2CCH_2C(OH)(CO_2)CH_2CO_2]_2\ Ca_3\ 4H_2$	Calcium citrate tetrahydrate
$Ca(C_2H_3O_2)_2$	Calcium acetate
$Ca(NO_3)_2 \cdot 4H_2O$	Calcium nitrate tetrahydrate
CH_4N_2O	Urea
NaOH	Sodium hydroxide
$NaNO_3$	Sodium nitrate
C_2H_6O	Ethylene glycol
ΔH	Enthalpy of reaction or standard enthalpy
ΔG	Gibbs energy
SiO_2	Quartz
Na_2CO_3	Sodium carbonate
Al_2O_3	Aluminium oxide
TiO_2	Titanium oxide
ZrO_2	Zirconium oxide
MgO	Magnesium oxide
$P/P°$	Relative pressure
P	Pressure
$P°$	Saturation pressure
T	Temperature
n^a	Amount of gas physisorbed at certain relative pressure
n_m	Monolayer capacity
A_s	Total surface area
a_s	Specific surface area
L	Avogadro constant
M	Mass of the adsorbent
V	Molar volume
σ	Surface tension of the liquid adsorbate
θ	Contact angle among adsorbate-adsorbent layer on pore wall
r_k	Kelvin radius (for cylindrical shape)
t	Thickness of the adsorption layer
r_p	Geometric radius of a pore
δ-Al_2O_3	Saffil fibres
rpm	Revolutions per minute
n	Number of cycles
T_{min}	Room temperature
$T_{calcination}$	Temperature of calcination
$T_{capture}$	Temperature of capture
CC_N	Carrying capacity at Cycle N
m_i	Mass of the sorbents post-activation

$m_{f,N}$	Mass of sorbent in the course of the cycle N
X_r *or* a_α *or* $a_{cc,N}$	Residual conversion
X_n *or* a_N	Conversion at cycle N^{th}
k	Deactivation constant
N	Cycle N^{th}
a	Pre-exponential decarbonation factor
$k_{1,D}$ *and* $k_{2,D}$ *(chapter 5)*	Degradation rates
A_1 *and* A_2 *(chapter 5)*	Pre-exponential factors
α	Conversion
d_α/d_t	Isothermal reaction rate
d_α/d_T	Non-isothermal reaction rate
k(T)	Temperature-dependent rate constant
h(P)	Pressure function
f(α)	Reaction model function
E, E_a *or* E^e *(chapter 2, 6-7)*	Activation energy
A (chapter 7-6)	Pre-exponential factor
R	Gas constant
β or d_t/d_T	Heating rate
g(α)	Integral reaction mode
k_1 *and* k_2 *(chapter 6-7)*	chemical reaction and diffusion rate constants
A and B	Pre-exponential kinetics factors

Acronyms

Acronym	Definition
GHG	Greenhouse gases
IPCC	Intergovernmental Panel on Climate Change
UNFCCC	United Nations Framework Convention Climate Change
GCCA	Global Climate Change Alliance
E&H	Energy and heat
GHE	Greenhouse effect
CCS	Carbon Capture and Storage
IGCC	Integrated gasification combined cycle
PFBC	Pressurized fluidized bed combustor
SRP	Steam reforming process
SMR	Steam methane reforming
ATR	Autothermal reforming
POX	Partial oxidation of hydrocarbons
WGS	Water gas shift
PSA	Pressure swing adsorption
SESR	Sorption-enhanced steam reforming
SESMR	Sorption-enhanced steam methane reforming
PV or SPV	Specific pore volume or Pore volume/size
SEM	Scanning Electron Microscopy
MEA	Monoethanolamine
CLC	Chemical-looping combustion
HT-WGS and LT-WGS	High and low temperature water gas shift reactor
XRD	X-Ray diffraction
PXRD	Powder X-Ray diffraction

EDX	Energy-Dispersive X-Ray spectroscopy
IUPAC	The International Union of Pure and Applied Chemistry
SDD	Silicon dry detector
CFE	Cold field emission
SA	Surface area
PSD	Pore size distribution
BET	Brunauer-Emmett-Teller
BJH	Barrett-Joyner-Halenda
SSA	Specific surface area
TA	Thermal Analysis
TGA	Thermogravimetric analysis
TEM	Transmission electron microscopy
DTA	Differential Thermal Analysis
XRF	X-ray fluorescence
ICDD	International Centre for Diffraction Data
DSC	Differential scanning calorimetry
DTA	Differential thermal analysis
ICTAC	International Confederation for Thermal Analysis and Calorimetry
OFW	Ozawa-Flynn–Wall
KAS	Kissinger-Akahira-Sunose

Chapter 1 Introduction

1. Background and Context

1.1 Greenhouse gases and global warming

The atmospheric mean temperature is a key factor that made the Earth a habitable planet through the presence of certain gasses that have the ability to trap long-wave radiation (infrared) emitted from the conversion of solar radiation to heat energy by the Earth's surface. As a result of the interaction radiation-gas, the Earth's surface is warmed, maintaining a 15 °C average surface temperature [1]. Evidently, the lack of gasses that block emissions of longer wavelength radiation would cause the opposite effect, namely an estimated mean temperature of -19 °C [1]. The observation of this natural process is traced back to Jean-Baptiste Fourier who observed how the Sun's radiation warmed the Earth's surface [2]. He compared the effect aforementioned with that of the glass in a greenhouse. Hence, the Fourier perceptions and predictions gave raise not only to denominate it as the "greenhouse effect (GHE) but also to assume that climate changes might be strongly subjected to activities developed by humans. As might be inferred, with the absence of the natural greenhouse effect, the planet would present adverse effects such as lacking of life as we know it and freezing [3].

The most active, abundant and long-lived greenhouse gases (GHG) in the atmosphere are carbon dioxide (CO_2), nitrous oxide (N_2O) and methane (CH_4). In lower concentration but with an impact in the evolution of the climate system are the halogenated organic compounds, fluorinated gases and ozone (upper and lower atmosphere) [3]. In proportion, it is well-known that the water vapor contributes approximately twice the effect with relation to the second most potent greenhouse gas, namely CO_2. As must be expected, the concentration of water vapor also varies indirectly as a consequence of human activities [3]. Hence, a

good understanding of the water vapor role in the climate system is of vital importance.

Figure 1-1 [4], presents the upward concentration trend of the most abundant greenhouse gases (not counting water vapor) over the last 2000 years. The measurements of recent data were obtained straight from the air whilst old data comes from the analysis of air bubbles trapped in ice located in the North and South Poles (Greenland and the Antarctic) [4]. As can be seen from Figure 1-1, for the period of time from 0 to 1800 years, no substantial alterations in the concentration levels of CO_2, N_2O and CH_4 were discernible. In the interval 1800-2000, severe fluctuations in the atmospheric composition mainly of CO_2 and CH_4 were recorded, namely from 278 ppm to 370 ppm for CO_2, and 615 ppb to 1930 ppb for CH_4. The drastic increase of the concentration of these three greenhouse gases experienced in this period was associated not only with the industrial revolution but also to other human activities (e.g. soil and its use) [4].

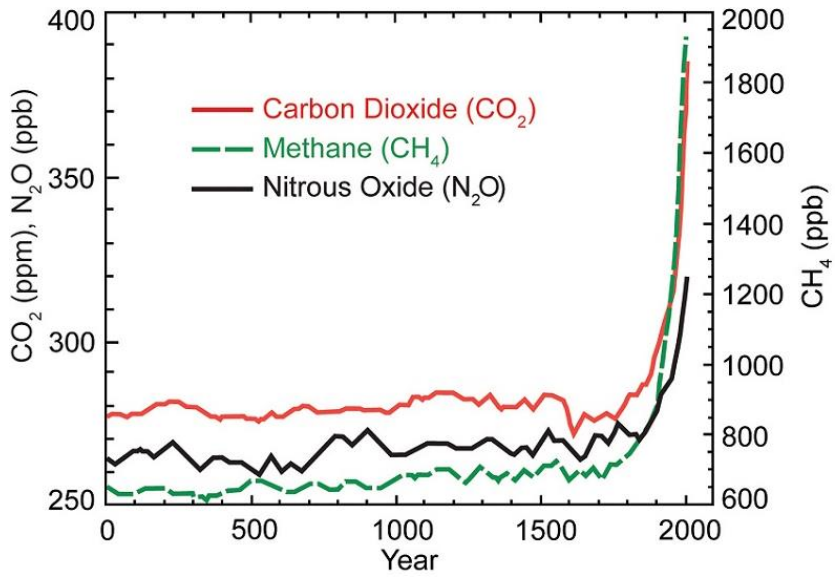

Figure 1-1. Fluctuation in the concentration (ppm) of greenhouse gases in the atmosphere in the last 2000 years. The abundance of CO_2, N_2O (scale of left Y-axis in ppb) and CH_4 is expressed in parts per million or parts per billion (molecules of greenhouse gas per billion or million of air molecules) [4].

Concentrating on the circumstances that have caused the drastic increase of emissions of greenhouse gases in the last century, it is well-known the energy demand generated by the economic development, technological evolution (industry growth), and demographic development around the world were primary

sources [5]. Albeit the utilization of non-emitting energy sources have grown considerably, the combustion of fossil fuels such as oil, coal and gas has been the backbone of the world primary energy. With respect to the total energy production, the burning of hydrocarbons accounts for about 82% [5-8]. Our extensive reliance on compounds with high-carbon content have occasioned substantial emissions of greenhouse gases into the atmosphere. Based on the global emission assessment performed by the Intergovernmental Panel on Climate Change (IPCC), CO_2 was identified as the greenhouse gas with the highest contribution, with just over 65% [9]. Consequently, the CO_2 originated by the anthropogenic drivers make this GHG the foremost contributor of global warming (gradual growth of the average temperature of the Earth). From Figure 1-2 that reports the total annual anthropogenic GHG emissions by gas, it must be highlighted that CO_2 and CH_4 have been emitted in greater percentage with regards to other GHG since 1970 [9].

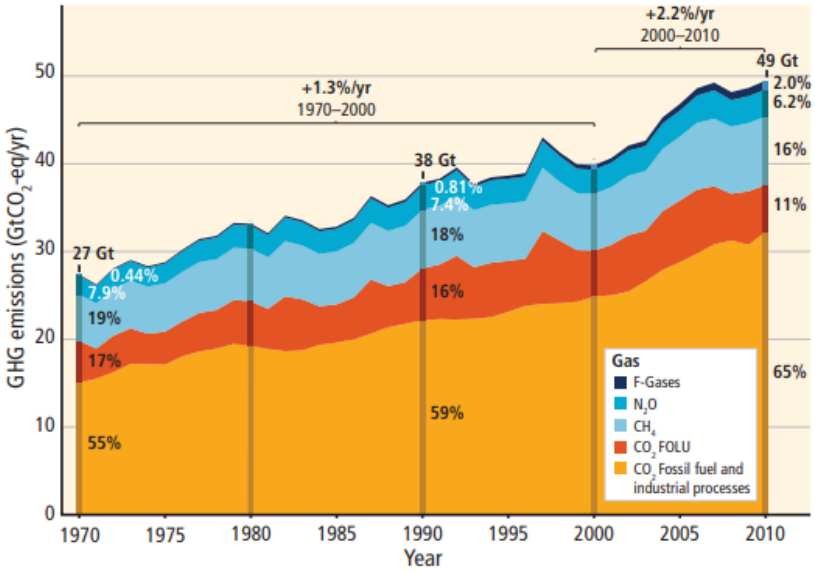

Figure 1-2. Anthropogenic greenhouse gas emissions expressed in gigatonne of CO_2-equivalent per year ($GtCO_2$-eq/yr) reported from 1970 to 2010. The gases covered in the plot are support under the Kyoto protocol. The sources of CO_2 considered are fossil fuel combustion, forestry and industrial processes [9].

Concerns regarding the wide spectrum of adverse effects that climate change generates such as the decrease in upper ocean pH (acidification), significant changes in snow cover, high-latitude ice cover, changes in global average temperatures, etc. have led to develop and design novel strategies and initiatives to stabilize anthropogenic CO_2 emissions (more details of global warming effects

will be provided in the next section) [3]. The United Nations Framework Commission on Climate Change (UNFCCC), Intergovernmental Panel on Climate Change, and the Global Climate Change Alliance (GCCA) are among the organizations responsible for developing such initiatives/strategies [10-13]. More details concerned with detected changes in the climate system will be provided later.

According to the report published by IPCC in 2014, the concentration of CO_2 has risen by a third over pre-industrial levels (~280 ppm in the mid-1800s), to above 396 ppm in 2018. The IPCC analysis indicated that the global CO_2 content in the atmosphere must be reduced or limited to avoid increasing the earth's temperature in 2 °C by 2050 [14]. This increase was established as a rational threshold taking into consideration that certain changes in the climate system would become significantly risky for society.

Recent emissions trends (2014-15 study) reported by the International Energy Agency (IEA) point toward the global CO_2 emissions derived from the combustion of fossil fuels undergoing a sharp increase from near zero in 1870 to above 33 $GtCO_2$ in 2014 (see Figure 1-3-(a)) [15]. In terms of countries with a very high-collective emissions influence, Figure 1-3-b) shows China and the United States lead the top emitting countries with 28% and 17% respectively. As it is evident from the pie chart (b) in Figure 1-3, the minority is associated with southern countries from geographical areas like Africa (3%), Latin America (4%) and Middle East (6%) [15].

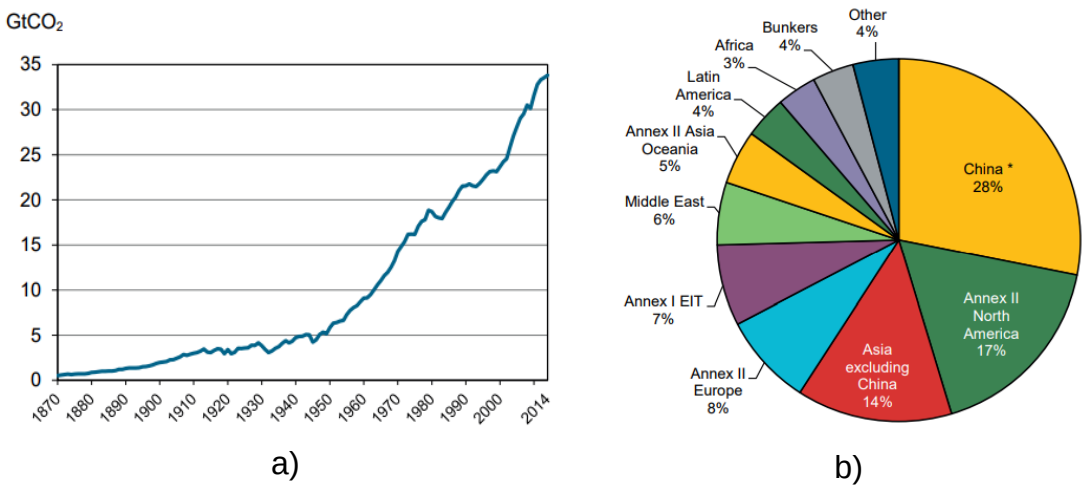

Figure 1-3. a) CO_2 released from combustion of fossil fuels, trend 1870-2014 and b) CO_2 emissions in 2015 classified by region [15].

In relation to the contribution of Mexico on the total annual emissions of greenhouse gases worldwide, the report “atlas of CO_2 geological storage” edited by the department of energy reported that Mexico contributes by approximately 1.67% [16]. Albeit the contribution is relatively low in contrast with industrialized countries such as those aforementioned, Mexico still have a significant contribution when compared with countries such as France, Australia, United Kingdom, etc. [17]. According to Figure 1-4, it can be seen that CO_2 accounts for almost three-quarters of the total emissions of GHG in Mexico. As expected, the human activities make of carbon dioxide the most abundant gas followed by methane with 26%. In reference [16], it was stated that ~709 millions of tonnes of GHG are emitted of which 493 millions of tonnes are associated to CO_2.

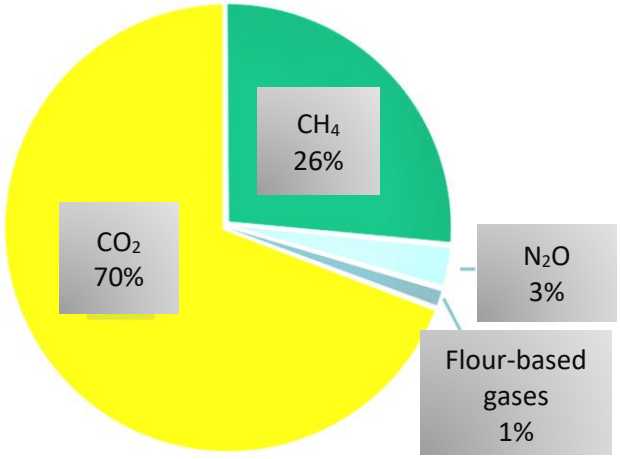

Figure 1-4. GHG emissions by gas in Mexico (2012). Plot customized for a better understanding (converted from Spanish to English) [16].

From the perspective of the worldwide CO_2 emissions by sector, Figure 1-5-(a) indicates that the heat generation and electricity sectors yielded two-thirds of this greenhouse gas in 2015 [15]. As might be inferred, the largest contributions belong to electricity and heat (E&H) with the proportion of 42%, followed by transport with accounted for 24%. From the total CO_2 emitted, it is clear that industry as an end-user represents a majority with 17%, residential emissions also have a high proportion of 11 whilst the minority correspond to transport with only 1% [15].

In terms of the $GtCO_2$ emitted by the combustion of fossil fuels such as gas, oil, coal, etc. for electricity and heat generation during 1990 to 2015, Figure 1-5

shows considerable variations between how fuels were used in this sector 25 years ago with respect to more recent years (2015) [15]. As might be seen, there has been a constant decline in the oil consumption since 1990. Conversely, the share of gas and coal have exhibited an upward trend in the course of these 25 years for the generation of electricity and heat. For instance, coal has shown an abrupt increase from 65 to 72% in contrast with the use of gas, which had a modest rise. Recently, technologies for energy production have started switching from coal to gas although this process has been gradual [9, 15, 18].

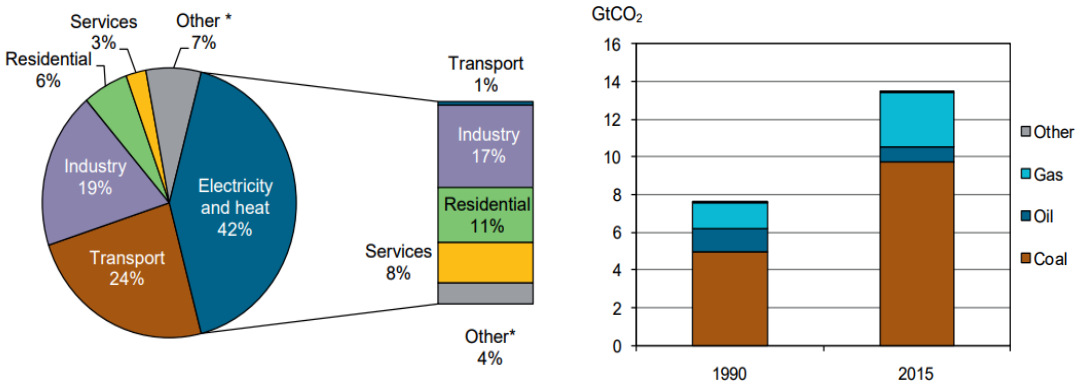

a) b)

*other takes into account agriculture/forestry, energy industry other than enegy and generation (E&H), fishing and other emissions not included.

Figure 1-5. a) Global CO_2 emissions in 2015 classified by sector and end-use. b) $GtCO_2$ emitted into the atmosphere through the electricity and heat generation (E&H) during 1990-2015. The amount released came from the combustion of different fossil fuels such as oil, coal, natural gas, etc. [15].

1.1.1 Climate changes caused by Global Warming Effect

Global warming by definition is the rise of mean atmospheric temperature. As mentioned earlier, the retention of radiation into the atmosphere has been the major driver for the dynamic increase in temperature [19]. The influence of higher temperatures has been such that natural phenomena (disasters) including hurricanes, heat waves, droughts, storms and floods have increased. Some of the common indicators of global warming are presented in Figure 1-6-(a) [20]. As might be inferred, the up/down arrows into the image indicate the direction in which the indicator will impact. Figure 1-6-(b) shows different branches with their respective impacts caused by global warming [21]. The warmer the climate, the

higher the retention, collections and releases of water in the atmosphere. Fluctuations in weather cannot only cause for dry areas to become dryer but also for wet zones to be wetter. Over the last hundred years, the global land-ocean temperature has shown an increase of 0.9 °C [19, 22]. More details of the effects caused per climate change impact will be provided in the course of the present section.

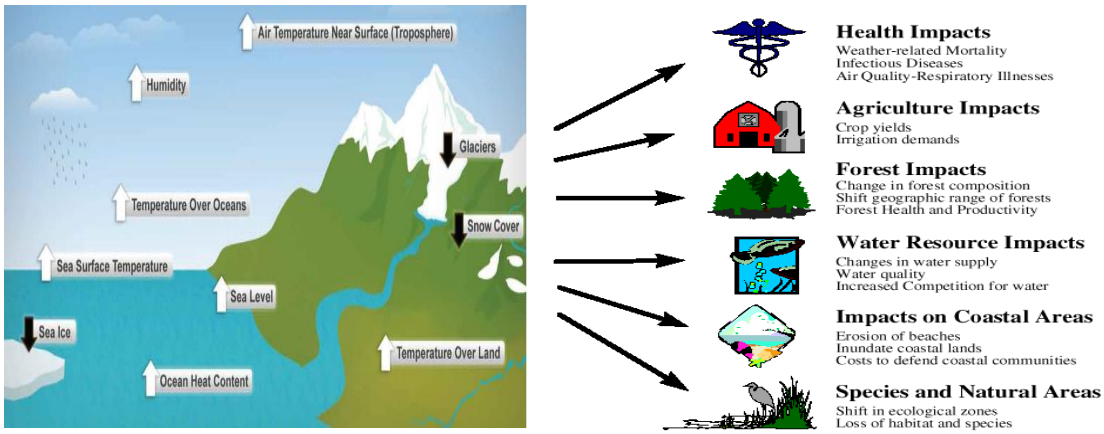

Figure 1-6 . a) Indicators of global warming and b) potential climate change impacts emerged from climate change [20, 21].

From Figure 1-6-(b), it can be observed that hostile effects of global warming also affect indirectly human health causing diseases like malaria. Current research works have pointed out that seasonal distribution changes spread infection vectors. In the case of the dispersion of infections like malaria, weather changes produce relapses of this life-threatening disease in areas where it had been previously suppressed [21].

Changes in weather patterns produced from the warming of the Arctic and Antarctic poles have resulted in extreme changes in the climate systems such as cold winters over certain areas of Europe and Central Africa whilst the Mediterranean could be affected by a very limited rainfall [23]. In addition, another detectable impact on Earth with a steady fluctuation in the surface's temperature is the melting of ice [24]. As might be expected, melting of land ice (poles) has the adverse effect of expansion of the oceans in terms of sea levels (discussed in detail below). With respect to alteration in the precipitations patterns, consequences are devastating. For instance, the power of the

hurricanes witnessed in the last 35 years has been such that coastal towns have been razed [24].

As far as adverse effects of oceanic global warming are concerned, the rising in the sea levels has been manifest since the 20th century. Basically, the expansion of the levels is due to melting of ice layers and glaciers [25]. In addition, this increment produces severe changes in the sea temperature like thermal stratification (temperature variations due to water's density fluctuation at different ocean depths). As it forecasted, the abrupt acceleration of the sea-level will come with catastrophic effects like is a large expansion of the sea in the order of meters. This ongoing secondary effects visualized in oceans will also encourage massive fluctuations in ocean currents [22, 25].

Moreover, it is well-known that one of the ocean functions is absorbing CO_2 from the atmosphere. The mechanism of soaking up carbon dioxide is as simple as putting in contact this gas and mixing it with water. Studies have shown that the ocean is able to capture around one-quarter of the total CO_2 emissions produced by burning fossil fuels [19]. However, if the temperature of the sea surface increases as a direct effect of the global warming, then the ability to uptake CO_2 will be reduced drastically, leaving in the atmosphere higher concentrations of CO_2 that will interact with radiation, further promoting a rise of the average temperature [24]. Additionally, the greater the sorption of CO_2 by the ocean, the higher its acidification. As a consequence, the alkalinity needed to conserve life in the ocean would be unbalanced, causing alterations in flora and fauna [24, 26].

In the context of sea level fluctuations generated by climate changes in Mexico so far, the coastal zone of the Caribbean and Gulf of Mexico have been the most susceptible to the increase of sea levels [27]. The acidification of the oceans has also been a crucial factor in the deterioration of coral reefs mainly in the South-eastern Mexico of the Yucatan Peninsula. As a result of changes in the climate system, Mexico has vulnerabilities in terms of rain, tropical cyclones, droughts, health, access to water and food, etc. [27]. An itemized analysis of those vulnerabilities is provided further down.

Mexico has also shown alterations related to natural phenomena like El Niño. This climate pattern is caused when the water's surface is warmed in the eastern

tropical region of the Pacific Ocean. It has been assessed that El Niño phenomenon has been intensified in the last years not only causing floods but also has impacted in the natural environment and economics of the country [28].

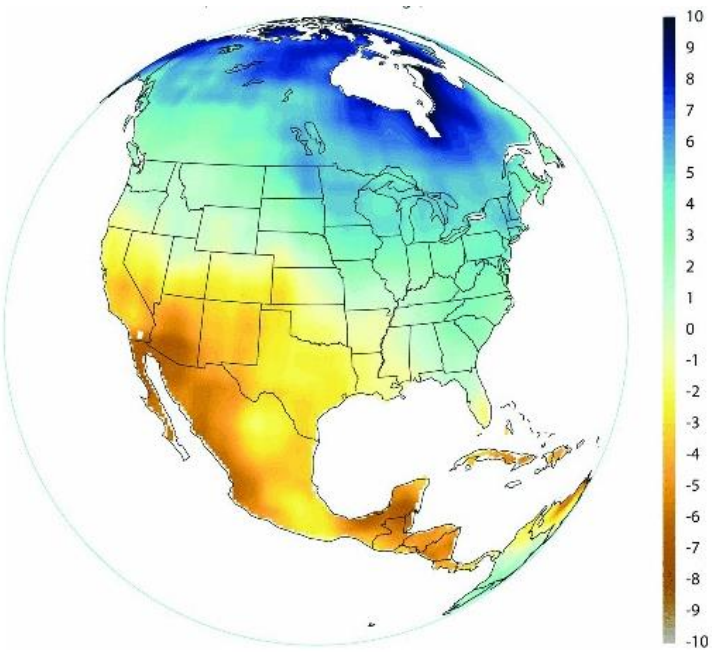

Figure 1-7. Projected change in precipitation for the periods of 1950-2000 to 2021-2040 in Mexico. Map obtained from the National Oceanic and Atmospheric Administration (Geophysical Fluid Dynamic Laboratory) [29, 30].

Although rising sea and ocean levels will not have the same impact in Mexico (giving its high altitude) compared to countries like China, India, Vietnam, Japan, U.S., Brazil. Etc., its low-lying coastal areas are susceptible to changes [29]. The map presented in Figure 1-7 is built on the basis of the mean over 1950-2000 and shows the projected changes in precipitation during 2021-2040. According to this map, Mexico has a high possibility of intensified impacts derived from global warming. Furthermore, it is clear that the northwest, center and southeast of Mexico will present a severe depletion in rainfall owing to the increase of temperatures [29]. Harrison et al. [31] in 2009 reported the possibility of a severe expansion of these phenomena for coming years. Based on their estimations, close to 10 years later, the predicted impacts of global warming are confirmed through the sharpness of some adverse effects such as energy and water demand, droughts, etc. In the agricultural sector, the most arid part of Mexico (Northwest) has exhibited a decline in rainfall. The absence of water induced by

the increase in temperature observed in the projections has started generating conflicts in the agriculture sector as well. The forecast shown in the map of Figure 1-7 has allowed confirming that arid and semi-arid regions have been also affected in terms of the affluence of rivers [27, 29, 30].

1.2 Approaches to global climate stability and mitigation of CO_2

The timeline of greenhouse gases emissions since the industrial revolution transition points out that, to avoid reaching 550 ppm in this century and maintaining the warning levels in a limit of 2 °C, preventive strategies must be implemented [32]. Projection suggested by Allen et al. [33] indicates that the boundaries in emissions of CO_2 released to the atmosphere must be lower than 200-400 GtC. In regards to the effects of fossil CO_2 emissions, adverse effects are most notorious during the first 300 years upon the release of the gas [32]. However, a great drawback of fossil CO_2 is its longevity in the atmosphere, with the cumulative mean life of 30 000 years. The long-life and timescale of the effects caused by carbon dioxide can be comparable with the hazard period of radioactive wastes. The plot presented in Figure 1-8 gives evidence of the prolonged life and adverse effects of CO_2 in the atmosphere [32].

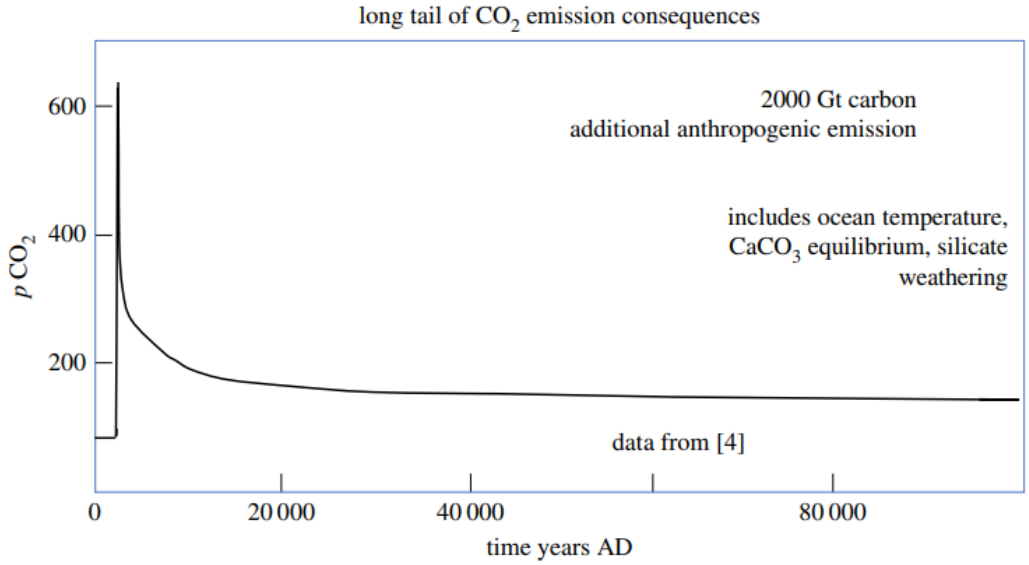

Figure 1-8. CO_2 timeline showing three negative characteristics of this GHG: long residence time, adverse effects still notorious for 30000-100000 years and depletion of CO_2 atmospheric concentrations are gradually at a very slow rate [32].

In the endeavour to mitigate the cumulative emission of the second most abundant and important greenhouse gas after water, climate agreements have been encouraged to make nations adopt compromises to either control or eradicate the release of CO_2 into the atmosphere by anthropogenic sources. Evidently, in order to reach this target, the amount emitted by the CO_2 source must be equal or lower than to that removed from the atmosphere. In the Paris Agreement held in 2015, there was a clear aspiration for counteracting the GHG emissions to achieve an average temperature rise of 1.5 °C below pre-industrial levels, and a solid target to remain below 2 °C. Evidently, the Paris agreement specifies that to achieve the qualitative temperature limits aforementioned, a net-zero anthropogenic emissions concept must be applied. Basically, it is conceptualized as reaching a balance between emissions released by CO_2 sources and CO_2 uptake in sinks of GHG by 2015 [34]. According to an assessment performed by the International Energy Agency (IEA), it was predicted that a considerable contribution of carbon capture and storage (CCS) technologies ought to play a role in the reduction of the global CO_2 emissions, namely between 15 and 20% (6000 $MtCO_2$/yr) by 2050 [35].

Categorizing the options available to remediate the climate change, three are conceived: 1) cause and effect, wait for consequences caused for the adverse effects of climate variations, 2) create, develop, improve and deploy technologies related to protection from solar radiation by reflection and 3) control (reduction in the emission rate) and mitigate emissions of CO_2, this includes removal/recapture this CO_2 emitted previously [32]. More specifically, the strategies considered for reducing CO_2 emissions around the globe encompasses: 1) promoting the use of fuels with low-carbon content comprising natural gas or hydrogen/nuclear energy, 2) expanding usage of renewable energy where wind, bioenergy and hydropower would represent the most important ones, 3) deployment of geoengineering such as afforestation and reforestation, 4) optimization and 5) improvement in the conservation and efficiency of energy and carbon capture and storage (CCS) [36]. The last option has been conceived as a promising option since technologies linked with CCS can have immediate large-scale impact. The intrinsic advantages and limitations of the aforementioned five approaches are presented in Table 1-1. As can be seen, approaches fare well and badly in different aspects such as energy

conservation, usage of clean fuels, source emission reduction, technologies with clean coal, etc. Evidently, those technologies must also cover requirements established by the IPCC in terms of CO_2 emissions by 2050. Taking into consideration the relevance of CCS for the present research, the literature review will be focused in all matters related to this area.

Table 1-1. Summary of strategies for mitigation of CO_2 [36].

Strategy	Application area/sector	Advantages	Limitations
Enhance energy efficiency and energy conservation	Applied mainly in commercial, domestic and industrial buildings.	Energy saving from 10% to 20% easily achievable.	May involve extensive capital investment for installation of energy saving device.
Increase usage of clean fuels	Substitution of coal by natural gas for power generation	Natural gas emits 40–50% less CO_2 than coal due to its lower carbon content and higher combustion efficiency; cleaner exhaust gas (lower particulates and sulphur dioxide emissions).	Higher fuel cost for conventional natural gas. Comparable cost for shale gas.
Adopt clean coal technologies	Integrated gasification combined cycle (IGCC), pressurized fluidized bed combustor (PFBC) etc. to replace conventional combustion.	Allow the use of coal with lower emissions of air pollutants.	Significant investment needed to rollout technologies widely.
Use of renewable energy	Hydro, solar (thermal), wind power, and biofuels highly developed	Use of local natural resources; no or low greenhouse and toxic gas emissions.	Applicability may depend on local resources availability and cost. Power from solar, wind, marine etc. are intermittent and associated technologies are not mature; most current renewable energies are more costly than conventional energy.
Development of nuclear power	Nuclear fission adopted mainly in US, France, Japan, Russia and China. Nuclear fusion still in research and development phase.	No air pollutant and greenhouse gas emissions.	Usage is controversial; development of world's nuclear power is hindered due to the Fukushima Nuclear Accident in 2011, e.g. Germany will phase out all its nuclear power by 2022.
Afforestation and reforestation	Applicable to all countries.	Simple approach to create natural and sustainable CO_2 sinks.	Restricts/prevents land use for other applications.
Carbon capture and storage	Applicable to large CO_2 point emission sources.	It can reduce vast amount of CO_2 with capture efficiency >80%.	CCS full chain technologies not proven at full commercial scale.

Chapter 2 Literature Review

2.1 World energy consumption and production

In the last 20 years, the world energy demand has presented a drastic rise propelled by a sharp economic growth in countries with a prominent urbanization and industrialization. A projection indicates that the global energy consumption will increase from 2015 to 2040 by around 28% [37]. It has been estimated that the cumulative energy consumed by economies like China and India would account together by half of the global amount over the period projected (25 years). In the list of regions with high-energy consumption is America at which Canada, United States, Brazil and Mexico demand the greatest supplies (Figure 2-1) [37].

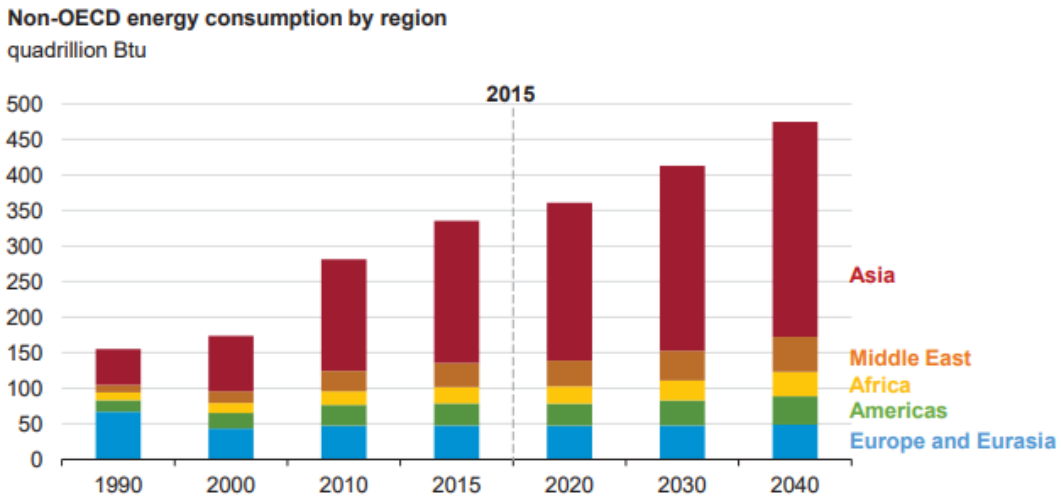

Figure 2-1. Energy consumption by region in the period 1990 to 2040 (Projection) [37].

As it might be inferred, the economic growth is a key factor that affects the world energy demand. The energy market forecast that the electricity consumed will be supplied mostly by fossil fuels (coal, oil and natural gas) with a contribution of around 77% by 2040 [37]. Evidently, the percentage corresponding to renewable sources is the rest and amounts to 23%. Presumably, the long-term projections indicate with the energy source with the sharpest growth is associated to renewables with a consumption average rate of 2.3%/year during 2015-2040 whilst the second one is attributed to nuclear power with an energy consumption rise of 1.5% over the same period of years [37].

In terms of global primary energy consumption derived from fossil fuels, oil has had the greatest contribution with 44% in 1971 and 32% in 2015 (see Figure 2-2-(a)). However, projections indicate that natural gas will be positioned as the primary source of energy with an annual increase of 1.4% towards 2040 [38]. Clearly, the natural gas market has presented a noticeable rise due to the existence of plentiful natural reserves proved worldwide with a rising production specifically of shale gas, coalbed methane and tight gas. Figure 2-2-(b) indicates that the Middle East and Eurasia harbour the greatest natural gas reserves proven by 2016 [39].

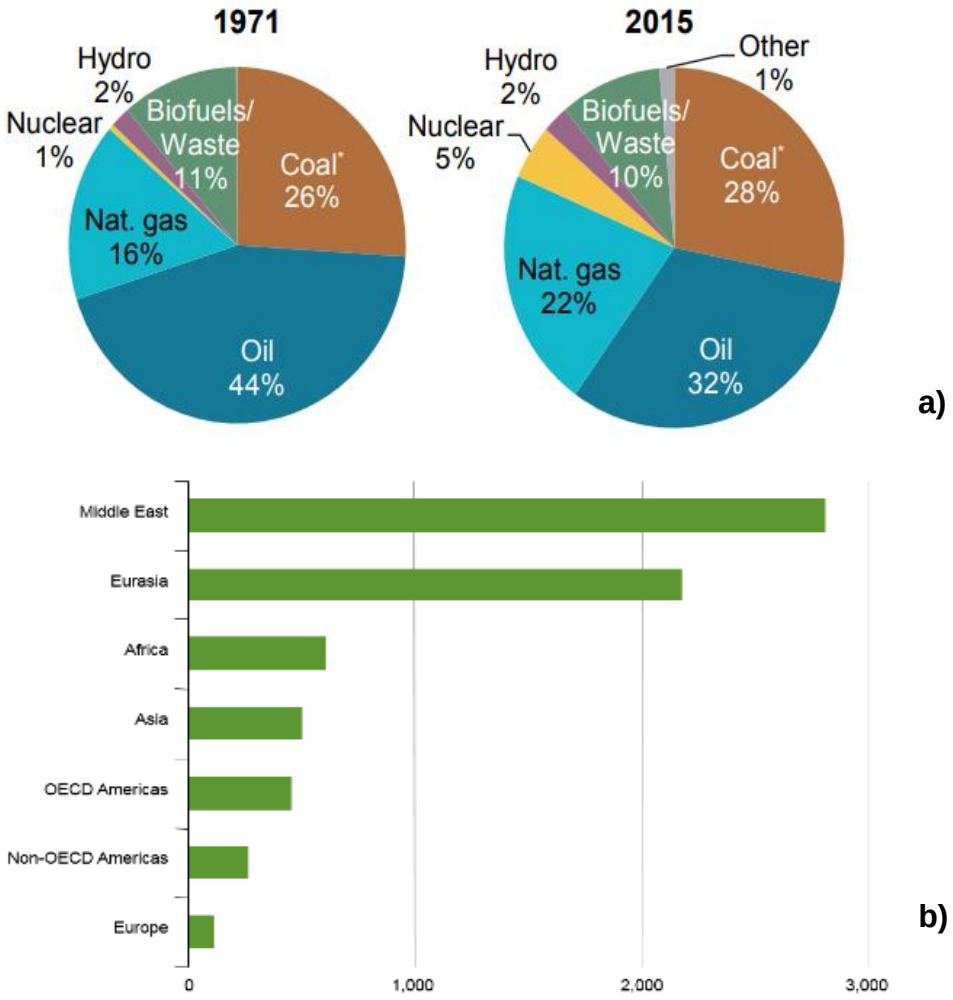

Figure 2-2. a) Global primary energy consumption by fossil fuel in 2015 [39] and b) world's biggest natural gas reserves verified in 2016 [40].

According to the International Energy Agency, coal reaches the crest in use in the 2000s. Although the role of coal has remained steady in the last years, this fossil fuel has been vital to cope with the world energy demand up to date. With

the development of renewable energy and the use of nuclear power and natural gas, the replacement of coal has been increasing. A forecasting indicates that the global coal consumption by country will reduce by 2040. In the particular case of the largest coal consumer, which is China, this decrease would have a yearly rate of 0.6%. The predicted share of coal will decline from 28% (Figure 2-2-(a)) to 22% towards 2040 [37, 38].

2.1.1 Energy production from natural gas and benefits

Natural gas has become one of the primary energy sources due to lower pollution and environmental impacts compared to oil and coal. Natural gas contributes substantially in the control of emissions of GHG into the atmosphere. Natural gas's advantages can be seen in Table 2-1, as reported by the US Environmental Protection Agency [41]. In terms of CO_2, sulphur dioxide (SO_2) and nitrogen oxides (NO_X), coal and oil present higher ratios and contents owing to these two fossil fuels' more complex molecular structure. Evidently, due to the nature of natural gas, its combustion releases a lower amount of harmful gases into the atmosphere whilst coal not only emits particulates but also metals, including mercury [41].

Table 2-1. Emission levels of different fossil fuels in tonne per million kWh of energy input [41].

Pollutant	Natural Gas	Oil	Coal
Carbon Dioxide	181039	253764	321847
Carbon Monoxide	62	51	322
Nitrogen Oxides	142	693	707
Sulphur Dioxide	1.5	1736	4009
Particulates	11	130	4246
Mercury	0	0.011	0.025

Natural gas for energy production has also inherent advantages that include cost, abundance, continuity of supply and ease of transportation by means of the pipeline [42]. From the efficiency perspective, cogeneration using natural gas permits increasing the efficiency in the production of electricity and heat, which

directly impacts in amounts of fuel consumption, and the proportion of GHG released during the industrial process. Reburning as a method of industrial NO_2 control at coal or biomass fired power stations is another benefit that encourages the industry's use of natural gas. This process implies partially feed natural gas in industrial boilers that conventionally burn oil, coal or biomass. The advantages of reburning is related to environmental issues since injecting natural gas can diminish between 50 to 70% the total emissions of NO_2, whilst the impact in depleting SO_2 is 20-25% [42].

In combined cycle power plants, the use of gas contributes with a substantial increase in efficiency with respect to traditional fuel-based power plants, namely up to 50%. The suitability of the combined cycle generation process comes from the recuperation of waste heat from the natural gas turbine. The heat recuperated is routed to a steam turbine aimed to produce supplementary power. In addition, benefits in this process can be seen in fuel savings and reductions of GHG emissions [43].

From the standpoint of investment, burning natural gas rather than coal would represent a decrease in the number of operation units required to scrub SO_2 from flue gas. Due to the minimum content of SO_2 in the burned natural gas, which was easily desulphurised by scrubbing its H_2S at the point of gas extraction, no SO_2 scrubbers are needed downstream of the combustion process and no sludge will be produced in the industrial processes (power plants).

Application of natural gas in fuel cells is apparently another advantage as energy with very low emissions can be obtained. Although fuel cells have shown a considerable efficiency improvement and they are able to produce electricity with fewer net CO_2 emissions compared with fossil fuel-based processes, incorporating natural gas straight or as a H_2 source into fuel cells is still in development.

Adding to the list of benefits derived from applying natural gas to reduce pollution, emission of CO_2 and simultaneously generating energy, hydrogen produced from natural gas as an energy carrier has contributed not only to cope with electricity demand but also deal with issues concerned with the preservation of the environment. Clean fuel (H_2) is produced with less environmental impacts by reforming natural gas rather than gasifying coal (harmful fuel) or biomass. Taking

into consideration this PhD's research is focused on the study of materials for capturing CO_2 emitted from steam reforming of natural gas, technicalities of this chemical process and importance of H_2 production will be provided in the upcoming sections [43-45].

2.1.2 Hydrogen Basics - Demand and Economics

Hydrogen has been identified as a potential solution to cope in a medium and long-term with the demand in the energy and transport sectors. Hydrogen has caught the attention of researchers and investors since it is a clean energy carrier that can be obtained from a wide variety of sources [46]. H_2 fuel has also as a major benefit being able to generate heat and power with net-zero emission (e.g. fuel cells with an environmental friendly energy production) [47]. Because of its suitability in different fields, the global market of H_2 not only has grown but also has driven to invest in research and development for deploying novel routes and technologies for H_2 production and utilization [48]. Despite an outstanding deployment of systems for covering the demand of H_2 in the market, there is still plenty of work and improvements to be overcome in order to transform a hydrogen economy in a reality. Undoubtedly, the biggest hurdle to achieve a complete evolution on this energy sector is developing its infrastructure [49].

Particularly, the transport sector is one of the greatest challenges as the world's demand currently represent roughly one-third of primary energy. An analysis of hydrogen demand performed by Balat et al. [50] has shown that a key factor that must be taken into consideration is the development of feasible energy conversion techniques. For instance, aircraft as a transportation mode could potentially use hydrogen fuel but this technology is immature. H_2-based aircrafts require enhancement not only in fuel-conversion systems but also in developing devices with high-storage capacity able to provide enough fuel during long trips, particularly in view of the low density of H_2 gas. A forecast showed that the strongest contributions of hydrogen as an energy carrier would be marked by 2050 just when substantial amounts of fossil fuels (petroleum) represent a constant displacement by hydrogen [50]. In the same investigation, Balat et al. [50] estimate that in addition to transportation, the second hydrogen demand as

fuel is associated with cogeneration applications, which in other words means a sequential production of heat and power mainly for the industrial and residential sectors.

Hydrogen demands for stationary fuel applications have different constraints with respect to the transport sector. In stationary systems, hydrogen supply infrastructure represents the main issue and challenge to overcome. This issue can be sorted out confining the hydrogen to a bonded region where the supply's demand for energy might be covered successfully. This method will become attractive only when stationary applications manage to couple satisfactorily with carbon capture and sequestration technologies [51, 52].

As mentioned above, the demand for hydrogen has a great impact in the industrial sector, specifically in chemical processes. For instance, currently large amounts of hydrogen are used in petroleum refining because H_2 is fundamental to perform the hydrodesulphurization and hydrocracking operations. Additionally, hydrogen is extensively used for the manufacture of bulk chemicals such as ammonia as basis for fertiliser production and alcohols [53].

2.1.3 Technology for Hydrogen Production

Hydrogen can be found naturally as a chemical element in water and in small amounts mixed with other hydrocarbons (natural gas). Hydrogen gas can be produced from three main sources; the reforming of fossil or bio-derived fuels, water electrolysis and thermochemical cycles powered by nuclear, and water electrolysis powered by intermittent renewable energy. Nowadays, a wide range of industrial processes can be used for the production of high-purity hydrogen; among them, we can find thermochemical processes, electrochemical processes, photocatalytic processes or photo-electrochemical processes, photochemical processes and biological processes. Figure 2-3 illustrates alternative technologies proposed for hydrogen production in small and large-scale using different energy sources [52-57].

Figure 2-3 confirms that thermochemical processes can be a versatile way of obtaining H_2. These methods involve water splitting at high temperatures (500-

2000 °C) where a series of chemical reactions drive the dissociation of water molecules. The global efficiency and lower production costs permit to consider thermochemical processes as a profitable option to produce pure H_2 [58]. With respect to electrochemical processes, hydrogen is produced by a forward electrolysis of water producing hydrogen and oxygen. The electrolysis systems termed solid-oxide electrolysers are designed for operating at high temperatures (650-950 °C) [59].

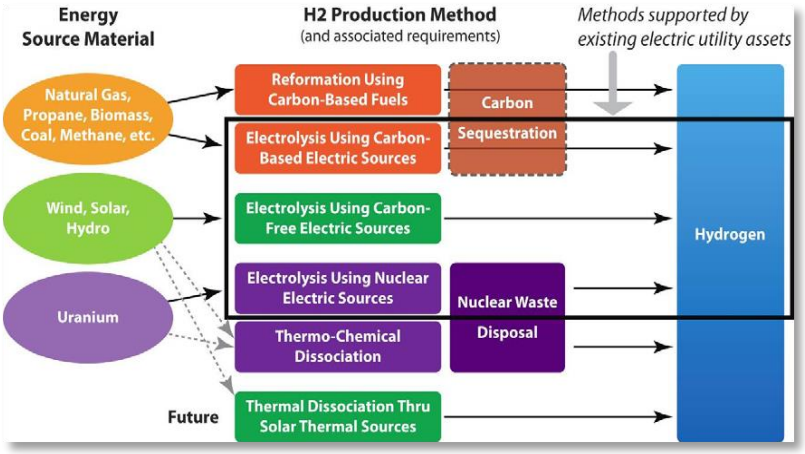

Figure 2-3. An overview of proposed methods for high-purity hydrogen production [54].

In the same window of feasible methods for producing H_2 by means of water splitting, we find photochemical processes. A consistent example is a photolysis at which the process is carried out by a direct extraction using only solar radiation as a primary energy source [51, 55]. The principle of hydrogen production by photolysis offers a significant cost reduction compared with other technologies that performs the splitting of molecules of water in several steps like the particular case of photocatalytic water splitting. In order to increase the production of hydrogen, a hybrid system coupling both photolysis and a photobiological system would help substantially [50]. Evidently, hybrid systems are designed to reach the highest yield and conversion in only two steps: 1) photosynthesis and 2) hydrogen production. During the second stage, the efficiency also might be increased adding a hydrogenase catalyst (for instance: aquatic organisms).

In regards to hydrogen production using a chemical process, biomass conversion has attracted the attention of researchers and the industry sector due to the profitability of the method. Although it is considered an immature

technology, the potentiality of biomass conversion technologies not only comes from renewability of biomass but also from the low CO_2 emissions released. In general, biomass transformation consists in decomposing and partially oxidizing biomass; the result is a gaseous mixture stream composed by methane, hydrogen, nitrogen (N_2), carbon monoxide (CO), and CO_2. Then, the gas stream is fed into a shift reactor where hydrogen yield increases due to the high temperature and conversion. The last stage in the transformation of biomass implies the purification of the outlet gas coming from the reactor. The gas purification to H_2 is accomplished employing a pressure swing adsorption unit performing the separation and maintaining a hydrogen purity of 95-99% typically with an efficiency of 80-90%, i.e. 10 to 20% of the H_2 in the gas mixture is not separated [51, 55-57].

Despite efforts conducted so far to develop new systems for clean energy production, fossil fuels currently continue being the primary source for hydrogen production. Conventionally, fuels utilized like a feedstock for driving the conversion toward H_2 are mostly short-chain hydrocarbons and in smaller proportion coal or oil. As shown in Table 2-2, around 96% of the global hydrogen production comes from steam reforming processes (SR) and gasification, which obviously implement fossil fuels as the raw material such as natural gas or those aforementioned. Although SR is a mature chemical system with high H_2 yield, other routes based on reforming process or oxidation such as autothermal reforming (ATR) and partial oxidation of hydrocarbons (POX) could produce H_2 with a lower H_2 yield but more favourable energetics. In the case of ATR process, it is a configuration derived from the integration of both SRP and POX [56, 60].

Table 2-2. Amount and share of hydrogen produced annually classified by source [50].

Source	Bcm/year	Share (%)
Natural gas	240	48
Oil	150	30
Coal	90	18
Electrolysis	20	4
Total	500	100
Bcm: billions cubic meters		

Taking in consideration the relevance of SR not only in H_2 production but also in this research project, as the application of the sorbents prepared in the present work have application to SR enhanced with CO_2 capture, an overview of this chemical process will be provided in later sections.

2.2 Carbon capture and Storage

In recent years, the portfolio of applications for mitigating and controlling emissions of CO_2 into the atmosphere has been considerably extended. In the case of CCS technologies, they have been catalogued as one of the most promising solutions for reducing CO_2 released by the industrial sector [36]. A highlight in CCS systems is their flexibility due to their utilization being not only limited to the power generation sector but also its scope over economies with a marked reliance on fossil fuels. Figure 2-4 presents an intuitive scheme displaying a range of applications of carbon capture and storage technologies to both domestic and industrial sectors.

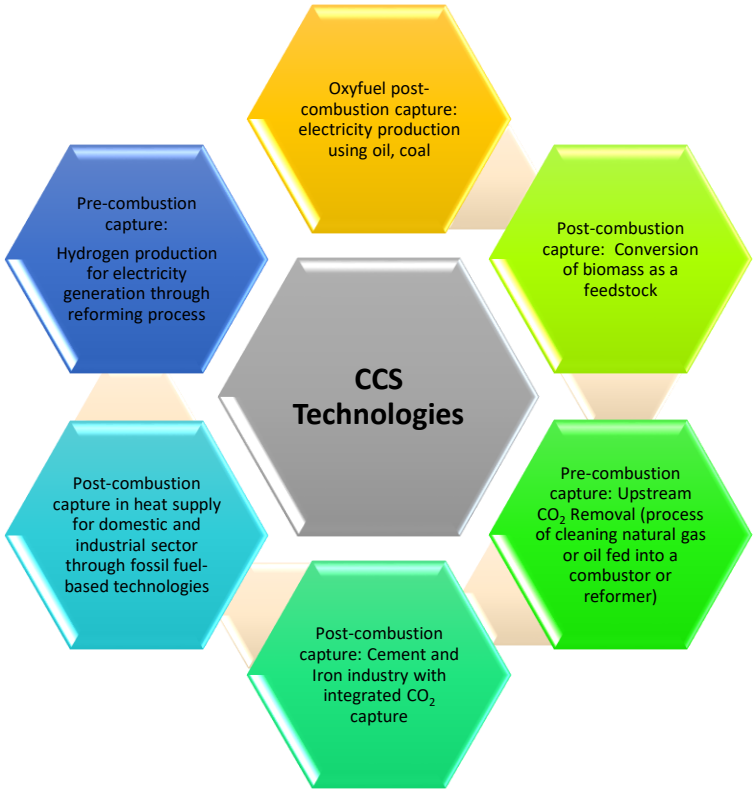

Figure 2-4. Portfolio of CCS applications in domestic and industrial processes with reliance in fossil fuels.

To visualize the role and relevance of CCS technologies in the portfolio of options to control the emissions of CO_2, Figure 2-4 is presented. In the power sector, different scenarios projected that CCS systems will have a contribution that would account for 19% on the basis of the total CO_2 savings by 2050 (Figure 2-5) [44]. Although CCS technologies are not the greatest contributor for depleting emission of CO_2, their roles are considered vital to maintaining atmospheric concentrations of GHG under allowable limits (2 °C scenario) [61].

In general, the CCS chain comprises a set of unified steps that initiate with the purification and separation of CO_2 from any feedstock/fuel or chemical process. Upon removal of CO_2, the subsequent process consists in transporting the CO_2 previously compressed to the final destination, namely a storage area. The last but not less important step is concerned with the final injection of CO_2 into a reservoir [32, 62, 63]. As might be inferred, a reservoir also termed storage formation must meet certain requirements: rocks with high porosity, and voids for enhancing the permeability of CO_2 during the injection [64]. Pores in the geological storage must be interconnected to have an acceptable distribution of the gas. In addition, to trap the CO_2 for thousands of years, the sedimentary basins must have a rock fence that keeps the injected gas in place [64].

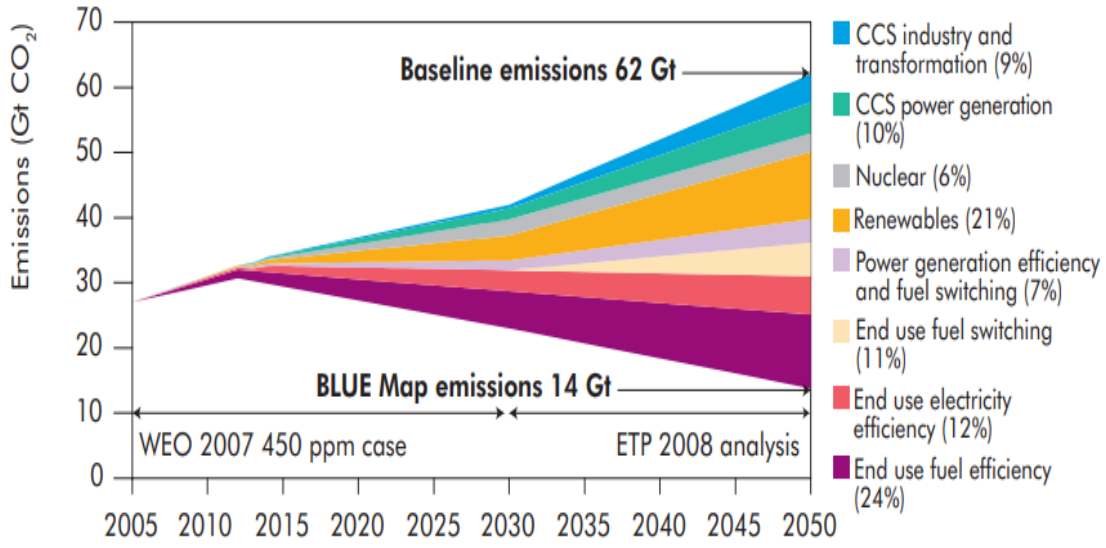

Figure 2-5. Contributions of CO_2 saving in the power sector by 2050. Projections based on scenarios targeting improvements in sectors related to energy efficiency [44].

2.2.1 Carbon capture technologies

The chemical and petrochemical sectors, petroleum refineries, production of cement, iron and steel are industrial sources producing 2755 $MtCO_2\ yr^{-1}$ of CO_2 emissions [65]. Their use in the energy sector, specifically in fossil-fuel and industrial processes, has not only exacerbated releases of CO_2 into the atmosphere but has also contributed worldwide with around 65% of total GHG gas emissions (contribution by gas) [9]. As might be inferred, any of those point sources are latent candidates for adapting CCS technologies [66, 67]. The nature, wide diversity and engineering design of the industrial processes aimed to generate energy preclude the existence of a multifunctional system with a unique configuration and dimensions. As a result of the design constraints and needs, compatibility and flexibility are two factors that have transformed CO_2 uptake systems in viable options [36, 68]. For instance, commercial technologies that have overcome difficulties of integration in which the management of streams and energy optimization have been a challenge are the production of compounds like “syngas”, ammonia and hydrogen. These chemical processes particularly conditioned for removing CO_2 from currents with gaseous mixtures not only represent mature technologies but also industrial systems designed with state-of-art CO_2 capture at a large scale [69]. Citing another instance, oil refineries are near scaling up a CO_2 capture system and implementing it at industrial scale [68]. Conversely, the manufactures of iron-steel and cement have had a slower evolution in the implementation of large-scale CO_2 removal systems since a number of barriers have been encountered to date in small demonstration plants [68].

Oxyfuel combustion, pre- and post-combustion carbon capture technologies able to remove anthropogenic CO_2 emissions from power generation and large-scale plants are currently undergoing intensive R&D efforts not only to increase the capacity of uptake of CO_2 but also to reduce energy penalties caused by the high temperatures and materials flows used to regenerate the CO_2 carrier. CCS systems are under severe scrutiny also to reduce the operating costs. The classification of capture systems for power plant applications and industrial processes using fossil fuels (coal, natural gas or oil) and biomass as a feedstock encompasses pre-combustion (pre-conversion), post-combustion (post-

conversion) and oxyfuel combustion. In the subsequent subsections presented below, is presented a detailed description of the three main options visualized in the scheme showed in Figure 2-6 taken from the special report published by IPCC in 2005 [65].

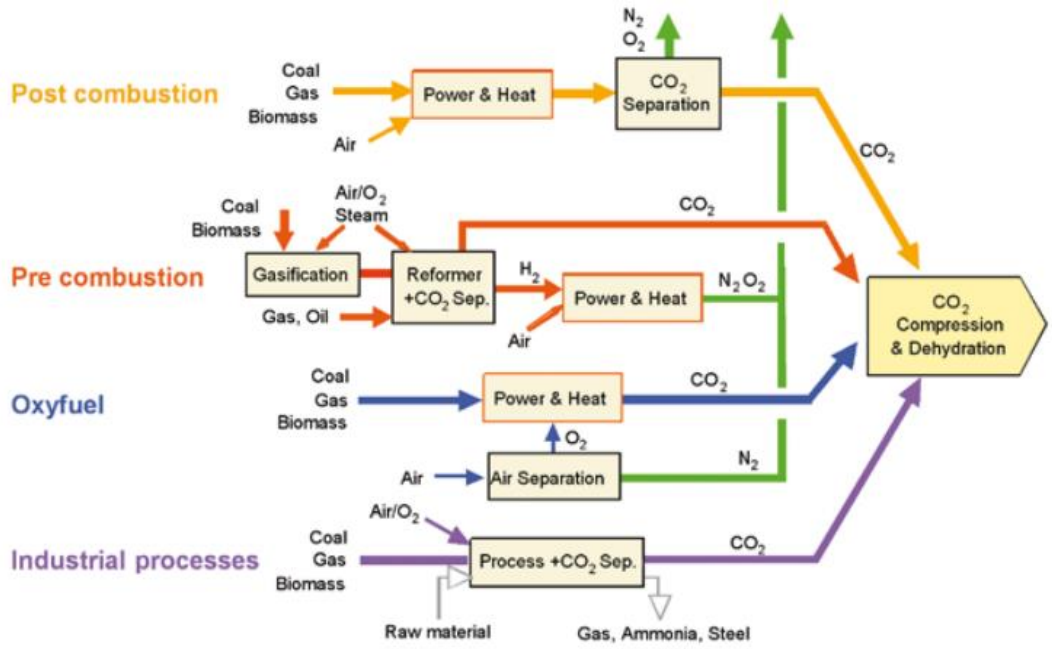

Figure 2-6. Carbon capture technologies for removing CO_2 from point sources such as power generation and large-scale plants.

2.2.2 Oxyfuel combustion capture

In the oxyfuel-combustion capture, oxygen (O_2) typically produced from air by means of a cryogenic air separation unit or using another technology such as membranes and chemical looping cycles, is introduced in conjunction with fuel into a reaction system [65, 68]. The burning process has a character merely exothermic (i.e. it generates heat). In presence of pure O_2, the flame temperature can reach 3500 °C. In order to control the temperature, flue gas mainly composed by CO_2, water vapour with excess O_2, diluents and inert is recirculated to the decrease the combustor temperature by up to 1300-1600 °C [70-72]. From there, the stream is subjected to water condensation to produce a dry gaseous mixture enriched with CO_2, namely with 80-98% purity [65]. Finally, oxyfuel-combustion technologies perform the separation of carbon dioxide in the last step. In Figure 2-7, it can be seen a conventional configuration of oxyfuel-combustion capture in a coal-fired power station.

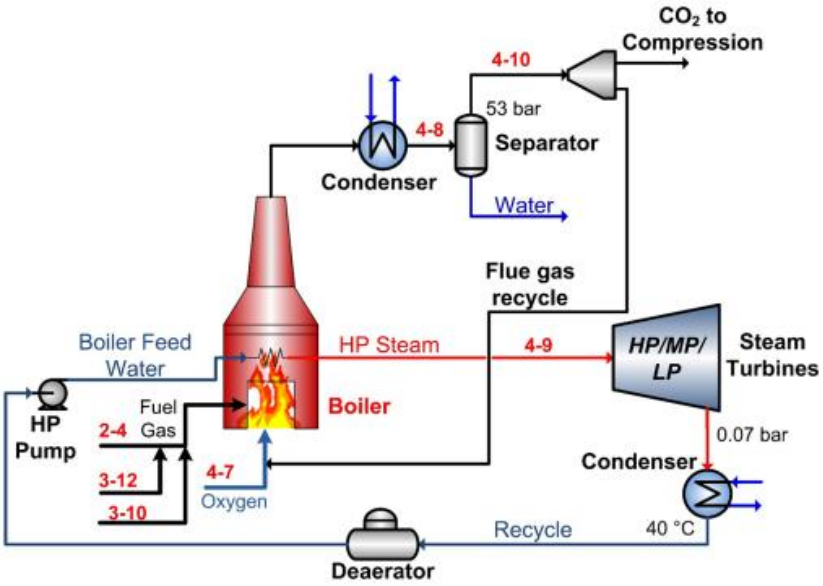

Figure 2-7. Capture of CO_2 using oxyfuel-combustion technology in a power generation process [73].

2.2.3 Post-combustion capture

In post-combustion capture systems, CO_2 is caught from gas streams (flue gases) once biomass or fossil fuels exposed to air produce a combustion reaction. The flue gas rich in CO_2 generated during the conversion is fed into a system that removes a very high percentage of CO_2. Evidently, after the separation process, flue gases with a slight portion of CO_2 are released into the atmosphere since investing in an additional CO_2-separation unit would imply large capital but also an energy (operation) penalty. The stream with almost pure CO_2 is compressed at high pressure (53 bar) and finally transported for storage in a geological reservoir [9, 65, 68].

Currently, the techniques used to capture CO_2 in post-combustion systems include physical sorption by means of sorbents for low temperature (>200 °C) such as membranes, metal-organic frameworks, cryogenic separation, pressure and vacuum swing adsorption and physico-chemical sorption with liquid sorbents (mainly amines-monoethanolamine (MEA)). Amines, in particular, have been extensively used not only because of their low cost but also due to their ability to being regenerated under low energy requirements [74]. To exemplify the removal

of CO_2 using post-combustion technology in an industrial process, Figure 2-8 was added.

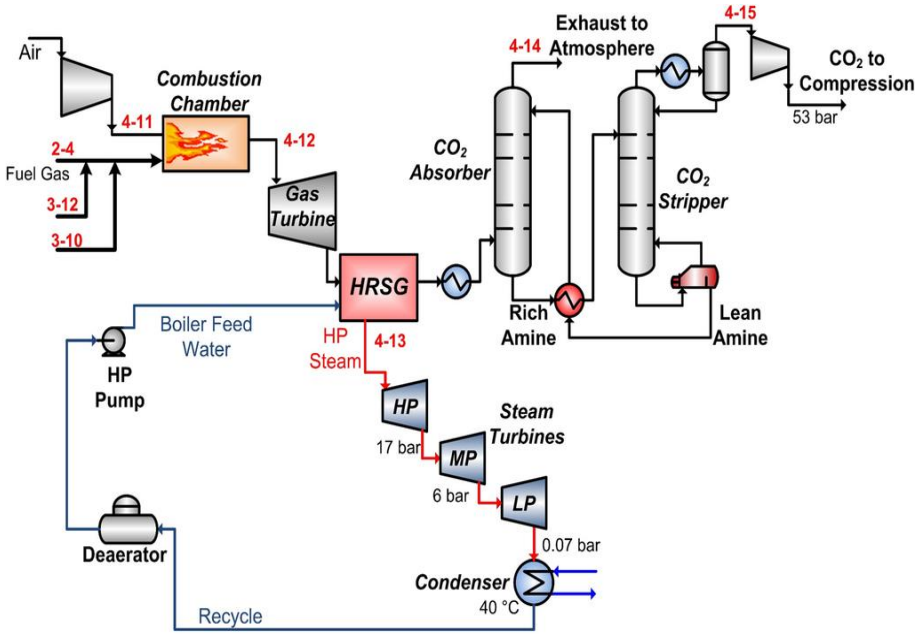

Figure 2-8. Solvent–based capture conducted in a power generation plant [73].

In the power generation system presented in Figure 2-8, which has integrated post-combustion conversion, the absorption of CO_2 is conducted using amines. A conventional amine-based absorption process consists of two units, namely an absorption and a stripper unit. In the absorption unit, amines retain most of the CO_2, and the gaseous mixture leaving the absorber is then released into the atmosphere. The CO_2-rich amine is driven by pumping towards a stripper column in which the captured gas is desorbed when chemical bonds are broken by the effect of temperature (whose heat is provided by a reboiler, representing the largest energy demand of this CO_2 separation process). The outlet stream (gaseous mixture with a CO_2 purity of 90-96%) is lastly compressed and transported for being storage [65, 73, 75-77]. This process represents an industrial reference of current applications of post-combustion conversion.

2.2.4 Pre-combustion capture

Pre-combustion capture systems aim to remove CO_2 from a gaseous mixture generated by gasification of coal, biomass or steam reforming of a volatile or

gaseous organic feedstock such as natural gas, naphtha or bio-oil. As a result of the gasification or reforming reactions where the fuel reacts with oxygen or steam respectively (or both) over a catalyst at high temperature (600-1200 °C), a mixture composed by mainly H_2 and CO is produced, but the operating pressure (ca. 30 atm) also creates significant methane by-product. The blend, also termed "syngas", is fed into a catalytic reactor at lower temperature (<300 °C, water gas shift or "CO-shift" system) to further react with steam. From the product mixture H_2 and CO_2, still polluted with unreacted CH_4, the gas of interest is treated and then physically separated by using an absorbent. As might be inferred, a physical absorption is preferred since it is cheaper with respect to not only the material but also investment and thermal efficiency (lower energy penalty). The CO_2 further separated is compressed and transported whilst the H_2 produced and unconverted methane can be used in many ways such as energy production (H_2 turbine), boilers, fuel engines, fuel cells, furnaces, etc… Clear examples of pre-combustion reactions are gas heated reformer, steam reforming, auto-thermal reforming and partial oxidation processes; all of them have in common feedstock gases based on light hydrocarbons [65, 70, 72, 78-80]. Figure 2-9 presents a conventional chemical process (integrated gasification combined cycle (IGCC)) at which the CO_2 is captured using pre-combustion technology.

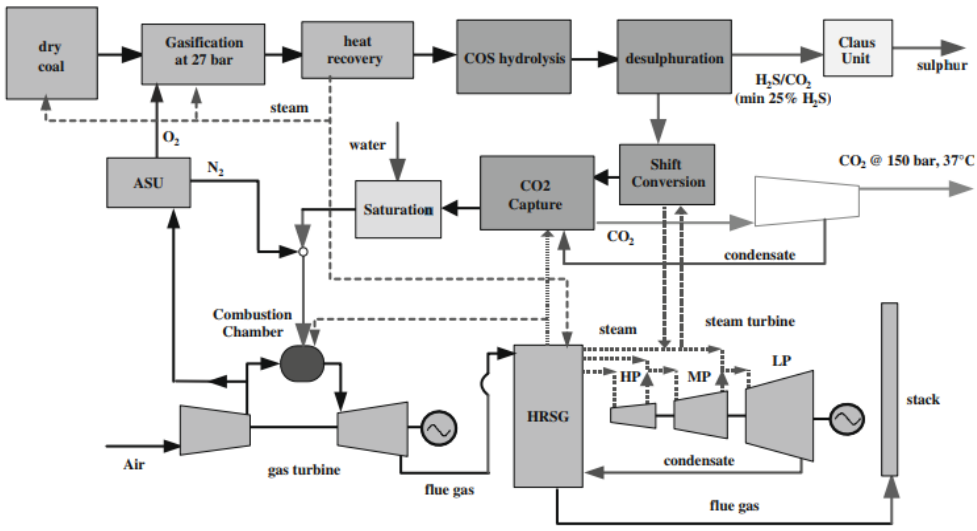

Figure 2-9. IGCC with integrated pre-combustion capture conducted by means of physical absorbents like amines [80].

Table 2-3. Advantages and implementation barriers in CCS technologies [71].

Advantages and disadvantages of different CO_2 capture approaches		
	Advantages	**Barriers to implementation**
Post-combustion	↓ Applicable to the majority of existing coal-fired power plants. ↓ Retrofit technology option.	Flue gas is . . . ↓ Dilute in CO_2. ↓ At ambient pressure
Pre-combustion	Synthesis gas is . . . ↓ Concentrated in CO_2. ↓ High pressure. . . . resulting in . . . High CO_2 partial pressure. ↓ Increased driving force for separation. ↓ More technologies available for separation. Potential for reduction in compression costs/loads.	Applicable mainly to new plants, as few gasification plants are currently in operation. Barriers to commercial application of gasification are common to pre-combustion capture. ↓ Availability. ↓ Cost of equipment. ↓ Extensive supporting systems requirements.
Oxyfuel-combustion	↓ Very high CO_2 concentration in flue gas. ↓ Retrofit and repowering technology option.	Large cryogenic O_2 production requirement may be cost prohibitive. Cooled CO_2 recycle required to maintain temperatures within limits of combustor materials. ↓ Decreased process efficiency. ↓ Added auxiliary load.

In order to highlight the advantages and drawback of carbon capture technologies covered in this section, Table 2-3 was presented. As might be inferred from the table, oxyfuel-combustion processes can be integrated into standing plants or also in newly created plants. Capture performed from pre-combustion systems are mainly applied to gasification and steam reforming plants whereas post-combustion works fine capturing CO_2 from power generators that use coal like fuel [71].

2.3 An overview of the Steam Reforming Process

As has been mentioned in the previous section, hydrogen production by steam reforming process has been the most suitable thermochemical process over the last century and it will continue being a key industry for coping with hydrogen

demand and long-term applications [81]. The versatility of this technology builds on infrastructure, operation cost, availability of feedstock, efficiency and compactness of the whole process [82]. Nowadays, steam reforming processes have been able to meet almost 50% the global demand for hydrogen equivalent to $55 \cdot 10^6$ tonne/year [83].

In brief terms, SR is carried out when hydrocarbons react with steam in a range of temperature between 450 to 900 °C. The set of reactions taking place into the reformer produce a gaseous stream composed primarily for H_2, CO and CO_2. Considering the nature of the reforming reaction, the overall process is endothermic (ΔH= positive) owing to heat must be supplied into the reformer to drive the reactions forward. Albeit the SR has both high-energy requirements and penalties, the benefits are evident in contrast with other technologies for H_2 production. For instance, in terms of the operating temperatures, other methods such as partial oxidation (POX) and autothermal reforming (ATR) would produce greater temperature. Evidently, the higher the temperature, the higher the resistance required by the materials and capital cost. In addition, SR does not require investment in a unit for producing pure oxygen. Another benefit of SR comes from the fact that adjusting the reformate ratio this process would be favoured thermodynamically producing an increase in the H_2 yield (e.g. H_2/CO ~ 3:1) [57].

Other advantages of the steam reforming process with respect to POX are associated with the operational conditions. Bearing in mind that POX works with H_2/CO ratios between 1:1 to 2:1, soot is formed due to the harsh temperatures used for reaching high yield, selectivity and conversion [84]. Although SR process also produces carbon residues that may cause damage to catalysts, S/C ratios (3:1 or lower) might be changed not only to reduce carbon deposition but also for energy savings.

As it must be expected, SR also presents drawbacks in contrast with POX and ATR. In the case of SR, a catalyst is required for increasing the hydrocarbons conversion but is susceptible to poisoning in presence of sulphur. In view of that, the non catalytic (thermal) POX system is more flexible as it can deal with sulphur particles that frequently are part of the composition of the hydrocarbons used as fuel, these are then emitted as the polluting SO_2. It is imperative mentioning that

thermal POX does not require an agent to increase the chemical reaction rate. In addition, owing to the exothermic character of the POX process, no heat is supplied externally into the process as the partial combustion reaction produced between fuel and oxygen provides enough energy. As a complete conversion of fuel is achieved in POX, there is not a need to treat the outlet stream in an additional conversion reactor due to the methane content is almost negligible.

Autothermal reforming implies the integration of both steam reforming and partial oxidation. The fusion of these processes not only permits to produce heat and an enriched H_2 stream but also an acceptable efficiency. A remarkable benefit of ATR is the capacity to harness the thermal behaviour of the combustion reaction produced by POX. Hence, ATR does not require an external source of heat, making this a thermo-neutral process. Additionally, the pressures needed to operate the ATR process are lower than in POX [84]. Nevertheless, ATR also needs a large investment in an air separation unit to generate the pure O_2 feed into the autothermal reformer, which avoids N_2 dilution of the syngas product. In general, the benefits provided by SR make this chemical process the most viable fuel-based technology to produce H_2 at industrial scale so far [53].

2.3.1 Steam Methane Reforming Process Description

Steam methane reforming (SMR) was proposed for the first time at industrial level over 70 years ago. Although natural gas is the most common feed material, the appellative of this process comes from the main component of the natural gas, namely “methane”. As might be inferred, SMR is a catalyst-based chemical process at which the reaction rate is favoured by the heterogeneity of the system (metal-based catalyst and natural gas). H_2 production using SMR technology is performed in six stages at plant level: (i) desulphurisation of the natural gas, (ii) pre-reforming (where the C2 and C3 components in the natural gas are autothermally reformed to methane), (iii) primary reforming, which produces syngas, (iv) water gas shift (WGS), generating H_2 and CO_2, (v) pressure swing adsorption (PSA), which produces pure H_2 and a tail gas consisting of unreacted CH_4, purge H_2 and CO_2 sent to burn in the (vi) reformer furnace which maintains

the primary reformer at high temperature. A deep description of the process at stages (iii) and (iv) is going to be led in the present section.

Primary reforming is carried out in a conventional reformer where methane and water steam are supplied. The chemical reactions (2-1) to (2-3) take place simultaneously under harsh operating conditions of temperature (>850 °C) and pressure (ca. 30 atm) in presence of a metal-based solid catalyst (nickel-based) [83, 85]. The endothermic reactions (2-1) and (2-3) require a significant amount of heat for achieving a conversion close to the theoretical (process limited by equilibrium thermodynamics). The heat provided into the reformer is produced by means of the combustion of a fraction of the incoming methane or well burning waste gases like purge gas coming from the third stage “pressure swing absorption (PSA) system” or heat exchangers [81, 85, 86].

$$CH_4 + H_2O \leftrightarrow CO + 3H_2 \qquad \Delta H°_r = 206\ kJ/mol \qquad (2\text{-}1)$$

$$CO + H_2O \leftrightarrow CO_2 + H_2 \qquad \Delta H°_r = -41\ kJ/mol \qquad (2\text{-}2)$$

$$CH_4 + 2H_2O \leftrightarrow CO_2 + 4H_2 \qquad \Delta H°_r = 165\ kJ/mol \qquad (2\text{-}3)$$

The temperatures used to operate the reformer furnace are between 450 and 600°C at the inlet whilst the effluent stream oscillate from 700 to 1000 °C as a result of the furnace heating supplying the positive enthalpy change required by the joint effect of the three main reactions. In terms of pressure, it must be maintained in 14-30 atm inside the reformer with the aim to stabilize the methane conversion ca. ~76%. Thus, upon reaching steady state in the reformer under those favourable temperature and pressure conditions, the effluent rich in hydrogen will contain H_2 (76%), H_2O, CO_2, CH_4 and 5-10% of CO, approximately [85-87]. It is worth mentioning that to diminish the methane percentage in the syngas mixture (enhancement of H_2 yield), the reformer should be operated at an optimized H_2O/C (steam/carbon) ratio close or equal to 3:1. In addition, this particular ratio will help prevent the formation of elemental carbon that generally is deposited in the surface of the catalyst [88].

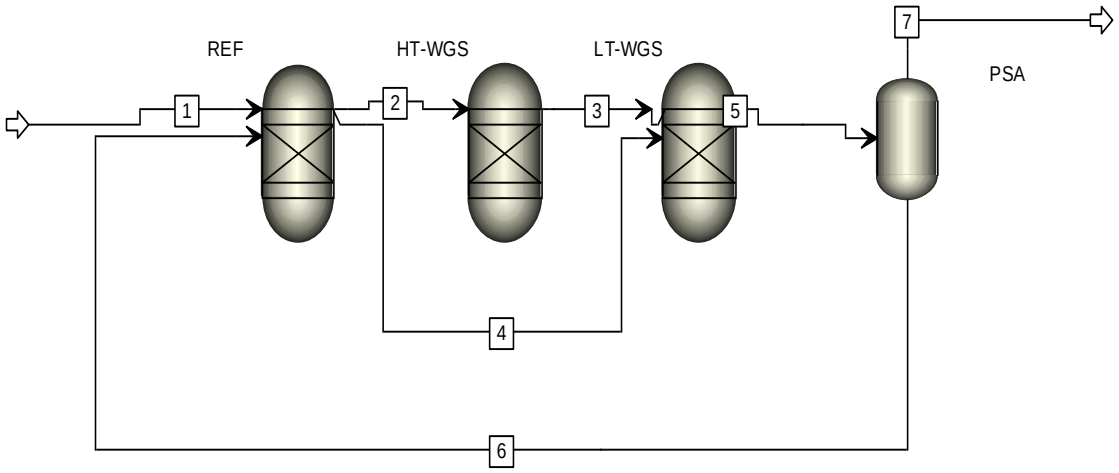

Unit	Name	Catalyst/Adsorbent
REF	Reformer	NiO, NiO/Al_2O_3
HT-WGS	High-temperature water gas shit	Fe_3O_4/Cr_2O_3
LT-WGS	Low-temperature water gas shit	$Cu/ZnO/Al_2O_3$
PSA	Pressure swing adsorption	Zeolites or activated carbons

Figure 2-10. Simplified diagram of H_2 production by conventional steam methane reforming process.

In order to minimize the remaining amount of CO in the hydrogen-rich stream generated by the catalyst-filled primary reformer tubes, the syngas is usually supplied into two water gas shift reactor settled in series (although increasingly only one WGS stage is used). The exothermic reaction (2-3 occurs in this water gas shift systems but like in the case of reactions (2-1) and (2-3), the process is limited by equilibrium thermodynamics. The first reactor is aimed to rise the conversion of CO maintaining a high equilibrium to increase H_2 yield. The elements contributing in the enhancement of the reaction are high temperature and the catalyst that shift (2-1) and (2-3) into rapid reactions with a favoured kinetics [89-92]. The optimal temperatures in this high temperature water gas shift reactor (HT-WGS) are between 310-450 °C and commonly contains an iron/chromium-based catalyst (Fe_3O_4/Cr_2O_3) [93]. In terms of conversion, the first HT-WGS system reduce by ~50% the CO content in the gaseous mixture fed [94]. Following the sequence of the process, the second reactor is operated under moderate temperature, namely between 180-250 °C. The bimetallic catalyst used into the low temperature water gas shift reactor to get a final

concentration of CO in the outlet stream of 500 ppm (LT-WGS) is a copper/zinc oxide/alumina-based catalysts ($Cu/ZnO/Al_2O_3$) [88, 94].

In the chain of steps corresponding to the SMR process, the last unit operation is associated with the purification of the off-gas coming from the stream after its sequential treatment in the set of WGS reactors connected in series. Nowadays, the purification unit known as pressure swing adsorption (PSA) has achieved the state-of-the-art and have been extensively used in petrochemical and chemical process for gas separation [95, 96]. A conventional H_2 separation process, the inlet gas is composed of H_2 (70-80%), CO_2 (15-25%), (3-6%) CH_4 and CO (1-3%). In regards to operating conditions, pressures between 8-28 atm and temperatures of 21-38 °C are used [97]. PSA systems are designed to produce a dry stream enriched with H_2, namely 95-99.99 mol %. The system also allows recovering H_2 in 70-90 mol % and producing a secondary CO_2 stream with a purity close to 100 mol % [97]. The adsorption in the PSA system is performed by activated carbon that selectively removes CO_2 and moisture from the inlet gas mixture. To recap the steam reforming process and identify the three stages or operation units required to reach H_2 production with CO_2-ready for storing, a simplified flow diagram was added, Figure 2-10. It is imperative to highlight that SR with separation of CO_2 belongs to the classification of pre-combustion capture technologies.

2.3.2 Thermodynamics of the Steam Methane Reforming Process

In the previous section, it was seen that reactions (2-1) to (2-3) govern the steam methane reforming process. Since chemical reactions are an inherent part of the transformation of CH_4 to H_2, the reaction units are limited by chemical equilibrium (thermodynamics). Hence, the intensive properties such as pressure and temperature play a significant role in the conversion, selectivity, yield and separation. Thus, the present section is intended to analyse the effect of these variables in the thermodynamics of the reforming and water gas shift stages during the production of H_2.

The analysis of chemical equilibrium and multiple thermodynamic studies have confirmed that CO_2 not only might be produced via shift reaction (2-2) taking

place in the second stage of the SRP but also, CO_2 is produced directly by a second route, namely reaction (2-3). It is worthy to mentioned that several research works emphasize that reaction (2-3) is the global reaction of the process which results from blending reaction (2-1) and (2-2) but undoubtedly is a fact that reaction (2-3) can be carried out simultaneously with reaction (2-1) during the reforming of methane [98, 99].

Bearing in mind the endothermic character of reaction (2-1), the most workable conditions for performing this reaction are high temperatures while low pressures would favour the forward transformation of CH_4 to H_2 because of the volumetric expansion effect following Le Chatelier's principle. Conversely, the exothermic water shift reaction (2-2) that occurs during the 2nd stage "WGS unit" has as optimal conditions medium temperatures (<450 °C). In regards to pressure, this parameter does not have a direct influence on the thermodynamic equilibrium of the water gas shift process [88, 100-103] as WGS is an equimolar reaction.

The efficiency of SR might be optimized varying temperature and pressure according to the thermodynamics of the system to operate. In addition to the variables mentioned above, CH_4 yield could be enhanced by raising the steam load into the reformer, in other words, by modifying the steam (S) to carbon (C) ratio. Studies conducted so far have demonstrated that SR can be operated in a range of S/C ratios between 2.5 to 5. The ratio is selected based on the desired conversion of the fossil fuel, selectivity towards CO_2 and H_2 yield. By adjusting the stoichiometric S/C ratio, it is possible to suppress and overcome carbon formation. Additionally, the average lifetime of the catalyst by poisoning (coke formation on the catalyst surface) is extended through a proper selection of S/C ratio [86, 103-106].

2.3.3 Background of the Sorption-Enhanced Steam Reforming Process (SESR)

As was discussed in the section of technologies for hydrogen production, most of the commercial hydrogen is produced by SMR at large scale [107]. In spite of SMR being considered a mature process, there is still a number of challenges to overcome. For a case in point, catalysts for reforming and CO_2 shift reactions

require an improvement in terms of mechanical and thermal properties (higher durability). Concerning efficiencies implicit in the SMR, they is plenty of work to do for an enhancement. A state-of-art separation unit not only for purifying H_2 but also for removing CO_2 must be also developed. In addition, due to the operation conditions of SR, namely close or equal to thermodynamic limits, the H_2 production is still costly. Then, improvements in the operating conditions and design of the SMR system could contribute to lowering the costs [108, 109].

In general, a path for enhancing a chemical process in terms of cost is process intensification by developing a hybrid system with a proper configuration that permits performing all reactions simultaneously in a single unit. Undoubtedly, this integration would offer synergic advantages over other chemical processes that implies multi-stages (several unit operations) to obtaining a product of high purity with high yield and favourable economics. In the particular case of SMR, some of the advantages would be an improvement of conversion from reactants to products, selectivity towards sorption of CO_2 and H_2 production, favourable thermodynamic equilibrium under standard operating parameters used in conventional steam methane reforming process, minimization of energy penalties etc. The integration of the reforming reaction, CO shift and the in-situ carbon capture reaction would also contribute substantially from the economic perspective since a H_2 production hybrid system would reduce the capital cost. In terms of energy consumption, the exothermic character of both the WGS and carbonation reaction contributes to diminishing the primary reformer operating temperature, saving ~20% energy in relation to the conventional technology for reforming methane [110]. In general, the result of integrating multiple chemical processes inherent to the SMR gives rise to a more environmental friendly configuration. The process derived from the synergy of reforming and water shift processes that offer benefits aforementioned is the “Sorption-Enhanced Steam Reforming process [85, 97, 111-116]. It is imperative to mention that when SESR is performed using methane (CH_4) as a H_2 feedstock, the terminology used for this particular technology is Sorption-Enhanced Steam Methane Reforming process (SESMR).

Bearing in mind that SMR is limited by the thermodynamics of the reactions (2-1) to (2-3), the proposed hybrid configuration SESR offers a mechanism at which

those reactions occur simultaneously in a reactor. From the thermodynamics perspective of removing CO_2 produced by reforming reactions from the reaction zone, the equilibrium of all reactions would be favoured in the forward direction (on the basis of Le Chatelier's principle). The benefit of capturing CO_2 in-situ can be also visualized considering that H_2 might be produced with high purity and ready for its utilization. Taking into consideration that SESMR process offers the ability to uptake CO_2, the PSA unit needed in a conventional SMR system for separating undesirable gases from gaseous mixture stream coming from the WGS unit might be excluded, provided fuel conversions are near 100%. Thus, the SESMR process would allow obtaining an enriched-H_2 stream with a purity ranging from 95 to 98% dry basis [116-121].

The performance of the SESR process is intrinsically related to the chemical, physical, mechanical and thermal properties of two kinds of solid materials involved in the reforming process, namely the CO_2 sorbent and the steam reforming catalyst. Both solid materials have been arduously studied with the aim to find workable solutions for improving their properties mentioned above, which in turn contribute to the enhancement of the SESMR process efficiency [112]. Scientists and engineers leading research & development have been taking different approaches to the durability of the materials. Between the approaches and criterion taken into consideration for diminishing the rapid loss of efficiency in those materials during the reforming are [112, 116, 122]:

- To achieve higher reaction rates at a lower range of temperatures (450-650 °C) with regards to conventional operating conditions in SMR,
- To synthesise novel catalysts and CO_2 sorbents with higher poisoning resistance, thermal resistance and structural stability (sintering resistance),
- To reduce the desorption temperature in order to mitigate sintering in the CO_2 sorbents
- To reach high sorption capacities in the sorbents under the most favourable parameters at the lowest production cost.

Because of the importance that solid materials for CO_2 removal in the SESR process have in the current research, a whole section dedicated to showing

particulars of conventional CO_2 sorbents available, physicochemical characteristics, capture capacity and durability will be presented later.

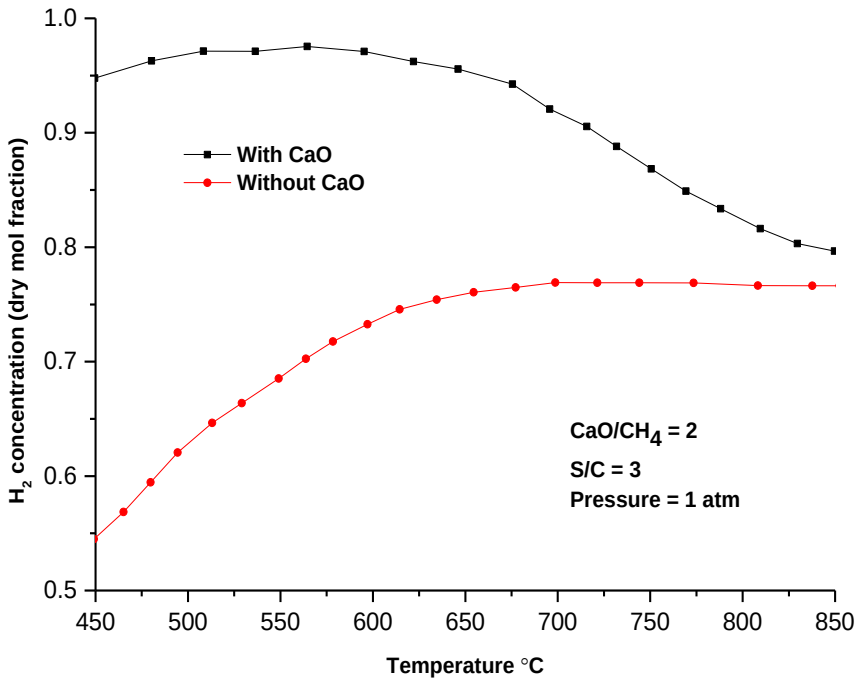

Figure 2-11. Equilibrium analysis showing H_2 concentration as a function of temperature produced with and without the presence of a CO_2-based sorbent. The analysis was conducted under isobaric conditions at 1 atm, S/C 3:1 and CaO/C 2:1 [121].

The thermodynamic advantages of integrating and intensifying a chemical process like SMR for hydrogen production with sorption enhancement are illustrated in Figure 2-11. From the plot, it is notorious that the CO_2 capture coupled with steam reforming process performed in a single reactor contributes substantially in the enhancement of H_2 production with respect of the conventional steam reforming process by the effect of the chemical equilibrium [121]. The thermodynamic equilibrium analysis presented in Figure 2-11 gives strong evidence that SR enhanced by sorption permits reducing the reaction temperature under isobaric conditions of 1 atm and a fixed S/C (H_2O:CH_4) ratio of 3:1. The high fuel conversions (>95%) expressed in H_2 concentration (dry basis) displayed in the plot of Figure 2-11 indicate that by incorporating a CO_2 sorbent (e.g. CaO-based sorbents, hydrotalcites (HT), Lithium-based sorbents, etc.) significant changes in the thermodynamics of the system emerge

(temperature is a case in point). It can be explained on the basis of the reaction enthalpies of equations (2-1), (2-3) and (2-4). Since the nature of the reaction associated with the capture process performed by the CaO sorbents through reaction (2-4) has an exothermic nature, heat is released into the system. The energy released during the carbonation process compensate significantly that energy required for carrying out the endothermic reforming reactions (2-1) and (2-3). Additionally, the heat released from reaction (2-4) also offset energy consumption needed to attain the optimal regeneration temperature to convert the carbonate phase to its initial crystallographic structure, namely CaO. As might be inferred, decreasing the temperatures for reforming CH_4 and regenerating $CaCO_3$, the net energy consumption in the SESMR process would be lowered [119-121].

$$CaO_{(s)} + CO_{2\ (g)} \leftrightarrow CaCO_{3\ (S)} \qquad \Delta H^0{}_r = -178\ \frac{kJ}{mol} \qquad (2\text{-}4)$$

As seen earlier, thermodynamics plays a vital role in SMR since the chemical reactions taking place along the overall process limits conversion by the effect of chemical equilibrium. It is relevant mentioning that the pioneers in demonstrating the feasibility of integrating the reforming and CO_2 capture using a sorbent in a single reaction vessel were Hand and Harrison [123]. In the work conducted by both researchers, a natural sorbent like CaO was apparently the solution for achieving the integration. The results revealed that is possible to reach almost a complete CO conversion when CaO-based sorbents allocated into the catalytic reformer capture CO_2 in-situ. In the set of experiments conducted by Harris et al. in a fix-bed reactor for determining the versatility of removal CO_2 also considered the use of dolomite ($CaMg(CO_3)_2$) as a potential CO_2 sorbent. Later on, Hufton et al. introduced for the first time the concept “sorption-enhanced reaction process” for hydrogen production [124]. In addition to CaO, Hufton et al. proposed K_2CO_3-promoted hydrotalcites for removing the CO_2 from the reaction zone. Although this layered double hydroxides showed a modest CO_2 uptake capacity, their hydrothermal stability was outstanding. From both research works, Hand-Harrison and Hufton et al. demonstrated that the chemical equilibrium in the reactions inherent of the reforming process is favoured by

integrating hydrogen production and carbon capture in a single reaction system [124]. Based on results presented in a wide number of investigations reported so far, the configuration adopted in the SESR process allows reducing energy up to 20-25% in contrast with the supplementary energy used for running the conventional SR [85].

As a manner of summary, the potential advantages of implementing a hybrid configuration like SESR process for high-purity hydrogen production are listed below [110, 125, 126]:

- The methane reforming reaction can be carried out at a significantly low temperature than the SR. The SESR process also permits an enhancement of the fuel conversion, selectivity and yield.
- Cost benefits are accomplished by reducing the high operation temperatures. For instance, expensive alloyed steel for the construction of the reformer is avoided. Hence, moderate operating temperatures allows building cheaper vessels made of stainless steel.
- High efficiency of the process toward H_2 production with less by-products (CO and CO_2).
- Reduction of the carbon amount formed during the operation of the reformer.
- Reduction of the energy requirements with relation to the conventional SMR process (energy penalty decrease of 20 to 25 %).
- Significant decline of CO_2 emissions into the atmosphere; high-purity CO_2 can be obtained for its further disposal into a geological reservoir.
- Reduction of the excess of steam used in conventional SR.

As has been discussed so far, operating conditions represent a crucial factor in not only the selectivity, yield and purity of the reactions involved in the production of H_2 by SMR and SESMR processes but also on the physicochemical properties of the materials involved, namely the sorbent and catalyst. Based on the importance of operating conditions, Table 2-4 summarized the main variations existing between SESMR process and the conventional SMR. From Table 2-4, it is clear the suitability of operating all reactions in a single vessel like in the case of SESR.

Table 2-4. Operating conditions between conventional SMR and SESMR during H_2 production [125].

	Conventional SRP	SESMR Advantages
Operating temperatures	800 – 1000 °C	450 – 650 °C
CH_4 to H_2 Conversion	75 – 85%	90+%
Reaction Product Composition (Dry Basis)	73.7% H_2 + 9.4% CO_2 + 12 % CO + 4.8% CH_4	98 +% H_2
Product Pressure	14.7 - 400 psig	14.7 - 400 psig

2.3.4 Reactors used in Sorption-Enhanced Steam Methane Reforming

2.3.4.1 Fix-Bed Reactor

Recently, various research works have been interested in study different patterns to enhance the hydrogen production in SESR process using two kinds of chemical reactor configurations, namely those using fixed-bed and fluidized-bed reactors. Both models have been extensively studied due to their widespread application at bench-scale and pilot scale. Albeit on a specific chemical process, their design and scale-up are in a state-of-art phase, several concerns arise when both systems are intended to be applied in the SESR process. Despite fixed-bed reactors being predominant in the production of high purity H_2, its industrial scale-up has showed complications for solving issues concerned to make of the SR a cyclic process [127]. To carry out simultaneously the reforming of methane and regeneration of the catalyst, at least two reactors are needed. Evidently, the cyclic process give rise to mismatches between the two processes. Therefore, issues are not only coming from the synchronization needed to perform the reforming and the CO_2 desorption unit (sorbent's regeneration) but also from the mechanical and thermal properties of both catalyst and CO_2 sorbent. For the solid sorbents, the most common difficulties faced during the operation are attrition, sintering and loss of capture capacity as the number of carbonation /decarbonation cycles increases [127, 128]. Overcoming this set of complications has represented a challenge, hence the necessity to optimize the system through the design of novel configurations with enhanced CO_2 sorbents.

Although many challenges need to be surpassed in the SESR process when using fixed-bed reactors, there are still plenty of advantages offered by these systems such as low loss of (toxic) fines, high selectivity towards carbon, an outstanding H_2 yield and a great flexibility for using different fuels as a feedstock [127].

2.3.4.2 Fluidized-Bed Reactor

The fluidized-bed reactor applied to hydrogen production using fossil fuels as a raw material also provides benefits in contrast with a fixed-bed reactor. In terms of heat transfer, fixed-bed reactors are not able to reach a homogeneous distribution of temperature along the tubes packed with catalyst. As a result, fluctuation in temperature cause variations in the degree of purification, poisoning of the catalyst and capacity of capturing CO_2 by means of the solid sorbents. Conversely, fluidized-bed reactors keep negligible temperature variations as the solid catalysts work like heat carriers [129]. Additionally, other benefits that the fluidized-bed reactors offer are high mass transfer, low specific heat capacity and fast heat-up attained through the contact between the solid-gas phases (minimization of the external energy requirements) [127].

Fluidized-bed reactors are also very flexible systems for treating a wide range of fuels like feedstock with impurities such as sulphur species. In addition, this kind of reactor inhibits the deposition of carbon species in the reactor and over the surface of the reforming catalyst due to the fluidization of catalyst and sorbent (transitory state). Despite this reactor design being suitable for reforming applications, there are also drawbacks that affect the performance of the process, for instance, attrition of both CO_2 sorbents and the catalyst (energy carriers). The configuration of a fluidized reactor promotes drastic changes in the textural properties of the materials packed into the interconnected reactors, namely particle-volume (PV) and pore-size distribution (PSD). Hence, it is imperative to improve the thermal and mechanical properties of the catalyst and sorbent to ensure that stringent operating conditions (temperature, partial pressures and constant fluidization) will not affect their behaviour [128, 130]. Attrition of the catalyst is of particular concern in fluidised bed configuration as it

results in loss of fines, which in case of leakage, can become airborne, and the inhalation of nickel particulates is hazardous to health.

Some of the differences between the fluidized-bed reactor and fixed-bed reactor are summarized in Table 2-5. As can be seen, both configurations show advantages and limitations at industrial scale. Concerning fixed-bed reactors, their suitability is limited to the costs for setting a cascade of coupled fixed-bed reactors. For chemical plants targeting a higher yield, the capital cost for the implementation of the process would suffer a rise of approximately 10% with respect to plants at which the production of H_2 is carried out using fluidized-bed reactors [130, 131]. In addition to those benefits and adverse effects shown in Table 2-5, other factors such as agglomeration of heat carriers and global conditions of temperature and pressure and synchronization of vessels must be considered. In the particular case of the application of fluidized bed reactor for H_2 production, the technology at the industrial level is considered immature, hence, its start-up would absolutely cause problems of configuration [131].

Table 2-5. Summary of advantages and drawbacks among a fixed-bed and a fluidized-bed reactor.

Fixed bed	Fluidized bed
(+) Control of temperature rise.	(+) Improved heat transfer by the catalyst and solvent circulation (small transfer gradients).
(-) Heat transfer resistance.	(-) Hydrodynamics of participles between the reformer and regenerator.
(+) Low maintenance cost.	(+) High mass transfer rate.
(+) Minimal loss owing to attrition and wear.	(-) Attrition on particles.
(-) Non- isothermicity.	(-) Pressure difference between the reformer/carbonator and the calciner.
(-) Diffusional resistance in the pores of the catalyst and sorbent (when applicable).	(+) Minimization of carbon deposition on the catalyst surface.
(-) Catalyst bed uniformity	
(+) Easy to design and operate.	

2.4 CO_2 capture by solid sorbents

As seen earlier, the last years have been productive in the field of climate change control with special emphasis in pathways to mitigate emissions of CO_2 into the atmosphere. In section 2.2.1, it was seen that the worldwide scientific efforts related to CO_2 removal from power generation plants approach design, develop and deploy novel technologies for pre-combustion and post-combustion capture, oxyfuel combustion, CO_2 storage or CO_2 utilization. It is imperative to highlight that most of the proposals have been developed contemplating sorption-based processes and usually the technologies involve CO_2 sorbents. Consequently, solid materials for removal of CO_2 play an important role in the control and abatement of anthropogenic emissions of GHG.

From the industrial perspective, the application of CO_2 sorbents to CCS technologies must comply with certain requirements such as mechanical stability, high CO_2 sorption capacity and low production cost (Lime cost: $54-144.6/tonne) [132, 133]. In addition, a hypothetical CO_2 sorbent must comply with the points mentioned below [12, 76, 134-140]:

1) A CO_2 adsorption/desorption kinetic rate faster than unsupported CaO within an appropriate range of temperature (550-1000 °C) as a function of its application.
2) Being selective toward CO_2 in streams with SO_2-CO_2 mixtures as well as high CO_2-adsorption capacity (close to its theoretical capacity, e.g. CaO= 0.786 g CO_2/g CaO).
3) Thermal stability that permits avoiding sintering effect under drastic changes in temperature (harsh conditions > 550 °C).
4) Mechanical strength after cyclic exposure to high-pressure streams.

The solid CO_2 sorbents proposed and studied so far have been classified in several ways; one of them is according to the pore size that each CO_2 acceptor has as inherent structural property. Another common classification of sorbents is considering the attraction energy (adsorption forces) between the individual molecules of the adsorptive (gas) and the atoms or ions composing the solid sorbent [140]. Also, they can be classified according to the range of temperature in which they will be applied. For instance, solid CO_2-sorbents for low-

temperature (< 200 °C), intermediate-temperature (200-400 °C) and high-temperature (> 400 °C) capture [136, 141, 142].

2.4.1 Physical and chemical CO_2 sorption on solids

According to theory, physisorption and chemisorption are conceived as routes that solid sorbents follow to interact with CO_2 and hold it chemically or physically. Due to their textural properties, solid sorbents usually exhibit a heterogeneous energy distribution over their surface. Hence, gas, vapour or liquid phases can adhere to the surface of solid sorbents. The interaction depends on the existing proximity between gas or vapour and the surface of the CO_2 acceptor. During the sorption process, the solid is referred as an adsorbent whilst the gas or vapour molecules prior to being linked to the surface are called adsorptive. Upon binding on the solid surface of the sorbent, gas molecules are referred to adsorbate [140, 143].

Physical adsorption also named as physisorption can be defined as an adsorption process in which relatively weak intermolecular forces arise from the solid-gas interactions. These weak forces are also well-known like Van der Waals forces. The intermolecular interactions are of the same type of those responsible for generating imperfections in real gases (deviation from an ideal behaviour) and condensation in vapour molecules. Usually, this adsorption energy does not exceed 50 kJ/mol. Physical adsorption solid-gas does not involve important changes on the electronic orbital patterns of species involved in the interaction, hence, the sorption/desorption is a process with reversible characteristics [141, 143, 144]. Physical absorption can be reached in smooth and rough surfaces under favourable conditions of pressure and temperature.

Chemical adsorption also termed chemisorption occurs under specific conditions for each adsorbate owing to the surface binding being stronger than a physical bond, with an adsorption heat that can be higher than 200 kJ/mol (energy characteristic of chemical bonds). The chemical adsorption process involves valence forces between the adsorbate and adsorbent (sharing of electrons). In contrast to physisorption, chemisorption is selective and the chemical bonding

can take place most probably if the surface has been previously prepared for achieving a clean contact between adsorptive-adsorbent [140, 145, 146].

Chemical adsorption is driven as long as the adsorptive molecules get enough proximity to the adsorbent surface and form a monolayer of molecules. Contrary to physisorption, the sorption is carried out in multilayers. Exemptions exist when the adsorptive is polar like ammonia (NH_3). In this case, the chemisorption and physisorption occur at the same time, namely, the sorbent is chemisorbed and a monolayer of molecules is formed, after that, the adsorptive compound remains adsorbed layer by layer physically. Another adsorption sequence is taking into consideration the effect of temperature. The physisorption and chemisorption can be carried out during the same process but at different intervals of temperature [140, 143, 147].

Typical differences between physical and chemical adsorption are summarized below [140, 148, 149]:

- Physical adsorption is a phenomenon with a relatively low or negligible degree of specificity, whilst chemical adsorption is dependent on the reactivity of the adsorptive and adsorbent.
- Chemisorption is intrinsically associated with active sites located on the adsorbent surface. Hence, the adsorption phenomena only occur over the periphery of the adsorbate. Thus, the chemisorption phenomenon is carried out in a monolayer. Bearing in mind that physisorption processes do not have this reliance, the arrangement of molecules is performed in multilayers.
- A physisorbed molecule preserves its identity and once desorption is reached, its original shape remains unaltered. Moreover, if a chemisorbed molecule undergoes a reaction or dissociation, it will lose its identity. Consequently, a chemisorbed species does not have memory effect when desorption takes place.
- The energy of chemisorption is comparable in order of magnitude with the amount of energy needed to drive a chemical reaction. Physisorption is always exothermic, thus, the energy required to carry out the deposition of adsorptive molecules by physisorption is close in magnitude with the energy required to reach the condensation of a fluid.

The sorption phenomenon can also be visualized from standpoint of energy required to bond the molecules on the solid surface. The adsorbate-adsorptive interactions are the result of several types of forces that are expressed as follows:

$$E_r = E_D + E_p + E_{F\mu} + E_{FQ} + E_R \quad (2\text{-}5)$$

Where:

E_r = Overall energy of a molecule at distance *r* from the surface.
E_D = Interaction energies due to dispersion forces.
E_P = Electronic field caused by polarity of the surface.
$E_{F\mu}$ = Electric dipole of the molecule.
E_{FQ} = Quadrupole Interaction of the molecule with the surface field gradient.
E_R = Short-term repulsion forces.

E_P, $E_{F\mu}$, and E_{FQ} variables are considered in equation (2-5) only if the magnitude is appreciable during the interaction between the gaseous molecules and the surface of the sorbent. Conversely, E_D and E_R are always present in the sorption process giving rise to specific interactions [150].

To identify physical or chemical adsorption, Figure 2-12 illustrates the progress of an adsorption process in terms of Lennard-Jones potentials. Potential energy (E_r) as a function of the distance between species *i* and the solid adsorbate are known as the Lennard-Jones potentials. In equation (2-6) that describe the potential energy, the first term $\left[\frac{-A}{r^6}\right]$ denote the attraction energy of molecules whilst $\left[\frac{B}{r^{12}}\right]$ represent the repulsion forces among particles.

$$E_r = \frac{-A}{r^6} + \frac{B}{r^{12}} \quad (2\text{-}6)$$

As can be seen in Figure 2-12, species *i* are distributed uniformly over the solid surface for both chemical and physical sorption processes. In relation to physisorption, the energies of weak bonds formed between adsorbent-adsorbate are within the range of energy of 10-50 kJ/mol and with a binding distance of 4 to 5 nm whilst for chemisorption, the energy required for binding is around 50-200 kJ/mol with a bond length of 1-3 nm. From Figure 2-12, it is shown that the

barrier needed to change from a physisorption state to a chemisorption one is the activation energy conventionally represented as E_a or E [140, 147].

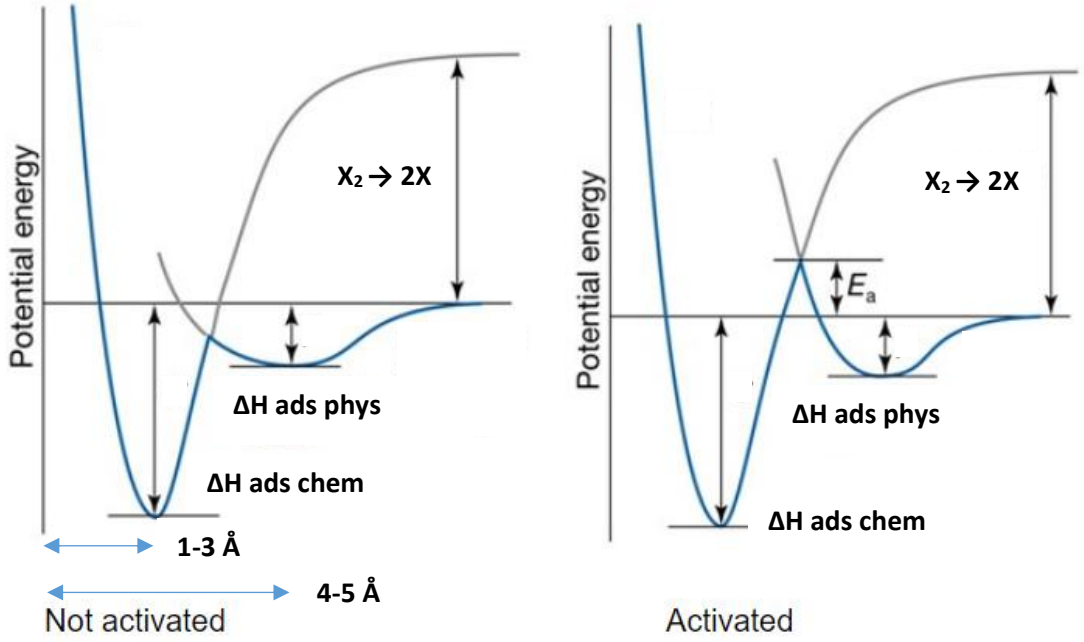

Figure 2-12. The state of adsorption depicted in terms of Lennard-Jones potential (E_r). The species X_2 can be either in a state of physical or chemical adsorption. $\Delta H_{ads\ phys}$ and $\Delta H_{ads\ chem}$ are the enthalpies of adsorption. On the right, E_a is the activation energy of chemical adsorption. On the left, the adsorption process is non-activated [140, 147, 148].

2.4.1.1 Mesoporous materials applied to CO_2 uptake

Before examining individually advantages and drawbacks of solid sorbents with potential capabilities for being applied in the SESR process, it is imperative to discuss another classification also applicable to sorbents for removing CO_2. The categorization based on the textural properties (pore size distribution) of a solid material is of great relevance since physical, chemical, thermal and mechanical properties are intrinsically associated to any particular change in the morphology or texture during the carbonation-calcination reactions taking place during the CO_2 capture process.

The classification of materials with respect to pore size distribution considers three different ranges; the first contemplates those solids that fall within 0.2 to 2 nm (200 to 2000 pm) and are denominated microporous materials. Pores with

pore-diameter ranging between 2 nm to 50 nm (2000 to 50000 pm) correspond to mesoporous materials, and pore size above 50 nm (50000 pm) are categorised as macroporous materials. For the sorption of CO_2 taking place in pre- and post-combustion processes, mesoporous sorbents would be more effective compared with macroporous solids because they could provide higher CO_2 uptake and stability due to having less susceptibility to pore plugging and shrinkage. The inherent suitability in SESR process would be associated to pore size (PS), shape, void space, volume and surface area as these textural properties permit an improvement in the kinetics of CO_2 sorption, which in turns means enhancing the ability to capture CO_2 in a shorter period. Hence, mesoporous sorbents not only would be suitable for catalysis, physical sorption and ion exchange but also in chemical CO_2 sorption for pre and post combustion capture technologies [136, 151-153].

Mesoporous sorbents encompasses inorganic (e.g. CaO, Li-based sorbents, Na-based sorbents, etc.), organic (e.g. activated carbon, dimethylacetamide, etc.), metal-organic frameworks (MOFs) and MOF's hybrids. There is a wide portfolio of mesoporous materials appropriate for CO_2 capture but specifically for pre-combustion technologies like sorption-enhanced steam reforming process, only materials with certain requirements must be considered. These characteristics for selecting a competent mesoporous sorbent to capture CO_2 at high-temperatures are listed below [153].

- High CO_2-capture capacity in a well-defined temperature range.
- Adequate mechanical strength (expansion and shrinkage) after the exposure of the sorbent to multiple sorption/desorption cycles at a harsh temperature.
- Tolerance to water impurities such as hydrogen sulphide, ammonia, mercury, hydrogen chloride, water, carbon monoxide, etc.
- Thermal stability after the regeneration of the sorbent.
- Suitable kinetics of sorption, desorption and diffusion when applicable.
- High selectivity towards CO_2 over other species present in a gas mixture under a fixed temperature.
- Ability to change the geometry of the adsorbent without any structural alteration (pellet or beads).

Screenivasulu et al. in reference [151] exhibit some of the most relevant mesoporous materials that are adequate for different carbon capture technologies such as absorption, adsorption, membrane separation, SESR process and chemical-looping combustion (CLC). In the case of organic CO_2 sorbents used in the SESR process, they have the ability to support medium and high temperatures (>200 °C). Concerning mesoporous organic materials, they have been extensively used in technologies for CO_2 removal that implies low operating temperatures due to high solvent losses produced by evaporation (low thermal stability and ease of thermal degradation).

2.4.2 Solid sorbents for CO_2 capture at high temperature (>400 °C) and selection of potential candidates

As has been seen so far, the temperature is a variable that has a great impact in the selection of an adequate sorbent for CO_2-capture purposes at high-temperatures (>400 °C) due to the materials being very susceptible to sintering (structural densification). Recently, several research groups worldwide have been concentrating efforts into novel strategies for stabilizing thermally CO_2 sorbents for their utilisation in the SESR process. Evidently, the studies aim to preserve the textural properties of the sorbents under carbonation-calcination cycles. As might be inferred, the interest in avoiding densification is associated with the decline in capture capacity faced (also termed carrying capacity) and a drive to increase durability. Results from several investigations reported so far reveal that a marked contribution to overcoming the challenges exposed above has been done. The improvements obtained in the sorbents comes from [142, 151, 152]: 1) using cutting-edge synthesis methods or adapting the existent ones (e.g. sections 3.2.1 and 3.2.2). This option consists to modify the conventional preparation methods such as wet impregnation and precipitation for tuning the textural properties of the CO_2 sorbents. 2) using different precursors for obtaining the active phase; the morphology, SSA. PSD and capture capacity of CaO are intrinsically related with the precursor used to synthetically prepare CaO, and thus, its selection plays a vital role for enhancing thermal stability whilst increasing uptake performance. 3) introducing supports into the sorbent structure (e.g. section 3.3) and 4) reactivating sorbents through a thermal pre-treatment,

chemical treatment or hydrating the CO_2 sorbent. In general terms, sorbent reactivation offers an opportunity to prolong the lifetime of the solid materials by modifying the textural properties on the surface of the CaO particles as well as enhancement of diffusion of CO_2 toward the interior of the bulk.

A proper selection of the CO_2 sorbent for high-temperature applications includes a preliminary evaluation of the material using conventional paths like sophisticated characterization techniques. The analysis using powerful techniques provide valuable information regarding chemical composition, geometrical arrangement of the structure (crystallographic properties). In addition, other physicochemical properties exhibited by the characterization techniques encompass thermodynamic, mechanical and thermal as well as morphology and textural features (shape, pore size distribution and pore geometry and specific surface area). Evidently, a sorbent should be evaluated using the optimum combination of characterization techniques in order to determine their suitability [154]. As a commonly found part of the selection, a solid sorbent for high-temperatures CO_2 capture is usually tested in a rig or TGA under stringent conditions in order to demonstrate its performance. The starting point to establish if the solid sorbent is a strong candidate for CO_2 removal would be to determine its capture capacity, mesoporosity and sorption kinetics [153, 155-157].

Thermodynamic properties represent an essential criterion to find potential CO_2 sorbent candidates in an early selection stage. Prior to assessing the suitability of the CO_2 captor in a lab-scale reactor, a simulation of the chemical equilibrium behaviour during CO_2 sorption/desorption cycle is conducted. The results of using a simulation software are the elucidation of the thermodynamic properties such as heat of reaction and Gibbs free energy. Furthermore, simulating the chemical equilibrium of a solid sorbent in presence of CO_2 aims to predict the maximum conversion, yield and selectivity in an ideal reaction system under certain temperature and pressure conditions. A clear instance of an outstanding thermodynamic analysis for elucidating theoretical behaviours of several metal oxides during the capture of CO_2 is presented in Figure 2-13. The enthalpy and Gibbs energy (ΔH and ΔG) in conjunction with the capture capacity (mass of CO_2 gained in %) give valuable information which helps to assess the spontaneity of

the interaction CO_2-sorbent, the energy needed to conduct the reaction and the capacity of the sorbents to remove CO_2 in a specific process [153, 158].

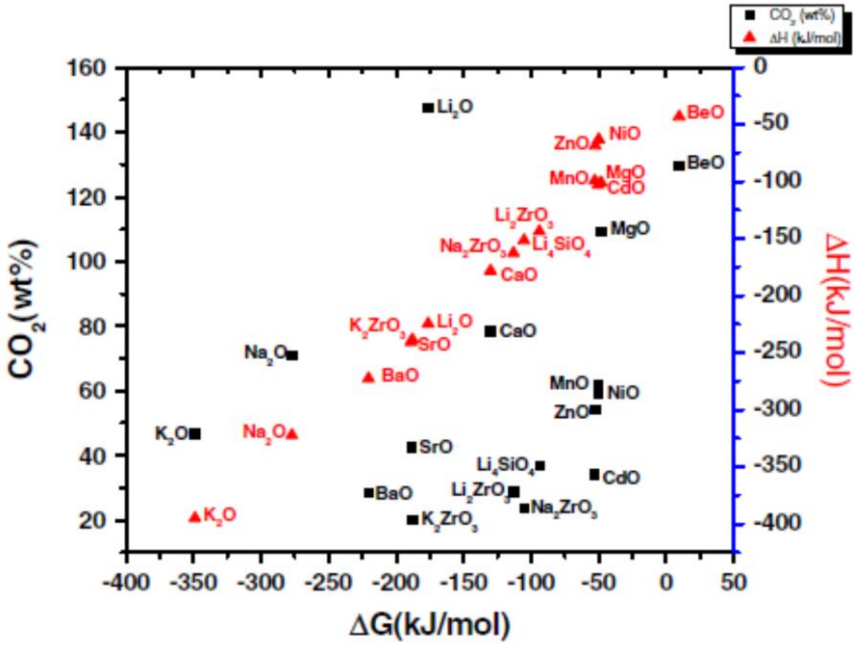

Figure 2-13. Carbon capture capacity and thermodynamic properties of metal oxides under the reaction $MO_{(S)} + CO_{2\,(g)} \leftrightarrow MCO_{3\,(s)}$ [153].

As might be inferred from the notional thermodynamic analysis presented in Figure 2-13, beryllium oxide (BeO) is apparently the metal oxide with the most favourable thermodynamic behaviour due to its uppermost position in the plot of CO_2 carrying capacity, reactivity and spontaneity. However, the downside of BeO stems from the fact that this oxide is toxic and its use is considered hazardous for industrial purposes. Therefore, it is not a viable option for its implementation in CO_2 capture processes. It is noteworthy that the exothermic or endothermic character of the reversible reaction $MO_{(S)} + CO_{2\,(g)} = MCO_{3\,(g)}$ makes a substantial difference in the viability of a given metal oxide as CO_2 captor. In terms of the endothermic character of the calcination or desorption reaction (release of CO_2), lower energies at moderate temperatures are preferred for reactivating the metal oxide sorbents. In regards to the exothermicity of the forward carbonation reaction, the energy released from this process serves to compensate the heat supplied into the processes. Clearly, the highest the energy released during the carbonation, the lower the energy required for running the chemical process.

Hence, the enthalpies determined from the thermodynamic study strongly supports the selection of the most suitable candidate for CO_2 uptake [153, 159].

2.5 Solid sorbents for in-situ CO_2-removal during the Sorption-Enhanced Steam Methane Reforming process (SESMR)

2.5.1 Ceramic Sorbents for CO_2 Capture

In the last decade, ceramic materials structured by alkali metals (Li, Na, K, etc.) in sorption applications have received considerable attention since these materials have shown fascinating properties as CO_2 acceptors. In the wide spectrum of alkali ceramics with the most outstanding abilities to capture CO_2 at high temperatures are lithium zirconate (Li_2ZrO_3), lithium orthosilicate (Li_4SiO_4) and sodium zirconate (Na_2ZrO_3). The benefits of these ceramic sorbents come from the great thermal and mechanical stability after their application under harsh temperature conditions. Evidently, resistance to attrition and sintering make of Li or Na-ceramic materials strong candidates with a superb durability. More details of those ceramic CO_2 sorbents will be provided along the present section [126, 155].

2.5.2 Li_2ZrO_3-based CO_2 sorbents

The lithium zirconate (Li_2ZrO_3) was firstly studied and introduced as a potential candidate for CO_2 capture at high temperatures by Nakagawa and Ohashi in 1998 [160]. In the beginnings, they found that Li_2ZrO_3 has a notional CO_2 capture capacity of ~0.287g of CO_2/g of Li_2ZrO_3 and slow kinetics of carbonation/decarbonation (>100 min). In addition, the morphology of this lithium-based zirconate allows slight volume changes after sorption/desorption cycles performed at temperatures ranging between 400 to 800 °C. The CO_2 uptake mechanism in Li_2ZrO_3 ceramic sorbents is carried out through two reactions expressed below [117, 161]:

$$Li_2ZrO_3 \rightarrow 2\,Li^+ + O^{2-} + ZrO_2 \quad (2\text{-}7)$$

$$CO_2 + 2\,Li^+ + O^{2-} \rightarrow Li_2CO_3 \quad (2\text{-}8)$$

$$Li_2ZrO_{3\,(s)} + CO_{2\,(g)} \leftrightarrow Li_2CO_{3\,(s)} + ZrO_{2\,(s)} \qquad \Delta H^0{}_r = -160\ \frac{kJ}{mol} \quad (2\text{-}9)$$

In the proposed sorption mechanism, the reaction showed in equation (2-7) corresponds to decomposition of Li_2ZrO_3. In there, lithium ions move from the core to the surface by diffusion, and then ions are exposed and become ready for the subsequent reaction that implies contact with CO_2 as shown in the reaction (2-8) producing as a final reaction (2-9). The Li_2ZrO_3-based sorbent with respect to other CO_2 acceptors like CaO-based sorbents (discussed in detail in section 2.5.5) offers apparently better thermal stability along cycling CO_2 sorption since small changes in the crystallographic parameters are experienced during their evaluation (~20 sorption/desorption cycles). Despite the great capacity for avoiding densification, the limiting aspect is the speed with which the carbonation reaction occurs, namely Li_2ZrO_3 has a slow reaction kinetics [153, 162].

Diverse efforts have been driven to improve the sorption/desorption kinetics as the capture capacity in Li_2ZrO_3-based sorbents is sharply influenced by the chemical kinetics. According to the wide window of methods for enhancing the speed of the reaction rate, synthesis methods offer the possibility to tuning the physical and chemical properties of the Li_2ZrO_3 sorbent (chemical reaction and diffusion kinetic). Bearing in mind the importance of the preparation methods, Jun et al. demonstrated that temperature is a synthesis variable affecting the final microstructure and texture. This research gives evidence that 850-1200 °C is the most adequate temperature range for obtaining Li_2ZrO_3-based sorbents. As might be inferred, temperatures lower than 850 °C results in an incomplete formation of the crystalline Li_2ZrO_3 structure while high temperature (>1200 °C) would promote the volatilization of lithium oxide (Li_2O). Consequently, temperature plays a crucial role in preparing Li_2ZrO_3-based sorbents with auspicious sorption/desorption kinetics [163].

Promoters have also been considered as a viable pathway for improving the capture of CO_2. In that matter, Li_2ZrO_3 has been modified by the addition of

sorption promoters like lithium carbonate (Li_2CO_3) and potassium carbonate (K_2CO_3). The incorporation of a promoter is considered a promising solution to overcome the challenge of boosting CO_2 uptake owing to a promoter's capacity to form a eutectic mixture [164]. The benefits emerged from a eutectic composition is the formation of particles with a zirconium oxide core and a liquid carbonate shell formed when the CO_2 sorption is performed at ~500 °C. Interestingly, the carbonate outer layer brings about a considerable increase in the migration rate of CO_2 particles inwards by mean of diffusion [162]. This effect can be visualized through the mechanism proposed by Ida and Lin in Figure 2-14 [162]. According to Qiang et al., high performace in Li_2ZrO_3-based sorbents can be achieved if the Li/K and Li/Zr ratios are varied during the synthesis method. The K-doped Li_2ZrO_3 CO_2 sorbents prepared with optimized ratios are able to increase the amount of CO_2 captured up to 23% under certain carbonation time and temperature, 15 min and 550 °C, respectively [165]. Beside previous proposals, Gabriele Pannocchia suggested Y_2O_3-based dopants as a path to improving the chemisorption kinetics in Li_2ZrO_3 sorbents. However, despite the effort performed in this investigation, Li_2ZrO_3-Y_2O_3 sorbents did not experienced an enhancement [166].

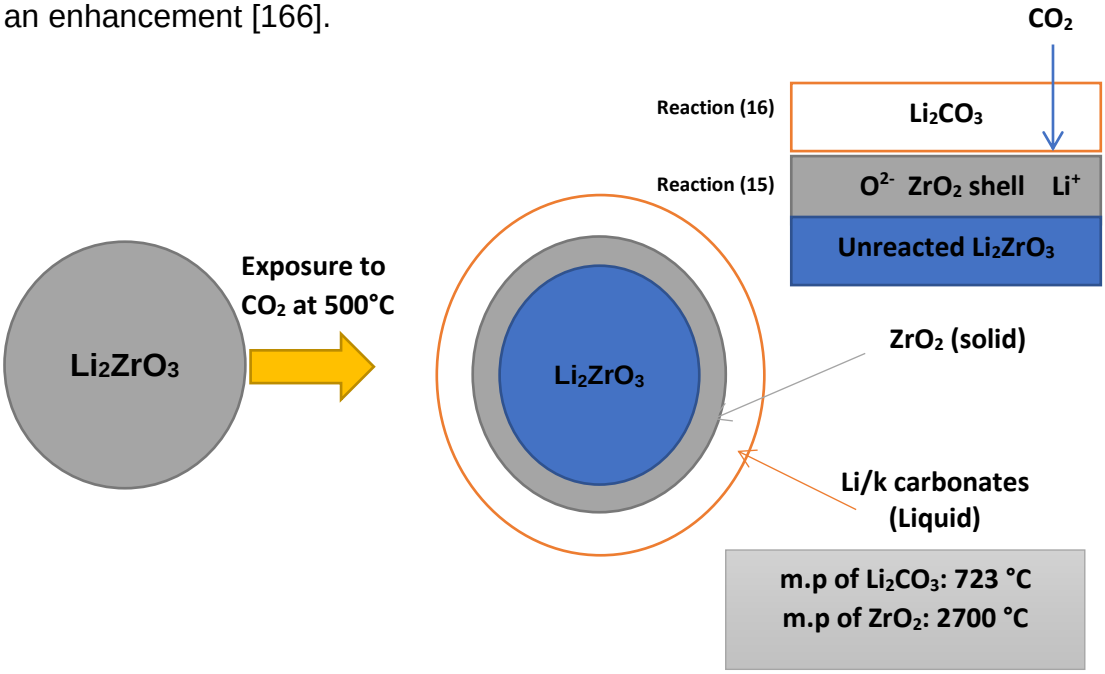

Figure 2-14. CO_2 sorption mechanism on Li_2ZrO_3 promoted by addition of Li/K carbonates [162].

2.5.3 Li_4SiO_4-based CO_2 sorbents

In the same range of temperature (>400 °C), another ceramic material which has received attention for CO_2 capture applications is Lithium Orthosilicate (Li_4SiO_4). Nakagawa's group reported the inherent uptake ability that this novel family of sorbents possess for the first time. In the beginnings, Li_4SiO_4-based sorbent was prepared by the conventional solid-state method likewise its ceramic analogous Li_2ZrO_3 [167]. Features that consent to consider Li_4SiO_4-based CO_2 sorbents as promising candidates are the notional capture capacity and the operating range of temperatures, up to 36% and 450-600 °C respectively. An investigation conducted by Xiong et al. reveals that the performance of Li_4SiO_4-ceramic CO_2 sorbents is strongly depended on the concentration of CO_2 mixed in the gaseous stream (2-20% ideal) interacting with the ceramic CO_2 acceptor [168]. Evidently, the partial pressure of CO_2 plays a key role in the velocity of the chemisorption reaction. Certainly, capture capacity of Li_4SiO_4-based sorbents is a highlight to bear in mind since evidence provided by Koto et al. indicates this sorbent is able not only to remove 50% more CO_2 (reaction (2-10)) than Li_2ZrO_3-based sorbents but also improve the sorption rate in 25 times [161].

$$Li_4SiO_{4\,(s)} + CO_{2\,(g)} \leftrightarrow Li_2CO_{3\,(s)} + Li_2SiO_{3\,(s)} \qquad \Delta H_r = -141.97\ \frac{kJ}{mol} \qquad (2\text{-}10)$$

Recent results have exhibited the suitability of Li_4SiO_4-based sorbents for pre-combustion technologies. Lithium orthosilicate has presented ability for removing CO_2 from different carbonaceous fuels such as coke, natural gas, coal, among others. In addition to the flexibility in treating a wide variety of feedstock, the efficiency of the capture process is maintained owing to its long-term durability. The negligible sintering and attrition are derived from the high mechanical strength and the thermal stability of Li_4SiO_4-based sorbent [71, 167, 169].

Since this Li_4SiO_4-based sorbent has been proposed as potential candidate for SESR processes, the scientific community has intensified endeavours to find solutions for overcoming drawbacks of these CO_2 acceptors present during hydrogen production. A case in point is the work performed by Hans et al. in

which high CH_4 conversions are apparently achieved when the carbonation of Li_4SiO_4 is low. The main factor that contributes in a poor sorption of CO_2 is the reaction kinetic order. For an unreacted solid, the reaction is described by a first order mechanism (Li_4SiO_4) whilst for the carbonation reaction is second order. Another disadvantage to deal with is the energy (heat) required to run SESR since the standard enthalpy (ΔH) of the overall process has a positive value. Evidently, the endothermic character forces the process to supply considerable amount of heat targeting to maintain a homogeneous temperature with minimum losses. To cope with this problem, an optimized network of heat exchangers must be designed and deployed. Thus, the drastic drops of temperature inside the fluidized-bed reactor or well fixed-bed reactor might be reduced [169-171].

The intensive and extensive properties implied in the SESR process are not the only patterns for enhancing CO_2 capture performed by Li_4SiO_4. Several research proposals like those of Hans et al. and Hongliang et al. has revealed that altering the texture and morphology of Li_4SiO_4-based sorbents promotes greater capture capacities. Taking the particular case of particle size, Hongliang et al. reveal that decreasing the size of Li_4SiO_4 particles, the efficiency of CO_2 sorption/desorption kinetics can be improved. This research provides strong evidence that controlling the particle size of the Li_4SiO_4 precursor (quartz: SiO_2) two different benefits emerge: 1) agglomeration or coalescence of Li_4SiO_4 particles is avoided and 2) reduction of particle size in the resultant ceramic [171, 172].

2.5.4 Na_2ZrO_3-based CO_2 sorbents

Besides lithium-based ceramic sorbents (Li_2ZrO_3 and Li_4SiO_4), a third alternative with a marked potential for CO_2 capture is sodium zirconate (Na_2ZrO_3). This synthetic sorbent has caught the attention of the scientific community due to its performance and theoretical CO_2 sorption capacity. It is imperative mentioning that albeit Na_2ZrO_3 belongs to the same family of materials made from alkali metals, the production cost is lower with relation to lithium-based sorbents. Hence, the economic aspect in conjunction with its abilities to chemisorb CO_2 allows considering Na_2ZrO_3-based sorbents as potential candidates for its application in the SESR process [161, 167, 173].

Lopez-Ortiz et al. have demonstrated that the performance of Na_2ZrO_3-sorbents are ascribed to its outstanding sorption kinetic, CO_2 capture capacity and thermal and mechanical stability [174]. In addition, Ochoa-Fernandez et al. and Jakobsen et al. [175, 176] have also highlighted the feasibility of Na_2ZrO_3-based sorbents by proving that this sorbent favours the equilibrium of the methane reforming reaction toward H_2 production (improvement in the conversion of methane). In addition, Na_2ZrO_3-based sorbents promote the production of high-purity hydrogen due to an increase in both selectivity and sorption kinetics in relation to lithium-based CO_2 sorbents. It is worth mentioning that this family of ceramic sorbents is very attractive since CO_2 is able to react easily with the lamellar crystalline structure of Na_2ZrO_3 (high surface basicity). Evidently, the basicity emerges from the presence of well-dispersed sodium ions situated on the top of the zirconate layer or well amidst layers [177, 178].

Several studies suggest that the mechanism of CO_2 chemisorption in Na_2ZrO_3-based sorbents (represented by reaction (2-11)) is favoured when the amount of CO_2 diluted in a gaseous stream is high. Bearing on mind the sorption process in lithium-based CO_2 sorbents has predilection at low CO_2 concentration, Na_2ZrO_3 sorbents show promising abilities as CO_2 captor. The capacity of Na_2ZrO_3 for capturing chemically CO_2 is easily understood through the model proposed by Pfeiffer et al. in reference [179]. The interaction of CO_2 molecules over the sorbent surface gives rise to form an outer carbonate layer. Thus, a diffusion process intervenes with a continuous migration of sodium atoms from inside out to activate the carbonation reaction, which in turn promotes a microstructural evolution causing the implicit formation of an external Na_2CO_3 shell [179]. The scheme proposed by Pfeiffer et al. [179] shows a chemisorption process (reaction (2-11)) where particles present microstructural changes and densification by the effect of temperature (Figure 2-15). However, the study conducted by Pfeiffer et al. also highlights that high temperature might also be a limitation in Na_2CO_3-based sorbents. For instance, temperatures above 550 °C promote sintering, triggering the collapse of a network of mesopores on the external shell. As a result, there would be an unavoidable decline in the CO_2 amount captured [179, 180].

$$Na_2ZrO_{3\,(s)} + CO_{2\,(g)} \leftrightarrow Na_2CO_{3\,(s)} + ZrO_{2\,(s)} \quad (2\text{-}11)$$

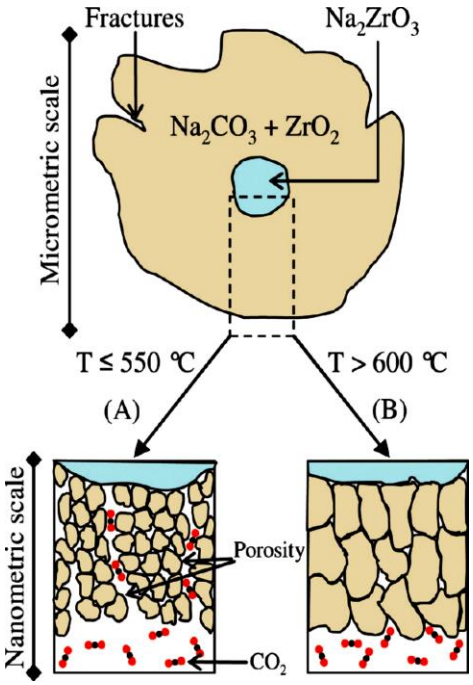

Figure 2-15. CO_2 chemisorption mechanism in mesoporous Na_2ZrO_3 structures performed at different temperatures [179].

Although Na_2ZrO_3 has a lamellar structure that promotes higher CO_2 capture, the regeneration process is considered the major concern of this ceramic material [181]. Being aware of the concerns related to Na_2ZrO_3, attempts have been done in order to extend the thermal stability during multiple carbonation/calcination cycles. To cope with depletion of carrying capacity in Na_2ZrO_3, the modification of conventional synthesis methods have been proposed. In this specific instance, soft-chemical routes, solid-state reactions and utilization of templates (sonication technique) were solutions applied to fulfil this aim [181]. The variations performed in each method chased in specific the following changes: production of small Na_2ZrO_3 particles, modification of textural properties by the effect of calcination of surfactant agents, which in other words means burning organic materials to form structures with different pore size, shape and distribution [181]. In the same manner, thermal treatments under controlled temperature conditions (800 °C) were contemplated to study the microstructural effects of Na_2ZrO_3-based sorbents when they were synthesized with a distinct crystallographic arrangement (from hexagonal to monoclinic). In that matter, Tiejun et al.

confirmed synthesizing Na_2ZrO_3-based sorbents with a monoclinic crystallographic arrangement that the chemisorption rate can be enhanced [182].

Not all endeavours in improving the durability of Na_2ZrO_3-based sorbent have succeeded. Evidence of that comes when surfactants are used as template agents. In that matter, surfactants are intended to produce a network of mesopores with pore diameter size ranging between 2 nm and 50 nm. Although it is possible to produce mesopores once the organic template is burned, the stability of the pores is compromised with any mechanical strain. Evidently, the decarbonation stage also plays an important role as the higher the temperature, the more significant would be the collapse of the pores (sintering or densification). Consequently, this method rather than improving the CO_2 sorption/desorption kinetics, produces a reverse effect since particles form agglomerates in which the CO_2 struggles to diffuse toward the interior of the agglomerates [181].

Pfeiffer et al. suggested enhancing CO_2 chemisorption by activating conventional Na_2ZrO_3-based sorbent through the insertion of sorption promoters (alkali metals) into their structure. The evaluation of the hybrid oxides $Li_{2-x}Na_xZrO_3$ formed provide enough evidence to confirm that forming solid solutions of alkali metals-Na_2ZrO_3 benefits to increase the CO_2 uptake capacity in relation with pure lithium or sodium zirconate [180, 183].

2.5.5 CaO-based CO_2 sorbents

In the last years, calcium oxide (CaO) has attracted the interest of industrial and academic sector owing to its high theoretical sorption capacity, favourable thermodynamic (high reactivity with CO_2) and versatility. In economic terms, natural CaO (obtained from limestone) and dolomite ($CaMg(CO_3)_2$) are viable CO_2 sorbents due to their low cost and wide abundance on nature. In that sense, the application of both CaO-based CO_2 sorbents at large-scale processes seems to be more promising in short term. Since advantages of using these alkaline earth metal oxides in CO_2 removal have been highlighted, CaO-CO_2 systems have been extensively studied.

In addition to those benefits aforementioned, a primary property that permits to consider CaO-based sorbents like a suitable approach for reducing the emission of CO_2 in pre-, post- and oxyfuel combustion process is the reversible carbonation reaction. In reaction (2-4), the reverse reaction carried out between $CaO_{(s)}$ in solid phase and $CO_{2\ (g)}$ gas is presented. The forward step is related with an exothermic process well known as carbonation whilst the reverse reaction with an endothermic character is defined as decarbonation (2-12). As might be inferred, the dissociative capacity of calcium carbonate ($CaCO_3$) formed upon completion of the exothermic carbonation process allows CaO behave under the sorption/desorption principle. The sorption in CaO-based sorbents is basically a carbonation reaction performed above 550 °C. Under this particular temperature, two different processes, namely chemisorption and diffusion, govern the CO_2 uptake process. In the first stage, the adsorptive molecule (CO_2) is chemically adsorbed over the sorbent surface at a very fast reaction rate. Then, an immediate transition takes place and the adsorbate diffuses towards the interior of the particles (slow reaction rate). It is imperative to mention that the limiting stage during the exothermic process (2-4) is diffusion due to its slow reaction rate [117, 142, 153, 156, 184]. Moreover, the CO_2 desorption also named calcination characteristically occurs speedily. The most adequate temperature and pressure requirements for proceeding with both carbonation and calcination reaction can be visualized in the diagram showed in Figure 2-16 (Platzki and Barin correlation [185]) [186].

$$CaO_{(s)} + CO_{2\ (g)} \leftrightarrow CaCO_{3\ (S)} \qquad \Delta H^0{}_r = -178\ \frac{kJ}{mol} \qquad (2\text{-}12)$$

Conveniently, it is relevant at this point to specify that the amount (moles) of carbon dioxide reacted with CaO to complete conversion of $CaCO_3$ at the last stage of the fast carbonation period in each carbonation-decarbonation cycle is known as maximum carbonation conversion, CO_2 capture capacity or carrying capacity. The manner to refer carrying capacity is in grams of CO_2 per gram of calcined sorbent (g CO_2/g CaO or g Sorbent). In theory, the capture capacity of CaO related with 1 mol CO_2 per mol of active phase CaO is 0.786 g CO_2/g CaO.

Evidently, the notional carrying capacity is considering that CaO is selective and reacts only with CO_2 molecules to form pure $CaCO_3$ (100% purity).

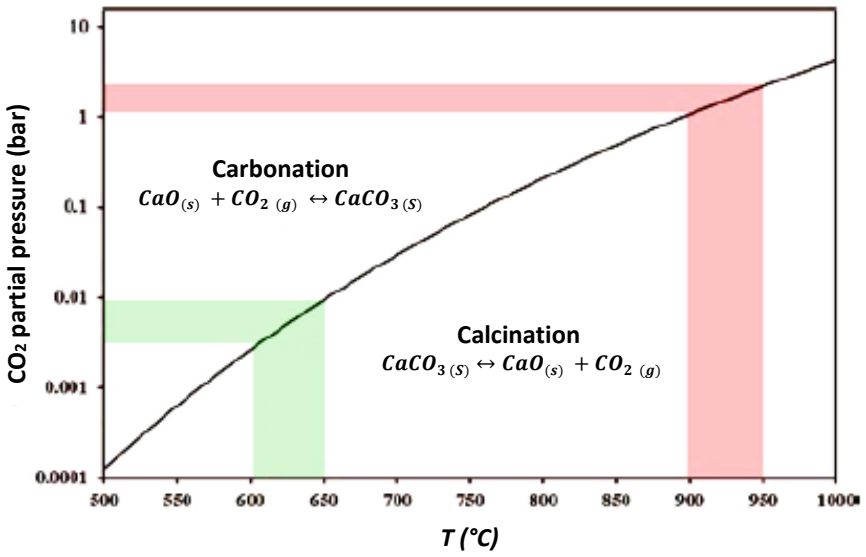

Figure 2-16. Equilibrium partial pressure as a function of temperature for the carbonation and calcination reaction using correlation of Platzki and Barin [185].

In contrast with other CO_2 sorbents for high temperature, carbonation and calcination reactions occur in a very simple way with a mechanism that implies theoretically a direct reaction. Although the reversibility process is a straightforward operation that implies a change in working variables, factors like exothermicity of the carbonation process, solid volume changes and the calcination temperature itself play a very important role not only in achieving the full desorption of CO_2 and then complete the cycle but also in extending the life of the CaO-based sorbent. Since the Tamman temperature (substantial sintering or densification caused when species are transported by diffusion at high temperature) of CaO (533 °C) is markedly below the calcination temperature (> 800 °C), attention must be paid to the calcination temperature to avoid a significant decay in the carrying capacity [187]. Consequently, volumetric expansion in CaO particles occurs when carbonation reaction take place, namely from 1.69 x 10^{-5} m^3/mol to 3.41 x 10^{-5} m^3/mol. This drastic volume change promotes the collapse of the porous network, causing sintering and a decline in the CO_2 capture capacity [117, 136, 188]. In terms of the exothermicity of the carbonation reaction, it can also produce significant structural changes as the temperature in the conversion zone increases.

Figure 2-17 shows a study in which 30 carbonation-calcination cycles under controlled conditions (carbonation: 650 °C under 90% CO_2/N_2 balance and calcination: 850 °C in pure N_2) were conducted to evaluate capture capacity and durability of CaO obtained synthetically from calcium acetate ($Ca(C_2H_3O_2)_2$). As can be seen in the plot embedded in Figure 2-17, the carbonation implies two stages, a fast process in which a chemical reaction takes place and the subsequent slower carbonation controlled by diffusion. To complete the cycle, a very fast calcination or decarbonation happens. It can be seen that the higher the number of cycles, the higher the loss of carrying capacity. In the course of 30 continuous cycles, a decline of ~56% is experienced. Noting the trend of Figure 2-17, it is evident that the decay in carbon capture goes beyond with a maximum loss of 80-85%. To comprehend and describe in more detail the degradation process shown in the typical carbonation/decarbonation study presented in Figure 2-17, there is a clear need to deepen the understanding of the effects produced during the carbonation/decarbonation reactions as well as how they can be avoided or improved for mitigating the loss of carrying capacity in CaO-based sorbents.

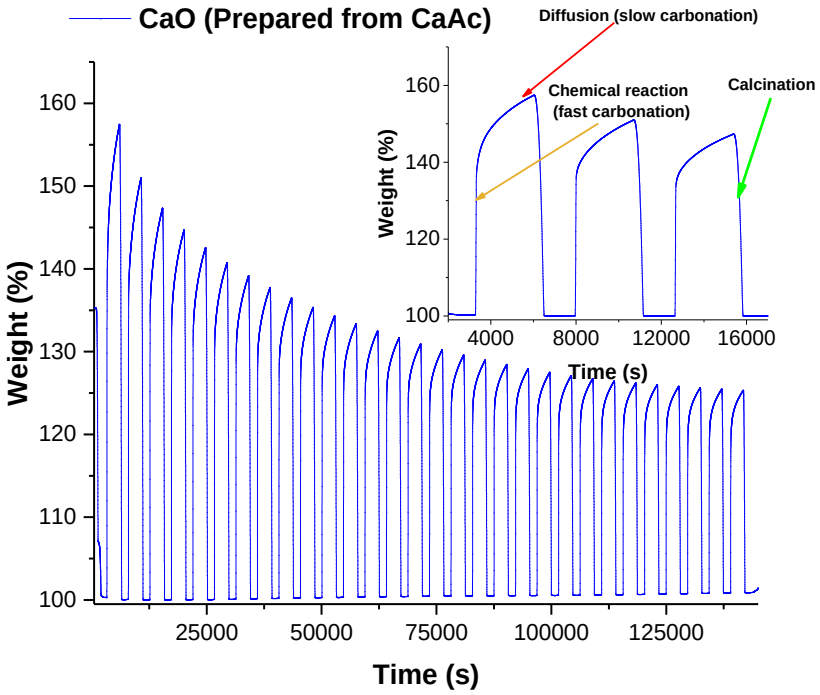

Figure 2-17. Conventional multicycle carbonation/calcination test performed over synthetic CaO using thermogravimetric analysis. A whole cycle comprehends a fast sorption stage (chemical reaction), a diffusion controlled regime (slow carbonation) and the calcination (CO_2 release).

2.5.6 Effect of carbonation and calcination reactions on CaO-based sorbents

In the last years, several research groups have been studying broadly adverse effects in CaO-based sorbents (natural and synthetic) caused by their exposure to multiple carbonation-calcination cycles. Countless studies have been carried out in order to explain the deactivation of CaO. However, a deep understanding requires identifying each phenomenon that might have an influence in the course of the multicycle CO_2 capture tests. Figure 2-18 presents those steps that can limit the sorption and desorption of CO_2 during the cycling process. In the literature, different research has reported results to justify the defeat of durability in CaO-based sorbents but disagreements still exist to conciliate a conclusion between the numerous studies performed so far. Hence, some of the most critical outcomes for explaining the loss of efficiency in CaO-based CO_2 acceptors are discussed in the present section.

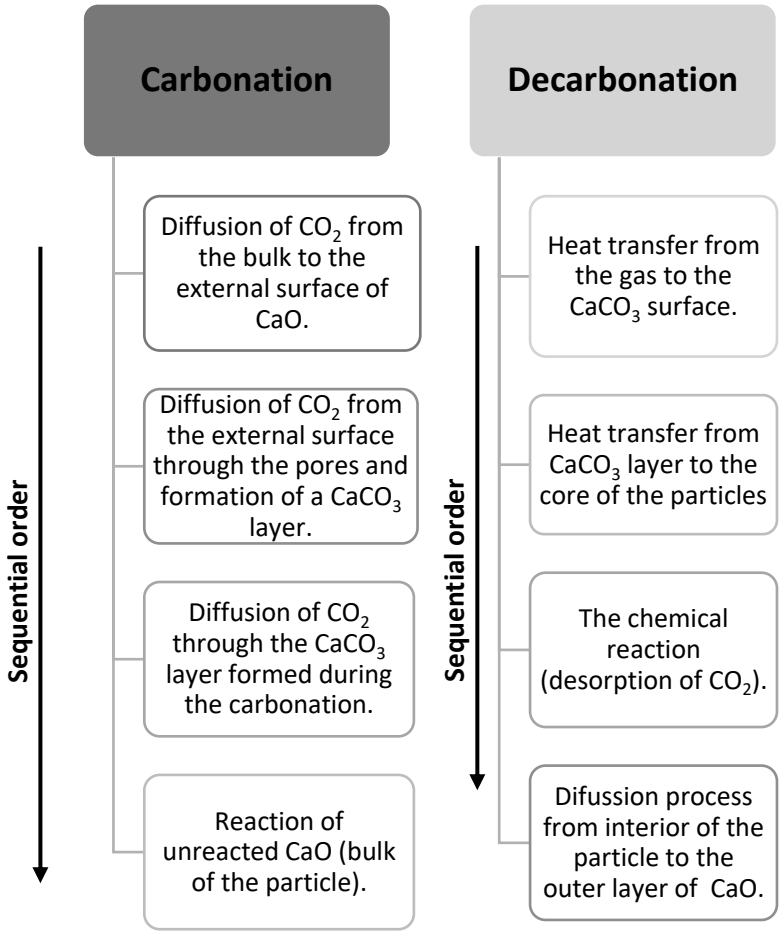

Figure 2-18. Steps that might limit the performance of a CaO-based sorbent during multicycle carbonation/decarbonation tests.

As might be expected, changes in textural properties arise even upon completion of the first carbonation/calcination cycle. Detailed studies based on analysis of pore size distribution performed over CaO sorbents evaluated in multiple CO_2 capture cycles revealed that calcination promotes the formation of a porous network with bimodal porosity, namely of small and large pores. Results indicate that small pores are produced because of the release of CO_2 molecules from the $CaCO_3$ structure, whilst large pores are created by minimization of surface energy throughout the sintering process [189-194]. Bimodal pore size distribution has been confirmed through experimental work performed under controlled temperature conditions by authors such as Barker, Abanades and others. The research works conducted so far have demonstrated that the deterioration in CO_2 uptake is a function of the time employed to conduct both carbonation and calcination reactions [194]. A prolonged carbonation time encourages blockage of open pores located in the surface of particles. In addition, carbonation causes a drastic expansion in which CO_2 will diffuse through pores with narrow size producing with the negative effect of a sorption governed by diffusion (slow kinetics) [188, 190, 191, 193].

Scanning electron microscopy (SEM) has also served as a valuable instrument to elucidate factors affecting carrying capacity during sorption/desorption cycles. Fennell et al. using the SEM technique found that a transition from a rough surface to a smooth one (corroborated by mercury porosimetry) could be a potential justification of this loss of carrying capacity [195]. Micrographs showed CaO particles presented microstructural changes from the first calcination process and became more substantial as the cycles progressed. Evolution in the morphology created by sintering of particles promoted formation of large cracks of around 1 μm. These defects derived from the constant volumetric expansion and contraction affected drastically the performance of CaO-based sorbents [195].

Moreover, authors like Lysikov et al. in the attempt to explain the behaviour of CaO-based sorbents tested under stringent calcination conditions and under multiple carbonation-calcination cycles, proposed a scheme that explains the sintering effect (Figure 2-19) [196]. In the diagram proposed by Lysikov et al., after the first calcination process, CaO is homogeneously dispersed in small

particles. In the first carbonation process, the chemical reaction and diffusion process produces an incomplete carbonation that is most probably caused by changes in the textural properties of CaO particles. As the sintering effect is evident, subsequent cycles will keep decreasing conversion from CaO to $CaCO_3$ and vice-versa. From Figure 2-19, it is evident that as the number of cycles increases, particles become grains with a constant evolution in magnitude. This trend continues until the solid structure of CaO loses almost completely its reactivity [196].

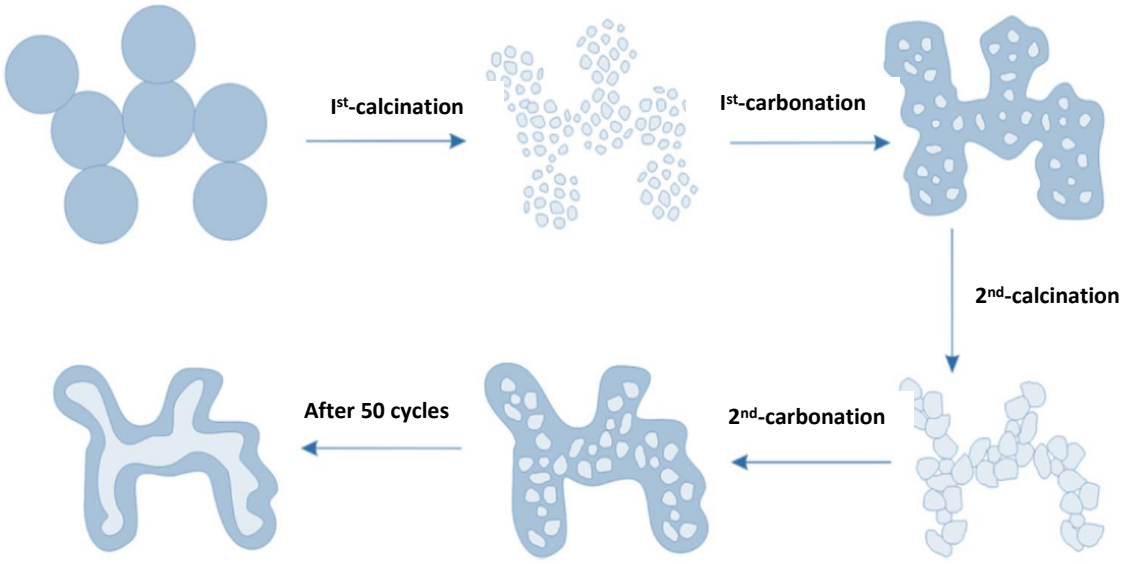

Figure 2-19. Diagram of CaO after several calcination/carbonation cycles with evident textural changes derived from pore obstruction due to sintering [196].

2.5.7 Potential options to mitigate deactivation of CaO-based sorbents

Although CaO-based sorbents have been considered promising solid materials for CO_2 removal at pre- and post-combustion capture (e.g. sorption-enhanced steam methane reforming), different approaches have been followed to cope with their susceptibility to harsh capture conditions. Junya et al. through the intuitive diagram presented in Figure 2-20 summarize the most relevant strategies adopted to overcome difficulties in CaO-based sorbents, namely the loss of carrying capacity [155]. As seen in Figure 2-20, an alternative to improve the mechanical and thermal properties of CaO is by means of modifying its

morphology and porous structure. A suitable option in this line comes from supporting CaO over a matrix of inert material acting like a stabilizer of its structural arrangement. The support must present certain characteristics such as being a refractory material, resistant to chemical attack (sulphur), possessing a high melting point and tensile strength, large surface area. Evidently, these set of properties will grant CaO an ability to resist not only sintering but also attrition and particle coarsening occasioned by volume changes during the calcination stage [155, 197].

Synthesis methods have also been playing a crucial role so far in those efforts conducted to improve the durability of CaO-based sorbents. As might be assumed, modifying the preparation process, textural properties and morphology of CaO-based CO_2 sorbents such as pore size, specific surface area, particle size, could be improved. Novel preparation routes, besides modifying the texture of a solid material, also endeavour to alter the sorbent's microstructure like in the particular case of CaO-hollow particles. Another promising pathway to preserve durability is through developing hybrid CO_2 sorbents that are prepared by blending CaO with other metal oxides. In addition to the intuitive scheme proposed by Junya et al. [155], valuable contributions performed to enhance the thermal resistance of CO_2 sorbents so far are presented in Table 2-6. This detailed table also illustrates advantages and disadvantages of those strategies proposed and their start-up.

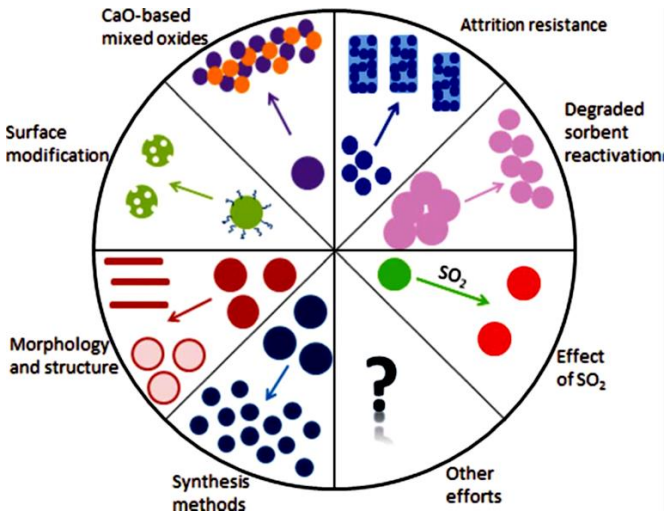

Figure 2-20. Outline of strategies for enhancing thermal and mechanical properties of CaO-based sorbents [155].

Table 2-6. Research works conducted to enhance the carrying capacity of CaO-based sorbents using different approaches [126].

Sorbent	Treated by	Reaction conditions		Reactor	N° of cycles	CO_2 uptake
		Adsorption	Regeneration			
Limestone	Acetic acid	650 °C, 15% CO_2, 20 min	920 °C, 80% CO_2, 15 min	DFR	20	0.39 [198]
Limestone	Propionic acid	700 °C, 15% CO_2, 20 min	850 °C, 100% N_2, 10 min	DFR	100	0.24 [199]
Limestone	Pyroligneous acid	700 °C, 15% CO_2, 30 min	850 °C, 100% N_2, 15 min	DFR	103	0.26 [200]
Limestone	Citric acid	700 °C, 15% CO_2, 20 min	750 °C, 100% Ar_2, 30 min	TGA	18	0.48 [201]
Limestone	Ethanol	700 °C, 15% CO_2, 30 min	920 °C, 80% CO_2, 15 min	DFR	15	0.31[202]
Limestone	Steam (hydration)	700 °C, 15% CO_2, 20 min	850 °C, 100% N_2, 10 min	TGA	10	0.55 [203]
$CaCO_3$	Steam (hydration)	780 °C, 100% CO_2,	960 °C, 100% CO_2, 10 min	TGA	10	0.47 [204]
Limestone	Pre-heat	800 °C, 50% CO_2, 30 min	800 °C, 100% N_2, 20 min	TGA	30	0.39 [205]
$Ca(Ac)_2$	Ethanol/water solution with the volume ratio of 3	600 °C, 50% CO_2, 45 min	700 °C, 100% N_2, 5 min	TGA	11	0.62 [206]
Limestone	Pre-heat (950 °C, 100% air, 12 h) and recarbonation (850 °C, 90% CO_2, 3 min)	650 °C, 15% CO_2, 5 min	850 °C, 100% air, 10 min	TGA	50	0.27 [207]
$CaCO_3$	Steam (hydration)	650 °C, 15% CO_2, 25 min	900 °C, 100% N_2, 10 min	TGA	10	0.40 [208]
Limestone	Acetic acid	650 °C, 15% CO_2, 20 min	920 °C, 100% CO_2, 10 min	TGA	20	0.09 [209]
Limestone	Steam	650 °C, 15% CO_2,n 15% H_2O 20 min	925 °C, 60% CO_2, 15% H_2O, 5 min	TGA	15	0.11 [210]
Limestone	Steam	650 °C, 15% CO_2, 20 min	925 °C, 60% CO_2, 40% H_2O, 5 min	TGA	15	0.16 [210]
Limestone	Acetic acid	650 °C, 15% CO_2, 20 min	850 °C, 100% N_2, 5 min	TGA	20	0.23 [211]
Limestone	Vinegar	650 °C, 15% CO_2, 20 min	850 °C, 100% N_2, 5 min	TGA	20	0.15 [211]
Limestone	Formic acid	650 °C, 15% CO_2, 20 min	850 °C, 100% N_2, 5 min	TGA	20	0.22 [211]
Limestone	Oxalic acid	650 °C, 15% CO_2, 20 min	850 °C, 100% N_2, 5 min	TGA	20	0.25 [211]
Limestone	10 wt.% Aluminate cement, 10% Starch	700 °C, 15% CO_2, in air, 30 min	900 °C, 100% air, 20 min	-	10	0.65 [212]
Limestone	Steam (hydration)	650 °C, 15% CO_2, in air, 15 min	940 °C, 70% in air, 20 min	FBR	5	0.37 [213]
Al_2O_3-stabilized CaO-based	Steam	600 °C, 20% CO_2/20% H_2O/60% H_2 10 min	900 °C, 20% CO_2, in N_2	TGA	10	0.52 [197]
Pelletized Al_2O_3-stabilized CaO-based	Steam	600 °C, 20% CO_2/20% H_2O/60% H_2 10 min	900 °C, 20% CO_2, in N_2	TGA	10	0.31 [197]
$Ca(OH)_2$	Pre-heat	650 °C, 15% CO_2, 5 min	850 °C, 100% dry air, 5 min	TGA	50	0.17 [214]
Limestone	Recarbonation after each carbonation	650 °C, 50kPa, CO_2, 10 min	875 °C, air, 5 min	TGA	75	0.13 [215]
Limestone	Heat-pretreated	650 °C, 15% CO_2, 5 min	900 °C, 70% CO_2, 5 min	TGA	20	0.09 [216]
Limestone	Heat-pretreated	650 °C, 15% CO_2, 5 min	950 °C, 70% CO_2, 5 min	TGA	20	0.05 [216]
Limestone	Heat-pretreated & recarbonation	650 °C, 15% CO_2, 30 min	950 °C, 70% CO_2, 5 min	TGA	20	0.03 [216]

2.6 CaO-based sorbents improved by the presence of a solid support

Endeavours for avoiding loss of carbon capacity includes the realization of a wide research work in preparing synthetic CaO-based sorbents with improved mechanical, textural and thermal properties. Although an enhancement in terms of durability has been exhibited by synthetic CaO prepared using an extensive variety of precursors such as calcium hydroxide ($Ca(OH)_2$), nanosized (<160 nm) calcium oxide, calcium carbonate, nanosized (<70 nm) calcium carbonate, calcium l-lactate hydrate ($[CH_3CH(OH)COO]_2Ca\ xH_2O$), calcium acetate hydrate ($Ca(C_3H_3O_2)_2 \cdot xH_2O$), calcium formate ($Ca(HCOO)_2$), calcium d-gluconate monohydrate ($C_{12}H_{22}CaO_{14}\ H_2O$), calcium citrate tetrahydrate ($[O_2CCH_2C(OH)(CO_2)CH_2CO_2]_2Ca_3\ 4H_2$), etc., sintering is still the main cause of the carrying capacity loss. Strategies have also considered not only the use of different synthesis routes for preparing CaO-based sorbents but also doping CaO with sorption promoters like alkali metals, namely Li, Na and K. Despite all efforts aforementioned, a drastic decrease in sorption capacity is still experienced along multiple carbonation-calcination cycles. As a result of those unsuccessful attempts, preparation of hybrid systems (supported sorbents) were also proposed as a way to stabilize the CaO active phase [126].

With regards to the selection of a suitable CaO support, it must fulfil certain features such as thermostability, specific morphology, appropriate mechanical strength, Tamman temperature higher than CaO, be a refractory material and a structure constituted by a network of mesopores [217]. In the literature, a wide window of inert supports aimed to stabilize CaO has been evaluated, among them are aluminium oxide (Al_2O_3), zirconium oxide (ZrO_2), magnesium oxide (MgO), titanium oxide (TiO_2), yttrium oxide (Y_2O_3), silica (SiO_2), etc.. For instance, in the study conducted by Li et al. using Al_2O_3 as a CaO support, an inhibition of sintering under harsh conditions like high temperature and 56 carbonation-calcination cycles was exhibited. The results showed a residual carrying capacity of 0.22 g CO_2/g Sorbent, which is almost three times higher than unsupported CaO (natural or synthetic) [218, 219].

In the same line than Li et al., Zhou et al. proposed the preparation of supported CaO-based CO_2 sorbents with improved durability for their application in the

sorption-enhanced steam methane reforming process. The synthesis implied a very simple route like wet mixing technique where different CaO and aluminium precursors were employed as well as changes in composition were evaluated with the aim to determine the best conditions and CaO amount offers the highest performance [220]. Evidently, Zhou et al. showed that the conjunction of an appropriate preparation method with a suitable CaO precursor and a refractory support gives rise to obtain CaO-based sorbents with extended lifetime during multicycle capture tests (high thermal stability and minimization of carrying capacity loss) [220]. The viability of using inert solids to support CaO was also demonstrated through the research work performed by Koirala et al., where CaO-based sorbents were prepared by a state-of-the-art technology as is nozzle flame spray pyrolysis. The authors reported that aluminium/calcium ratio has a strong influence on the stability of the CO_2 acceptors. According to the author, a molar ratio aluminium/calcium (Al/Ca) 3:10 assured good stability after 100 cycles as well as a great preservation of CO_2 capture capacity (0.40 g CO_2/ g Sorbent) [221].

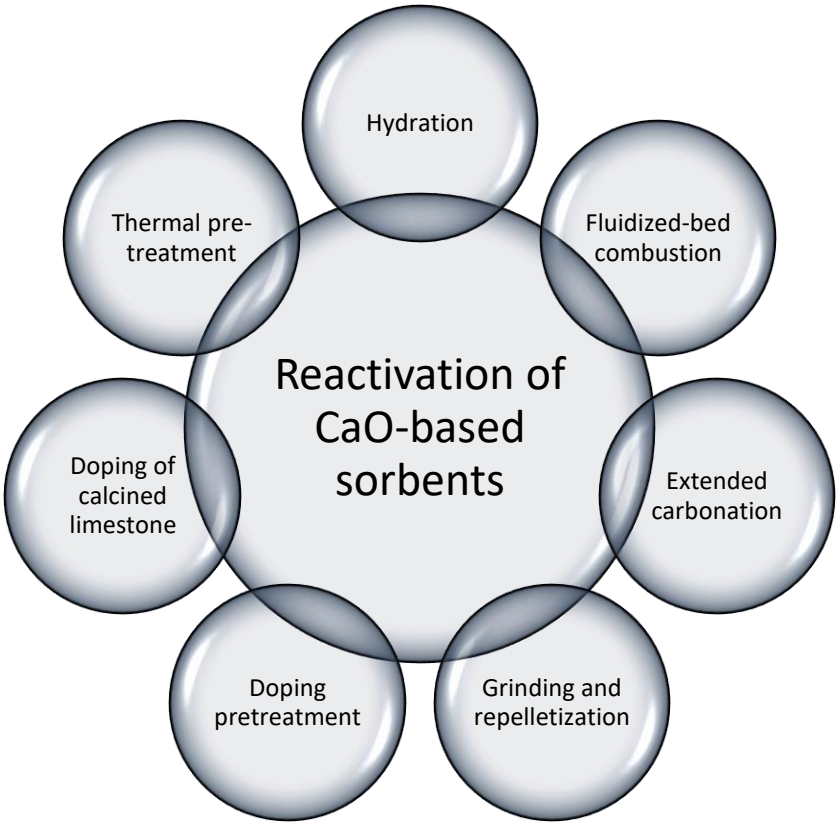

Figure 2-21. Techniques implemented for reactivating the carrying capacity in used CaO-based sorbents.

As has been seen, previous proposals for sorbents enhancement were more related with the preparation routes and incorporation of stabilizer agents. Although a great progress was attained applying in both paths, there is still pronounced reactivity decay as the carbonation-calcination cycles proceed. Another interesting approach is concerned with the reactivation of spent CaO-based sorbents. In that matter, a wide range of potential options has been implemented with successful results. Figure 2-21 highlights techniques such as hydration, thermal pre-treatment, extended carbonation, grinding and repelletization, among others, examined in order to extend the lifetime of CaO used in the calcium-looping process.

Evidence compiled from previous investigations have driven the present work to take into consideration the use of inert supports with resistance to high temperatures in order to prolong the durability and preserving the carrying capacity of high temperature CaO based CO_2 sorbents during their application in the SESMR process. Reactivation methods will be considered for future work due to initials stages of the evaluation of a novel sorbent would imply:

- Finding suitable preparation methods for loading high amount of CaO
- Estimating parameters for a controlled nucleation-growth of CaO with a specific morphology
- Characterizing the novel CaO-based sorbents
- Evaluating CaO-based sorbents as CO_2 acceptors
- Studying the durability
- Predicting the residual reactivity of the CO_2 sorbents (carrying capacity at a very high number of cycles)
- Elucidating sorption/desorption kinetics.

A wide range of research works performed to enhance CaO stability using approaches mentioned in section 2.5.7 is available in the literature. However, the majority of the investigations to prepare CaO-based sorbents aims only diminish sintering during their application in fluidized or fixed-bed systems. It is evident that other primary drawbacks exist such as attrition, pressure drops, heat exchange, distribution of the CO_2 sorbent through the length of the reactor, etc.. A potential option to treat with most of this issues is by creating a multifunctional material ready to increase fuel conversion. The sorbents must be also designed

with an open structure to permit a fast diffusion of gases (CO_2, CO and H_2, H_2O) along the bed of the fixed-bed system, and thus, pressure drops would be diminished. Evidently, there exist a big gap in this point as the commercial CaO-based sorbents maintain a pellet-like shape. In terms of the distribution of the sorbent into the tubular reactors, which must be combined with a reforming catalyst, the geometry and morphology of the material play an important role. Enhanced distribution could be reached preparing a material with enough proximity between sorbent and catalyst in order to promote faster CO_2 sorption and shift the thermodynamic of the reforming reaction toward H_2 production. Hence, problems associated with thermal stability of CaO, simultaneous distribution of the sorbent and catalyst and pressure drops in the fixed bed reactor can potentially overcome by preparing supported CaO sorbents using a fibrous refractory material (Saffil polycrystalline fibres catalytic grade) that possess an open structure as well as allows to reach a closer distribution between catalyst and sorbent.

2.7 Research rationale

2.7.1 Aim

World energy demand has presented a drastic growth driven by an economic raise not only caused through the industrial development but also urbanization. Natural gas has become a primary energy source with a global contribution of 22% by 2015 and with an upward trend towards 2040 [39]. The inherent benefits includes abundance, cost and low release of harmful gases into the atmosphere in contrast with other sources like coal, crude oil, or bitumen. Energy generation using natural gas has been efficiently led by steam reforming process in the last century. Although SR as a part of pre-combustion capture technologies is a mature technology, operation cost (including CO_2 separation) and compactness of the process have led researchers and the industry sector to find different plant designs with optimised features. A case in point is the sorption-enhanced steam methane reforming process (SESMR) at which methane is transformed to H_2 and CO_2 is produced with high purity after the captured process carried out by CaO-based sorbents. Even though SESMR process is an attractive proposal, its

success and performance have intense reliance in the physicochemical, mechanical and thermal properties of both catalyst and CO_2 sorbent.

A considerable number of studies so far has been driven for prolonging the durability of CaO-based sorbents. However, although attempts have produced positive results, there is plenty of work still left to do in order to prolong the lifetime of CaO as a CO_2 sorbent. Evidently, sintering is still the main challenge to overcome since the CaO reactivity and CO_2 capture capacity keep dropping as carbonation-decarbonation cycles proceed. Hence, the present research work aims to cope with structural densification by developing novel CaO-based sorbents with enhanced thermal stability at high temperature (>600 °C). To diminish sintering of CaO, the use of Saffil fibre supports with very high alumina content and outstanding resistance to demanding temperature conditions and chemical environments were proposed [222, 223].

2.7.2 Objectives

The objective of the present research work is to investigate routes for producing CaO-based sorbents with enhanced durability and carrying capacity for their application in sorption-enhanced steam reforming process. The project was focused on issues related to the synthesis where loading CaO with particular morphologies over Saffil fibre supports were sought. In addition, characterization, evaluation as CO_2 captors, estimation of durability, determination of structural changes after usage, and kinetics of carbonation-calcination reactions were pursued. In particular, the primary lines considered in the present research can be highlighted as:

i. *Synthesis of synthetic CaO-based sorbents using Saffil fibre supports by conventional preparation routes* - to investigate ideal synthesis methods for loading CaO with specific morphologies under controlled conditions (nanoflakes and octahedra) over Saffil supports. This line also includes the characterization of the CaO-based sorbents not only in terms of quantification of the amount of CaO loaded but also for estimating their physicochemical properties.

ii. *Carrying capacity measurements and analysis of durability* – to investigate efficiency and performance of CaO-based sorbents prepared by the selected routes and conditions. Thirty continuous carbonation-calcination cycles performed in a thermogravimetric analysis apparatus (TGA) were run in order to evaluate durability of the as-prepared sorbents. This number of cycles were proposed as natural CaO typically losses more than 80% of its carrying capacity in the first 15 cycles, and thus, CO_2 uptake trials on CaO-Saffil sorbents were extended to confirm the enhancement in their thermal resistance by incorporation of Saffil fibres. Exponential models were applied to predict residual reactivity considering $n \rightarrow \infty$ number of cycles.

iii. *Characterization of CaO-based sorbents used in carbon capture experiments* – to determine morphology and microstructural changes derived from densification effect produced during the CO_2 uptake experiments. Conventional techniques such as scanning electron microscopy (SEM) and energy-dispersive X-ray spectroscopy (EDX) were used for this study.

iv. *Kinetics study intended to determine kinetic parameters associated with CO_2 sorption/desorption processes* – to estimate model mechanisms, activation energies, rate constants and frequency factors for both CO_2 sorption and calcination reactions using isothermal and non-isothermal methods. This primary study was conducted in a TGA system using experiments in dynamic and isothermal modes under controlled temperatures and atmospheres.

2.8 Outline

Chapter 1 provides an introduction related to emission of greenhouse gases and their contribution to global warming. In addition, indicators and potential climate change impacts are exhibited and discussed. The chapter concludes on approaches for controlling and mitigating CO_2 emissions into the atmosphere.

Chapter 2 presents a detailed literature review that points out the importance of energy production and consumption, hydrogen economy and demand, technologies for H_2 generation, CCS technologies and SESR (perspective as a process for energy generation). The chapter concludes with an overview of CO_2 capture conducted at high temperature, solid sorbents available for in situ CO_2 removal in the SESR process and potential options for diminishing sintering and deactivation of CaO-based sorbents.

Chapter 3 discusses experimental methods and materials behind chapters 4 and 5. This chapter includes background about those methods utilized for preparing CaO-based CO_2 sorbents using Saffil fibre supports. Variables affecting the effectivity in the deposition of CaO over Saffil are also investigated. Characterization and thermal techniques used to elucidate the physicochemical properties, durability and carrying capacity of the as-prepared sorbets are presented and discussed.

Chapter 4 reports on the preparation of CaO-based sorbents by two different routes, namely wet impregnation and precipitation. Challenges and how they were overcome during the synthesis are presented. As a crucial part of this chapter, a deep study of physicochemical properties and their interpretation on the prepared CaO-based sorbents is conducted. To conclude, a discussion of morphology modifications obtained through changes in synthesis parameters is performed.

Chapter 5 reports results related to the evaluation of carrying capacities in CaO-based sorbents. Cyclic carbonation-decarbonation tests under controlled conditions performed using a TGA system provide information about durability. In addition, evidence of sintering signs after the multicycle CO_2 sorption experiments are discerned through an exhaustive characterization analysis using conventional techniques. To conclude, a comparative analysis of CO_2 capture capacities with relation to other CaO-based sorbents available in the literature is carried out.

Chapter 6 presents a thermo-kinetic study associated with the carbonation process using the isothermal method. Conversion data collected from a TGA system is fitted in conventional solid-state kinetic models for determining the kinetic parameters. Activation energies obtained using isothermal data are compared with values available in the literature to confirm their reliability.

Chapter 7 is concerned with the estimation of kinetic parameters linked with the CO_2 desorption stage. This chapter exhibits outcomes coming from the application of both isothermal and non-isothermal methods for data collection. Activation energies are obtained fitting conversion data in solid-state reaction models and model-free equations. The conclusion compares the kinetics of the calcination reaction with respect to those available in previous research works.

Chapter 8 provides a general conclusion of the work conducted over chapters 3 to 7. This chapter also presents future recommendations for not only complementing the research conducted so far but also work needed for scaling-up the use of the as-prepared CO_2 sorbents prepared in this research to a pilot scale.

Chapter 3 Methodology, Experimental methods and Materials

In this chapter, a detailed explanation regarding the selection of the CaO support (Saffil fibres) and its physicochemical properties is presented. As far as sorbents preparation is concerned, this chapter provides valuable information of these methods selected for the synthesis of the active CO_2 sorbents (wet impregnation and precipitation). As part of the methodology conducted throughout the experimental section, a meticulous discussion of the characterization techniques and the equipment used for the evaluation of the chemical and physical properties of the prepared sorbents is shown. In this particular section, a brief introduction of the principles that govern each technique is stated. The current chapter addresses the methodology used for carrying out the evaluation of thermal stability and capture capacity through capture-regeneration cycles. In addition, methods selected for determination of kinetic parameters associated with the carbonation and calcination reactions for the different families of sorbents prepared are presented.

Moreover, problems, constraints and solutions associated with the experimental section and characterization of sorbents performed for multiple techniques such as scanning electron microscopy (SEM), X-ray diffraction (XRD), N_2 physisorption (BET method) and thermogravimetric analysis (TGA) are exposed in the current chapter.

3.1 An overview of the design of novel sorbents

Solid sorbents for carbon capture can be designed and shaped in multiple morphologies. There is a wide variety of preparation methods that can be accompanied by very simple steps, or they can be carried out under complex procedures, which in some particular cases, are far from being understood [224]. The CO_2 sorbents can be prepared unsupported or supported according to the requirements of the process in which the sorbents will be exposed. The synthesis of the sorbents is strongly linked to the desired structural characteristics as well as the physico-chemical properties required for performing the carbonation reaction with a favoured selectivity and reactivity along the exposure cycles

[225]. However, the preparation method plays an important role as it could generate radical variations in the sorbent's performance.

As far as the design of efficient sorbents for CO_2 capture is concerned, a wide range of variables must be considered. An exhaustive and rigorous selection of the active phase and the support as well as the preparation method are among those factors which play a key role in the inherent characteristics and physicochemical properties expected in CO_2 acceptors. As has been mentioned in the literature review chapter, a promising sorbent must possess some structural features to enhance the capture capacity, diminish the sintering effect and prolong the lifetime of the sorbents along carbonation-calcination cycles. A suitable approach to obtain the properties aforementioned is by means of the method chosen for preparing solid sorbents. In the particular case of supported sorbents, the preparation technique will permit a homogeneous dispersion of the active phase. In terms of efficiency, the preparation route of sorbent materials can potentially promote higher capture capacity whether the supported sorbent is designed with a mesoporous structure and sufficient surface area to permit fast reaction rates [194, 226, 227]. Considering the impact of the preparation over the efficiency of CaO-based sorbents, a careful analysis of available preparation methods for supported sorbents was conducted. More details and specifications are provided in the succeeding sections.

3.2 Methods for preparing supported sorbents

In the literature, an extensive variety of methods for preparing supported sorbents has been published. The most often applied preparation routes comprise impregnation, precipitation, coprecipitation, sol-gel, ion-exchange, spray pyrolysis, etc. (Table 3-1) [224, 228]. It is worthy of note that some of the preparation methods rely on costly and sophisticated technologies because of the steps and procedures required for their successful application. For instance, in the sol-gel method, metal alkoxides are the most preferred precursors but they are much more expensive than other precursors such as nitrates, organic compounds, etc. used in precipitation or wet impregnation methods. In the case of the ion-exchange method, its complexity relies on controlling pH and ionic

strength of the solution, which in turns, it could limit the capacity of ion absorption [228]. Based on that, it is unavoidable to perform a meticulous selection of the method for preparing heterogeneous sorbents. Among the most important factors which must be taken into account are the features and properties of the raw materials, the expected characteristics in the sorbent, the possibility to scale-up the method, etc.. The combination of these elements will reflect a noticeable enhancement over the selectivity, activity lifetime and regeneration capacity [224]. The pros and cons of the most widely used synthesis methods to prepare CaO-based sorbents listed in Table 3-1 contributed to narrow down to two methods the preparation of CaO-Saffil sorbents, namely wet impregnation and precipitation.

Table 3-1. Advantages and disadvantages of the most widely used methods to prepare CaO-based sorbents.

Precipitation and Coprecipitation methods	
Advantages	**Disadvantages**
• Phase homogeneity • Particle size control • Crystallinity • Purity • Capacity to tailor morphology and textural properties	• Control of pH • Supersaturation • Susceptible to mixing sequence • Small variations in temperature alter morphology • Additives required to increase porosity
Wet impregnation method	
Advantages	**Disadvantages**
• Low cost • Solvent is typically water • Good reproducibility • Excess of solvent removed by drying	• Maximum loading limited by solubility of the precursor • Wetting time is prolonged • Rigorous control of temperature • Mass transfer limited by presence of pores
Sol-gel method	
Advantages	**Disadvantages**
• Control of texture • High depositions of active phase • Homogeneity • Control of the final structural properties	• Control of hydrolysis rates • Rate of condensation • Gelation time • Control of pH and temperature • Cost
Spray pyrolysis method	
Advantages	**Disadvantages**
• Formation of micro-spherical solids • Size control • Microgranulates (20-100 μm)	• Optimal viscosity of the liquid • Solid content in the suspension • Forming characteristics • Type of atomized • Control of temperature • Gas space velocity

In order to achieve “state-of-the-art” in the synthesis of supported CO_2 sorbents, the technology required to conduct the treatments involved in the preparation method must be also considered. Occasionally, the preparation steps are accompanied by very complex procedures which in some particular cases are far from being understood. Consequently, their implementation could potentially be uneconomical. Therefore, the preparation of solid sorbents should preferably involve simple routes that final characteristics of the sorbents in the deposition of the CO_2 active phase [229, 230]. However, despite of the simplicity in the synthesis methods selected, several variables must be controlled to optimize composition, texture, structural properties and homogeneity in the distribution of the CO_2 acceptor. Figure 3-1 illustrates a classification of the roles that the preparation parameters play on the physical and chemical properties of CaO-based sorbents.

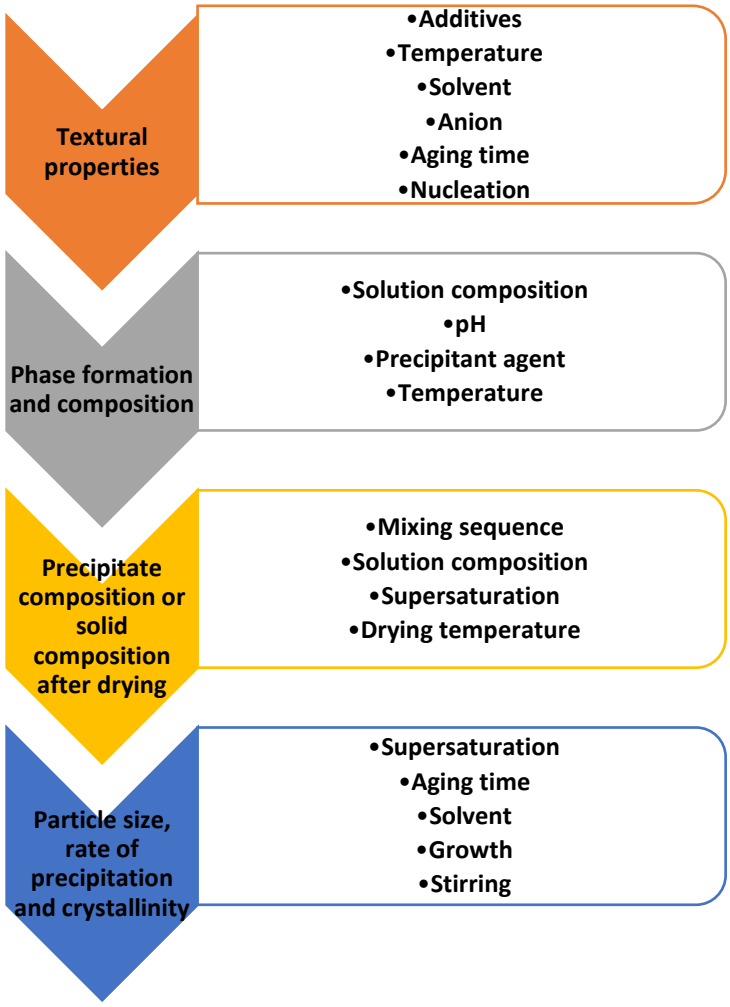

Figure 3-1. Preparation variables involved in the optimization of the final properties of supported sorbents. The variables depend of the method employed for preparing the supported sorbents.

Once an outline of the conventional methods for preparation of supported sorbents has been presented, precipitation method and wet impregnation methods were selected as the most suitable routes for synthesising CaO-based sorbents enhanced by the presence of Saffil fibre supports. In view of the importance of these methods, a review of both synthesis routes highlighting their advantages and disadvantages is conducted in the following section.

3.2.1 Impregnation in aqueous solution (wet impregnation)

Impregnation in aqueous solution also referred as wet impregnation is a widely used route for preparation of supported sorbents. This method permits dispersion of the active components on the external and internal surface of a matrix also named support. Therefore, the impregnation process relies on the surface area and pore size of the solid support. In the particular case of pre-shaped supports (fibrous materials), the impregnation of small crystals or particles is directed toward the external surface area owing to the presence of micro or meso pores.

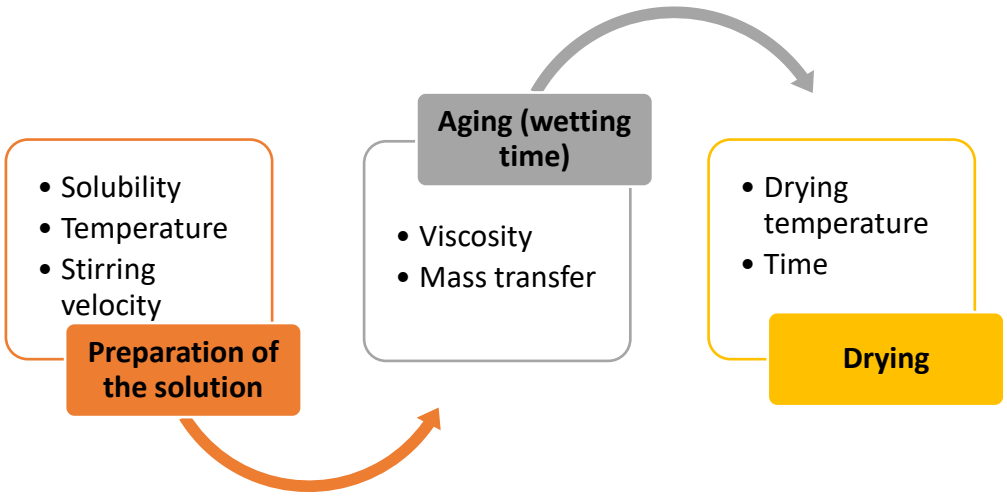

Figure 3-2. Workflow diagram emphasizing the relationship between unit operations and variables used in a conventional wet impregnation.

In general, wet impregnation is a chemical preparation route in which a solution is prepared with the aim of promoting the contact between a solid support and the precursor of an active crystalline or amorphous phase. This synthesis technique is performed with an excess of solvent that subsequently is removed by drying. The workflow diagram (Figure 3-2) lay out the steps required to

conduct wet impregnation and the variables that contribute to achieve a great effectiveness in the application of this method. For instance, the solubility has a strong influence on the active phase content loaded. In addition, mass transfer limitations caused by the size and shape of pores also has a substantial impact on the concentration of the active solid deposited. This effect is visualized in the unit operations, which involve mass transfer, namely, impregnation and drying [224, 228, 230].

3.2.2 Precipitation method

The precipitation method has emerged as an adequate approach for the preparation of supported and unsupported catalyst and sorbents. This technique was introduced by Marcilly in the 80's [231]. The precipitation occurs when a solid emerges from a homogeneous liquid phase or a mixture of liquid phases. The components integrated into the liquid solution can be considered as intermediates or precursors of the expected solid phase. As a whole, the precipitation of a crystalline solid is accomplished in three steps: supersaturation, nucleation and growth. In the course of the first step, the precipitation takes place in a region of instability (supersaturation) when a perturbation occurs. The supersaturation state in a solution can be attained by chemical or physical transformations. As the second step, the formation of a different phase is conducted by nucleation. The main requirement for attaining this step relies on the ability to be stable under the precipitation conditions. In the last step, i.e. growth, an agglomeration process of particles takes place. It is imperative to mention that at high supersaturation environments, the nucleation rate can be greater than particle growth. Under these specific conditions, small particles are more likely to be formed rather than agglomeration of particles. For a better understanding, Figure 3-3 outlines the steps and the most relevant factors affecting the precipitation process.

Properties of the precipitates such as purity, pore size distribution, chemical composition, surface area, etc. can be tuned by altering the parameters referred in Figure 3-3. On account of that, positive and negative aspects can emerge during the adjustment. In Table 3-2 is stated some of the most relevant benefits

and adverse points of the precipitation method. The same table also includes the economic side.

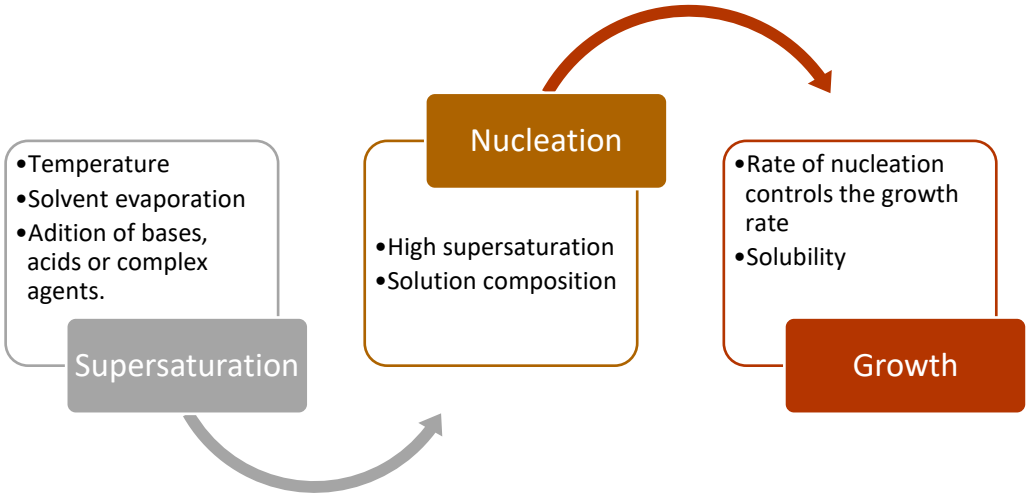

Figure 3-3. Diagram of the three steps involved in the precipitation of unsupported and supported sorbents. The main parameters affecting the physical-chemical characteristics of the precipitates are also pointed out.

Table 3-2. Pros and cons of precipitation techniques.

Advantages	Disadvantages
Texture and morphology	
• Small particles with high surface area can be formed. • Homogeneous nucleation. • Rapid precipitation rate • The particle size can be controlled by modifying the supersaturation process. • Recrystallization from an amorphous precipitate to a crystalline active phase. • Preparation of precipitates with high surface area. • Control of the nature of the phase obtained. • Control of the active phase porosity by the incorporation of additives.	• Preferences in precipitating agents • Residuary ions can cause loss of performance (poisons) • Rigorous control of pH • Nature of the anions can form undesirable phases. • Expected morphology of the final product can be altered by the raw materials. • Aging time must be determined experimentally. • Extremely sensitive to temperature variations. • Variations in pH have significant impact in the final structural characteristics of supported sorbents.
Cost	
Economic benefits since water is used in most precipitation processes. Equipment required to scale up this method is simple	Solvent cost (organic solvents).
Reproducibility	
High reproducibility at a large scale	

3.3 Properties and applications of Saffil fibres as CaO supports

Saffil fibres is a processed polycrystalline solid with high purity levels mainly composed of alumina (>95%, low silica content and trace compounds) and with a very minor content of non-fibrous particles. In 1970's, saffil fibres emerged as a potential alternative to overcome problems in a wide range of applications, among them can be mentioned filtration devices, electrical systems, protective clothing, reinforcement of ceramic composites, catalyst support, etc. [222, 223, 232]. A point to highlight in Saffil fibres is the inherent refractory properties that are outstanding considering a resistance at high temperatures, namely above 1400°C. Additionally, Saffil is very resistant to chemical attacks even in harsh environments like in presence of acids [222, 223, 232]. Beside the aforementioned thermal and chemical properties, the great surface area (up to 150 m^2/g) in which CaO could be deposited, make of Saffil fibres catalytic grade with a mean diameter value of 3.5 – 4.5 µm suitable refractory candidates. In Figure 3-4 is presented a SEM micrograph showing the morphology, texture and dimension of Saffil supports.

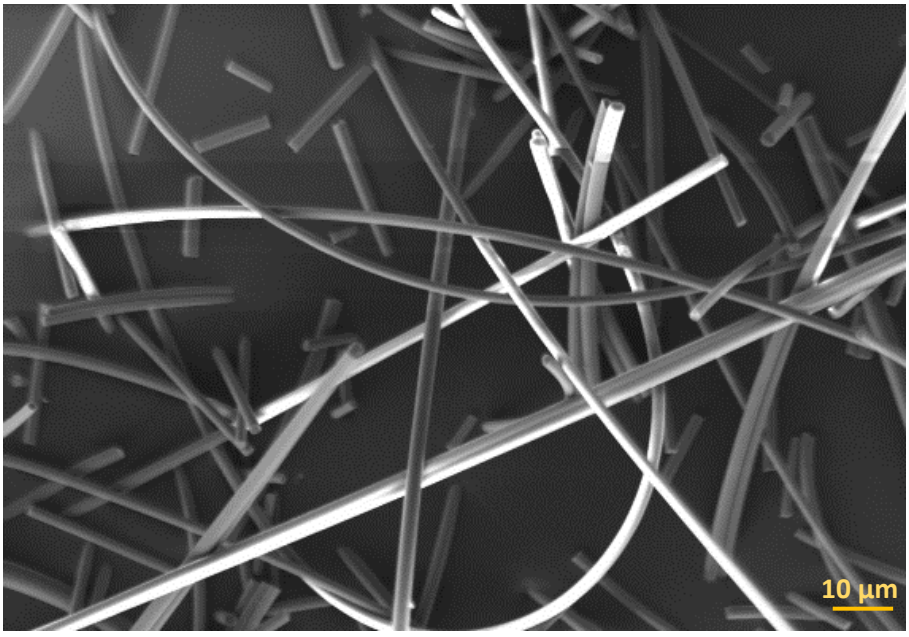

Figure 3-4. SEM micrograph of synthetic Saffil fibres catalytic grade with narrow diameter distribution (3.5 – 4.5 µm) employed as support of the CO_2 acceptor (CaO).

3.4 Characterization techniques used for the analysis of CaO-based CO_2 sorbents

In order to discern how efficient and versatile solid sorbents are with applications to SESMR, it is essential to understand the inherent properties of each CO_2 capture material. Among the properties with great relevance to the sorption behaviour are structure, morphology, favourable conditions for the chemisorption process where the solid sorbents will be utilized, and other fundamental physicochemical properties. Powder X-ray diffraction (XRD), scanning electron microscopy coupled with energy-dispersive X-ray (SEM-EDX), BET surface area by N_2 adsorption, and thermal analysis (TGA) have been considered powerful characterization tools. Hence, Chapter 3 from section 3.3 onwards will be focused on describing each characterization methods individually [143, 233-235].

3.4.1 Powder X-ray diffraction

The identification, analysis and determination of qualitative and quantitative features of solids with a periodic atomic arrangement along the material network have been studied using several characterization techniques in the last century. However, Powder X-Ray Diffraction (PXRD) denominates the most powerful technique to measure properties of a wide range of powders such as crystallographic phases in a polycrystalline sample, phase transitions, particle size, quantitative elemental information, etc.. The sphere of this characterization technique includes inorganic and organic powder materials and those compounds derived from this classification such as polymers, catalyst, biomolecules, glasses, semi and superconductors, etc. [236, 237].

The operational principle of powder XRD (PXRD) is focused in the nature of the crystalline solids. In other words, the materials have a unique identity that can be visualized and measured by means of the diffraction beam that crystals reflect because of the diffraction phenomenon. The diffraction effect in a crystalline phase takes place when constructive interference occurs as consequence of scattering of radiation at certain angles. The atomic arrangement conveys

information to the diffracted beam as is the case of a characteristic geometry that can be perceived in the diffraction pattern formed. Accordingly, the intensity and position of recorded reflections provide valuable information to deduct the chemical nature of solids as well as their crystallographic properties [238, 239].

3.4.1.1 Diffraction in powders and Bragg's Equation

Prior to describing the operating principle of an X-ray diffractometer, it is vital to provide an overview of the diffraction phenomenon in powders and the equations involved in the process. In general, X-ray diffraction is a scattering phenomenon in which atoms with a regular arrangement are involved. The long-term periodicity of atoms in a crystal permits scattering X-rays in phase and constructively interfere in particular directions. Scattering not only takes place on top row of atoms, X-rays can penetrate towards the interior of the crystal and interact with deeper atoms. Thus, constructive wave interference happens if the difference in path length of scattered rays coming from the top and lowermost planes of the crystal is equal to an integer multiple of the wavelength (*λ)*. The diffracted beams of sufficient energy are detected only they satisfy the "Bragg law" also termed "Bragg condition" (Figure 3-5) [235, 240, 241].

$$n\lambda = 2d_{hlk}sin\theta \tag{3-1}$$

Where:

d = interplanar spacing

θ = angle

λ = wavelength of radiation

n = order of diffraction (integer)

Figure 3-5 confirm that atoms with a periodic arrangement satisfies the condition derived by Bragg. This equation is obtained considering that the distance of the path from *AB'* to *B'M* is equivalent to *λ* (wavelength of the incident X-ray beam) (equation (3-1)), whilst the distance *LB' and B'M* is congruent to *d*sinθ* for each segment (equation (3-3)).

$$LB' + B'M = n\lambda \quad (3\text{-}2)$$

$$LB' = B'M = dsin\theta \quad (3\text{-}3)$$

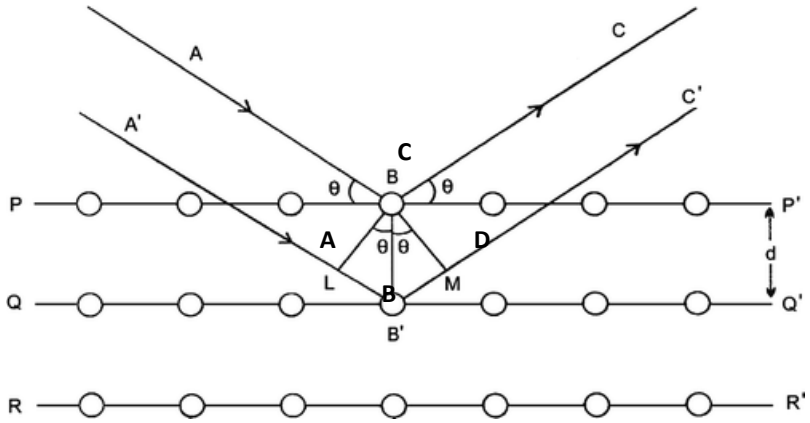

Figure 3-5. Geometrical arrangement corresponding to constructive interference of scattered radiation among planes [242].

3.4.1.2 Powder X-Ray Diffractometer

The powder X-ray diffractometer (PXRD) is a powerful analytical technique that enables phase identification of crystalline solids and determination of their structural properties. It is well-known that its working principle relies on the ability to collect signals from X-ray beams and turn them into a counts rate (cts.). Considering that radiation plays one of the most important roles in this characterization technique, a detailed description of how the X-ray beams are produced is presented below. In the first instance, a cathode tube constituted by a tungsten filament is responsible for generating electrons. Once the filament is heated, the electrons are released and then accelerated by applying voltage. Subsequently, the electrons are leaded toward a target material, which regularly are Cu, Fe, Mo and Cr. The radiation is filtered by a monochromator in order to produce characteristic X-rays with a specific wavelength (Cu-Kα= common radiation for conventional diffractometers). Afterwards, the radiation crosses a collimator and only constructive interference will contribute in the formation of X-ray beams that satisfies Bragg's Law. Finally, when the radiation has impinged onto the specimen, the interaction gives rise to a diffraction effect. As a result of this phenomenon, X-rays signals are released and recorded by a detector at

different angles, then, the measurements are represented as a diffraction pattern where counts per seconds and 2θ degrees will be the X-Y axis, respectively [233, 234, 243]. Moreover, in contrast with another characterization techniques, the advantages of PXRD can be summarized as follow: non-destructive technique, high accuracy, sensitivity, fast resolution, easy access to crystallographic database for identification of solid powders, simple procedure of sample preparation, etc. [234, 243].

The XRD analysis of the CaO-based sorbents prepared in the present investigation was carried out by means of a diffractometer Bruker D8 Advance with monochromatic Cu-K_α radiation of 154 pm (Figure 3-6). The parameters used to conduct PXRD were chosen according to references obtained through a literature search (step size= 0.108 °/s and angle of detection 2θ= 20 to 90°) [244]. Subsequently, the diffraction patterns acquired by means of XRD were analysed in order to identify the crystallographic phases corresponding to CaO, $CaCO_3$, $Ca(OH)_2$ and Saffil fibres (Al_2O_3). X'Pert HighScore Plus software provided by Bruker allowed identifying the diffraction planes by way of matching the peaks observed during the PXRD tests with those references acquired from the updated crystallographic database coming from the Joint Committee on Powder Diffraction Standards "JCPDS".

Figure 3-6. Diffractometer Bruker D8 advance used for identification of crystalline phases in CaO-based sorbents [245].

3.4.2 Determination of textural properties of CaO-based sorbents

In recent years, special interest in the scientific and industrial community has arisen in studying how the carbon capture performance in solid CO_2 sorbents is correlated with the physical properties such as particle size distribution (PSD), specific surface area (SSA), specific pore volume (SPV) and pore size distribution (PS). As a result, focus has concentrated on the ability to evaluate the texture of sorbents using non-destructive characterization techniques based on physisorption mechanisms (e.g. gas adsorption analysis).

As discussed in chapter two, SSA (specific surface area) and SPV (specific pore volume) play a vital role in the effectiveness of the CaO-based sorbents prepared by aqueous solution methods and precipitation methods. It is well-know that a typical effect of augmenting the SSA of CO_2 sorbents is the enhancement of the sorption kinetics as a result of increases the contact area between a solid phase sorbent and gaseous phase sorbate. From this argument, the evaluation of SSA and SPV was conducted in order to define the impact of these properties over the thermal stability, capture capacity and sorption-desorption kinetics in the CaO-based sorbents prepared in the present work.

Several methods applicable to the determination of specific surface area and specific pore volume by means of physisorption of gases (e.g. N_2, CO_2, etc.) have been developed in the last decades. However, the methods introduced by Brunauer-Emmett-Teller (BET-SSA) and Barrett-Joyner-Halenda (BJH-SPV) have been the most widely used owing to the grade of accuracy achieved by both techniques [246]. Bearing in mind the significance of BET and BJH methods, the subsequent section presents a comprehensive discussion of the equations governing the methods and the parameters considered to perform the calculation of SSA and SPV.

3.4.2.1 Surface area analysis: IUPAC classification of adsorption isotherms and hysteresis loops

The surface area estimated is the product of calculating the number of molecules adsorbed over a single layer and the effective area covered for them. The

prediction is basically conducted through the information obtained by kinetic theories. The estimation of SSA is usually conducted using N_2 as adsorptive molecule. The N_2 physisorption test can be reached only under equilibrium conditions of pressure at a fixed temperature. The inherent relationship between the molecules physisorbed at equilibrium is denominated adsorption isotherms. This dependence for micro, meso and macro porous materials is governed by the equation (3-4) [229, 247].

$$n = f\left(\frac{p}{P^o}\right)_T \tag{3-4}$$

Where:

n = amount of gas physisorbed

P = pressure

P° = saturation pressure

T = temperature

The adsorption isotherms in monolayer-multilayer processes obtained by N_2 physisorption over solid powders show six different trends with the exception of minor particular cases with slight fluctuations in the trend of the isotherm. For instance, materials with non-conventional pore shape, the trend of the curve differs from those of the conventional classification. Brunauer et al. proposed a classification of the adsorption isotherms for first time and only five types of trends were included. Later on, the International Union of Pure and Applied Chemistry decided to perform adaptations over the Brunauer classification in 1985 (Figure 3-7–(a)) [229]. At present, it is possible to infer results of adsorption-desorption isotherms through this valuable hierarchy classification. In Figure 3-7-(a), can be observed which some adsorption isotherms are accompanied with hysteresis loops. This effect can occur when the pores exceed certain width (~4 nm) or also depending on the pore network connectivity. In consequence, a typical scenario of capillary condensation or cavitation begins to take place [229]. For a better understanding, the six adsorption isotherms with their associated hysteresis loops are examined on detail below [248, 249].

Type I. This isotherm is characteristic of solid materials constituted by microporous (small external surface). This isotherm is concave at small values of P/P°, it means that N_2 uptake is intensely reliant on the accessible micropore

volume instead of physisorption over internal surface area. Zeolites, activated carbons and some oxides are usual cases in point of materials with stepwise isotherm [229, 248, 249].

Type II. Macroporous sorbents and materials of different natures with negligible porosity have an adsorption isotherm with a characteristic shape type II on accordance to the IUPAC's classification. As can be seen in the Figure 3-7, a), there is an inflexion point in low values of relative pressure, this is an indication that the molecules have covered the adsorbate surface and a multilayer adsorption process is set in motion, namely, this physisorption isotherm is considered as monolayer-multilayer adsorption [229, 249].

Type III. The convex tendency over all *P/P°* range without inflexion point B (displayed in isotherms type II) makes this isotherm an uncommon type despite several materials adopting this trend (bromine deposited on silica gel, some polymers, etc.) [229, 249].

Type IV. This isotherm is a variation of type II. The powder materials that obey this trend are those with an adsorption process governed by adsorption and capillarity phenomena. The inflexion point B is associated with changes from monolayer to multilayer adsorption whereas capillarity is intrinsically related to condensation as can be seen at high s *P/P°* value. In response to displacement of N_2 molecules by capillarity, hysteresis loops are formed [229, 248, 249].

Type V. This physisorption isotherm is derived from weak interactions between adsorbate and adsorbent. It is considered as a variation of type III but is unusual, so that, a limited number of porous sorbents have this behaviour [229, 249].

Type VI. According to the IUPAC classification, this isotherm corresponds to uniform surfaces with negligible porosity. The inflexion points form a stepwise tendency on account of the multilayer physisorption. The temperature plays a key role in this process because the intensity of the steps is dependent on this variable. Common examples are noble gases physisorbed on carbon [229, 249].

In particular, mesoporous sorbents have the distinctive feature that the adsorption process is carried out in multilayers. As mentioned above, mesoporous materials also exhibit N_2 condensation (capillarity) as an ordinary effect caused by pore size. As a result of the adsorption mechanisms and capillarity phenomena, four main hysteresis loops have been associated and

categorised by IUPAC (Figure 3-7-(b)). The shape of the hysteresis loops is closely related to the pore structure, which means the pore geometry can be predicted through an exhaustive analysis of hysteresis loops. For instance, porous materials with cramped pore size distribution and regular pore shape (cylindrical) are associated to hysteresis loops type H1. This hysteresis loop result from a retarded condensation rather than from network effects. The isotherms with hysteresis loop type H2 are tricky to analyse owing to the number of variables immersed in the adsorption-desorption behaviour. For example, pore geometry, pore dimensions and network effects are crucial factors linked to shapes type H2. As part of the same classification, hysteresis loop type H3 is mainly caused by slit-shaped pores or by plate-like particles. This hysteresis loop can also show N_2 physisorption has no restrictions at high relative pressure. Complex materials with a combination of mesopores and micropores usually exhibit isotherms with hysteresis type H4. Materials with slit–like pores have H4 loops [248, 250, 251].

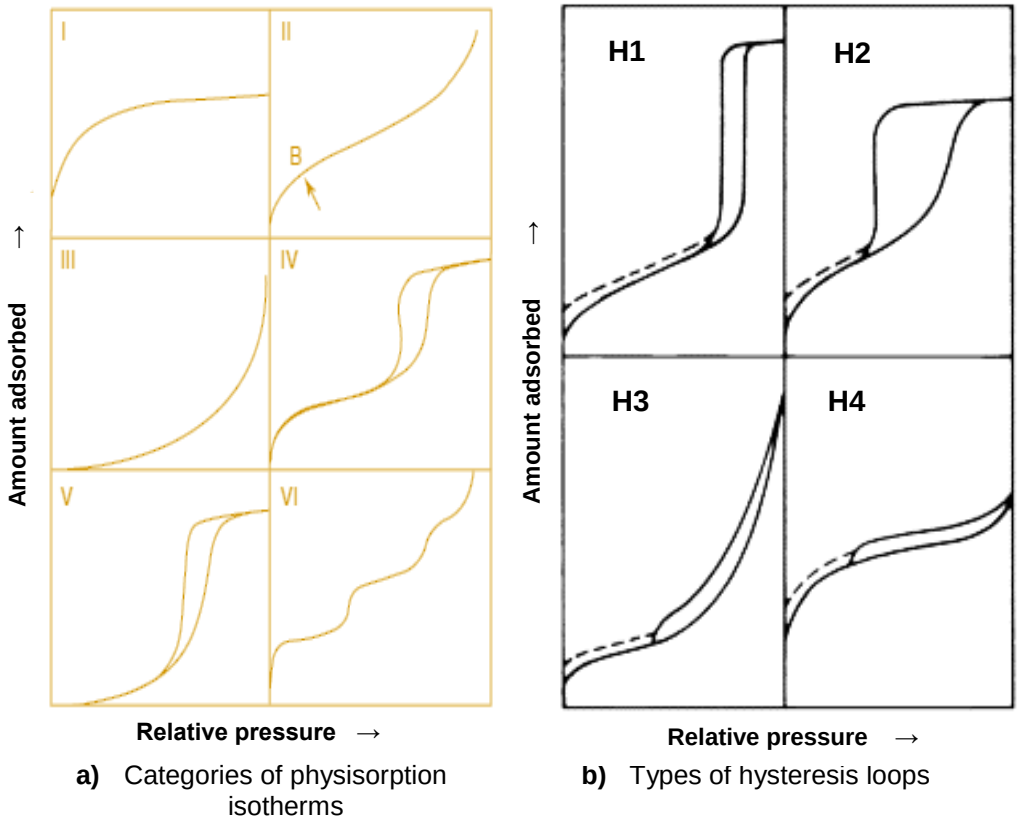

Figure 3-7. a) Classification of physisorption isotherms and b) Conventional hysteresis loops according to the IUPAC [250].

3.4.2.2 BET method for determination of surface area

After establishing the concepts that relate adsorption isotherms with their associated hysteresis loops and surface area, it is necessary to explain the operational mode of the BET method, which has been considered as the most accurate way to calculate the specific surface area for a vast variety of materials such as sorbents, supports, catalyst, etc.. In theory, the BET analysis can be accomplished in two steps described as follows: 1) resolving BET monolayer capacity (n^{α}) by means of the BET plot derived from the transformation of a common physisorption isotherm. 2) The prediction of the specific surface area (a_s) (equations (3-6) and (3-7)). In order to conduct this calculation, an assumption needs to be considered, namely, the value of molecular area, which usually takes the value of a_m= 0.162 nm^2 (see equation (3-5)) [246].

$$\frac{p}{n^a(p^\circ - p)} = \frac{1}{n_m^a \cdot C} + \frac{(C-1)}{n_m^a \cdot C}\frac{p}{p^\circ} \quad (3\text{-}5)$$

Where:

n^a = amount of gas physisorbed at certain relative pressure

n_m^a= monolayer capacity

$\frac{p}{p^\circ}$ = relative pressure

C = this value is intrinsically related with the enthalpy of adsorption. Its amount is the result of the interaction adsorbate-adsorbent when a layer of molecules is formed. C can also vary with respect to the shape of the physisorption isotherm.

In order to perform the calculation of *SSA,* is necessary to know with accuracy the value of the average area of the active area covered by N_2 molecules (n_m^a). Through substituting these measurements in (3-6) and (3-7) is possible to predict the SSA value.

$$A_s = a_m \cdot L \cdot n_m^a \quad (3\text{-}6)$$

$$a_s = \frac{A_s}{m} \quad (3\text{-}7)$$

Where:

A_s = total surface area; a_s = specific surface area

L = Avogadro constant; m = mass of the adsorbent

Beside the calculation of SSA, N_2 physisorption is useful for measuring other textural properties such as pore breadth, pore volume and pore-size distribution by employing a suitable method for assessing these properties. The Kelvin equation (3-8) derived from thermodynamic considerations allows the prediction of pore size by effect of stepwise reduction of *P/P°*. This equation is derived from thermodynamic considerations; it means that the measurements of pore size distribution are strongly influenced by relative pressure. Capillary condensations are also taken into account to convert the relative pressure into pore size distribution [246, 251].

$$ln\left(\frac{p}{p^{\circ}}\right) = \frac{V}{RT}\left(\frac{2\sigma cos\theta}{r_k}\right) \qquad (3\text{-}8)$$

$$r_p = r_k + t$$

Where:

V = molar volume

σ = surface tension of the liquid adsorbate

$\frac{p}{P^o}$ = relative pressure

θ = contact angle among adsorbate-adsorbent layer on pore wall (estimation 0).

m = mass of the adsorbent

r_k = Kelvin radius (for shape cylinder)

t = thickness of the adsorption layer

r_p = geometric radius of a pore

The pore size distribution (PSD) can also be calculated by using Barret-Joyner-Halenda method that essentially is an extension of the Kelvin equation [252]. The PSD is calculated once the pore volume is totally filled. This conjecture can be attained only when the relative pressure ($\frac{p}{P^o}$) reaches in excess of 0.95.

The surface area, pore volume and pore volume distribution for the CaO-solid sorbents prepared in this research work were measured in a Nova 2200e system from Quantachrome instruments. The BET surface area system carry out the analysis by means of the patented helium free method being capable to determine textural properties with high performance. This instrument has an integrated degassing station aimed at releasing contaminants over the surface of the samples such as water or hydrocarbons. For our study, the CaO-based

CO_2 sorbents were subjected to degasification for 3 h at 200 °C. The method selected for conducting the analysis was full adsorption-desorption isotherm. The analysis of SSA and PVD were carried out considering all relative pressure region (*P/P°*), namely, from 0 to 1. It is noteworthy that SSA is calculated in the relative pressure range of 0.1 – 0.35, whereas PV is estimated at higher relative pressures as pores must be filled with condensed N_2. This condition is regularly reached at *P/P°* values above 0.95.

3.4.3 Scanning electron microscopy (SEM) and energy dispersive X-ray spectroscopy

In recent years, Scanning Electron Microscopy (SEM) has been considered as one of the most effective, accurate and reliable characterization techniques for the evaluation of morphology in solid materials owing to the valuable information obtained by means of the analysis of electrons. The SEM study is accomplished using the signals generated during the scanning of a focused beam of high-energy electrons. As a result of the elastic and inelastic interaction between the incident beam and the specimen surface, characteristics X-rays and three sort of electrons are emitted, namely: secondary electrons, backscattered electrons and auger electrons (Figure 3-8). It is relevant to mention that those scattered electrons will possess different resolutions level because of the specimen volume depth from which they come. This inherent property of the electrons can be visualized in Figure 3-9 [253, 254].

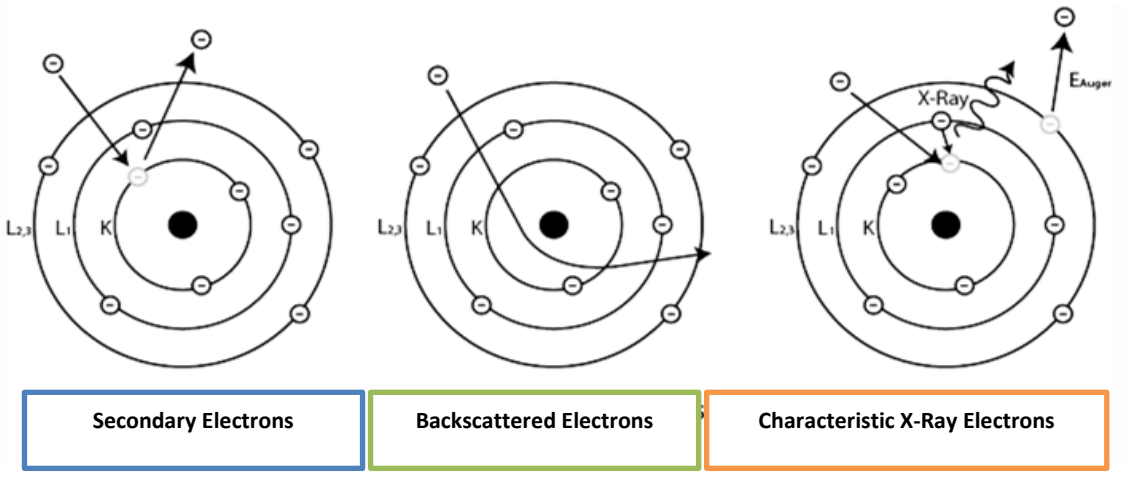

Figure 3-8. Secondary electrons, backscattered electrons and characteristic X-rays emitted from impinged electrons over a certain area of a specimen [255].

The information provided by the electrons collected from a specific region selected according to the criteria of the visualizer is processed by way of images. The resolution of SEM system in terms of magnifications oscillates in the range from 20X to roughly 30,000X, which corresponds to a spatial resolution of 50-100 nm. The SEM is not only able to perform qualitative analysis but it is also possible to conduct a semi-quantitative analysis as long as an energy-dispersive X-ray (EDX) detector is coupled to the SEM chamber. The EDX detector will estimate the chemical composition, crystals orientation and crystals structure of powders with different geometries and shapes. Therefore, the quantitative analysis, the elemental mapping and the line profile analysis will depend on the resolution, sensitivity and intensity of signals derived from the electron-specimen interaction [255].

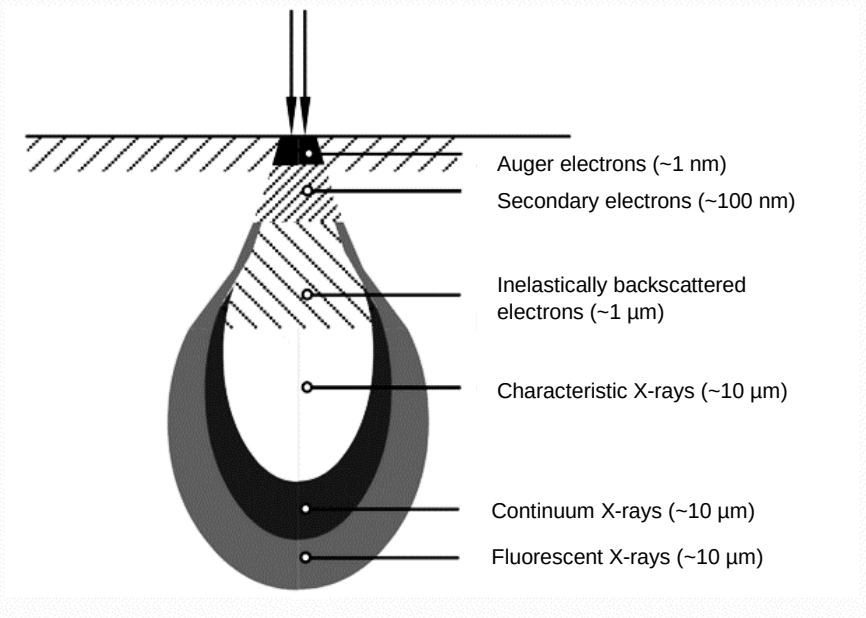

Figure 3-9. Relation of interaction among incident electrons and depth range on image resolution in SEM and EDX [255].

For a better understanding of the EDX technique, its working principle and scope in terms of resolution and sensitivity are also described in the present section. The EDX microanalysis is achieved when characteristic X-rays emitted from the interaction between a focused beam of electrons and a specimen are detected and processed. The X-rays generated will strike the detector with certain energy peculiar of each element. Then, this energy will be converted into voltage pulses. Instantaneously, the EDX detector will analyse the intensity of those voltage pulses with the aim to define the concentration of each element distributed over

the area chosen for performing the study. It is relevant mentioning that the amount of energy emitted by each element which conforms to a crystalline or amorphous phase will be proportional to the relative abundance of x-rays emitted [256].

The sensitivity of the EDX detector tolerates measurements of chemical composition in elements with atomic number higher than 9. It means that, the EDX detector has the atomic weight of the microconstituents as a limitation. Based on that, uncertainty could be triggered because of overlapping in signals produced by the elements with close values of molecular weight. Another constraint in EDX detectors is the spatial resolution governed by the volume of the specimen. Consequently, to attain sufficient emissions of characteristic X-rays, appropriate dimensions of the specimens must be considered (~1 μm laterally and ~2-5 μm in depth). Then, reliable EDX outcomes will only emerge when the specimen is made up of particles larger than 2 μm [254].

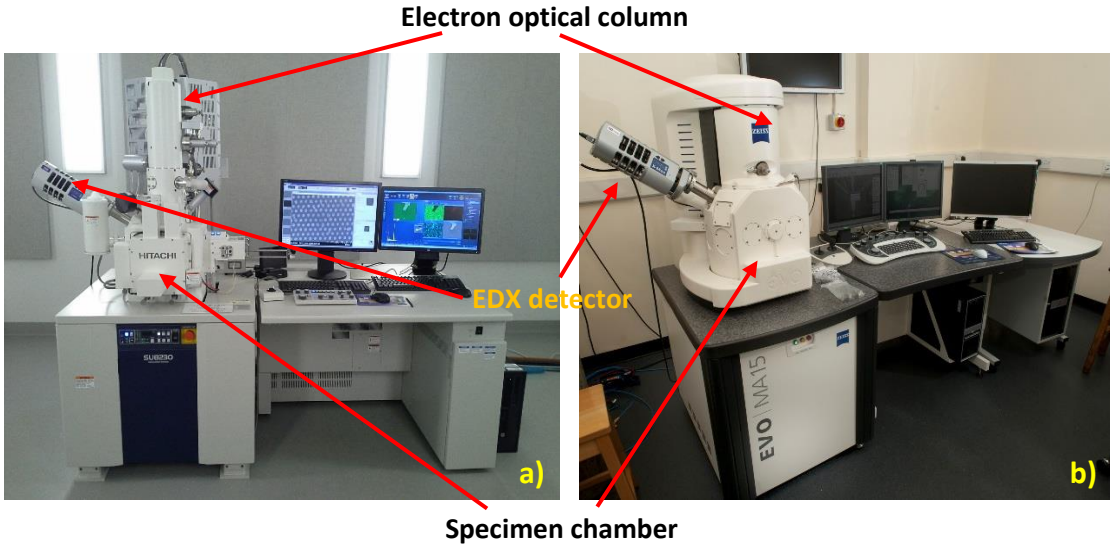

Figure 3-10. Hitachi SU8230 (a)) and Carl Zeiss EVO MA15 (b)) equipped with an Oxford Instruments EDS detector. Both SEM-EDS systems were employed for morphology determination and elemental distribution analysis in CaO-based sorbents prepared by wet impregnation method and precipitation using urea and NaOH as precipitants.

In the present research work, the topographical and morphological properties of CaO-based sorbents were carried out using an ultra-high resolution SEM (Hitachi SU8230) equipped with cutting-edge cold field emission technology (CFE). In addition, the elemental distribution analysis was conducted utilizing

EDX technique incorporated in both SEM apparatus used. The EDX systems were supplied by Oxford Instruments and have an integrated 80 mm X-max silicon dry detector (SDD). The acquisition and analysis of the results were performed by means of the AztecEnergy software provided by the same company (

Figure 3-10).

Prior to the SEM-EDX analysis, the CaO-based sorbents are coated owing to their non-conducting nature. The thin carbon film deposited over the specimen surface are fixed at 10 nm (thickness), approximately. The equipment used to coat the specimens is a Q150T-E turbo-pumped system. As additional information, it is pertinent mentioning that this particular carbon coating apparatus is highly recommended for samples to be analysed by high-resolution scanning electron microscopes or transmission electron microscopes (TEM). Figure 3-11 shows the automatic turbo-pumped coater supplied by Quorum technologies employed for coating the CaO-based CO_2 sorbents.

Figure 3-11. Automatic turbo-pumped coater with a precise control of carbon thickness enhanced by the suppression of sparking.

Samples coated with carbon are inevitably polluted with hydrocarbons owing to the exposure of the specimens to environment conditions, as well as throughout preparation procedure and/or storage. With the aim of enhancing the quality of micrographs recorded also by electron microscopy, a sample cleaner system ZONESEM supplied by Hitachi (see Figure 3-12) was used. Evidently, this system is considered as an inherent part of the preparation instrument since the

surface of the solid is cleaned under vacuum conditions prior to the SEM-EDX analysis.

Figure 3-12. Sample cleaner ZONESEM used for specimens preparation pre-SEM analysis.

3.4.4 Thermogravimetric analysis (TGA) and its applications

The durability and carbon capture capacity are vital properties that must be considered during the assessment of a solid sorbent. As has been discussed in the previous chapters, two effects could arise whether the thermal stability in solid sorbents is enhanced: 1) the CO_2 uptake capacity could be stabilised throughout multiple carbonation-calcination cycles and 2) the sintering effect at microstructural level could be diminished. The evaluation of both properties can be achieved by using a characterization technique that permits studying the behaviour of a solid material under controlled conditions such as temperature and atmosphere. Thermal analysis methods (TA) has been extensively used for studying a wide range of materials (mixture of phases, compounds or elements) in recent years. The ability to measure changes in the physicochemical properties of materials as a function of customized increments of temperature allows TA to be considered as an efficient characterization techniques. TA comprehends three methods: 1) thermogravimetric analysis (TGA), 2) differential thermal analysis (DTA) and 3) differential scanning calorimetry (DSC). According to their operation principle, TGA measures weight variations with respect to temperature changes whilst DTA estimates changes in heat content with respect to sequential fluctuations of temperature as well. The most important applications of TGA and DTA are listed in the Table 3-3 showed below [257-260].

Table 3-3. Applications of thermal analysis (TGA and DTA) [258, 259].

Chemical Properties	Physical properties
Chemical sorption	Phase transitions
Decomposition	Absorption
Oxidative degradation	Adsorption
Dehydration - degradation	Desorption
Solid state reactions	Vaporisation
Solid-gas reactions	Crystalline transition

As far as instrumentation is concerned, a TGA is equipped with a microbalance in which a crucible (alumina, aluminium, platinum, glass, gold, steel, sapphire, etc.) holds a sample during thermoanalytical measurements. The crucible plays an important role in the quality of the results acquired, consequently, it is relevant to know the chemistry of the solid in study. The microbalance is surrounded for a furnace capable to accurately controlling temperature. The characteristics of the furnace rely on the work temperatures required to perform the analysis. For instance, a ceramic or silica-made furnace resists to up to 1100 °C and a furnace made of a platinum or platinum/rhodium alloy can reach 1600 °C. The system integrated by the furnace and microbalance is termed thermobalance. TGA with cutting-edge technology is capable of controlling with high degree of accuracy rates of heating and cooling, or it can be programmed to hold a certain temperature after a heating regime [38].

Conventional TGA systems use inert gases (nitrogen or argon) as protective atmosphere and static air as reactive gas (oxidising or burning). However, numerous chemical transformations such as reduction reactions where an oxide is converted to metal requires an unconventional ‘reducing’ atmosphere such as CO, H_2, etc.. Hence, the TGA thermobalance in most circumstances is designed to support diverse atmospheres (mixed gases). On account of that, thermogravimetry may be employed to assess mass loss or mass gain during the progress of a reaction like carbonation CaO and calcination of $CaCO_3$ [240, 260, 261].

In the present study, thermogravimetric analysis was applied during different lines of investigation, one of them is for the determination of optimal conditions

for complete decomposition of the CaO precursors (calcium acetate ($Ca(CH_3CO_2)_2$) and calcium nitrate ($Ca(NO_3)_2$)). The thermogravimetric analysis was performed on the raw precursors and on the materials loaded with the CaO precursors using both wet impregnation and precipitation as preparation routes. The preferred regime for determining the calcination temperature was non-isothermal in a range of temperature between 25-850 °C under pure N_2. The heating rate was maintained constant at 20 °C/min.

Besides of determination of the calcination temperature, TGA has been used to estimate the CO_2 capture capacity over 30 continuous carbonation-calcination cycles. This study can be considered as a benchmark to elucidate the thermal stability of CaO-saffil fibre sorbents. Moreover, a kinetic study for carbonation and decarbonation reactions was also performed. The chemical transformations were activated varying temperature and the reactive atmosphere (CO_2 as adsorptive molecules). This kinetic study was conducted isothermally and non-isothermally setting different work temperatures according to the reaction under study. In particular, mass gain was measured for carbonation of CaO whilst mass loss was detected on the reverse reaction ($CaCO_3 \leftrightarrow CaO + CO_2$). A deeper explanation and description of each study conducted by TGA is provided in their corresponding chapters.

Bearing in mind the instrumentation requirements needed to carry out the TGA experiments, two separate TGA apparatuses were utilized: 1) Stanton Redcroft TGH1000 equipped with a large aluminium crucible capable to deposit bulky sample weights (high storage capacity) (Figure 3-13 - a)). This particular TGA was employed to evaluate the optimal temperature in which the CaO precursors reach their full decomposition to the phase of interest (CaO). 2) Mettler Toledo TGA/DSC outfitted with a gas box where two different mass flow controllers supplied a protective purge gas (N_2) and a reactive gas (CO_2) into the reaction chamber (Figure 3-13 - b)). The second system was aimed at running both CO_2 capture tests (carrying capacity) over multiple cycles as well as determining kinetic parameters.

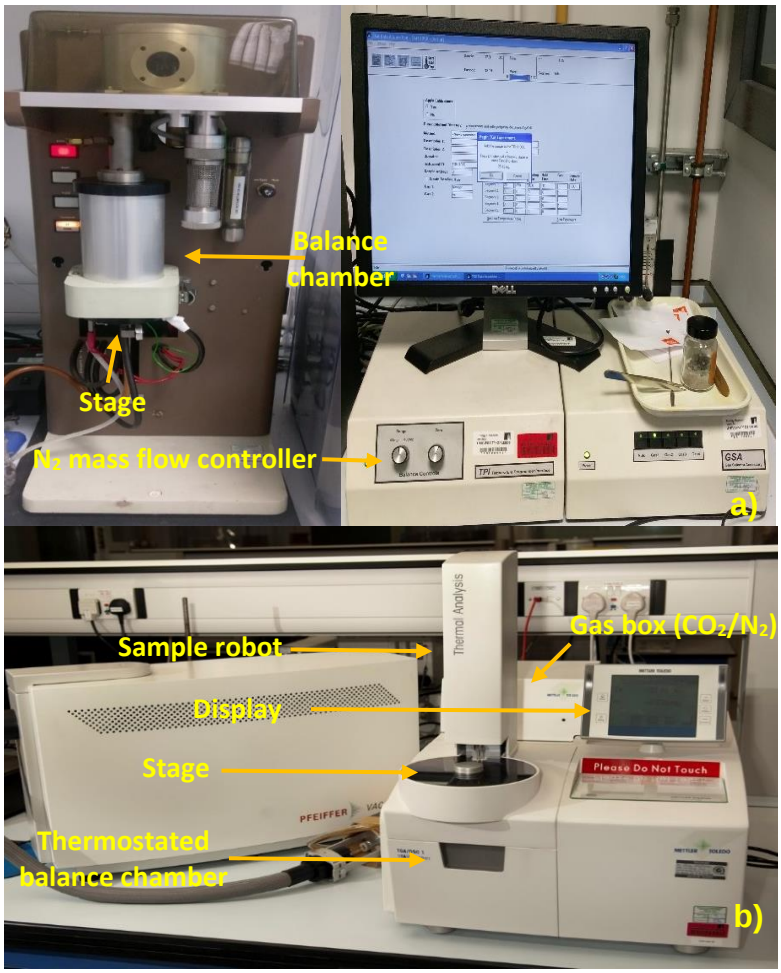

Figure 3-13. Thermogravimetric analysers used to evaluate the optimal conditions for the thermal decomposition of the CaO precursors (Stanton Redcroft TGH1000, (a)), the CO_2 capture capacity, the thermal stability and kinetic parameters (Mettler Toledo TGA/DSC1, (b)).

3.4.5 X-ray fluorescence analysis (XRF) and samples preparation

The X-ray fluorescence spectrometry is a routine characterization technique for resolving the chemical composition of bulk specimens. The concept of this technique comes from the same principle of all spectrometers in which a source of energy irradiates a specimen, and then a detector estimates the radiation released from the sample and compares it with that from a standard specimen. The ability to detect elements such as Mg, Al, Si, Ca, Na, etc. within the range from 1 to 10 ppm has positioned XRF as one of the most viable techniques to analyse solid or liquid specimens [262].

As an inherent part of this research, the notional amount of CaO attempted to being loaded over the fibrous support needed to be determined. In order to attain

this chemical composition analysis, a Rigaku ZSX Primus II apparatus of high sensitivity and precision was used (Figure 3-14). As the nature of the CO_2 sorbents is particles supported in a fibrous material whilst also there is the presence of CaO agglomerates (free-standing particles) with a random grain size, inhomogeneity and particles segregation could disturb the XRF analysis. In order to minimize reading errors, a convenient technique was utilized. The fusion bead method applied to oxides consists in fusing the materials at 1000-1200 °C for a certain period in an electric fusion machine. The flux used to fusing the CaO-based sorbents was a lithium borate mixture composed basically by 66.37% $Li_7B_4O_7$, 32.83 % $LiBO_2$ and 0.5% LiBr. The mixing ratio CaO-based sorbents/Lithium borate selected was 1:7. It is noteworthy that this ratio was used to lowering the melting point and this resulted in an easier fusion of the metal oxides to analyse. The beads preparation was conducted through a Katanax K1 prime electric fluxer in which an automated control of fusion parameters such as temperature, time, mixing velocity, cooling rate and stirring time was conducted

Figure 3-14. Rigaku ZSK Primus I system used for the elucidation of the chemical composition of the CaO-based sorbents by means of the XRF technique.

Chapter 4 Preparation of CaO-based Sorbents by Conventional Routes

In the progress of this chapter, a detailed description of the preparation procedure followed to obtain CaO-based sorbents is presented. Furthermore, in order to understand the physicochemical properties of the synthesized sorbents, an analysis of their morphological and microstructural features is conducted, including results from characterization techniques such as SEM-EDX, TGA, N_2 physisorption (BET and BJH methods) and XRD. Based on the outcomes obtained, the current chapter includes an interpretation of the apparent formation mechanism of CaO grown with non-conventional shapes (nanoflakes and octahedra) over the surface of Saffil fibres (catalytic grade). Finally, a comparison in terms of structural changes observed among the CaO-based sorbents prepared by wet impregnation and precipitation is performed.

4.1 Preparation of CaO-based sorbents by wet impregnation and precipitation methods

As mentioned in the chapter related to experimental methods and materials, wet impregnation and precipitation were chosen for performing the synthesis of the supported CO_2 sorbents. Various criteria such as equipment required for implementing each synthesis procedure, the final properties desired on the CO_2 sorbents, the raw materials, etc. were considered to select these methods among the wide range of available options. From the perspective of operational steps during the preparation process, it is advantageous from a cost viewpoint that both methods share mixing, drying and thermal decomposition .

Although the wet impregnation and precipitation routes have steps in common, the major differences result from the physicochemical transformations involved in the first two steps of the whole preparation process. As will be seen in the following sections, the CaO precursor was different for both methods. From the side of wet impregnation, calcium acetate monohydrate ($Ca(CH_3CO_2)_2 \cdot H_2O$) was used, as it has been reported that CaO-based sorbents derived from this precursor present better performance in CO_2 uptake than others (e.g. calcium citrate tetrahydrate, calcium formate, etc.). In the case of the precipitation route,

the use of a metal salt solution such as nitrates, oxalates and sulfates is justified owing these compounds having the ability to form hydroxides or carbonates over a support (see process (4-1)). Other reasons are summarized below:

- Lower safety and environmental impacts since calcination of carbonates and hydroxides do not generate toxic gases. Hence, it is an environment-friendly unit operation.
- Decomposing both species is simple and there is no poisoning of the sorbent or catalyst, in contrast with in the particular case of a direct calcination of sulfates.
- Hydroxides and carbonates derived from alkali metal salts have very low solubility. Therefore, a high supersaturation can be reached easily, giving rise to the formation of particles with small sizes.

(4-1)

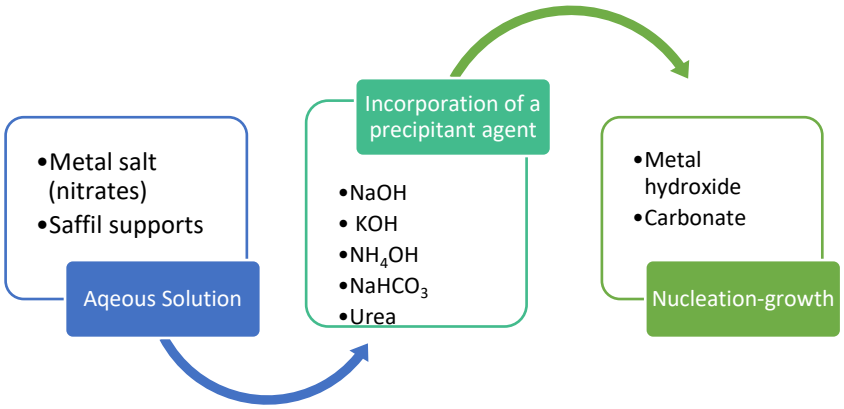

For a better understanding, further details of both preparation routes will be provided in following sections not only in terms of the procedure but also related to the synthesis parameters and their influence on the morphology, microstructure and textural properties of the as-prepared sorbents.

4.1.1 Preparation via wet impregnation

To prepare the CaO-based sorbents with different loads of active phase by the wet impregnation method, Saffil fibre (catalytic grade), distilled water and calcium acetate monohydrate (CaAc) were utilized as support, dissolution media and CaO precursor, respectively. The sequence followed throughout the whole

synthesis process is described below. Initially, a certain amount of CaAc was added into a 500 ml beaker containing 160 ml of DI water (CaAc varies depending on the notional CaO content expected after calcination of the organic matter). In order to dissolve the solid phase, the mixture labelled as solution 1 was subjected to stirring (450-500 rpm). Subsequently, Saffil fibres were incorporated into solution 1 forming a blend of CaAc-Saffil fibres (δ-Al_2O_3). It is worth mentioning that the second step of the wet impregnation process was performed with and without stirring. As significant morphological changes resulted from this parameter, a detailed discussion of the influence of stirring will be provided in the section relevant to characterization. Once the active phase precursor and the support were in interaction, the mixture remained for 4 h at 70°C until the solution volume was significantly reduced by evaporation. Afterwards, excess water was removed by drying the solids overnight using a tubular furnace with a fixed temperature of 120 °C. The last stage during the preparation was associated with a thermal decomposition of the CaO precursor. The optimal calcination temperature was investigated through subjecting the solids dried in the previous step to different decomposition times. According to the SEM analysis, the calcination conditions were 850 °C for 4 h. In order to summarize the stages encompassed in the synthesis method, an intuitive evolution diagram is presented in Figure 4-1.

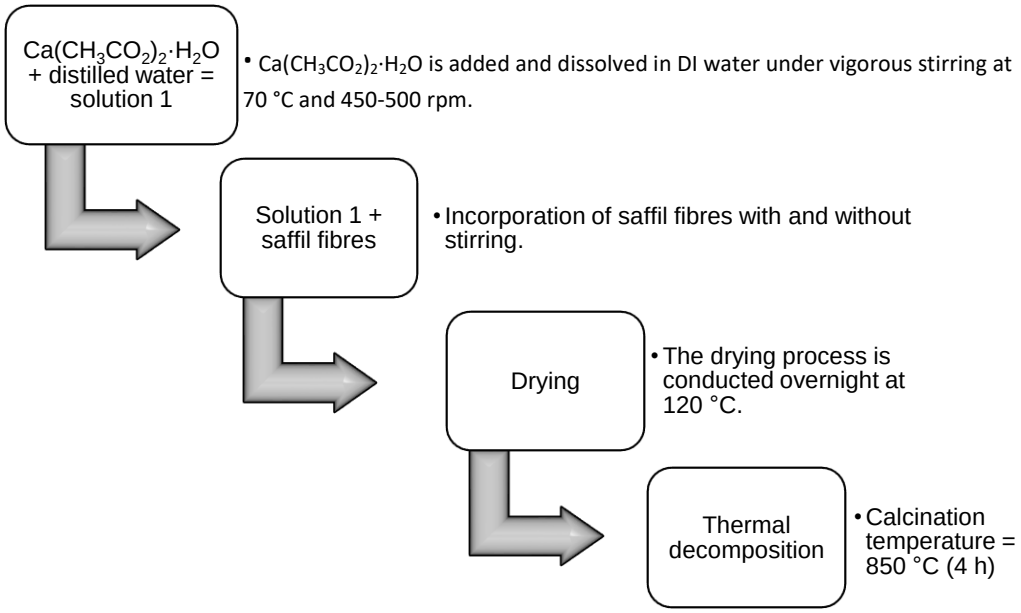

Figure 4-1. Diagram representing the sequence followed for the preparation of the Ca-Sa-%-WI sorbents using the wet impregnation method.

Figure 4-2 shows the physical appearance of the solutions prepared to impregnate CaO over the surface of the fibrous support as well as the texture of the sorbent upon its calcination. Evidently, to attain a homogeneous impregnation, CaAc needed to be totally dissolved as segregation of particles or grains diminished the amount of active phase that could be loaded on the support (see Figure 4-2-(a)). Moreover, the aspect of the solid calcined under parameters aforementioned is presented. As can be seen in Figure 4-2-(c), there was no evidence of segregation of CaO even in the solution prepared under static state.

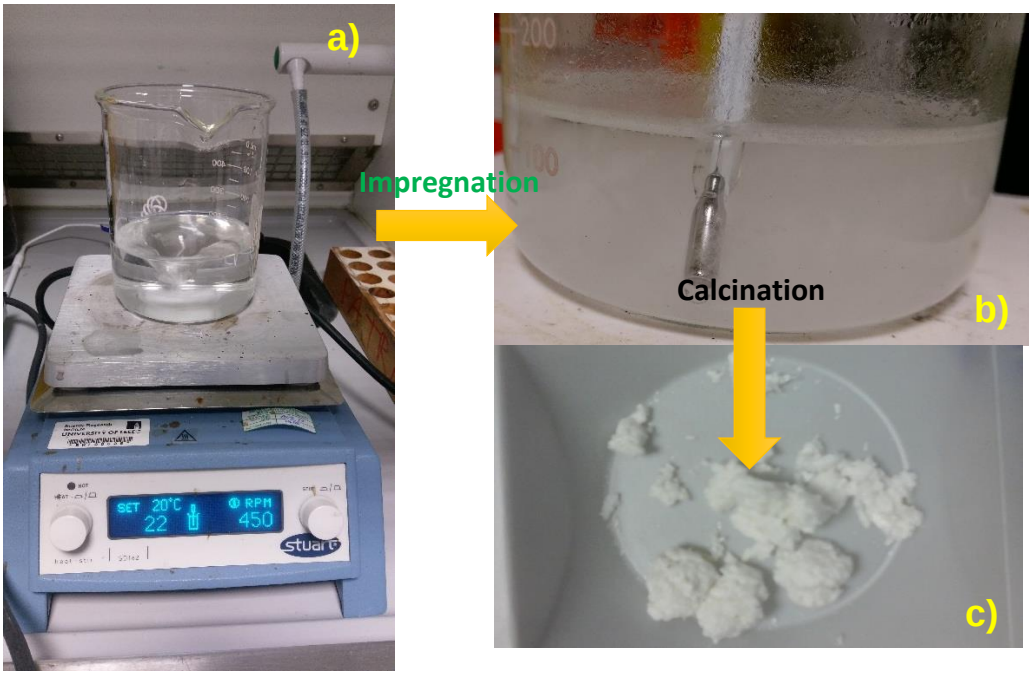

Figure 4-2. Images of the solution containing CaAc dissolved in water (a)), the blend of CaAc-Saffil fibres in aqueous solution (b)) and the aspect of the sorbents once the calcination of the active phase was reached (c)).

For simplicity, the prepared sorbents were labelled as Ca-Sa-%-WI, where Ca, Sa, percentage (%) and WI are associated with the sorbent, Saffil fibres as CaO support, notional content (also referred as theoretical content) desired over the surface of the support and abbreviation of wet impregnation method, respectively. A list of the sorbents prepared using WI is exhibited in Table 4-1. This table also contains the optimized synthesis parameters to attain a successful impregnation of the CO_2 sorbent.

Table 4-1. Ca-Sa-%-WI sorbents prepared by wet impregnation using optimised ageing and calcination parameters.

Sorbent name	Preparation parameters	Drying process conditions	Calcination settings
Ca-Sa-25%-WI	**Temperature:** 70 °C **Ageing time:** 4 h	**Drying time and temperature:** 120 °C for 12 h **Heating rate** 5 °C/min	**CaAc decomposition:** 850 °C **Heating rate:** 10 °C/min **Calcination time:** 4h
Ca-Sa-20%-WI			
Ca-Sa-15%-WI			
Ca-Sa-12%-WI			
Ca-Sa-8%-WI			
Ca-Sa-5%-WI			

4.1.2 Preparation of CaO-based sorbents using precipitation, with urea as the precipitant agent

Precipitation was proposed as another option for the synthesis of CaO-based sorbents since this route not only permits the nucleation of small particles on the surface of the support of interest but also the growth of larger particles with a well-structured shape through Ostwald ripening (explained in section 4.6.1). There are several factors playing a crucial role in the synthesis such as temperature, pH, ageing time and concentration of the solutions containing the precursor and the precipitant agent. Other relevant factors that alter the precipitation method were the properties of the CaO support. Because δ-Al_2O_3 fibres have a mean diameter between 3.5 to 4.5 µm, particles with nanometric dimensions must coat the support. To achieve the intended characteristics on the CaO-based sorbents, two different precipitation routes were used, as both offer a wide spectrum of options for tuning the morphology of the CO_2 sorbents. This section will present in a detailed manner the methodology used to prepare the supported sorbents. For practical purposes, the sorbents will be labelled as CaO/Sf-%-U sorbents where CaO corresponds to the CO_2 sorbent, Sf means Saffil fibres, % is associated with the notional amount of CaO loaded and U is linked to the precipitant agent (urea - CH_4N_2O).

As far as the preparation procedure is concerned, the CaO/Sf-%-U sorbents with different active phase contents were obtained as follows: initially, a solution containing the CaO precursor was prepared by dissolving calcium nitrate tetrahydrate ($Ca(NO_3)_2{\cdot}4H_2O$) into DI water. The optimal concentration for

reaching the precipitation of CaO precursor over Saffil supports was 0.085 mol/L as it permits to obtain pH above 7.5 when mixing with an urea solution (preparation described below). Then, 0.5 g Saffil fibres were added into the beaker in which the precursor was dissolved. This solution was stirred vigorously (450-500 rpm) for a short time with the aim of dispersing the solid support. Simultaneously, urea solution was obtained by blending urea and DI water. The concentration of this basic solution was 6 mol/L [263]. To reach precipitation, the urea solution was incorporated dropwise into the solution containing the CaO precursor and the Saffil fibres. The resultant mixture was maintained at 85 °C at pH 8. It is noteworthy this step was conducted under steady state. The parameters settled in the course of the synthesis process were preserved with the aim of achieving a slow hydrolysis of urea and thus providing a consistent concentration of ligands (OH^- and CO_3^{2-}) on the external surface of saffil fibres (interaction zone of interest) [228, 264].

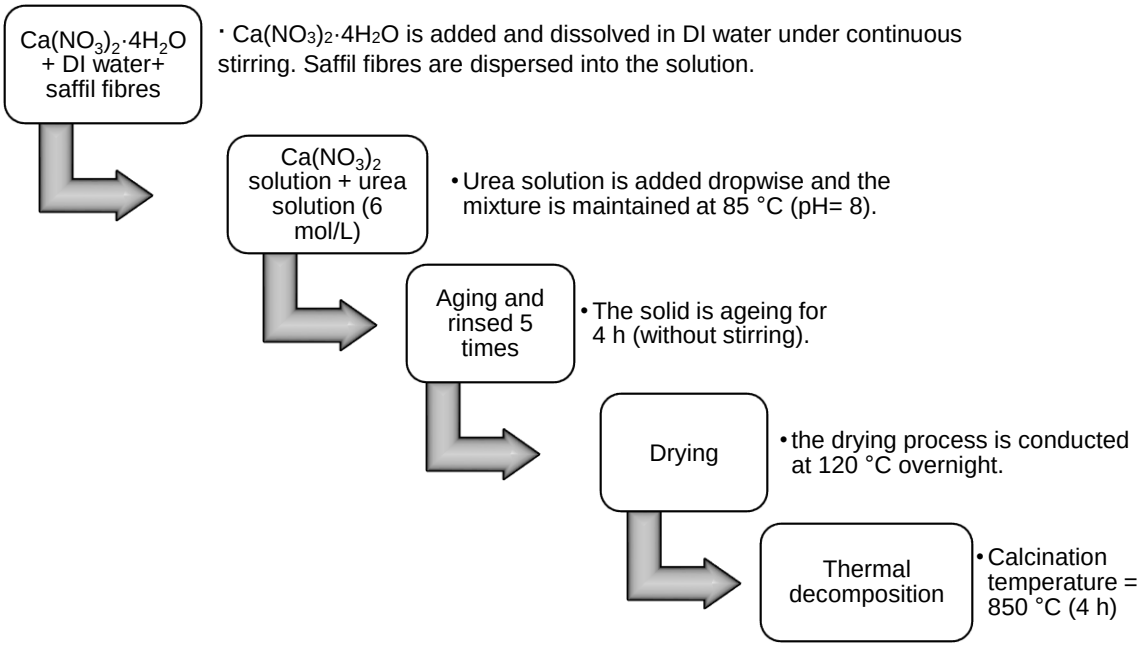

Figure 4-3. Procedure followed to achieve the synthesis of CaO/Sf-%-U sorbents by means of the precipitation method via urea combined with a thermal decomposition of the CaO precursor.

As shown in the step-down scheme depicted in Figure 4-3, the sequence indicates that once the blended solution was aged for 4 h, the solid was collected

by filtration. To complete this step, the material was rinsed 5 times using DI water. The last two steps consisted in getting rid of water excess by drying at 120 °C overnight and calcining the resulting solid at 850 °C during a period of 4 h into a tubular furnace. The optimal thermal decomposition time was found on the basis of the outcomes revealed by the Ca-Sa-%-WI sorbents (analysis presented in the section 4.1.1). A summary of all steps encompassed throughout the synthesis of the sorbents is shown in Figure 4-3.

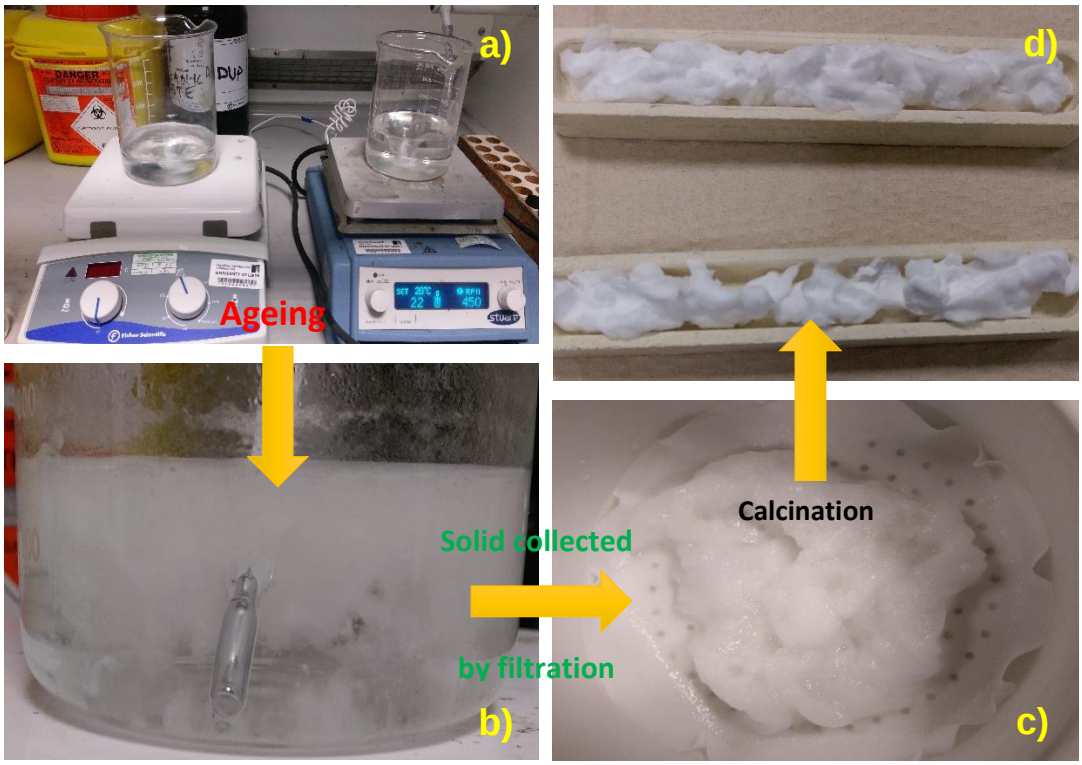

Figure 4-4. Aspect and texture of the solutions prepared to precipitate different amounts of CaO over Saffil fibres (a), the blended solution under ageing (b), the solid filtered and rinsed (c) and the sorbent coming from the drying and calcination processes.

To complement the description of the synthesis method, images which exhibit the physical appearance of the solutions (CaO precursor plus Saffil fibres and urea) (a), the blended mixture containing precursor/support and urea (b), the solid rinsed (c) and the material thermally decomposed (d) are presented in Figure 4-4. In addition, a table that point out the sorbents synthesized by precipitation via urea is included below. Preparation parameters such as synthesis temperature, ageing time, drying and calcination are also included into Table 4-2. As can be seen, the CaO notional amounts were preserved as a

straight comparison is intended to be conducted throughout the discussion of the results aimed to evaluate the performance of the sorbents as a function of the synthesis method.

Table 4-2. Set of synthesis conditions for preparing CaO/Sf-%-U sorbents with different active phase contents via urea.

Sorbent and content of active phase	Preparation conditions	Drying parameters	Calcination conditions
CaO/Sf-25%-U	**Temperature:** 85 °C **Aging time:** 2 h	**Drying time and temperature:** 120 °C for 12 h **Heating rate** 5 °C/min	**CaAc decomposition:** 850 °C **Heating rate:** 10°C/min **Calcination time:** 4h
CaO/Sf-20%-U			
CaO/Sf-15%-U			
CaO/Sf-12%-U			
CaO/Sf-8%-U			
CaO/Sf-5%-U			

4.1.3 CaO-based sorbents prepared through precipitation using NaOH as the precipitant agent

Several investigations have reported the synthesis of nanosized CaO particles using a wide variety of methodologies such as solvothermal, hydrothermal, precipitation, etc. [265]. The aim of depositing CaO particles with sizes between 200 nm and 1 µm over Saffil fibre supports has led this research to find another potential preparation methodology. According to a literature survey, it was found that precipitation method via sodium hydroxide (NaOH) not only allows the formation of particles with nanometric dimensions but also varying the morphology in which CaO can grow, namely amorphous, nanoflakes, octahedral, etc. [265]. In addition, another benefit is that no significant technical changes (same laboratory setup) are needed to conduct precipitation via NaOH than using urea as a precipitant agent. The operation units used to conduct the experiments would remain unaltered but only modifications in concentrations, dissolution media and pH were needed.

The synthesis of CaO-based sorbents using NaOH as precipitant agent was carried out as follows: pre-calculated amounts of calcium nitrate tetrahydrate were added into a beaker containing 25 ml of ethylene glycol (>99% Aldrich) (solution 1). Grains of $Ca(NO_3)_2 \cdot 4H_2O$ were dissolved at 115 °C by means of a hotplate stirrer apparatus (450 – 500 rpm). Separately, a solution containing the

precipitant agent was prepared by incorporating 2.1 g of NaOH into distilled water (solution 2) [265, 266]. Subsequently, 0.5 g of Saffil fibres were incorporated and then dispersed into solution 1. To attain the precipitation of the CaO precursor in accordance with equation (4-2), a given volume of solution 2 was added dropwise into solution 1. The pH reached by the mixture was above 12. Later on, the viscous solution was aged for 4 h and thus the solid was collected through filtration and rinsed 5 times using DI water. To complete the synthesis process, the material was placed in a combustion boat with the aim of drying the specimen overnight. Lastly, the active phase precursor was thermally decomposed (reaction (4-3)) using a tubular furnace at 850 °C for 4 h. The drying and calcination parameters were established based on the outcomes revealed by the methods employed previously. The steps adopted in the course of this preparation route are summarised in Figure 4-5.

$$\mathrm{Ca(NO_3)_2 + 2\ NaOH \leftrightarrow Ca(OH)_2 \downarrow + 2\ NaNO_3} \quad (4\text{-}2)$$

$$Ca(OH)_2 \leftrightarrow CaO + H_2O \quad (4\text{-}3)$$

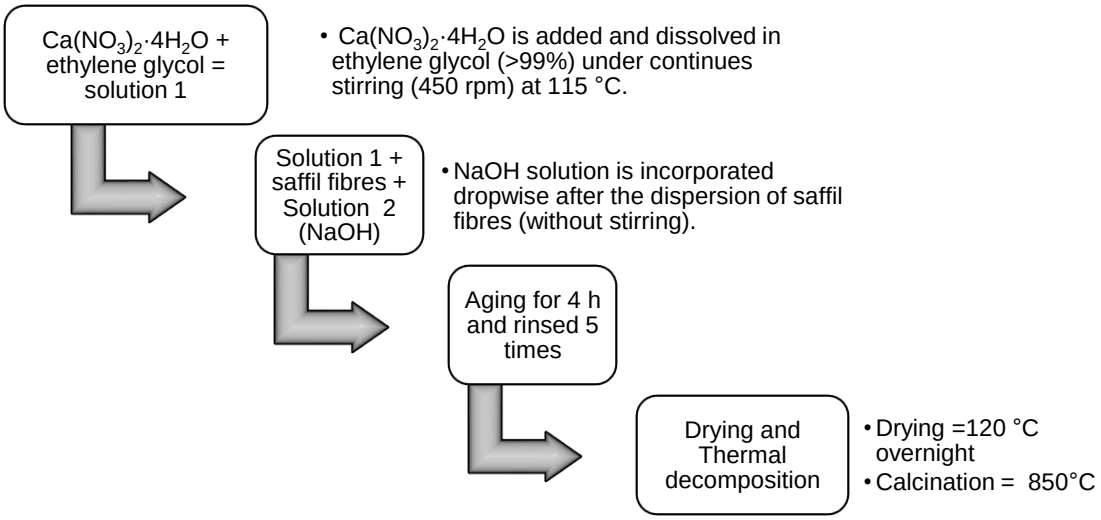

Figure 4-5. Step-down process for the synthesis of supported sorbents CaO/Sf-%-SH by using the precipitation method via NaOH at pH above 12.

Figure 4-6-(a) shows the laboratory equipment utilised to control the parameters mentioned so far. In contrast with precipitation via urea, the blended solution containing CaO precursor, Saffil fibres and the precipitant agent turn very viscous as the NaOH solution is added. It was due to a fast displacement reaction

(precipitation) (Figure 4-6-(b)). In regards to the two last operational steps (drying and calcining), there was no notable difference achieved in the texture of the CaO-based sorbents (see Figure 4-6-(c) and (d)).

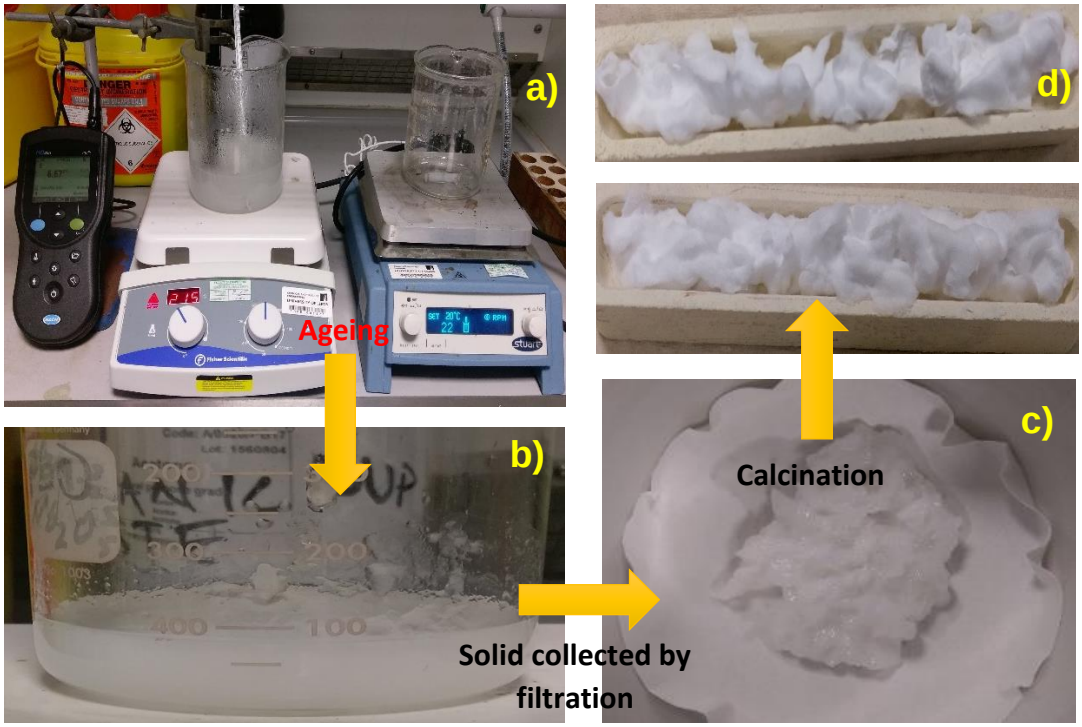

Figure 4-6. Images presenting the lab equipment employed to control the synthesis variables (a), appearance of blended solutions (b), solid collected after filtration-rinse (c) and texture of the calcined specimen (d).

In the same way as the CO_2 sorbents obtained by wet impregnation and precipitation via urea, the sorbents prepared by precipitation using NaOH were labelled as CaO/Sf-%-SH. This nomenclature follows the same structure as previously, however, the abbreviation SH (NaOH) replaced U associated with urea. Table 4-3 lists all sorbents prepared via NaOH. As before, the optimized synthesis parameters are also provided.

Table 4-3. Sorbents and synthesis variables employed throughout the preparation of CaO/Sf-%-SH sorbents.

Sorbent, content of active phase and synthesis method	Preparation conditions	Drying parameters	CaO precursor decomposition and calcination parameters
CaO/Sf-25%-SH		**Drying time and temperature:**	**CaAc decomposition:**
CaO/Sf-20%-SH	**Temperature:**	120 °C for 12 h	850 °C
CaO/Sf-15%-SH	115 °C		**Heating rate:**
CaO/Sf-12%-SH			10 °C/min
CaO/Sf-8%-SH	**Aging time:**	**Heating rate**	**Calcination time:**
CaO/Sf-5%-SH	4 h	5°C/min	4h

4.2 Determination of optimal preparation conditions

As stated in the previous sections associated with the preparation of CO_2 sorbents, synthesis variables had a strong influence on the final microstructural features of CaO precursor impregnated or precipitated over the fibrous support. Hence, each set of conditions were determined in accordance with results revealed by SEM-EDX, XRD and TGA. This evaluation will begin with the notional CaO amount expected to have deposited. Then, the effects of temperature and stirring will be discussed and finally, the study of the optimal calcination conditions will be conducted.

The SEM images presented in Figure 4-7 reveals the effect of CaO concentration. As can be observed in Figure 4-7-(a), when high notional amounts of precursor are used to impregnate the fibres (50 wt. % CaO), there is formation of free-standing CaO agglomerates. Apparently, particles grew with irregular dimensions and random distribution. High contents of CaO precursor under continuous stirring avoid having control on the impregnation and promote coarsening of CaO particles outside the surface of Saffil supports. The dimensions of the agglomerates are considerably larger than the Saffil fibres, thus, the supports become trapped. In that manner, the function of Saffil as CaO stabilizer would be minimized. In addition, due to the presence of a non-localized formation of aggregates, there are vast areas in which Saffil supports are uncoated. From Figure 4-7-(a), it can be discerned that low CaO contents are preferred to get a better dispersion of the expected phase over the surface of the fibrous support.

To study more in depth the first batch of CaO-based sorbents prepared by wet impregnation and precipitation methods using vigorous stirring, the SEM technique was used. Figure 4-7-(b) shows a SEM micrograph associated with a Ca-Sa-%-WI sorbent prepared with 30 wt. % in presence of continuous stirring. From this image, it is clear CaO particles were deposited over the periphery of Saffil supports but the impregnation was conducted irregularly as the particles do not seems to cover uniformly the surface of a single Saffil fibre captured by SEM technique. Additionally, there is also undesirable manifestation of CaO agglomerates that grew outside of the high-temperature resistant supports. This

heterogeneous deposition of CaO was observed in all the CaO-based sorbents prepared by the different methods expecting an active phase load above 25 wt. % (maximum 50 wt. %). Accordingly, it was decided to prepare CaO-based sorbents with notional amounts equal or below 25 wt. % without stirring.

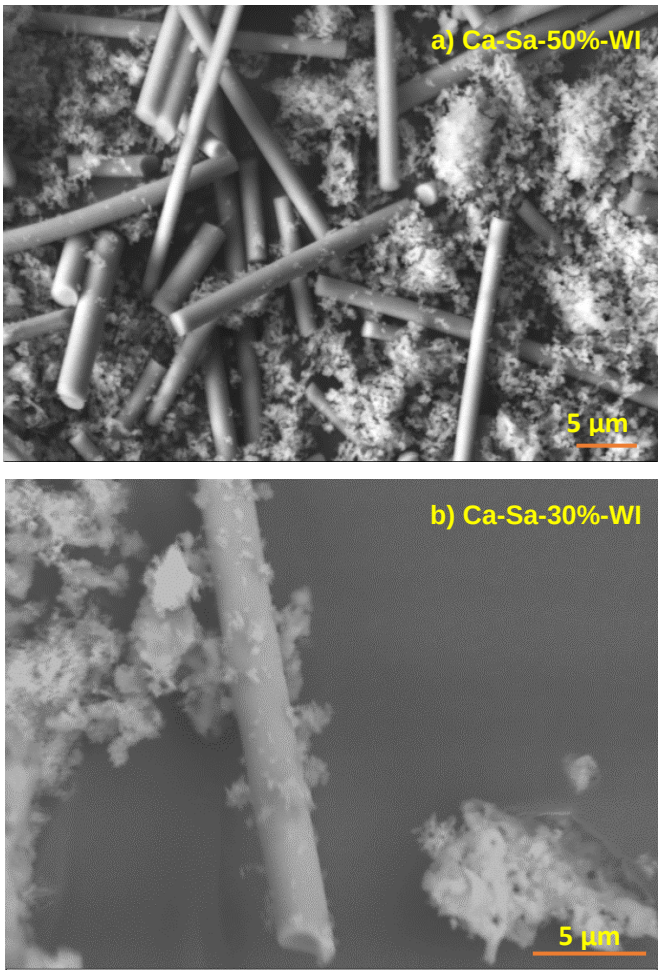

Figure 4-7. SEM micrograph showing the formation of CaO agglomerates when high amounts of active phase (50 wt. % CaO balance) are attempted to be loaded over the fibrous support by wet impregnation method (a) and heterogeneous deposition of CaO particles occasioned by the effect of stirring (b).

Apparently, a variable that also played an important role in the formation of freestanding CaO agglomerates was temperature. High synthesis temperatures promote fast evaporation of the solvent, which in turn can cause a nucleation-growth process in solution rather than on the surface of Saffil fibres. In other words, it means a heterogeneous deposition of active material. Hence, the temperature to evaporate the excess of aqueous solution was decreased from 85 °C to 70 °C. This change was performed just for the wet impregnation method.

In the particular case of precipitation, the temperature remained as indicated in the references used to reach a controlled deposition of CaO.

To confirm the formation of CaO agglomerates, EDX element-mapping technique was employed (Figure 4-8). This study allowed investigating the spatial distribution of Ca and other elements such as Al and O existent in a sorbent prepared via wet impregnation and with a very high content of CaO, namely 50 wt.% (Ca-Sa-50%-WI). According to this analysis, the density of blue dots associated with calcium signals (Ca kα in Figure 4-8) detected is more evident in certain regions. This heterogeneous distribution occurred as the Ca content varied from a scanned region to other. Oxygen as an inherent element of CaO and δ-Al_2O_3 was seen all over the mapped area (red signals in Figure 4-8). In the particular case of Al, characteristic X-rays emitted by this element indicated by yellow dots were located in positions where δ-Al_2O_3 fibres are present (see Figure 4-8). Similar outcomes were observed in EDX maps collected for CaO/Sa-%-U and CaO/Sa-%-SH sorbents.

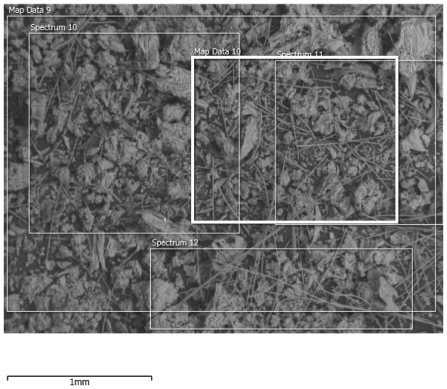

Analysed area of Ca-Sa-50%-WI sorbents

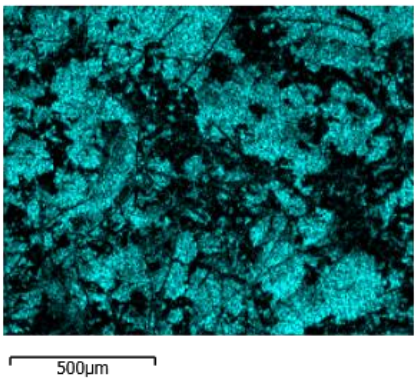

Calcium (Ca kα)

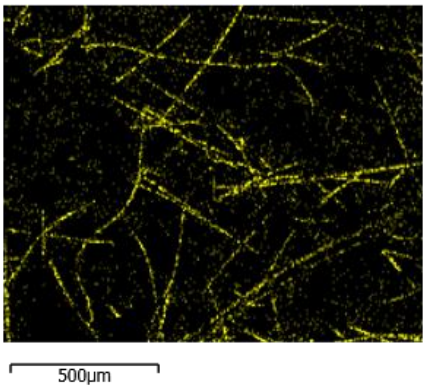

Aluminium (Al kα)

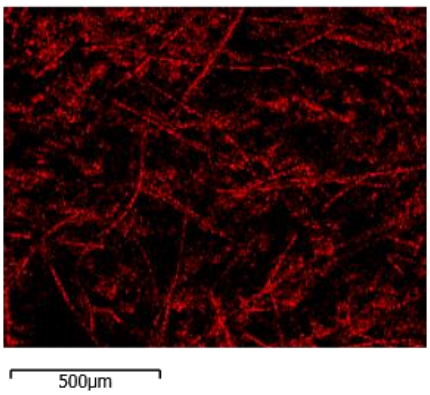

Oxygen (O kα)

Figure 4-8. EDX maps showing the elemental distribution of Ca, Al and O over a mapped area delimited by the white rectangle.

4.2.1 Effect of temperature and stirring on the final morphology of the CaO-based sorbents.

Based on the CaO morphology adopted, observation of the conditions leading to the undesirable formation of freestanding CaO aggregates and a scarce deposition of active phase on the fibrous support, experimental conditions were then optimized. The first variable studied was stirring since a substantial improvement in depositing CaO over Saffil supports could be achieved under static conditions (no stirring). Although it is well-known that stirring promotes a homogeneous dispersion of the components in a mixture, if the attraction forces between the support and hydroxide are weak, stirring might prevent contact between them, preventing deposition of the expected phase. Figure 4-9 presents SEM micrographs in which different amounts of CaO (25 and 5 wt. %, (a) and (b) respectively) were loaded on Saffil fibres by wet impregnation in the absence of stirring. As can be seen, a homogeneous deposition of CaO particles was reached. The micrographs (a) and (b) showed that although both CO_2 sorbents were synthesized with different amounts of precursor, CaO grew dispersed along the surface of the fibres as planned. Interestingly, the CaO particles that formed on the periphery of the support adopted a non-conventional morphology, namely nanoflakes. From a visual perspective, it can be seen in Figure 4-9 that the size of the CaO nanoflakes was a function of the CaO precursor amount present in the blended solution prepared for the impregnation or precipitation of the active phase. This effect is discerned because of the flake to flake distance decreases as the CaO load increases. Evidence of greater flakes will be confirmed later through thickness measurements performed in sorbents Ca-Sa-%-WI and CaO/Sf-%-U sorbents prepared with various CaO precursor loads (see Figure 4-29). It is important to highlight that the distance flake to flake in the sorbent Ca-Sa-5%-WI seemed larger than to that with 25 wt. %. Regions with darker contrast in the micrograph of Figure 4-9-b) are more prominent than in the high-resolution image a) portrayed in the same Figure. It can be explained by considering that the higher the amount of CaO available for forming nanoflakes, the larger the dimensions of the nanoflake. As a visual benchmark, a micrograph of polycrystalline Saffil supports is inset in Figure 4-9-b).

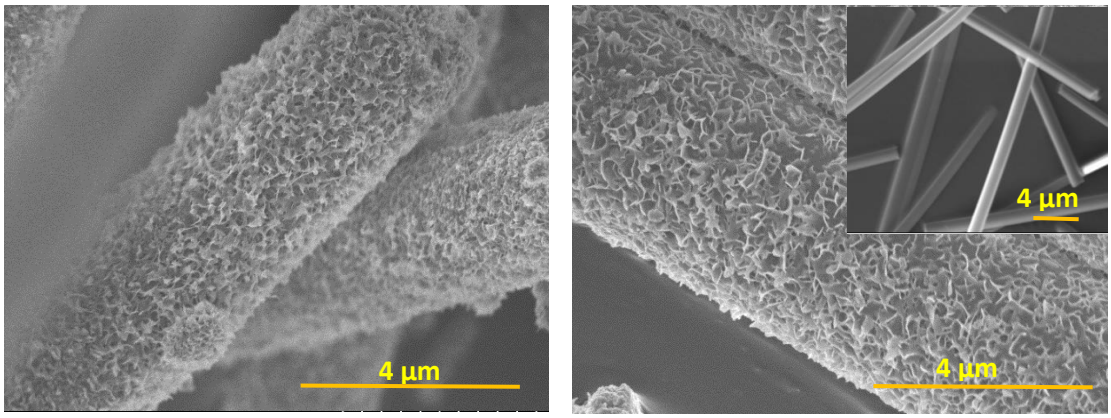

Ca-Sa-25%-WI sorbent Ca-Sa-5%-WI sorbent

Figure 4-9. Ca-Sa-%WI sorbents prepared under steady state at 70 °C with an ageing time of 4h. The inset in b) correspond to uncoated Saffil fibres.

In order to confirm the characteristics of the impregnation of calcium oxide, once again EDX-mapping of elements (Ca, O and Al) on the Ca-Sa-25%-WI sorbent was applied. As seen on the inspection field shown in Figure 4-10, regions with high content of Al associated to Saffil fibres had a dense distribution of green dots as intense characteristic X-ray were emitted. To corroborate that CaO was impregnated on the periphery of Saffil supports, signals of Ca kα must overlap the ones of Al kα. Comparing element maps from Figure 4-10, it can be seen that Ca was dispersed homogeneously along the surface of the support. It is relevant to mention that some blue dotted areas (overlapped with Al signals) in the CaO map are more intense since the position of the detector collects more signals from specific angles, and thus, the contrast would be different on account to the position of the incident beam and the X-Ray detector. Moreover, oxygen dispersion was as expected, in all areas in which CaO and δ-Al_2O_3 was present.

On the other hand, examining the CaO/Sf-%-U sorbents by SEM (see Figure 4-11), it was found that similar morphology was adopted via precipitation using urea as a precipitant agent. Although same notional amounts of CaO were employed during the synthesis with regards to sorbents prepared via wet impregnation, a thicker layer of nanoflakes was observed in all sorbents (Figure 4-11 - (a), (b) and (c))(further details of thickness is shown in a later section). This could be because urea in solution decomposes slowly at 85 °C, providing a uniform concentration of OH^- on the surface of the fibrous support. Thus, precipitation happens homogeneously as predicted. However, despite growing

monodisperse CaO particles, the SEM image of the CaO/Sf-25%-U sorbent depicted in Figure 4-11 – (d) give evidence of the formation of freestanding CaO agglomerates and rods with mean dimensions in the order of micrometres.

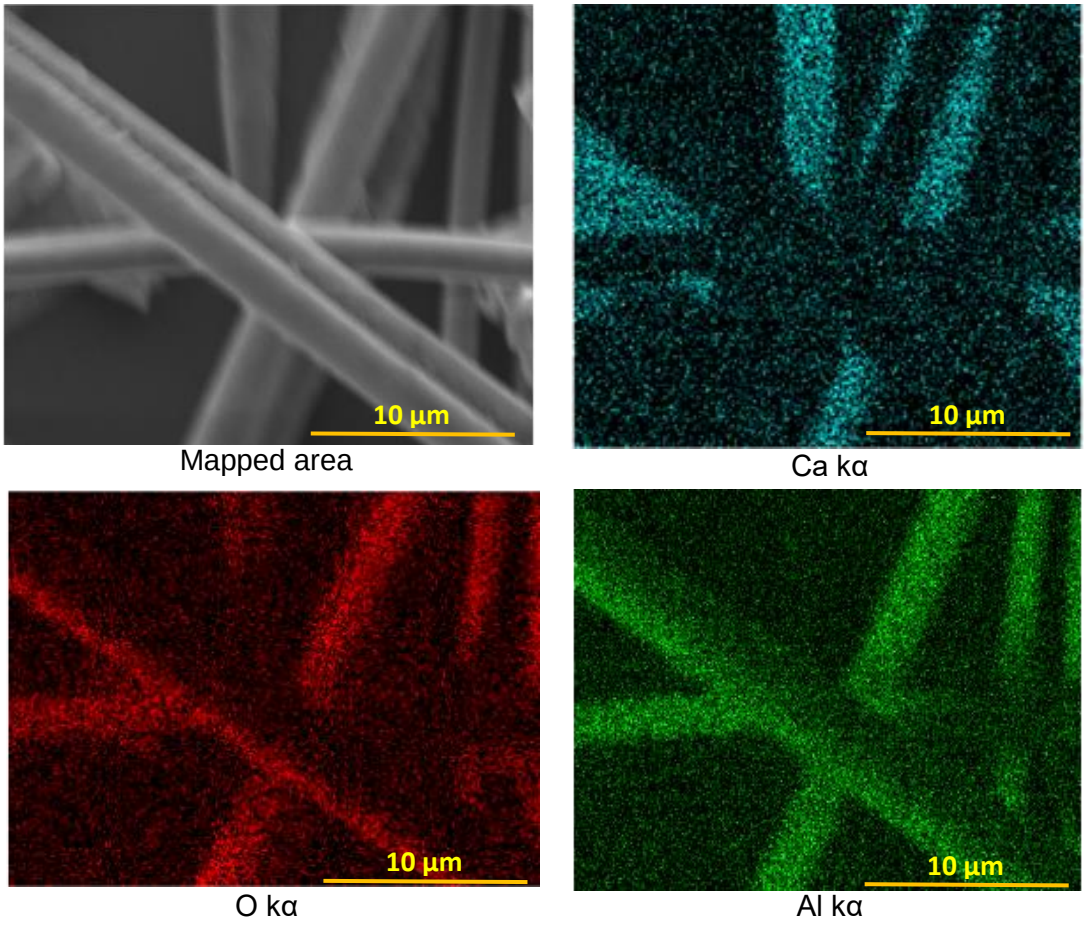

Figure 4-10. X-ray mapping of elements performed to the Ca-Sa-25%-WI sorbent through EDX technique.

The micrograph with higher magnification attached to the same figure shows that the agglomerates and rods have a microstructure characteristic of conventional unsupported CaO (inset on Figure 4-11 – (d)). Two theories are proposed to justify these CaO formations: 1) CaO agglomerates and rods grow after Saffil fibres were coated with a monolayer of nanoflakes. It means when the external surface of the support becomes saturated with CaO particles, there was no sufficient energy (CaO-Saffil fibre) to attract nuclei and grow particles beyond the outer layer of nanoflakes. Therefore, this CaO remnant grew anywhere outside the area of interest. The second theory considers the rods are Saffil supports coated with a significant amount of CaO. An attempt to confirm the 2nd theory was conducted through the EDX technique but unreliable results were obtained

due to the X-rays not penetrating the deep layer of CaO. Therefore, no signals related to Al were detected in the scanned area. Evidently, uncertainty caused by the lack of information related with the composition of the rods led to assume the possibility of formation of either CaO aggregates or rods or both.

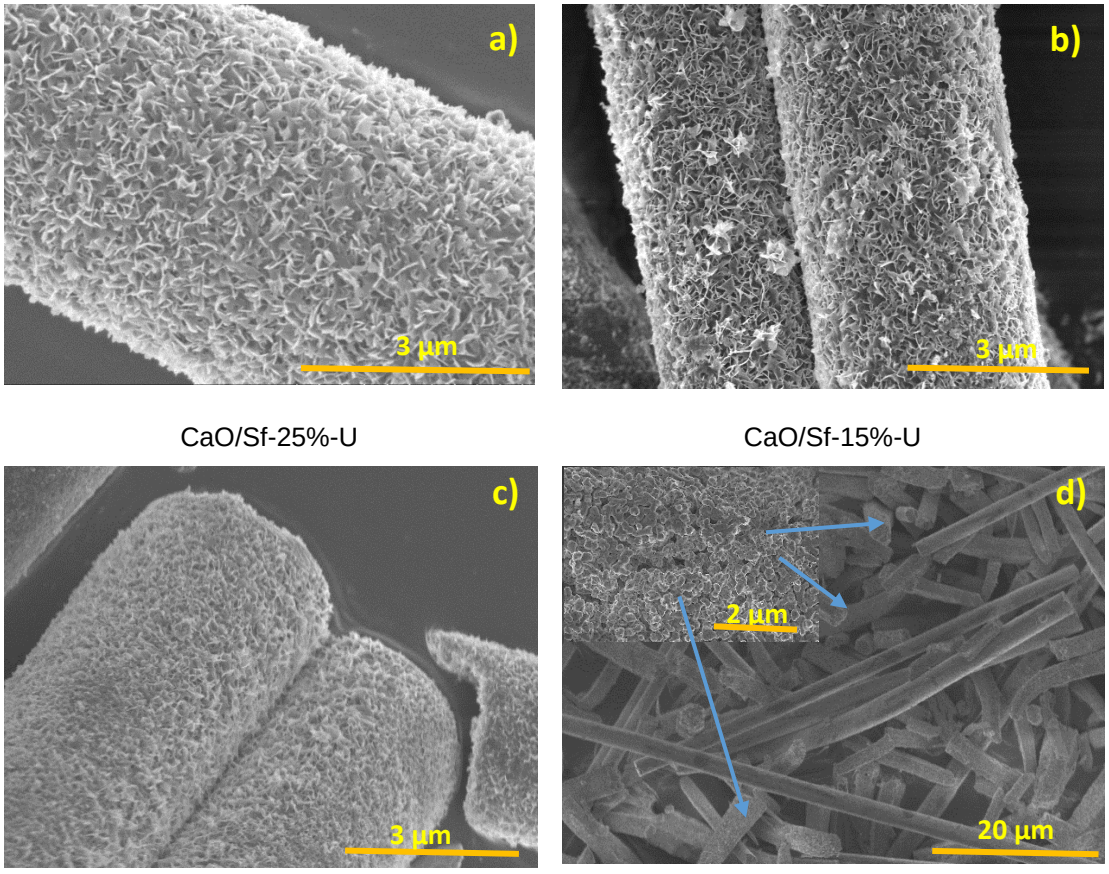

CaO/Sf-25%-U

CaO/Sf-15%-U

CaO/Sf-5%-U

Micrograph of CaO/Sf-25%-U sorbent registered with low magnification

Figure 4-11. SEM micrographs that reveal the morphology of CaO/Sf-%-U sorbents prepared with different notional amounts of active phase.

To complement the analysis of the effect of precipitation parameters and their impact on the final properties of the CaO-based sorbents prepared by precipitation, X-ray mapping of elements through EDX was conducted. As seen in Figure 4-12-(a) associated with CaO/Sf-25%-U, Ca exhibited a uniform distribution over the surface of the fibrous support. This was confirmed by overlapping of the signals emitted by both elements Al and Ca (Figure 4-12-(a) and (b)). Evidently, there was a significant improvement not only introducing urea

as a precipitant but also using static conditions for preparing this family of sorbents.

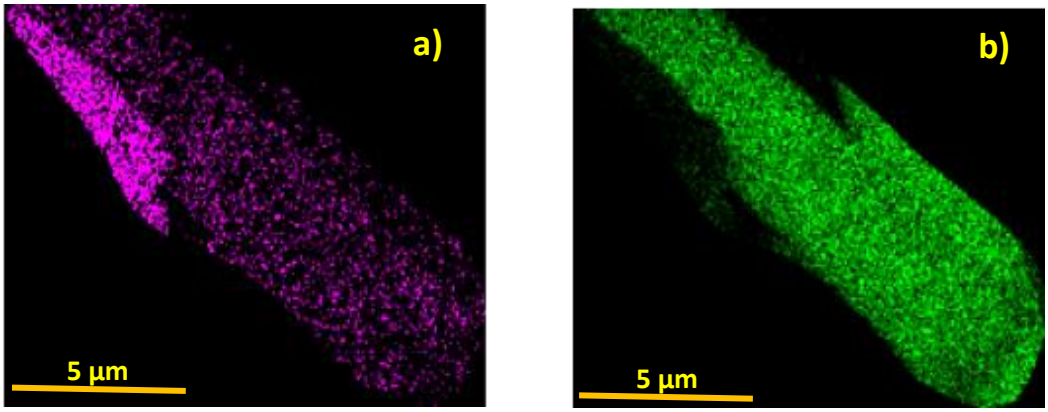

Ca Kα (CaO/Sf-25%-U) Al Kα (CaO/Sf-25%-U)

Figure 4-12. Element maps of Ca-(a) and Al-(b) performed using EDX technique.

As part of the analysis conducted to investigate the optimal synthesis parameters for coating CaO on the Saffil supports using precipitation in presence of an alkali solution (NaOH), SEM-EDX was employed once again. A set of SEM images presenting the morphology of CaO/Sf-%-SH sorbents are shown in Figure 4-13. The micrograph depicted in (a) gives an overview of the morphology adopted by CaO. From Figure 4-13- (b), (c) and (d), it can be seen that the growth of CaO over Saffil fibres is far from being as uniform as those obtained by precipitation via urea. In the case of NaOH, it promotes a rapid nucleation and growth of the active phase. In contrast with the sorbents prepared by the same method but via urea, CaO particles lack a well-defined structure, and in terms of size, the particles vary radically with each other.

The results obtained by SEM were supported with EDX mapping and a linescan profile of Ca and Al. Analysing element maps coming from the sorbent loaded with a notional amount of 25 wt. % via NaOH (Figure 4-14-(b)) evidence was found of dense and localized concentrations of Ca. The linescan profile carried out to figure out the abundance of Ca and Al along a particular traced line revealed that concentration gradients of Ca differed drastically along the analysis line whilst the Al counts detected did not present strong fluctuations, as its concentration was similar throughout the fibres (see Figure 4-15). Although linescan profiles belonging to CaO/Sf-%-SH sorbents prepared with 15 and 5 wt.

% were not incorporated as it could be redundant, amorphous Ca distributed heterogeneously over the Saffil fibres surface was also observed.

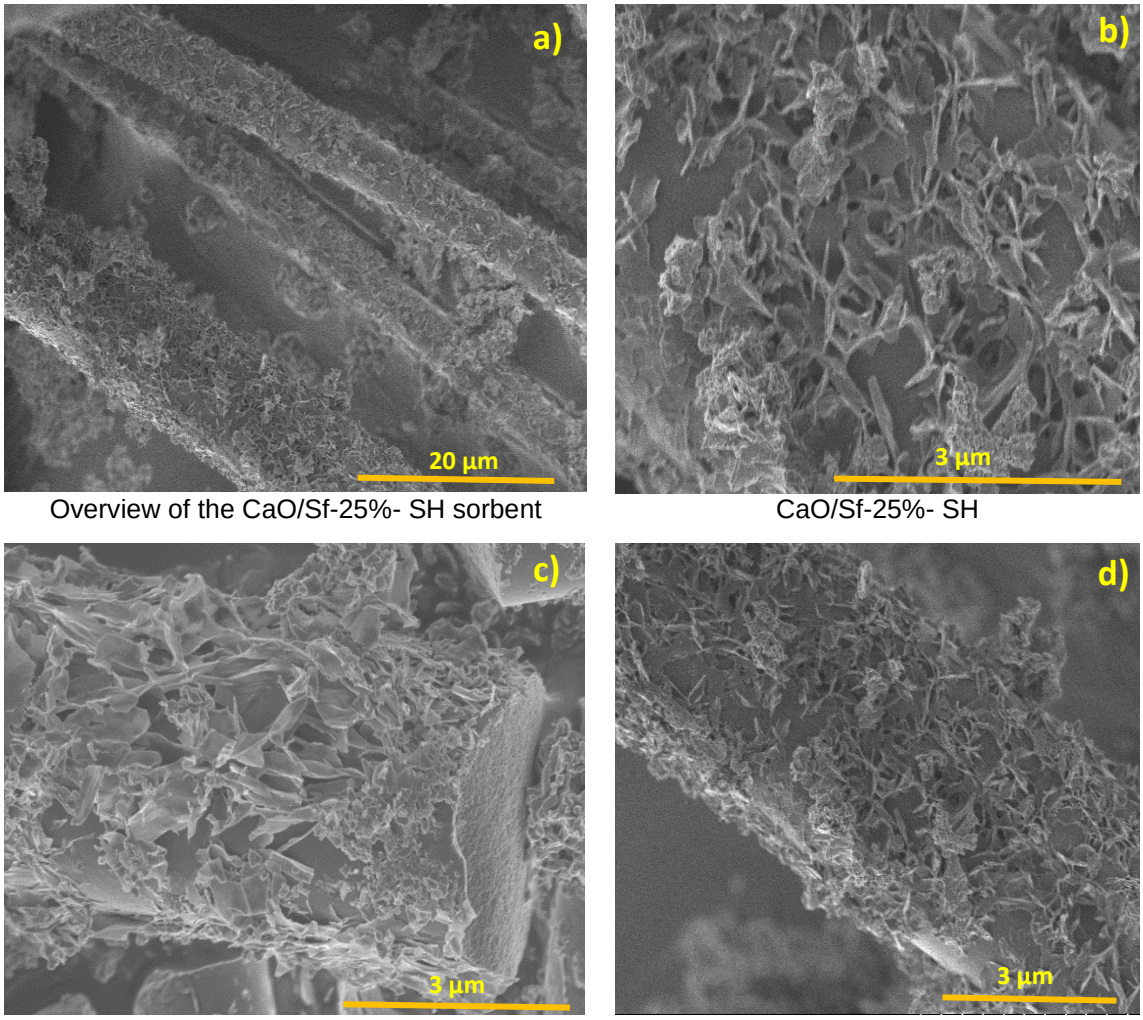

Overview of the CaO/Sf-25%- SH sorbent

CaO/Sf-25%- SH

CaO/Sf-15%- SH

CaO/Sf-5%-SH

Figure 4-13. Morphology adopted by CaO when loaded over Saffil fibres via precipitation method with NaOH as the precipitant agent.

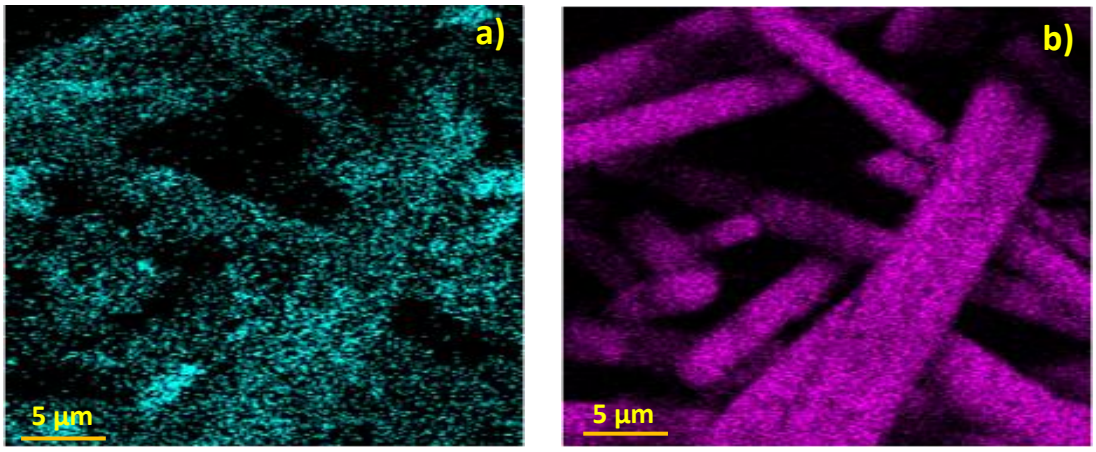

Ca Kα (CaO/Sf-25%-SH)

Al Kα (CaO/Sf-25%-SH)

Figure 4-14. EDX element maps showing the distribution of Ca (a) and Al (b) in the sorbent CaO/Sf-25%-SH.

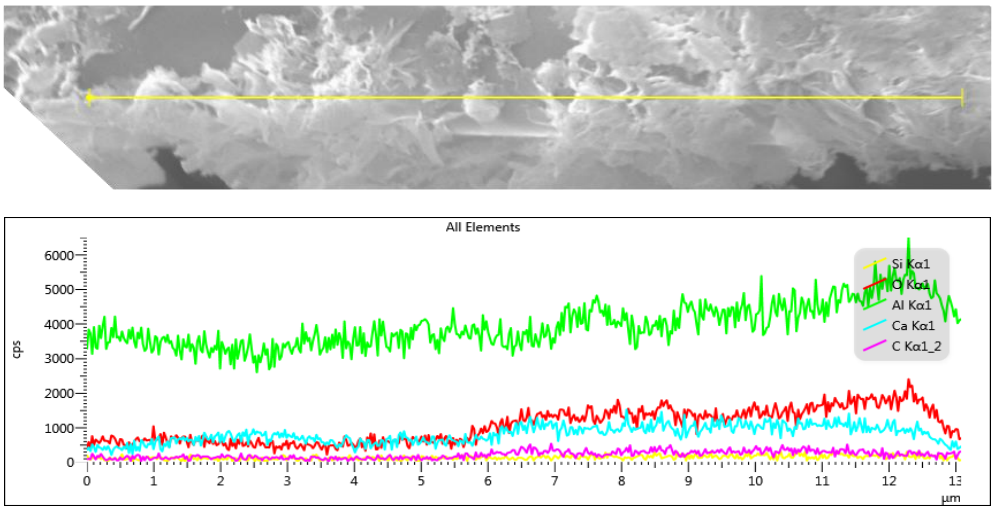

Figure 4-15. EDX linescan profile showing the abundance of Ca, Al and other elements in the CaO/Sf-25%-SH sorbent. Linescan performed for 20 min with no counts variation after this analysis time.

4.2.2 Apparent formation mechanism of CaO nanoflakes over Saffil fibre supports

To explain the peculiar morphology adopted by the CaO (nanoflakes) an apparent formation mechanism is proposed and justified in Figure 4-16. According to this figure, it can be assumed that the growth of nanoflakes or nanoflakes was reached in three different stages. During the first one, CaAc particles dispersed in aqueous solution interact electrostatically with the surface of Saffil fibres (solution prepared with a pH above isoelectric point of alumina (pH= 7) with the aim to promote attraction forces). As a result, the particles, also termed nuclei, were incorporated in a controlled manner over the surface of the support. In the course of the second stage, there is a presumable growth of nuclei into seeds. As must be assumed, the seeds are small elementary particles that had stability at precipitation conditions. Lastly, a heterogeneous nucleation of particles (seeded growth) took place. It is noteworthy this step was reached through a vertical growth (hierarchical nucleation). Considering this mechanism, the final crystal morphology was attributed to both the structure of grown seeds and the relative binding affinities.

Based on SEM results observed in Figure 4-7, Figure 4-9, Figure 4-11 and Figure 4-13, it is clear that the mechanism of a sequential formation of CaO particles shaped as nanoflakes is only apparent in those sorbents prepared by wet

impregnation and precipitation via urea under static conditions. In addition, the optimized synthesis parameters such as temperature, concentrations and ageing times played a vital role as well.

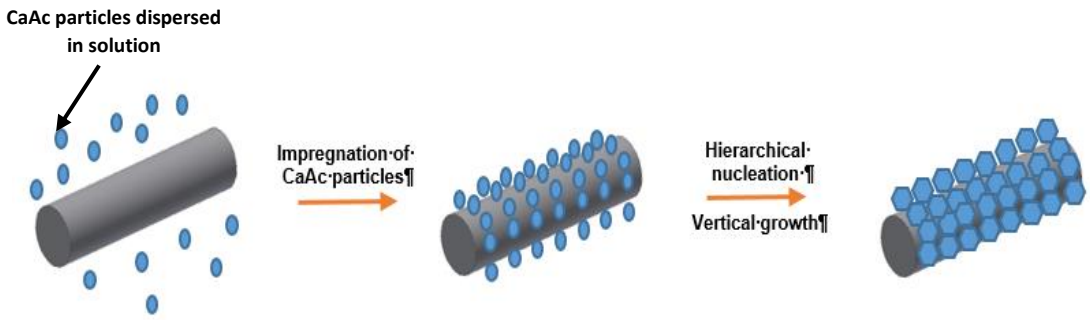

Figure 4-16. Apparent hierarchical crystallization process (nucleation and vertical growth) of CaO nanoflakes over the surface of saffil fibres.

4.3 Determination of optimal calcination conditions and phase identification XRD analysis

The analysis conducted so far has been related to the determination of optimal preparation conditions during the impregnation or precipitation stages. However, calcination parameters also must be investigated, as the active phase expected is the metal oxide crystalline phase. It is relevant to identify an adequate decomposition time of the CaO precursor because modifications of texture could arise when sorbents are exposed to extended calcination time. Selecting appropriate conditions for performing heat-treatments, beyond preparing the materials and drying, might help avoiding structural changes and stabilization of mechanical properties. To obtain the active metal oxide phase, techniques such as XRD and TGA were widely employed

4.3.1 Decomposition study of the CaO precursor

Before predicting the temperature and the optimal period of time for which CaO phase can be obtained through the precursor calcination, the behaviour of the CaAc at high temperatures must be understood. Figure 4-17 presents the thermogravimetric analysis conducted to decompose the CaAc to CaO. The

analysis was carried out in a dynamic mode (heating rate 10 °C/min) to study the temperature in which phase transitions occur. This experiment was performed in a range of temperature between room temperature to 900 °C using pure N_2 (protective gas) and 50 ml/min flow.

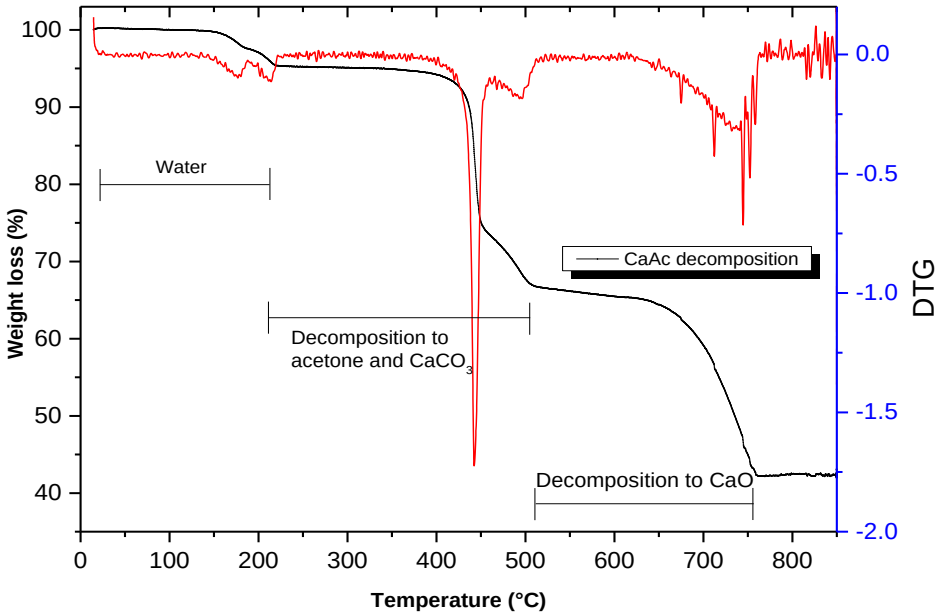

Figure 4-17. Dynamic TGA showing the thermal decomposition of CaAc. Analysis performed in a temperature range between 30 to 900 °C in presence of N_2 (50 ml/min).

The TGA curve indicates that transformation of CaAc to CaO takes place in three temperature ranges. The initial weight loss visualized was ascribed to the release of water molecules. This process occurred in two steps where the first one occurred at 150-200 °C, and the following one at 200-240 °C. The mass loss associated with both decomposition processes was ~ 6%. Subsequently, a great transformation was observed between 410 °C to 505 °C. According to the literature [267], the decomposition of the dehydrated CaAc is carried out in two stages which can be seen in the derivative of the TGA curve indicated in Figure 4-17. The first encompasses break down the CaAc molecules to $CaCO_3$ and acetone, then, acetone is released at ~450 °C. The dynamic TGA reveals that the mass loss from both stages accounts for ~28%. Finally, the calcination of the $CaCO_3$ phase comes between 630-755 °C. The mass loss due to decarbonation reaction represented ~23%. The thermal decomposition of CaAc was completed at 755 °C in a TGA. However, the decomposition temperature could vary in the synthesis of the CaO-based sorbents (calcination) because was conducted in an

open tubular furnace. Hence, the calcination conditions were expected to differ between the results obtained by TGA from those obtained through calcination of the CaO-based sorbents in a furnace, because of the gradient of temperature that exists in the axial section of the furnace.

4.3.2 Study of optimal conditions for the decomposition of the CaO precursor in a tubular furnace

As mentioned above, the experiments related with the calcination of the CaO-based sorbents were performed in a horizontal tubular furnace supplied by the Elite Thermal Systems. To figure out the optimal calcination time, two durations were chosen for running the tests, namely 1 h and 4 h. The heating rate selected to achieve the decomposition temperature was 10 °C/min, as sintering caused by drastic changes in temperature needed to be attenuated. Figure 4-18 shows the conditions and the equipment used to conduct the thermal decomposition experiments.

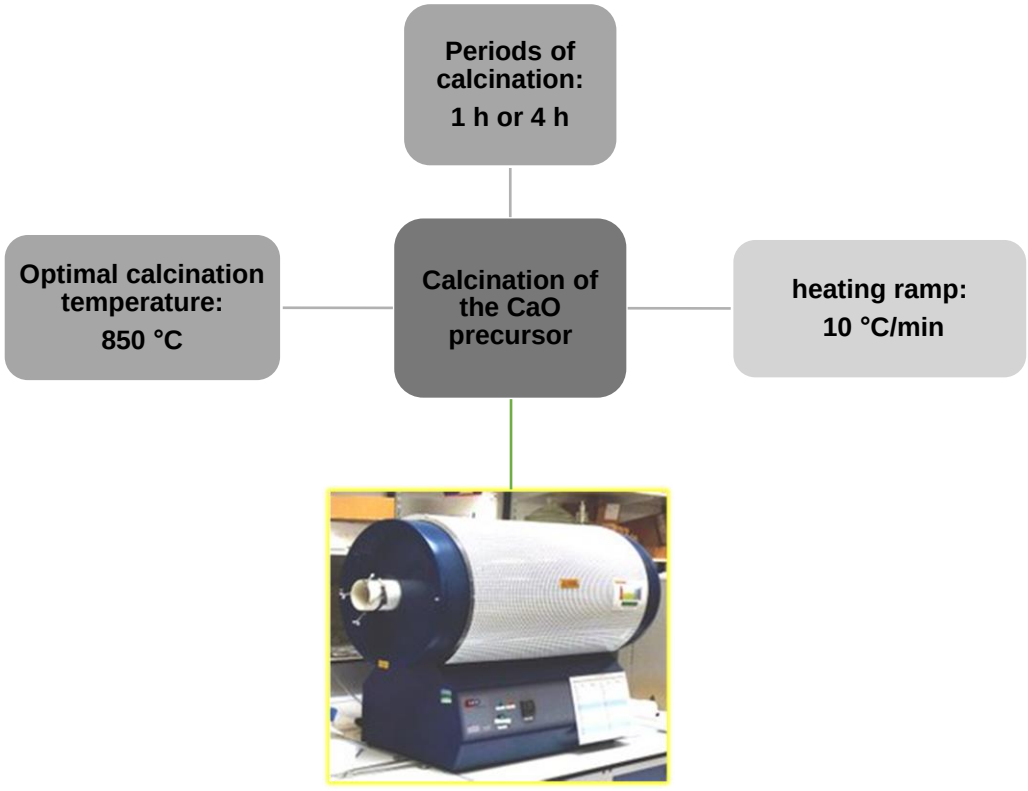

Figure 4-18. Tubular furnace and parameters settings to define the optimal calcination conditions for the thermal decomposition of the active phase precursor (CaAc).

Before calcining the sorbents of interest, CaAc was used to determine the time needed to reach a full conversion of the acetate to CaO in the tubular furnace. It is relevant to point out that the CaAc tested was hydrated and dried under same conditions under which the sorbents of interest were expected to prepare. XRD technique was employed to provide evidence of the phases present after the calcination attempts. A comparison between two samples calcined for 1 h and 4 h, revealed that exposing CaAc to 850 °C for 1 h, only a partial conversion of $CaCO_3$ to CaO was achieved (Figure 4-19-a)). From the XRD patterns shown below, peaks with the highest intensities located in 2θ values of 29.29°, 39.29°, 43.11°, 47.34° and 48.36° confirmed the presence of $CaCO_3$ (ICDD: 01-080-9776). With regard to the mass fraction converted, the Rietveld method indicated that ~60% of $CaCO_3$ was still unreacted upon 1 h of calcination.

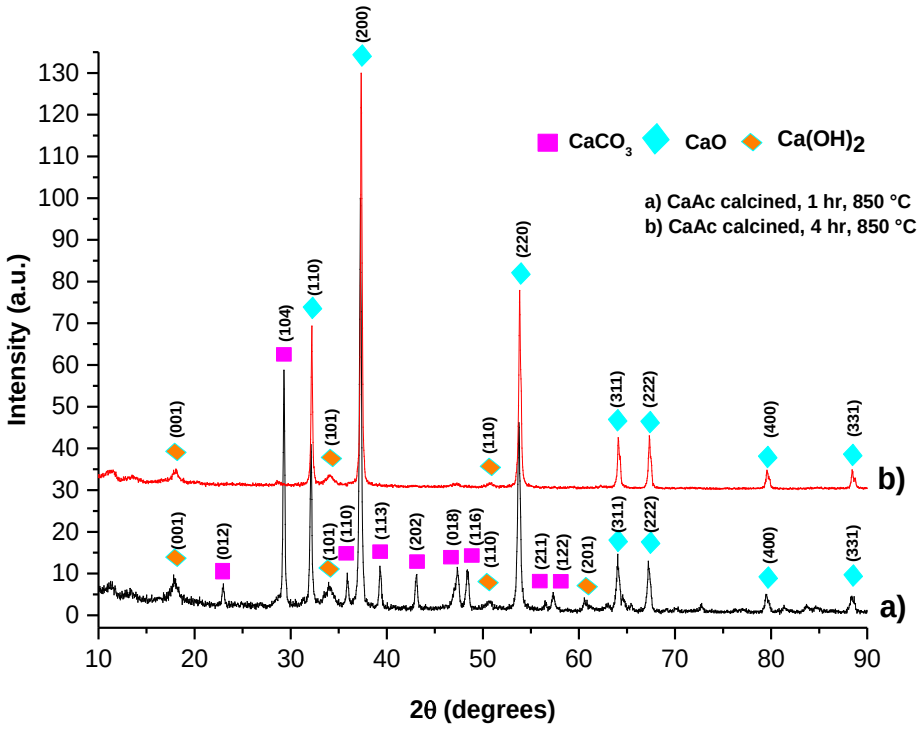

Figure 4-19. X-ray diffraction patterns collected from two CaAc samples subjected to hydration, drying and thermal decomposition at 850 °C for 1 h and 4 h, (a) and (b) respectively.

From the pattern shown in Figure 4-19-(b), a full transformation of the CaO precursor was attained by extending the calcination time from 1 h to 4 h. The crystalline phase identified in the specimen prepared and tested under these particular settings corresponded to a cubic structure characteristic of CaO. The

reflexions observed in positions 32.2°, 37.3°, 53.8°, 64.1° and 67.3° were in agreement with the reference pattern of CaO ICDD: 01-070-5490 reported in the ICDD crystallographic database. Rietveld analysis revealed that 96% of CaO was present in the sample calcined for 4 h whilst the 4% corresponded to $Ca(OH)_2$. Minor peaks owed to $Ca(OH)_2$ seen in both diffraction patterns were identified with the reference code 07-076-0570. The presence of $Ca(OH)_2$ phase was attributed to “air-slaking” that occurred via the reaction of the solid sorbent with moisture [268].

Considering the results exhibited in Figure 4-19, 850 °C and 4 h calcination were selected as the optimal conditions to decompose the CaO precursor used for the preparation of CaO-based CO_2 sorbents loaded with diverse notional amounts of CaO active phase. Saffil fibre supports were also characterized by XRD before and after 4 h of calcination in order to confirm their thermal stability. Evidently, the presence of any crystalline transformation was expected to appear in the XRD analysis.

Figure 4-20 shows the diffraction patterns registered for two samples of Saffil fibres in which one was untreated and other was exposed at 850 °C for 4 h. With the aim of identifying the crystalline structure of the fibrous supports, the ICCD 00-001-1308 pattern was used as a reference. As can be seen in Figure 4-20, despite testing Saffil fibres under the conditions mentioned above, the peak positions (37.6°, 45.5° and 67.3°) of both samples remained identical. Hence, It can be assumed that a temperature of 850 °C did not promote a phase evolution toward other transition alumina phases (θ-Al_2O_3 or α- Al_2O_3). Beyond doubt, δ-Al_2O_3 fibres presented high-thermal stability.

In regards to the CaO-based CO_2 sorbents prepared by wet impregnation and treated thermally in order to decompose CaAc, it can be seen from the XRD patterns shown in Figure 4-21 that the decomposition of calcium acetate was successfully achieved under the chosen experimental conditions. As this plot shows, the CaO, $Ca(OH)_2$ and δ- Al_2O_3 species were identified as the phases present in each sorbent. In contrast with sharp peaks of CaO observed in Figure 4-19-(b), broader CaO peaks were observed. According to XRD theory, small crystals cause broadening since incoherent scattering domains are generated [269]. As expected, the reflexions of Saffil fibres are in agreement with those

reported in Figure 4-20. In the case of the existence of $Ca(OH)_2$, the sorbents impregnated with notional amounts of 25, 20 and 5 wt.% exhibited conspicuous peaks. Air-slaking effect on the CaO phase was presumable the reason behind the presence of the hydroxide phase as these sorbents were not stored in vacuum. In addition, the dephasing of some peaks of $Ca(OH)_2$ or Saffil δ- Al_2O_3 is produced by peak broadening or nanometric dimensions of the hydroxide particles as well as due to a transition from a δ- to θ- Al_2O_3 phase.

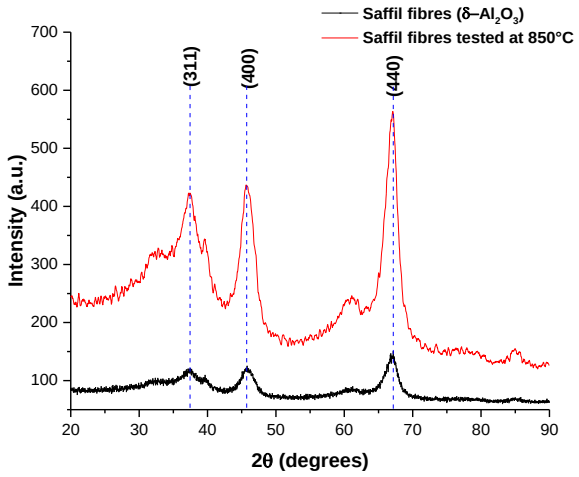

Figure 4-20. XRD patterns showing evidence of thermal stability (no phase transformation) of Saffil fibres during their exposure to high temperature (850 °C).

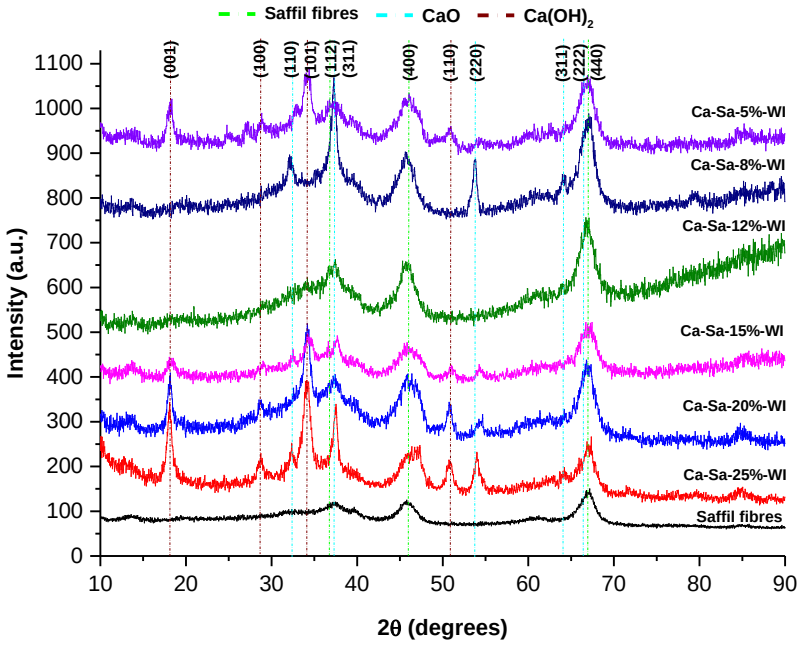

Figure 4-21. X-ray powder diffraction patterns of CaO-based sorbents prepared by wet impregnation with different notional CaO contents and calcined at 850 °C for 4 h. For comparison, CaO and Saffil fibre diffraction patterns are shown.

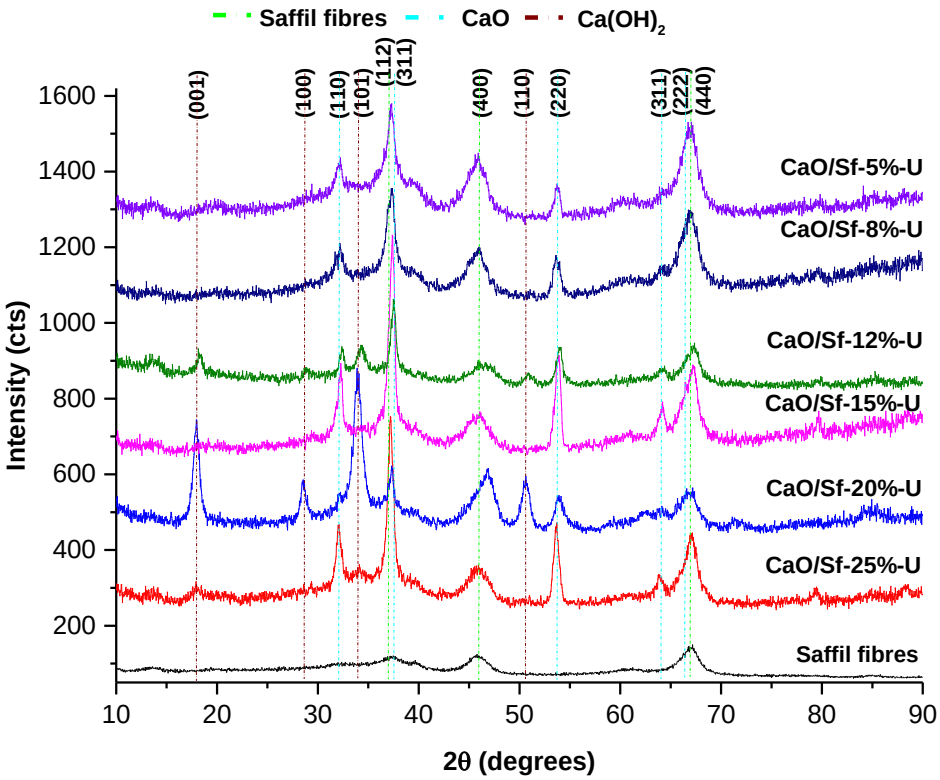

Figure 4-22. Diffraction patterns of CaO-based sorbents prepared by precipitation via urea. The XRD analysis was performed in a 2θ range from 10-90°.

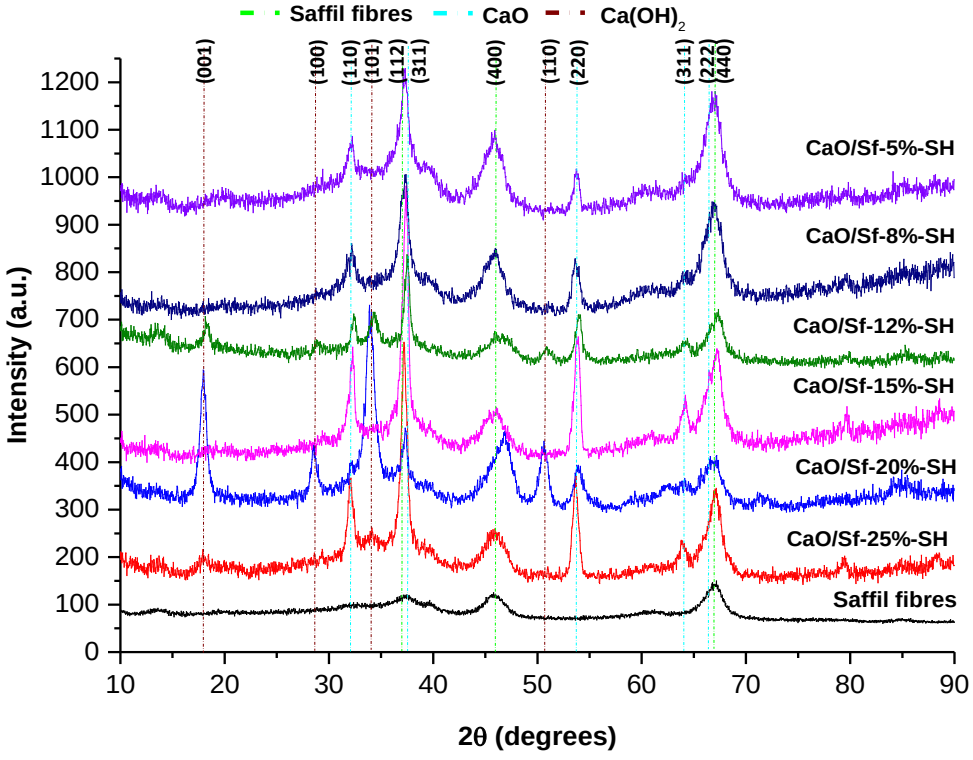

Figure 4-23. Phase identification study carried out in CaO/Sf-%-SH sorbents synthesised by precipitation via NaOH. The measurements was conducted in a Bruker D8 diffractometer.

Similarly to the CaO-based sorbents prepared by wet impregnation, a phase identification study was performed to CaO/Sf-%-U and CaO/Sf-%-SH sorbents, illustrated in Figure 4-22 and Figure 4-23 respectively. As was expected, the peaks associated with CaO present in both families of sorbents showed higher intensities than the reflexions recorded for $Ca(OH)_2$. Although two peaks of δ-Al_2O_3 overlapped with planes of CaO, the reflexion located in 45.5° allowed identifying the fibrous support. Interestingly, the sorbents with 20 and 25 wt. % of active phase in both precipitation routes (urea and NaOH) showed the most intense peaks of $Ca(OH)_2$. Certainly, the hydration derived from air-slaking effect must have been significant as the CaO content is greater with respect to the rest of the sorbents. Thus, this effect produced the appearance of $Ca(OH)_2$ peaks in Ca-Sa-%-WI, CaO/Sf-%-U, and CaO/Sf-%-SH sorbents.

4.4 Estimation of textural properties through N_2 physisorption

Textural properties such as specific surface area (SSA), pore volume (PV) and pore size distribution (PSD) play a vital role in sorption processes as the diffusion of CO_2 through the bulk of the sorbent or pores define the velocity at which this gas of interest will be absorbed. The concept of supporting CaO over Saffil fibre was not only to achieve thermal stabilization of the CaO, but also enhance the textural properties of the novel sorbents with respect to those coming from natural and synthetic CaO [229].

Upon confirmation of the optimal preparation conditions through SEM-EDX and XRD techniques, the textural properties of all the as-prepared sorbents were estimated by means of the N_2 physisorption technique. BET and BJH methods were used to evaluate SSA and PV and PSD respectively.

4.4.1 Textural properties of Ca-Sa-%-WI sorbents

The specific surface area values measured by BET method for the CaO-based sorbents loaded with various contents of the active material are depicted in Figure 4-24. According to SSA results, it is evident that as the CaO content

supported over the Saffil fibres reached the maximum target of 25 wt.%, a significant decline in the BET surface area with respect to the initial area calculated for the support (δ-Al_2O_3 fibres) was observed. Undoubtedly, this dependence was expected, considering the SSA of CaO (9 m^2/g CaO) was considerably lower than that of the Saffil support (138 m^2/g Saffil). The downward trend in the SSA illustrated in the bar chart (Figure 4-24)) clearly shows that the loss of surface area is proportional to the content of the active phase impregnated on each sorbent.

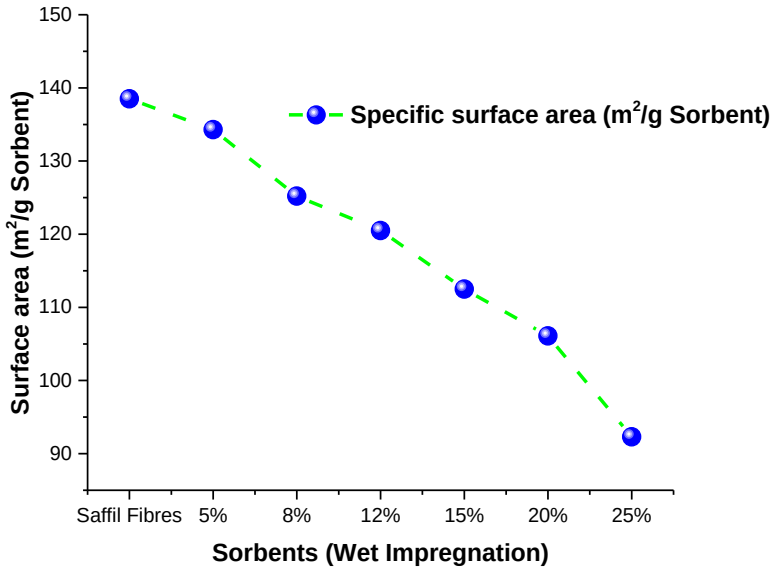

Figure 4-24. Specific surface area values of Ca-Sa-%-WI sorbents measured at the boiling point of N_2 (77 K). Saffil fibres were used as a reference to track down variations of SSA.

In support of the study related to the textural properties of the Ca-Sa-%-WI sorbents, pore size distribution curves obtained by BJH model are presented in Figure 4-25 and were analysed in detail. Despite the impregnation of CaO on the support, all the sorbents kept a similar pore radius within the range of 1.5-2.5 nm. According to IUPAC classification, the pore network of the Ca-Sa-%-WI sorbents can be categorized as mesoporous. It must be highlighted that pore volumes presented slight changes as the notional CaO content impregnated increased. Apparently higher amounts of active phase blocked large pores. This dependence could be traced through Table 4-4, which presents a summary of

the textural properties measured for all Ca-Sa-%-WI sorbents as well as a comparative to SSA expected through the physical mixture (benchmark).

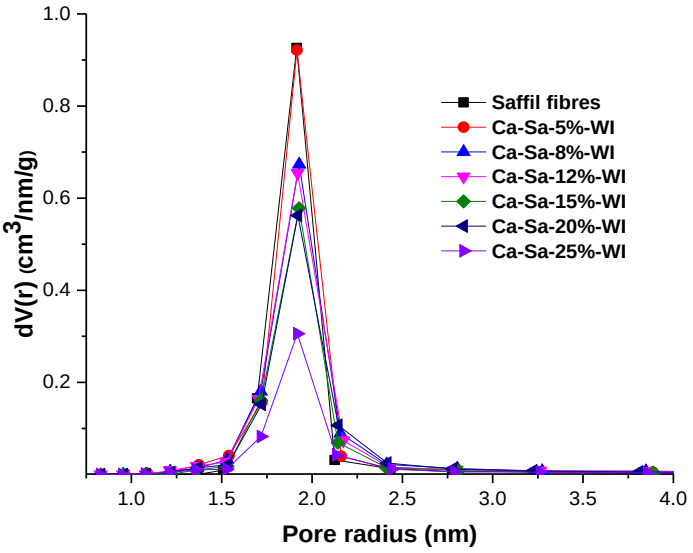

Figure 4-25. Pore size distribution curves of Ca-Sa-%-WI sorbents calculated based on the BJH method.

Table 4-4. Summary of textural properties measured by N_2 physisorption at 77 K applying BET and BJH method.

	Ca-Sa-%-WI sorbents			
Sorbent	**Surface Area ($m^2\ g^{-1}$)**	**Surface Area (Physical mixture) ($m^2\ g^{-1}$)**	**Pore volume $m^3\ g^{-1}$ ($x10^{-6}$)**	**Pore radii (nm)**
Saffil Fibres	138	138	0.29	1.95
Ca-Sa-5%-WI	134	132	0.28	1.93
Ca-Sa-8%-WI	125	127	0.28	1.93
Ca-Sa-12%-WI	120	122	0.27	1.92
Ca-Sa-15%-WI	112	118	0.22	1.93
Ca-Sa-20%-WI	106	110	0.22	1.92
Ca-Sa-25%-WI	92	103	0.16	1.92
CaO	9	9	0.06	1.89

To understand the porosity of the material, adsorption/desorption isotherms of Ca-Sa-%-WI sorbents were plotted in Figure 4-26. The Saffil fibres isotherm was included into the same plot as a standard of reference. The analysis indicated that all sorbents prepared by wet impregnation route followed a parallel

adsorption/desorption path with relation to the reference. According to the IUPAC classification, isotherms type IV with asymmetrical boundary hysteresis loop type H2 were observed in all specimens under study. Considering the shape of the loop, it was assumed that Ca-Sa-%-WI sorbents as mesoporous materials are formed by a 3D network of cavities with different sizes connected mainly by constrictions [249, 250, 270]. The wide condensation branches confirm the existence of pores in which evaporation of the physisorbed gas is governed by cavitation. This is confirmed through the pronounced N_2 desorption that occurred at a relative pressure of 0.5 and that concluded at 0.45 (P/P°). This assumption is consistent with PSD results as the pore radii range remained similar among sorbents.

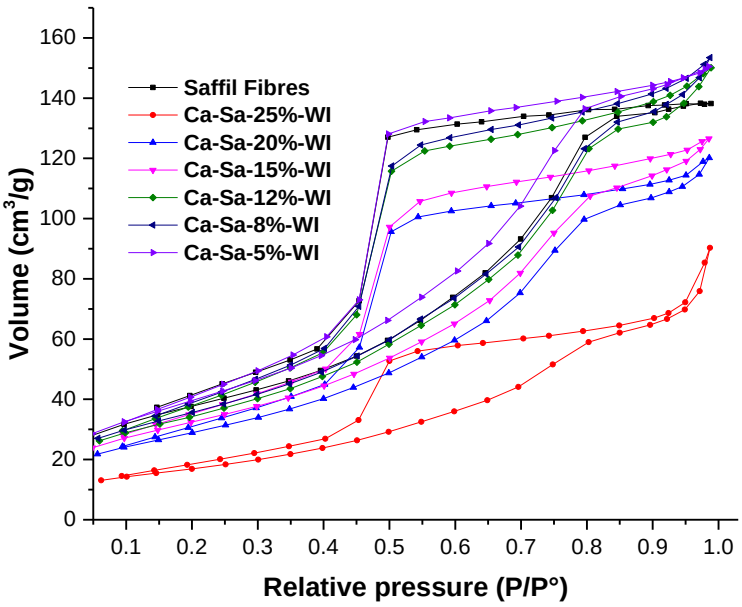

Figure 4-26. Adsorption isotherm curves type IV registered for the Ca-Sa-%-WI sorbents. The hysteresis loops present in all isotherms was classified as H_2 according to the IUPAC.

4.4.2 Textural properties of CaO/Sf-%-U and CaO/Sf-%-SH sorbents

To evaluate the textural properties of CaO/Sf-%-U and CaO/Sf-%-SH sorbents, N_2 physisorption technique was utilized once more. Looking to represent the global behaviour of both families of CO_2 acceptors, the sorption/desorption isotherms and pore size distribution curves for the most representative CaO

loads used (25, 15 and 5 wt. %) are presented in Figure 4-27. In terms of SSA, a decline in surface area in CaO/Sf-%-U and CaO/Sf-%-SH sorbents with relation to uncoated Saffil supports was observed (see Table 4-5 and Figure 4-27). The dependence "SSA-CaO loaded" is also linear as seen in Ca-Sa-%-WI CO_2 sorbents. By comparing SSA measurements from sorbents prepared by impregnation and those through precipitation, it is possible to discern that the sorbents prepared via precipitation with urea possess the highest SSA loss. SEM-EDX results shown in Figure 4-11 in conjunction with those presented in Figure 4-27 help explaining this fact. The thicker the layer of CaO nanoflakes, the greatest the depletion of SSA.

Table 4-5. Summary of textural properties of CaO/Sf-%-U and CaO/Sf-%-SH sorbents determined using BET and BJH methods.

Sorbents prepared by precipitation using urea as precipitant			
Sorbent	**Surface Area**	**Pore volume ($m^3\ g^{-1}$ ($x10^{-6}$))**	**Pore radius (nm)**
Saffil fibres	138.5	0.29	1.95
CaO/Sf-5%-U	128.2	0.24	1.92
CaO/Sf-8%-U	120.8	0.23	1.91
CaO/Sf-12%-U	117.6	0.32	1.92
CaO/Sf-15%-U	112.8	0.24	1.91
CaO/Sf-20%-U	99.3	0.3	1.92
CaO/Sf-25%-U	96.2	0.29	1.92
CaO	9.57	0.06	1.9
Sorbents prepared by precipitation using NaOH as precipitant			
Sorbent	**Surface Area**	**Pore volume ($m^3\ g^{-1}$ ($x10^{-6}$))**	**Pore radius (nm)**
Saffil fibres	138.5	0.29	1.95
CaO/Sf-5%-SH	132.8	0.24	2.17
CaO/Sf-8%-SH	125.7	0.26	2.45
CaO/Sf-12%-SH	120.9	0.28	2.28
CaO/Sf-15%-SH	116.6	0.22	2.23
CaO/Sf-20%-SH	99.8	0.25	2.21
CaO/Sf-25%-SH	96.8	0.22	2.14
CaO	9.57	0.06	1.9

The average pore sizes exhibited in Table 4-5 show that both CaO/Sf-%-U and CaO/Sf-%-SH sorbents fall into the meso-range (2 nm - 50 nm) according to the IUPAC classification. In addition, the pore size distribution curves depicted in Figure 4-27 reveals that both families of sorbents present a unimodal distribution. The CaO/Sf-%-U sorbents showed similar pore size distribution to the Ca-Sa-%-

WI sorbents (1.5-2.45 nm) due to their similar morphologies. In the particular case of CaO/Sf-%-SH sorbents, fluctuations in the pore radii dimensions arose. Evidently, a wide range of pore sizes was observed, namely from 1.5-4.5 nm. This effect can be associated with the synthesis method due to the fast nucleation and growth of CaO over the Saffil fibres, which promoted the formation of a more disordered pore network. The pore volumes measured by in CaO/Sf-%-U sorbents were in the same range of the Saffil fibres reference. However, a decrease in this physical property was observed in CaO/Sf-%-SH sorbents. The reason behind pore volume changes was apparently the inhomogeneous deposition of CaO on the support.

To complete the analysis of textural properties, adsorption/desorption isotherms of CaO/Sf-%-U and CaO/Sf-%-SH sorbents are shown in Figure 4-27. Isotherms type IV with a hysteresis branch H2 (asymmetrical boundaries) characteristic of mesoporous sorbents were categorized for both families of sorbents [249, 250, 270]. The adsorption/desorption hysteresis presented a decrease of physisorbed gas as the CaO content loaded increased. Figure 4-27 linked with the isotherms clearly exhibited changes in the hysteresis height. The branch contraction was also obvious by comparing these isotherms with those of the fibrous support. Interestingly, the shape of the hysteresis branch changed as a function of the synthesis method. As can be seen in the isotherms of CaO/Sf-%-U sorbents, the evaporation of N_2 for all sorbents with different CaO contents was conducted by cavitation at a similar relative pressure ($P/P° \approx 0.45$). The desorption at this specific relative pressure was also a strong indicator of a lack of pore blocking during the N_2 desorption process. So, the decrease of volume in the branches was mainly due to the filling of pores with CaO [271, 272]. This effect is consistent with the linear loss of surface area and pore size distribution observed in Figure 4-27.

The isotherms of CaO/Sf-%-SH sorbents shown in Figure 4-27 revealed that porosity in these solid sorbents was sensitive to microstructural changes derived from the synthesis method. As can be seen from the N_2 adsorption/desorption processes, there was a variation in the shape of the desorption branches. The transition between the hysteresis of uncoated Saffil fibres and CaO/Sf-%-SH is attributed to pore blocking. Considering evaporation was shifted towards higher

relative pressures, hysteresis H2(b) was identified [273-275]. This finding is consistent with the wide pore size distribution observed in the PSD plot inserted in Figure 4-27.

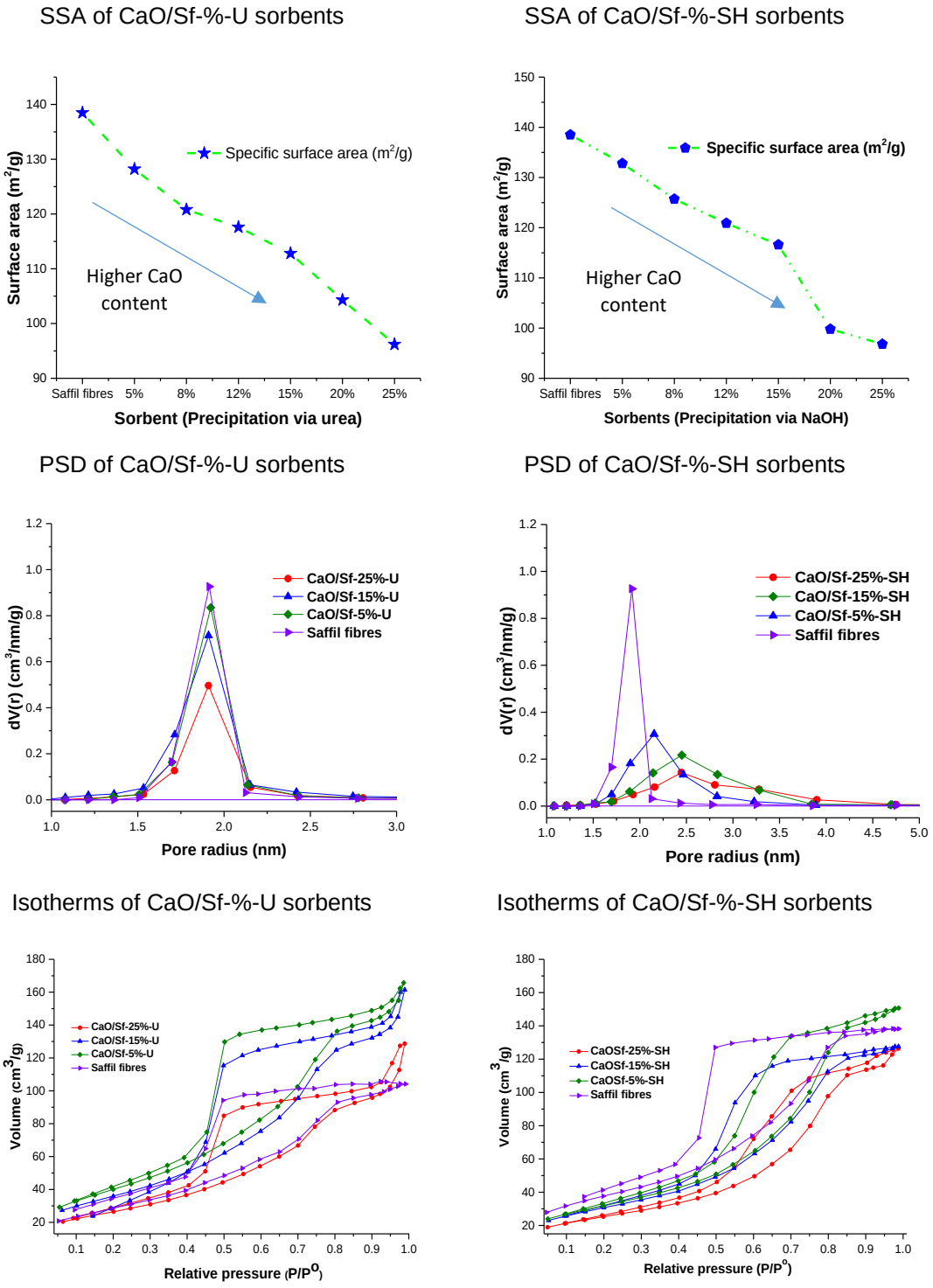

Figure 4-27. Specific surface area, pore size distribution and adsorption/desorption isotherm plots associated with both families of sorbents CaO/Sf-%-U and CaO/Sf-%-SH (loadings used 25, 15 and 5 wt. %).

4.5 Quantification of CaO present in Ca-Sa-%WI, CaO/Sf-%-U and CaO/Sf-%-SH sorbents

In the sections discussed so far, optimal conditions to load CaO over the surface of Saffil refractory fibres have been established. A nucleation-growth mechanism was proposed as an apparent path followed by the CaO precursor to coat the Saffil support. In addition, SEM revealed the peculiar morphology adopted by the CaO active phase, namely nanoflakes. However, uncertainty in terms of the suitability of the preparation methods exists since the real amount of CaO present in the sorbents is unknown. In order to quantify the content of the active phase, the XRF technique was employed. A table summarizing the outcomes obtained throughout the chemical composition analysis is presented in Table 4-6. Only sorbents with a notional 25, 15 and 5 wt.% were characterized as they were the most representative materials containing the highest, middle and lowest contents of CaO. In addition, the composition study was carried out on these specimens since they were chosen as potential candidates for demonstrating their efficiency of CO_2 capture as a function of the CaO content. Another reason to study only these sorbents was the destructive character of the technique employed to prepare the samples for XRF. As explained in the methodology section, the morphology and nanometric dimensions of CaO flakes do not permit a direct quantification in the XRD system because of peak broadening effect on reflections of CaO and $Ca(OH)_2$ phases. As a result, inaccurate estimations by means of Rietveld refinement are obtained. Therefore, the samples must be dissolved to form fused beads [276]. This destructive technique produces the dissolution of the as-prepared sorbents to form a bead at which the distribution of elements becomes homogeneous.

The bar chart exhibited in Figure 4-28 presents a comparison of the compositions evaluated by XRF in relation with the notional amount of CaO load over the surface of the Saffil fibres. According to XRF results, the wet impregnation method showed the lowest efficiency in impregnating the Saffil fibres with CaO. For instance, when a notional load of 25 wt. % was attempted, wet impregnation exhibited an efficiency of ~90%. For the case of 15 wt. %, this method attained only ~89%. Higher active phase load efficiency (>92%) were achieved when precipitation via urea was used. This was expected since the deposition of a

metal oxide by wet impregnation relies on the precursor-support interaction, mass transfer conditions, sorption-diffusion conditions, etc. whilst by precipitation, some of these phenomena can be overcome through a slow decomposition of a precipitant agent such as urea [224, 228, 230]. XRF analysis revealed that although a heterogeneous distribution of CaO was observed by precipitation via NaOH (see SEM-EDX images displayed in Figure 4-13 and Figure 4-14), this method also permitted to deposit amounts of CaO close to the notional desired (efficiencies >89%).

Table 4-6. Chemical composition of sorbents prepared by both wet impregnation and precipitation (urea and NaOH). CaO, Al_2O_3 and SiO_2 were the species analysed by XRF.

CaO-based sorbent	**CaO (%)**	**Al_2O_3 (%)**	**SiO_2 (%)**
Ca-Sa-25%-WI	22.4	73.9	3.7
Ca-Sa-15%-WI	13.3	81.6	5.1
Ca-Sa-5%-WI	4.8	91.5	3.7
Saffil fibres	-	96.4	3.6
CaO-based sorbent	**CaO (%)**	**Al_2O_3 (%)**	**SiO_2 (%)**
CaO/Sf-25%-U	24.2	71.4	4.4
CaO/Sf-15%-U	14.7	82.9	2.4
CaO/Sf-5%-U	4.6	92.3	3.1
CaO-based sorbent	**CaO (%)**	**Al_2O_3 (%)**	**SiO_2 (%)**
CaO/Sf-25%-SH	23.9	72.1	4.0
CaO/Sf-15%-SH	13.8	83.5	2.7
CaO/Sf-5%-SH	4.5	91.6	3.9

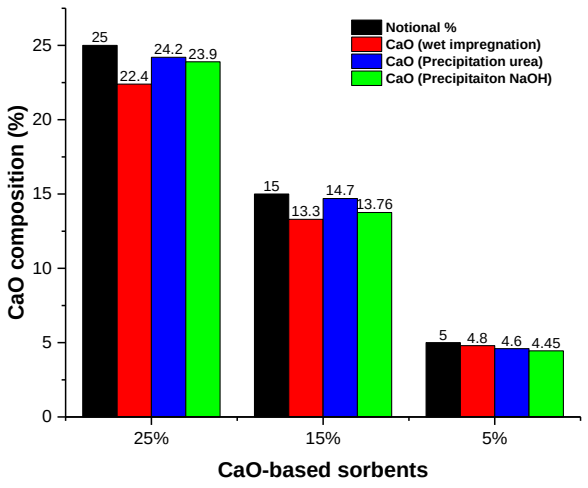

Figure 4-28. Bar chart presenting a comparison of CaO amounts loaded over Saffil support with respect to the notional percentage expected.

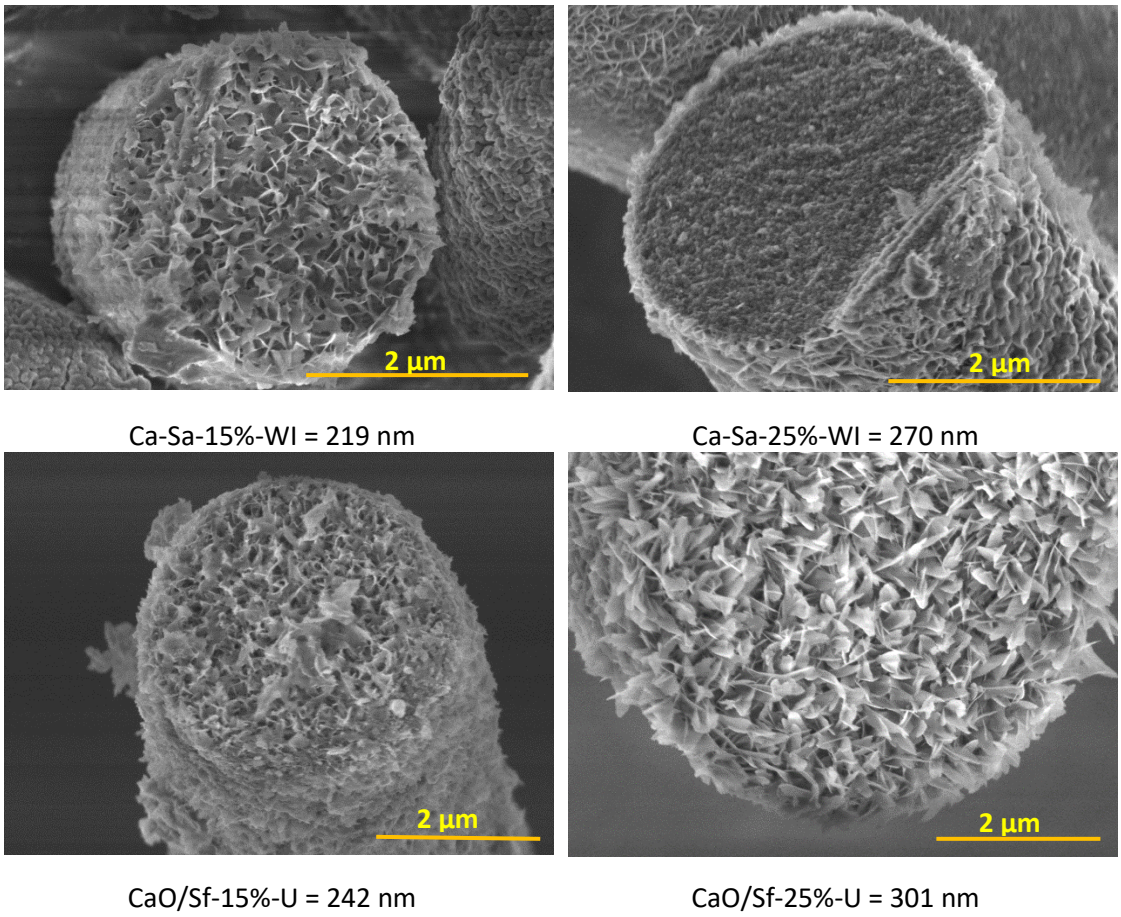

Figure 4-29. CaO coating thickness (nanoflakes) measured in the Ca-Sa-%-WI and CaO/Sf-%-U sorbents prepared with notional 15 and 25 wt. %.

As a mean to clarify why the precipitation method was more effective than wet impregnation when pursuing active phase contents close to those intended, an analysis of coating thickness was conducted. The estimations were performed by the software “ImageJ”, which has been extensively applied in image processing and analysis of SEM images. Figure 4-29 shows the SEM images of Ca-Sa-%-WI and CaO/Sf-%-U sorbents loaded with notional 15 and 25 wt. % of CaO that were used to determine the coating thickness. In regards to the estimated values, loading CaO onto the fibres by precipitating the CaO precursor in a controlled manner (via urea) allowed an increase in thickness of ~9.5% for the CaO/Sf-15%-U sorbents compared to that of the Ca-Sa-15%-WI sorbent whilst ~10% for CaO/Sf-25%-U compared to its homologue prepared via wet impregnation. The findings support the results presented in the section concerned with the characterization of the as-prepared sorbents, where it was

found that the slower was the urea decomposition, the better became the homogeneity in the deposition of the CaO precursor. Evidently, a controlled deposition of CaO enhanced the mass transfer towards the support surface. Consequently, higher amounts of CaO could be loaded using this controlled way (slow precipitation via urea). Undoubtedly, the thickness increase in both the families of sorbents studied explains the results obtained by XRF. In the instance of the sorbents loaded with 5%, it is worth mentioning which the thickness rise was indiscernible between both sorbents (185 nm).

In the particular case of the CaO/Sf-%-SH sorbents, coating thickness measurements could not be conducted as a heterogeneous deposition of CaO was observed in the SEM micrographs, as shown in Figure 4-13. In addition, it was inferred that the difference between the real amount deposited and the expected load was caused by the rinsing stage, as a bit of CaO was lost during this operation.

4.6 Preparation of CaO-based sorbents with unconventional morphologies via precipitation with NaOH as the precipitant agent

As has been seen so far, support CaO over Saffil fibres can be successfully conducted through both wet impregnation and precipitation methods. However, the effectiveness of the methods relies on the synthesis parameters. In the course of the synthesis of CaO/Sf-%-SH sorbents, it was found that nucleation and growth of the active phase occurred rapidly. SEM images presented in Figure 4-23 corroborated a non-uniform distribution of CaO. Apparently, this heterogeneous deposition was associated with a growth of particles in the bulk solution instead of the surface of the support. According to literature, this effect happens more intensely with some alkali solutions used to cause precipitation at high supersaturation conditions (NaOH, KOH, NH_4OH and $NaHCO_3$) [277]. Evidently, in order to enhance the precipitation conditions, control the growth of CaO and crystalize CaO with a well-define morphology over the support of interest, concentration, aging time and pH must be adjusted.

The upcoming sections are aimed to show the preparation and characterization of CaO-based sorbents in which the active phase grew with peculiar morphologies, namely platelets also termed as plates, multifaceted particles and octahedra. These unconventional microstructures were acquired not only varying the content of the CaO precursor but also the conditions of the final mixture (pH, stirring, ageing time, etc.). These sections also present an apparent formation mechanism of those supported CaO particles tuned with unconventional morphologies. Bearing in mind that the nucleation-growth mechanism implies Ostwald ripening (referred also as particle coarsening), this phenomenon will receive singular attention. The study of this family of novel CaO-based CO_2 sorbents includes the elucidation of physicochemical properties through conventional techniques used extensively along this chapter such as XRD, SEM-EDX and N_2 physisorption.

4.6.1 Effect of pH and aging time on the final microstructure of CaO deposited on Saffil Fibres

The first evidence of the possibility of synthesizing CaO particles with unconventional morphologies was found when attempts to homogenize the deposition of CaO through the precipitation method with NaOH were conducted. As was observed in the course of the preparation of CaO/Sf-%-SH sorbents, at pH >12, the distribution of CaO was heterogeneous over the surface of the supports (as per SEM analysis). It was also found that pH of the blended solution played a key role in promoting a very fast deposition of amorphous $Ca(OH)_2$ particles over Saffil supports. Based on the morphology adopted for the family of CaO/Sf-%-SH sorbents, the methodology presented in Figure 4-5 for the preparation of CaO-based sorbents using NaOH as the precipitant agent was improved. The adaptations in the synthesis procedure aimed at promoting not only a uniform deposition of CaO over the periphery of Saffil supports but also grow CaO particles with a well-defined morphology that would potentially provide thermal stability to the crystalline phase responsible for capturing CO_2.

The Ca-based CO_2 sorbents labelled CaO/Sf-%-Oct were intended to contain similar CaO loads (25, 15 and 5 wt. %) with respect to the most relevant CaO-based CO_2 sorbents belonging to the others families of CO_2 acceptors presented

so far. The first experiment performed in the attempt to improve a homogeneous distribution of CaO over Saffil supports was conducted considering a notional CaO content of 25 wt. %. This particular composition was selected due to the interest in depositing the highest CaO amount possible over the support surface. As in analogous experiments performed before through precipitation with NaOH, the quantity of Saffil fibres dispersed into the ethylene glycol solution (Sigma > 99.8%) was 0.5 g. The range of pH studied fluctuated between ~12 and 11. The pH of the final mixtures was reached by adding different volumes of NaOH solution dropwise. In regards to ageing times, different time slots (4, 8, 12 and 24 h) were tested to study morphological changes in the as-prepared solids. In addition, drying and calcination conditions were preserved at 120°C overnight and 850 °C for 4 h respectively.

In order to investigate the underlying effect of pH, SEM was used to register evidence once synthesis was completed. Surprisingly, the SEM micrograph shown in Figure 4-30 reveals that decreasing the pH from >12 to ~12, CaO supported over the periphery of Saffil experienced radical microstructural transformations. According to Figure 4-30, there is a formation of particles with multiple facets (multifaceted) with planar directions difficult to see. It is clear from the same figure that some CaO particles presented well-defined facets whilst others gave the impression to be in the process of facet formation and growth.

Although a wide literature review was performed in order to explain the formation of these multifaceted CaO particles, no previous investigations were found in which CaO was prepared with a multifaceted morphology via free-surfactant precipitation and using NaOH as the precipitant agent. Despite existing controversies in the formation mechanism of polyhedral particles, coarsening also termed Ostwald ripening is apparently the process associated with the formation of varied morphologies [278]. These first-order phase changes conceptually occur in two-phase mixtures containing the dispersed phase and the support (here the CaO precursor and Saffil fibres). The large surface area exposed by the support alter the thermodynamic equilibrium generating a total energy that can be minimized via scaling up the size of particles. As a result, the interfacial energy in the two-phase system will be attenuated. Thus, gradual ripening modifies the morphology of the solid phase. The enlargement of

particles is a function of time whilst the growth rate is constant along the particle-coarsening phenomenon. Consequently, in the course of the process, the number of small particles per unit cross-section area decreases as the average particle size rises [279-282].

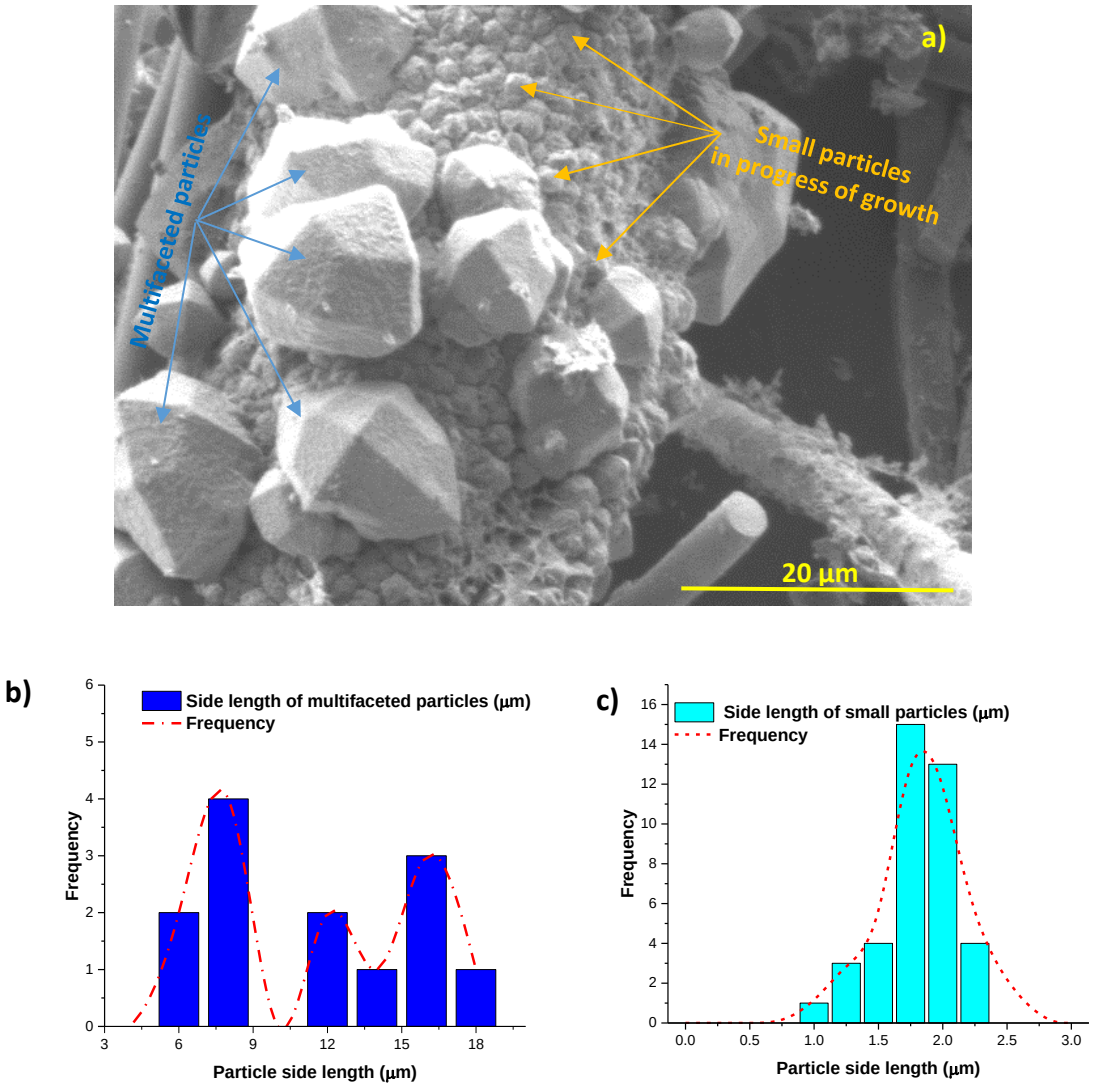

Figure 4-30. a) SEM micrograph showing morphologies adopted by CaO particles supported on Saffil prepared via precipitation (pH ~12 and 4 h ageing) using NaOH as a precipitant agent, b) and c) Side length distribution of multifaceted CaO particles and particles in the process of growth, respectively.

The SEM micrograph shown in Figure 4-30 reveals that ageing the two-phase mixture for 4 h at pH ~12, multifaceted particles were formed with dimensions ranging between 6-18 µm (see Figure 4-30-(b)). In addition, Figure 4-30-(a) also indicates the presence of small particles that are apparently in the process of growth or being dissolved into larger ones. According to the analysis of particle

length distribution shown in Figure 4-30-(b) and (c), the multifaceted particles grew with preferential lengths of 8.5 µm and 15.5 µm (higher frequency), whilst small particles had a preferential side length of 1.75 µm (frequency of 14 over 40 particles measured, see Figure 4-30-(c)). From the particle side length distribution plot, it is clear that within 4 h of ageing time, Ostwald ripening had not finished yet, as the presence of small particles (1-2.5 µm) indicated a process intent on minimizing energy. Hence, ageing time was also a key parameter in the synthesis process.

Upon the preparation of a CaO-based sorbent with a notional content of 25 wt. % at pH 11.5 and 11, SEM analysis indicated the formation of CaO particles with a distinct morphology from those observed through previous methods (nanoflakes and multifaceted CaO particles), namely octahedral (see Figure 4-31-(a) and (b)). As expected, the target of depositing CaO particles with tuned morphology over Saffil supports was reached either at pH 11.5 or 11. The SEM micrograph presented in both Figure 4-31-(a) and (b) show the coarsening phenomenon whose apparent formation mechanism is discussed in detail later. As one would expect, the octahedral shape was acquired via an evolutionary process in which small particles transfer their mass onto larger particles through a lack of energy equilibrium. It is imperative to highlight that pH 11 promoted the formation not only of CaO octahedra but also hexagonal plates also identified in literature as platelets (SEM image exhibited in Figure 4-31-(b)).

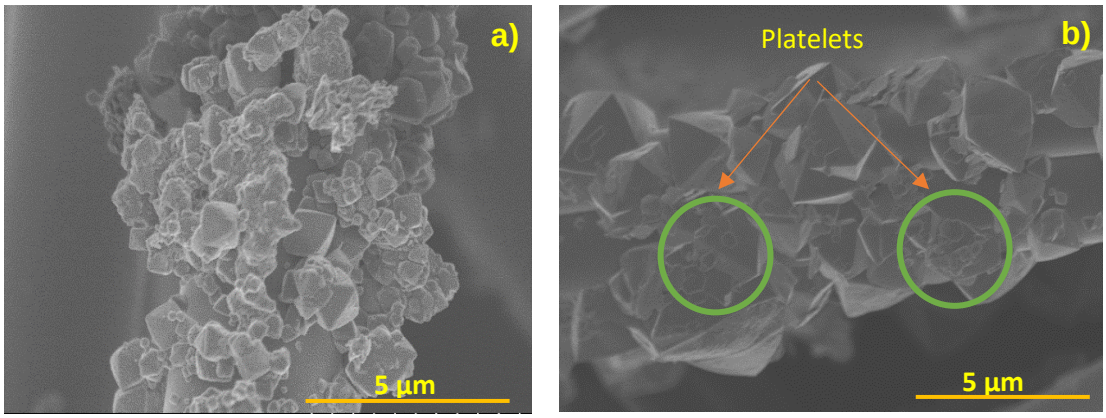

Synthesis conducted at pH= 11.5

Synthesis performed at pH= 11

Figure 4-31. A first sign of the growth of CaO octahedra over Saffil fibres under controlled synthesis parameters. Images (a) and (b) correspond to sorbents prepared with 25 wt. % of CaO at pH 11.5 and 11 respectively.

Based on the experiments proposed above, SEM analysis was conducted once again to discern any microstructural change derived from prolonging ageing from 4 h to 8, 12 and 24 h. Figure 4-32-(a) and (b) shows CaO-based sorbents prepared under ageing times of 8 h and 12 h respectively. Upon prolonging 4 h ageing time with respect to the experiment presented in Figure 4-31-(b), 8 h is not sufficient time for attaining dissolution of hexagonal plates over the flat surfaces of big particles (see Figure 4-32-(a)). However, ageing 12 h the solution containing the CaO precursor, NaOH and ethylene glycol, a marked evolution in the formation of octahedra with well-defined edges is produced. In addition, it is clear that at those conditions, a minor portion of CaO in shape of plates seems to be yet in progress of dissolution (Figure 4-32-(b)).

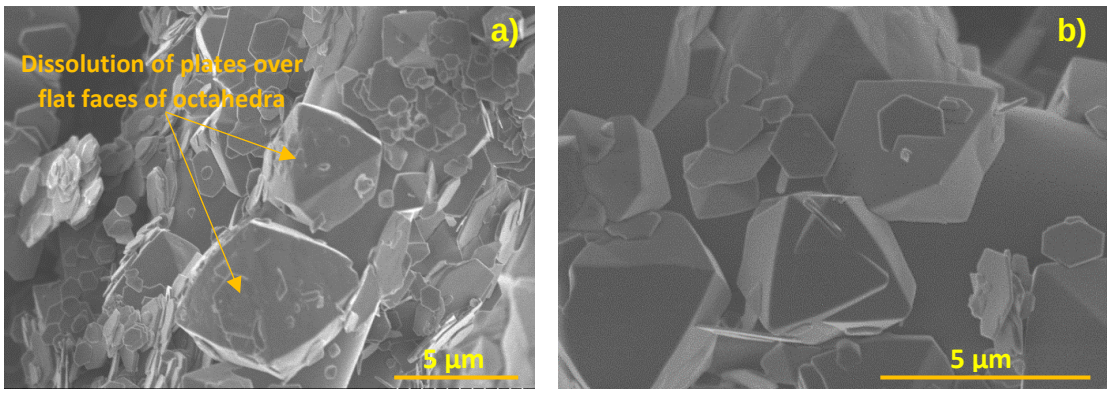

CaO-based sorbent prepared under 8 h of aging.

CaO-based sorbent prepared with 12 h of aging.

Figure 4-32. Hexagonal plates in the process of being redeposited by the effect of Ostwald ripening. Evidence of structural evolution as a function of the ageing time.

Microstructural changes exhibited in Figure 4-31-(a) and (b) when pH was varied from >12 to 11 are robust proof that precipitation method via NaOH using ethylene glycol as a solvent is highly sensitive to pH fluctuations. Figure 4-31-(b) shows that pH is an influential parameter that might be used to reach not only the formation of particles shaped in geometries able to reduce sintering but also to reach a homogeneous distribution of CaO over the surface of Saffil supports. Even though the chemical composition of the solution at pH 11 favours the solubility equilibrium, Ostwald ripening was incomplete due to parameters such as temperature, impurities and ageing time also had a strong influence in the solubility of small particle. The presence of plate-like particles exhibited in Figure 4-31-(b) gave rise to assume that ageing times must be modified in order to reach

redeposit or assemble these particles into larger particles. Bearing in mind this possibility, it was decided to conduct additional experiments in which solutions containing the CaO precursor and Saffil fibres were aged for periods of 8, 12 and 24 h preserving pH 11.

As a way to recapitulate the SEM findings on CaO-based sorbents with CaO particles growth in octahedral geometry so far, it is worth highlighting that a marked contrast in terms of CaO distribution over the support surface and morphology existed between sorbents prepared at pH 11 and those at pH ~ and > 12. For instance, micrographs with low magnification shown in Figure 4-33 demonstrate that pH 11 and 12 h of ageing promoted the growth of monodisperse CaO octahedrons over the surface of the fibrous support with a limited number of plates in progress of assembly located on the top of the octahedral particle faces.

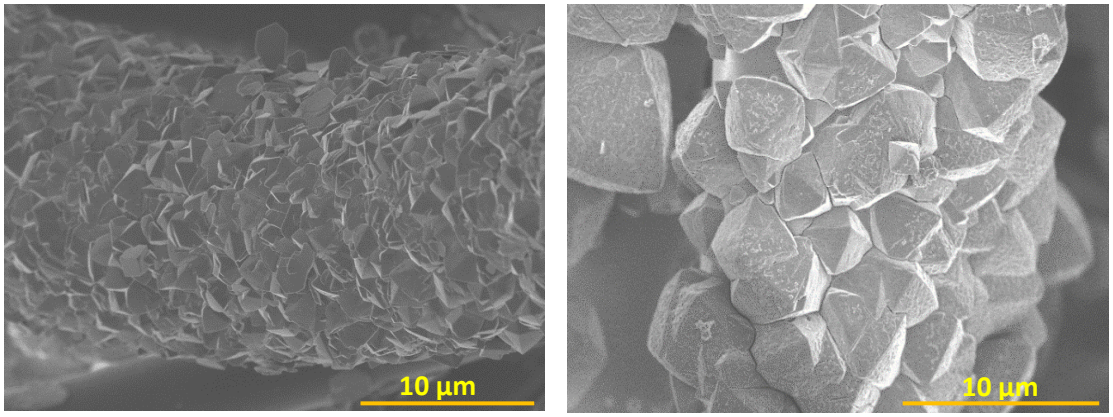

Figure 4-33. SEM images showing single fibres coated uniformly with particles with octahedral geometry. Hexagonal plates are present since Ostwald ripening has not been completed (aged by 8 and 12 h respectively).

With the aim of achieving the two-dimensional attachment of the hexagonal plates to terminate those flat triangular faces of the octahedral particles, the ageing time was in a final step extended up to 24 h. The micrograph presented in Figure 4-34 confirms that hexagonal plates can be dissolved by means of increasing ageing time. Upon completion of Ostwald ripening, particles progressively morphed toward octahedra with smooth surfaces and curvy edges. The rounded edge seemed to be generated as a part of the evolutionary process during the ageing time. It must be noted that the optimized parameters used to

prepare the sorbents presented in this section not only permitted the formation of octahedral particles but also controlling the particle size. The particle height distribution analysis performed on the SEM micrograph seen in Figure 4-34-(a) and (b) supports the suitability and flexibility of the precipitation method for preparing structures with a well-defined morphology (mean size of 3.75 µm). From the particle height distribution analysis shown in Figure 4-34-(b), it is possible to infer that in the neighbourhood of 3.75 µm, the surface energy was minimized and no significant morphological changes were observed beyond 24 h ageing. Thus, the statistical analysis performed to determine the mean particle heights for the octahedral, in conjunction with pH and ageing tests performed to optimize the synthesis, provide a sound foundation to consider precipitation via NaOH using ethylene glycol as dispersant media as a very viable route to grow octahedral particles of CaO over Saffil supports.

Considering the optimal preparation conditions to grow octahedral CaO over Saffil supports were determined above, the CaO-based CO_2 sorbents synthesised for further applications to CO_2 capture using these optimal conditions are presented in Table 4-7. As before, a nomenclature was applied to octahedral CaO over Saffil for their easier identification. The sorbents were labelled CaO/Sf-%-Oct where CaO is associated with the active phase expected afterwards the calcination of the precursor, Sf is Saffil fibre supports, % is the notional content of CaO expected of being loaded and Oct alludes to the octahedral morphology adopted by CaO particles.

Table 4-7. CaO/Sf-%-Oct sorbents prepared by precipitation via NaOH. The optimal conditions were investigated experimentally by varying pH and aging times.

Sorbent, content of active phase and synthesis method	Preparation temperature, pH and aging time	Drying conditions (time and heating rate)	Calcination parameters
CaO/Sf-25%-Oct	115 °C, pH 11, 24 h	120°C, 12 h, 5 °C/min	850°C, 4h, 10 °C/min
CaO/Sf-15%-Oct			
CaO/Sf-5%-Oct			

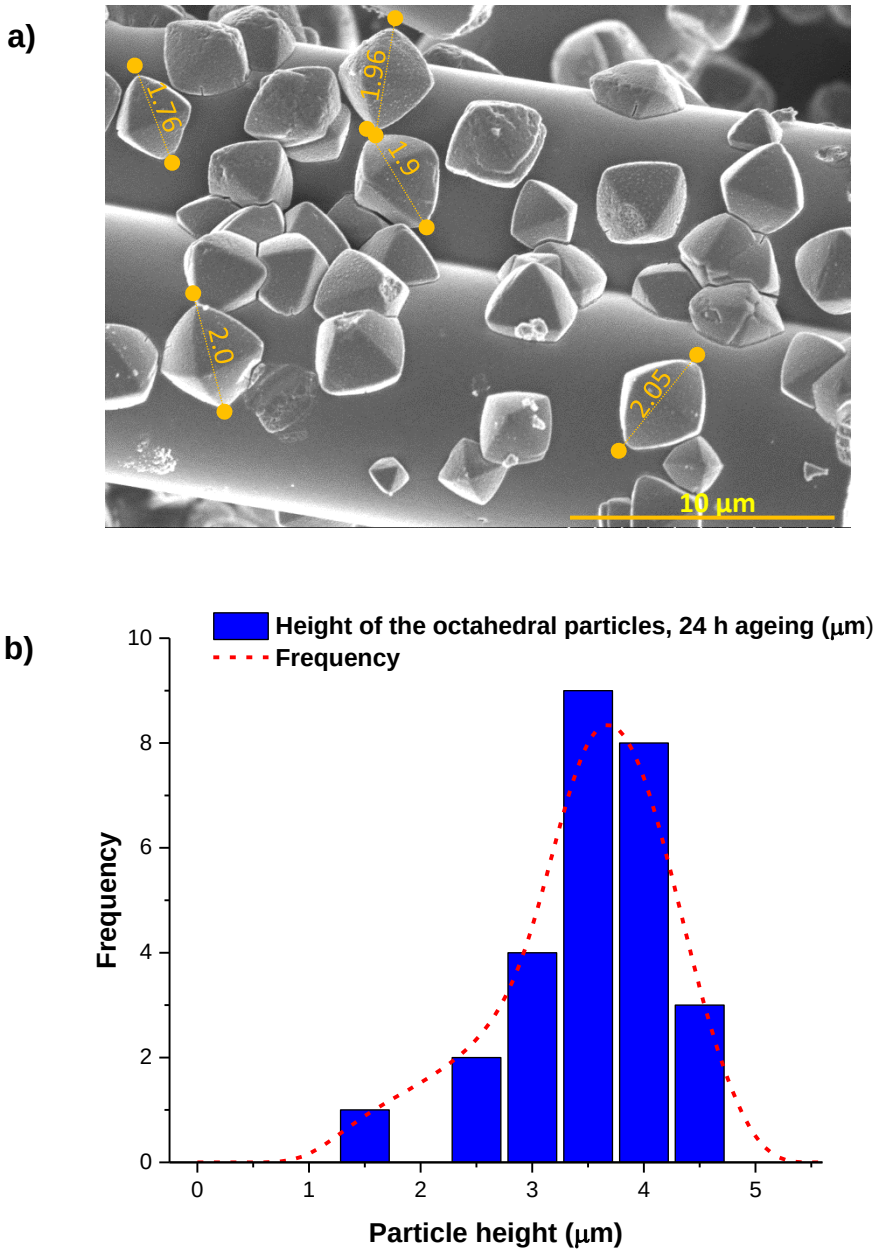

Figure 4-34. a) SEM micrograph showing octahedral-like morphology adopted by CaO via precipitation method with NaOH as the precipitant agent and b) particle height distribution plot showing octahedra with particle height dimensions ranging from 1.25-4.75 µm (higher height frequency at 3.5 µm).

4.6.2 Apparent formation mechanisms of CaO octahedral particles growth over Saffil supports

As presented in section 4.6, the precipitation method via NaOH was very sensitive to fluctuations in the synthesis parameters. Upon optimization of preparation parameters, CaO octahedra with flat faces and curvy edges supported over the periphery of Saffil refractory supports were obtained. Bearing

in mind the octahedral morphology adopted by CaO, understanding the mechanism of formation of octahedral CaO crystals would contribute to standardizing the methodology used to prepare the CaO/Sf-%-Oct sorbents.

In an attempt to find evidence associated with the formation mechanism, a wide number of publications was reviewed. Unfortunately, no evidence was found of previous research work in which CaO octahedra had been produced using precipitation method with $Ca(NO_3)_2$ as the CaO precursor without the presence of a surfactant. Conventionally, $CaCO_3$ or $Ca(OH)_2$ octahedra can be tailored via precipitation, hydrothermal, solvothermal and sol-gel using a tensoactive agent also termed surfactant like polyvinylpyrrolidone (PVP) [283-285]. This particular surfactant has multiple applications such as dispersant, reducing agent, surface stabilizer and growth modifier [286]. However, considering the degree of complexity for obtaining octahedral-like morphology without the presence of a directing compound, different theories arise for justifying not only the formation of octahedra but also the hexagonal plates observed through SEM. The first theory associated with the formation mechanism of octahedral CaO is presented in Figure 4-35. As can be seen in this illustration, the sequential process encompasses three stages. Initially, crystal centres (nuclei) aggregate into plates or platelets. Upon formation of hexagonal platelets with random sizes into the alkaline solution, they assemble over the surface of Saffil supports. Then, Ostwald ripening promotes merging plates into larger particles. This evolutionary mechanism is strongly dependent on ageing time, and finishes upon formation of octahedra in which lateral faces have smooth surfaces and edges become curvy. The experiments performed to refine the preparation conditions revealed that pH 11, precipitation temperature of 115 °C and 24 h of ageing are the optimal parameters for the support and tailoring of rigid octahedral structures. Evidently, the presence of remnant plates in the last stage of the proposed mechanism might be due to an incomplete coarsening process (e.g. hexagonal platelets exhibited in 12 h ageing - Figure 4-32).

The second particle growth mechanism proposed is not as direct as that depicted in Figure 4-35 in which Ostwald ripening is responsible for forming octahedra at expenses of dissociation of platelets. In this second theory, more steps and factors are involved in the crystallization of CaO octahedra. Although the effect

of CaO precursor concentration over the final morphology was not studied, its importance is evident as the number of calcium ions present in the mixture would change the pH. In addition, the speed of mixing, precipitation media (ethylene glycol, water, ethanol, etc.) and the nature of the calcium oxide precursor ($Ca(NO_3)_2{\cdot}4H_2O$) are factors involved in tailoring CaO toward octahedra [287-289].

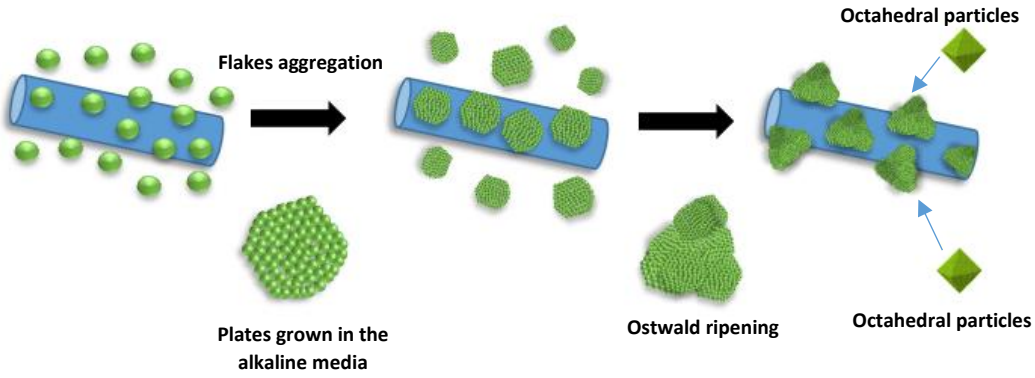

Figure 4-35. Formation mechanism proposed to justify the growth of CaO octahedral particles over Saffil fibres in ethylene glycol solution.

The first step considered in the second formation mechanism implies the dissolution of $Ca(NO_3)_2$ in water and a further reaction with NaOH (see equation (4-2). Slow addition of the basic solution led to the formation of well-structured $Ca(OH)_2$ particles with uniform sizes (hexagonal plates) [290]. It is well-known that growth of $Ca(OH)_2$ with a hexagonal morphology comes from its crystalline structure itself as well as from the preferential growth planes, namely (101) and (001) [291]. However, it must be mentioned that the morphology is also associated with the alkaline NaOH solution and the pH fixed for the preparation mixture (based on pH effect visualized in the section related to optimization of parameters) [292]. During the next stage, the solution containing $Ca(OH)_2$ absorbs CO_2 from the environment. From there, a more thermodynamically stable phase is formed, namely calcite. As has been extensively reported, a polymorph shape that $CaCO_3$ can adopt is rhombohedral [283]. The second proposed mechanism considers that the rhombohedral particles of $CaCO_3$ could come from the stacking of $Ca(OH)_2$ plates (coarsening effect) [293]. Subsequently, an evolution of rhombohedra particles toward octahedral-like

particles (curvy edges) takes place due to the excess of NaOH at an appropriate ageing time [291]. During the last step, energy minimization in the surface of the octahedral particles takes place. There, the remaining hexagonal plates unattached into the rhombohedra are assembled or dissociated over the flat faces of octahedral particles [294]. Evidently, after washing, drying and calcining of the CaO precursor, the pseudo-octahedral morphology is maintained since high thermal stability is gained by tuning CaO with this peculiar shape. For a better understanding, a very intuitive diagram exhibiting all the steps involved in the formation mechanism of octahedral CaO is presented in Figure 4-36 (route indicated by dotted lines).

An alternative formation route of CaO particles with octahedral-like morphology is presented in Figure 4-36 (indicated by the solid arrows). This sequential process begins with the dispersion of $Ca(OH)_2$ particles into the ethylene glycol solution. Then, aggregation of amorphous particles is carried out in presence of Saffil supports and NaOH. Self-assembly of particles occurs, giving rise to the formation of two diverse morphologies, namely rhombohedra and hexagonal plates [295]. As was observed in the section relevant to the optimization of preparation parameters, small fluctuations in pH produced severe alterations in the morphology of the CaO precursor. In the case of rhombohedral particles, they may originate from the interaction of $Ca(OH)_2$ with CO_2 absorbed from the environment whilst the hexagonal plates are conventional morphologies adopted due to the crystallographic properties of $Ca(OH)_2$ (hexagonal system) [284]. Afterwards, a recrystallization (structural evolution) of rhombohedral to octahedral morphology was effected by an excess of NaOH (added to preserve pH 11) [296]. The last step also implies a dissociation of those hexagonal plates of $Ca(OH)_2$ onto the flat and smooth surfaces of already formed $CaCO_3$ octahedra [294]. The pathway proposed in Figure 4-36 and indicated by solid arrows considers that the curvy edges in the octahedrons are shaped as a side effect of both drying and calcination stages performed at 120 °C and 850 °C respectively.

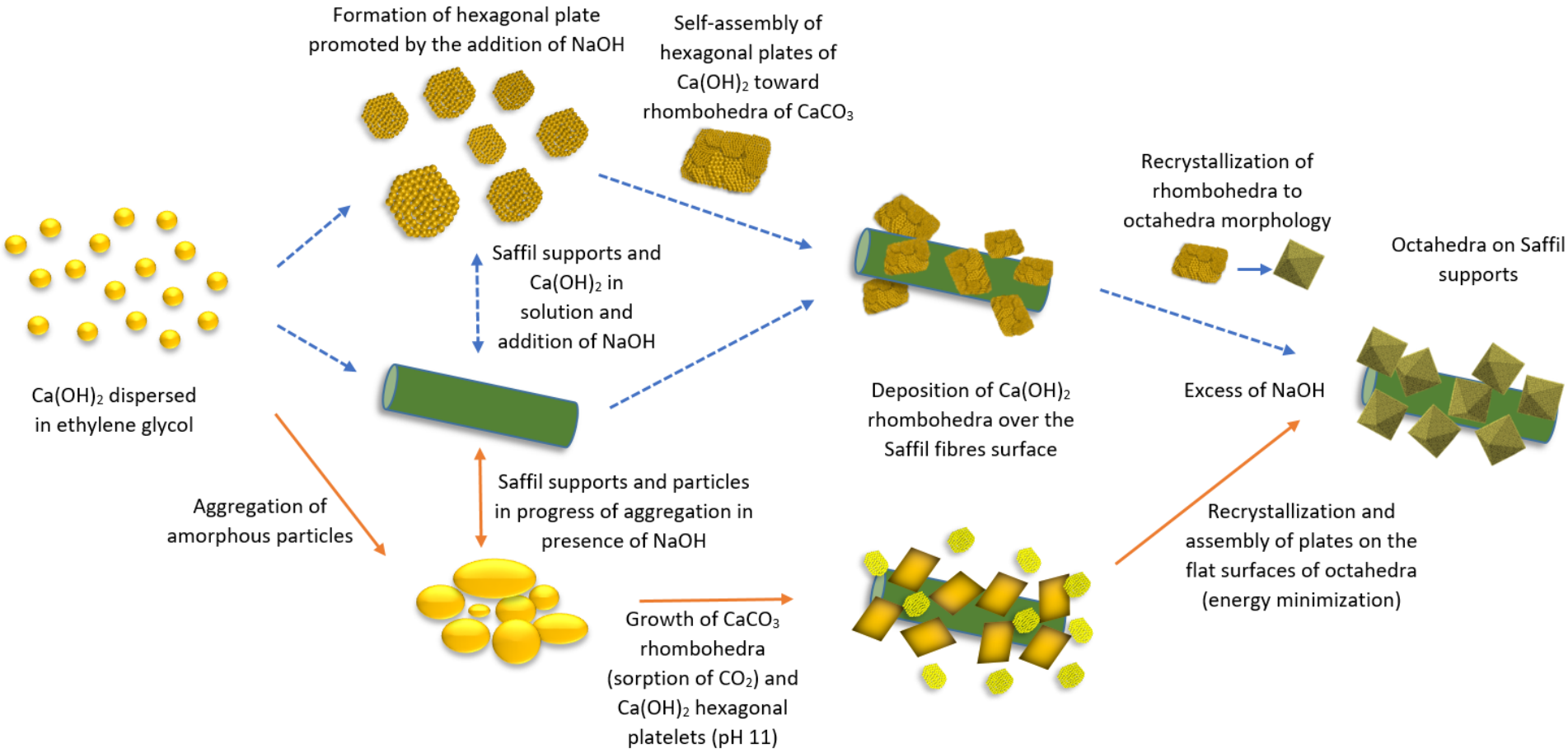

Figure 4-36. Mechanism proposed for the formation of CaO octahedra supported on Saffil supports via precipitation method using NaOH as a precipitant agent at pH 11 and 24 h ageing.

4.6.3 Physicochemical properties of CaO/Sf-%-Oct sorbents

In this section, the textural, morphological, structural and compositional properties of CaO/Sf-%-Oct are evaluated and discussed. The understanding of these physicochemical properties will provide the basis for associating drops or increases in carrying capacities during the use of CaO/Sf-%-Oct sorbents in the high-temperature CO_2 capture tests.

The characterization of the CaO/Sf-%-Oct sorbents began with an XRD analysis that permitted to identify the crystalline phases present upon completion of calcination of the CaO precursor. In the diffraction pattern shown in Figure 4-37, CaO, $Ca(OH)_2$ and δ-Al_2O_3 phases were identified in reference to 01-070-5490, 07-076-0570 and 00-001-1308 crystallographic codes respectively. Evidently, the lack of the $CaCO_3$ phase clearly indicates that the CaO precursor was decomposed towards CaO in the course of calcination conducted at 850 °C for 4 h. As can be also observed in the pattern of the CaO/Sf-25%-Oct sorbent (Figure 4-38), peaks with low intensities linked with the presence of $Ca(OH)_2$ arose as a side effect produced by air-slaking. In all sorbents with different notional loads there were clear sharp peaks associated with CaO. In contrast with Ca-Sa-%-WI, CaO/Sf-%-U and CaO/Sf-%-SH sorbents, the family of sorbents in which octahedral CaO coated the surface of Saffil fibres displayed sharp diffraction peaks.

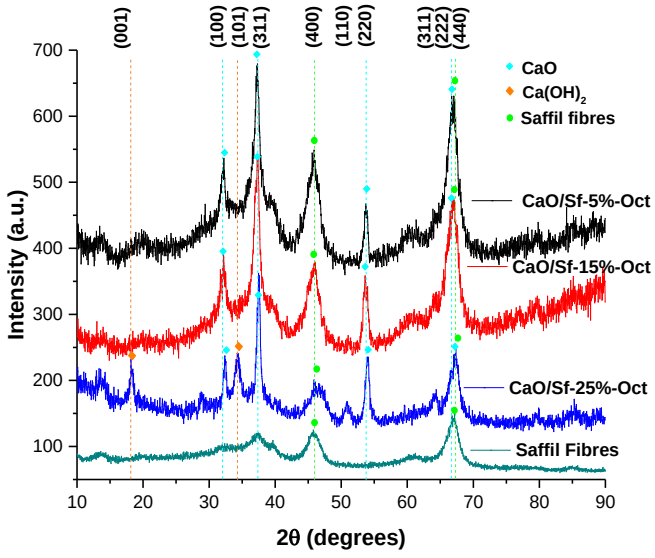

Figure 4-37. XRD patters showing the crystalline phases identified upon calcination completion at 850 °C for 4 h.

Absence of broadened peaks in the CaO phase was apparently caused as the particle size of the octahedra is substantially larger with relation to nanoflakes (micrometres vs nanometres). In theory, the narrower the peak, the larger the crystal size is. It is a consequence of the periodicity of the atomic arrangement in phase, which enlarge the diffraction effect, generating narrow reflexions with high intensity [297].

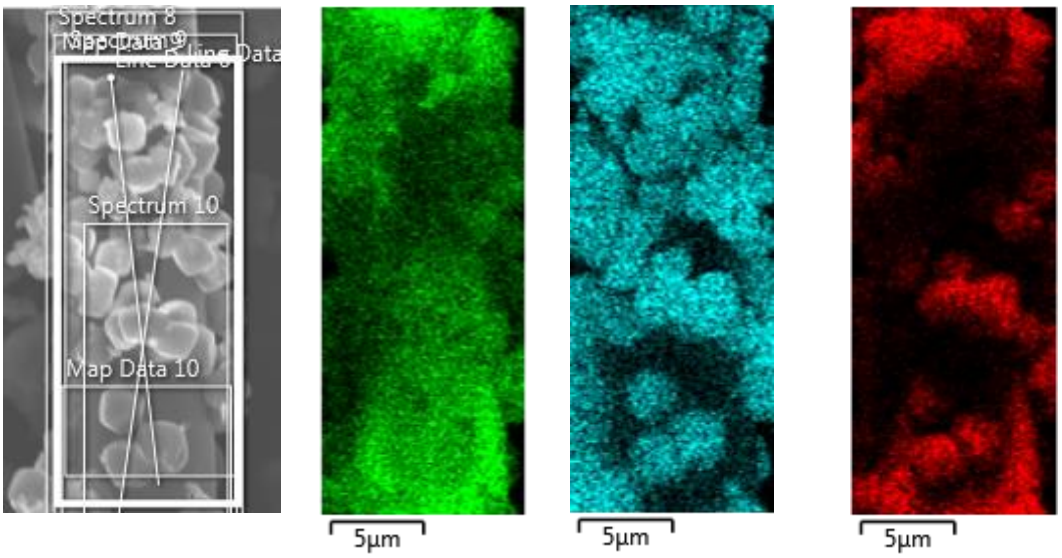

Mapped area in the CaO/Sf-15%-Oct | Al Kα | Ca Kα | O Kα

Figure 4-38. SEM image of a mapped area and the corresponding element maps of Ca, Al and O of a CaO/Sf-15%-Oct sorbent.

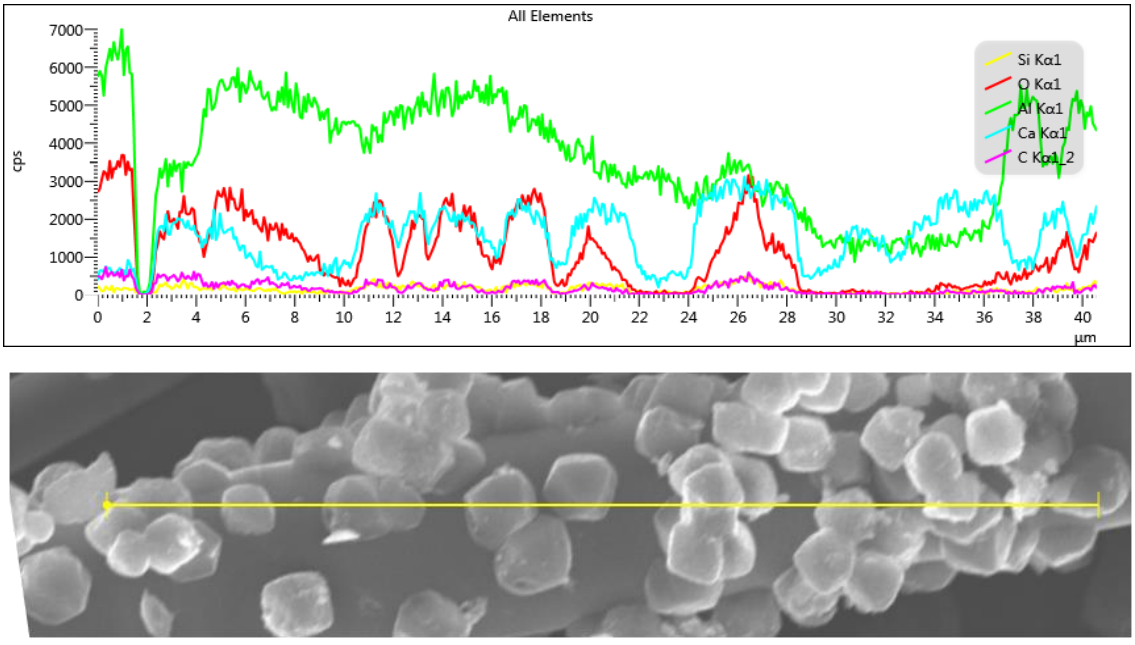

Figure 4-39. Linescan indicating the element distribution of Ca, Al, O, Si, and C in the CaO/Sf-15%-Oct sorbent.

As part of the characterization strategies to study the elemental distribution of Ca over the fibrous support, EDX mapping was employed. The elemental mapping images for the CaO/Sf-15%-Oct sorbent shown in Figure 4-38 demonstrate the existence of Ca deposited throughout the support. The mapped area showing dense regions with high contrast of blue dots mean the abundant presence of Ca. Robust particles with a mean size of 3.75 µm were responsible for the emission of a vast number of signals on these analysed areas. By means of the option “quick analysis” using the “linescan” technique on a single fibre loaded with CaO octahedra from the CaO/Sf-15%-Oct sorbent, it was possible to study the distribution of calcium (Ca). Figure 4-39 shows regions in which a high number of counts corresponding to Ca were detected. It is also clear that Ca was heterogeneously distributed over the fibre surface (void spaces between particle and particle) but this could be due to the content of CaO deposited being only a notional 15 wt. % on this sorbents under study. As observed in Figure 4-33, a homogeneous dispersion of CaO is attained upon deposition of higher CaO contents in the case of 25 wt. %. Regarding to CaO/Sf-5%-Oct, due to the notional CaO content loaded on Saffil fibres being significantly lower, EDX mapping exhibited by contrast of colours, the presence of CaO octahedra non-uniformly distributed along the length of Saffil supports (result not attached due to similar Ca distribution presented in In Figure 4-38).

4.6.3.1 Textural properties of CaO/Sf-%-Oct sorbents

Gas adsorption analysis was used to measure the textural properties of the family of sorbents CaO/Sf-%-Oct such as SSA, PV and PSD. This revealed the values reported in Table 4-8. The results clearly exhibit changes in surface area as a function of the notional content of CaO. In agreement with previous SSA studies, the recorded values dropped as the content of CaO deposited over the Saffil fibres increased. It must be kept in mind that a direct comparison with relation to sorbents coated with CaO nanoflakes could not be performed since their morphology was dissimilar.

Table 4-8. Summary of textural properties measured using BET and BJH methods on the N_2 isotherms collected for the CaO/Sf-%-Oct sorbents at 77 K.

Sample	Specific surface area m^2g^{-1}	Pore volume ($m^3 g^{-1}$ ($x10^{-6}$))	Pore radius (nm)
CaO/Sf-25%-Oct	110	0.28	3.3
CaO/Sf-15%-Oct	115	0.26	2.4
CaO/Sf-5%-Oct	123	0.24	2.2
Saffil fibres	138	0.29	1.9

The relationship between the quantity of N_2 physisorbed in the CaO/Sf-%-Oct sorbents and the relative pressure (equilibrium pressure) at 77 K is presented in Figure 4-40. As one would expect from the adsorption isotherms exhibited below, the family of sorbents can be classified as type IV according to IUPAC [249]. This type of isotherm is characteristic of mesoporous adsorbents. Their adsorption behaviour relies on the interactions adsorbent-adsorptive and molecule-molecule in the condensed state. In addition, all the isotherms presented a hysteresis loop type H2(b). Evidently, the complex pore structure of CaO/Sf-%-Oct sorbents plays an important role in the pore network effects.

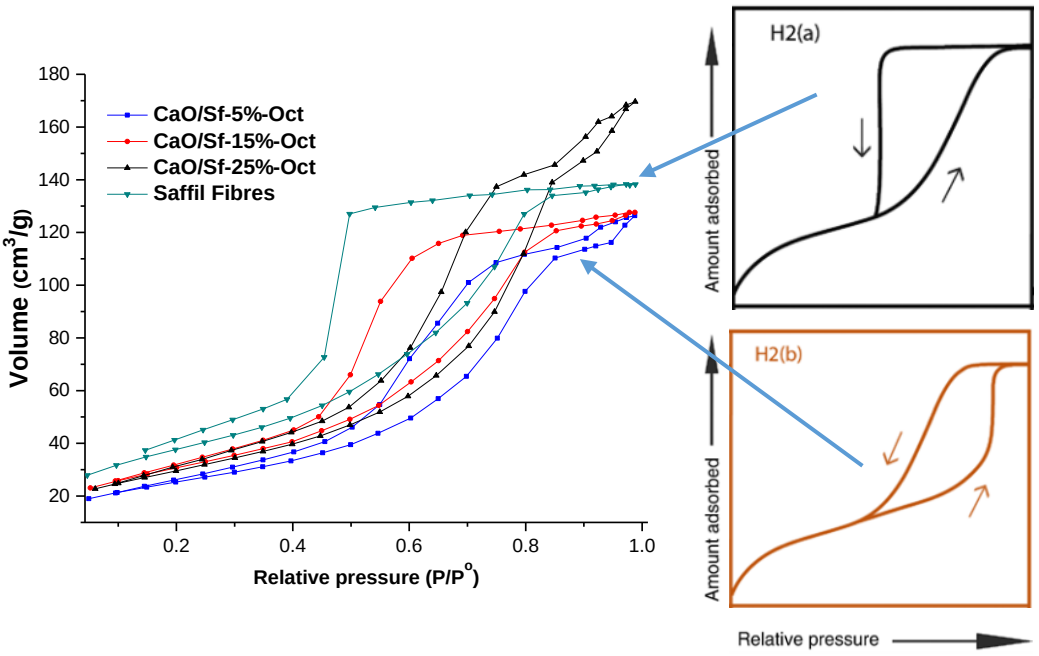

Figure 4-40. N_2 Adsorption isotherms of CaO/Sf-%-Oct sorbents obtained from a Nova 2200e apparatus. Degassing for elimination of contaminants (water and oils) was conducted at 200 °C for 3h. The hysteresis loop of the as-prepared sorbents was identified through the IUPAC classification [249].

Figure 4-40 features loops with very steep desorption branches, but comparing the adsorption/desorption trend of Saffil fibres with respect to sorbents coated with nanoflakes, they adopt a different branch shape (H2(a) vs H2(b)). This difference is apparently derived from pore blocking. As a result of it, the size distribution of neck widths will increase. Therefore, the branch breadths are considerably narrower compared to those registered by the Saffil fibres mat [273, 298]. Moreover, the pore blocking effect can be clearly observed when compared to the Saffil supports isotherm (reference). The N_2 evaporation was displaced towards higher relative pressures as the CaO amount increased. As seen in the sorbents with nanoflakes like CaO morphology, variations in the volume of N_2 adsorbed (height of hysteresis branch) were also correlated with the plugging of pores.

To investigate to what extent the porosity of sorbents is diminished by the deposition of CaO octahedra over the periphery of the Saffil fibres, a study of pore size distribution was conducted. The PSD results obtained through the application of the BJH method are presented in Figure 4-41 and Table 4-8. This technique revealed the CaO/Sf-%-Oct sorbents loaded with notional wt. % of 5, 15 and 25 presented unimodal pores with peaks centered at 2.2, 2.4 and 3.3 nm respectively. These measured average pore sizes gave a strong indication that this family of sorbents have pore networks classified in the range of mesoporous.

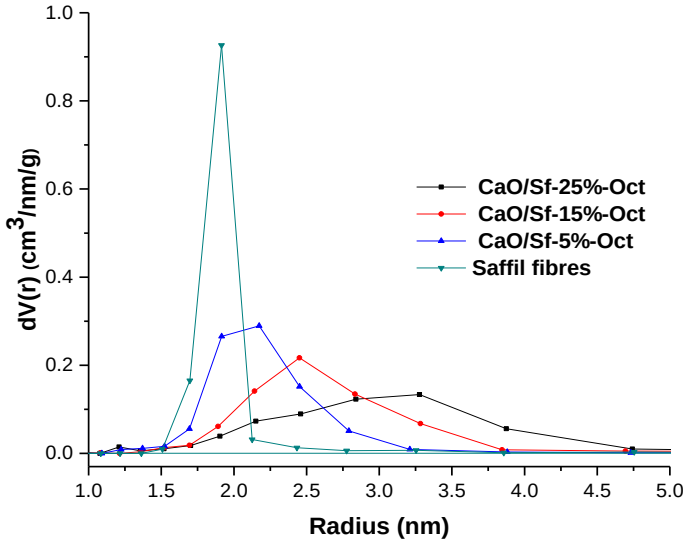

Figure 4-41. Pore size distribution curves of CaO/Sf-%-Oct sorbents calculated by applying BJH method in the adsorption isotherm shown in Figure 4-40.

In terms of PV, slight increments as the notional CaO amount deposited over the support increased were observed. The changes in PV, average pore size and broadening of the distribution in contrast with values measured on Saffil fibres could be justified by analysing the nature of the adsorption isotherms illustrated in Figure 4-40. As the branches had an H2(b) shape, it can be assumed that the deposition of CaO octahedra blocked pores but the neck widths became significantly larger. This effect is produced as the CaO remains around the mouth of the pores, and thus, pores apparently have a wider radius with a tight neck that produces an asymmetrical desorption branch type H2(b).

4.6.4 Quantification of CaO present in CaO/Sf-%-Oct sorbents

Formerly, the optimal synthesis conditions to prepare CaO/Sf-%-Oct sorbents were investigated. Subsequently, upon the synthesis of this family of sorbents with diverse notional amounts of CaO, their physicochemical properties were determined by means of conventional characterization techniques. However, the real amount deposited over the fibrous support was unknown. Hence, XRF was used to quantify the CaO present in the CaO/Sf-%-Oct sorbents. In the matter of the XRF results, the compositions measured were bordering on the notional amounts (see Table 4-9). Hence, it can be assumed that depositing notional percentages of CaO equal or below to 25% by means of the precipitation method with NaOH under controlled and optimized conditions was an effective approach.

Table 4-9. Real composition of the CaO/Sf-%-Oct sorbents prepared with notional CaO contents ranging from 5 to 25 wt.%. The quantification analysis was conducted using an XRF Rigaku ZSX Primus II apparatus.

CaO-based sorbent	CaO (%)	Al_2O_3 (%)	SiO_2 (%)
CaO/Sf-25%-Oct	24.7	71.4	3.9
CaO/Sf-15%-Oct	14.1	82.2	3.7
CaO/Sf-5%-Oct	5.0	92.5	2.5
Saffil fibres	-	96.4	3.6

4.7 Conclusion

In the effort to prepare CaO-based sorbents with enhanced resistance to sintering during its application to CO_2 sorption at high temperature, Saffil fibres as a CaO stabilizer were utilised. As presented throughout this chapter, CaO was deposited over the surface of the fibrous support using both wet impregnation and precipitation methods. Bearing in mind results showed using conventional characterization techniques, it was observed that both preparation methods presented sensitivity to preparation conditions. An optimization of these parameters (composition, stirring, preparation temperature and ageing time) permitted to achieve a homogeneous deposition of the active phase towards the sites of interest, namely the periphery of the Saffil fibres. EDX mapping in both methods once optimizing synthesis conditions confirmed the uniform distribution of CaO coating over the Saffil fibres supports. In terms of calcination temperature, which exposed the solids collected upon completion of drying at 850 °C for 4 h, a CaO phase shaped as nanoflakes on Saffil fibres was obtained.

Upon performing XRF quantitative analysis on Ca-Sa-%-WI, CaO/Sf-%-U and CaO/Sf-%-SH sorbents, slight variation in real compositions compared to the intended notional ones were observed. Evaluating the CaO coating thickness in CaO-based sorbent loaded with a monolayer of nanoflakes by SEM, it was found that a marked thickness increase occurred when the CaO deposition was shifted from wet impregnation to precipitation via urea, namely ~9.5% for the sorbents with 15% and ~10% for 25 wt.% of CaO. This difference was indiscernible for samples with 5 wt. % of active phase as their layers had similar dimensions. With respect to CaO/Sf-%-SH sorbents, although XRF demonstrated CaO depositions close to the theoretical expected, the CaO deposited over the Saffil supports was amorphous at the conditions selected for precipitating the active phase.

Regarding textural properties of Ca-Sa-%-WI, CaO/Sf-%-U and CaO/Sf-%-SH sorbents, a strong dependence between the CaO amount deposited and the SSA was found. Despite higher loads of active phase decreasing the SSA, they remained considerably high with relation to the poor surface area characteristic of unsupported CaO. In addition, their porous network typical of a mesoporous

material made these supported sorbents more attractive to CO_2 sorption applications.

With regards to the CaO/Sf-%-Oct sorbents, precipitation via NaOH was shown to be a promising way to load CaO over the fibrous support. Although CaO/Sf-%-SH sorbents attained an inhomogeneous distribution of the active phase, it was demonstrated that controlling pH and prolonging aging times CaO could coat the fibres in a homogeneous manner. Experiments at pH 12 revealed the formation of multifaceted particles with dimensions ranging from 8.5-15.5 µm, whilst decreasing pH to 11 caused drastic morphological changes, namely the formation of octahedral CaO with a mean particle size of 3.75 µm. As Ostwald ripening was apparently the phenomena associated with the proposed growth mechanisms, ageing time played a vital role in the formation of octahedra with smooth faces and tuned edges. Hence, experiments run at different ageing intervals revealed that 24 h was the optimal time to achieve completion of the particle coarsening.

In regards to the SSA and PSD, even though the CaO particles with octahedral morphology had dense bodies, the surface area of the CaO/Sf-%-Oct sorbents remained considerably high >110 m^2/g Sorbent. In addition, the pore size distribution results revealed the presence of a porous structure consisting of pores in the mesorange.

Finally, as evidenced from the results derived from both wet impregnation and precipitation method, CaO was successfully loaded over the surface of the support. Although the synthesis routes presented sensitivity to the preparation conditions, XRF analysis showed that compositions close to those expected were attained. Hence, it can be concluded that the routes and parameters selected for coating CaO as an active phase were effective. Moreover, it was found that using both synthesis methods, CaO grows with a well-defined microstructure (nanoflakes or octahedra) that potentially could enhance the thermal and mechanical resistance of CaO to avoid densification.

Chapter 5 Evaluation of Capture Capacity and Durability of CaO-based Sorbents

This chapter presents the study of CO_2 uptake performance carried out using CaO-Saffil sorbents prepared via wet impregnation and precipitation methods. The determination of the carrying capacity is conducted through multicycle carbonation-decarbonation trials performed under controlled conditions using a TGA apparatus. The durability of the as-prepared sorbents is evaluated experimentally within 30 continuous cycles, whilst the residual reactivities (stable uptake capacity attained after a large number of cycles) are forecasted theoretically by means of well-established mathematical models [196, 299]. The causes of the CO_2 uptake capacity loss are investigated using non-destructive characterization techniques such as SEM. The structural and morphological changes derived from the multicycle TGA trials are presented and discussed. Finally, the benefits of depositing CaO over Saffil are highlighted by comparing the CO_2 uptake performance of the as-prepared sorbents with respect to other promising sorbents reported in the literature.

5.1 Multicycle TGA trials for high-temperature CO_2 capture

The performance of Ca-Sa-%-WI, CaO/Sf-%-U, CaO/Sf-%-SH and CaO/Sf-%-Oct sorbents for the capture of CO_2 at high-temperature is assessed through isothermal experiments conducted in a Mettler Toledo DSC/TGA apparatus. The thermal stability of the as-prepared sorbents is confirmed in 30 continuous carbonation-decarbonation cycles. The length of the trials was selected as natural CaO typically loses more than 85% of its carrying capacity in this window of uptake cycles [300]. To run the CO_2 capture trials, a thermal program that involves four stages was made-up with the assistance of STARe thermal analysis software. The sequence used to perform the experiments is described below and displayed in the intuitive diagram of Figure 5-1. The first stage contemplates the activation of the CaO phase by means of a calcination process. In this stage, the CaO-Saffil sorbent is heated up at a rate of 20 °C/min (dynamic mode) from 25 to 850 °C using pure N_2. In the course of this calcination step,

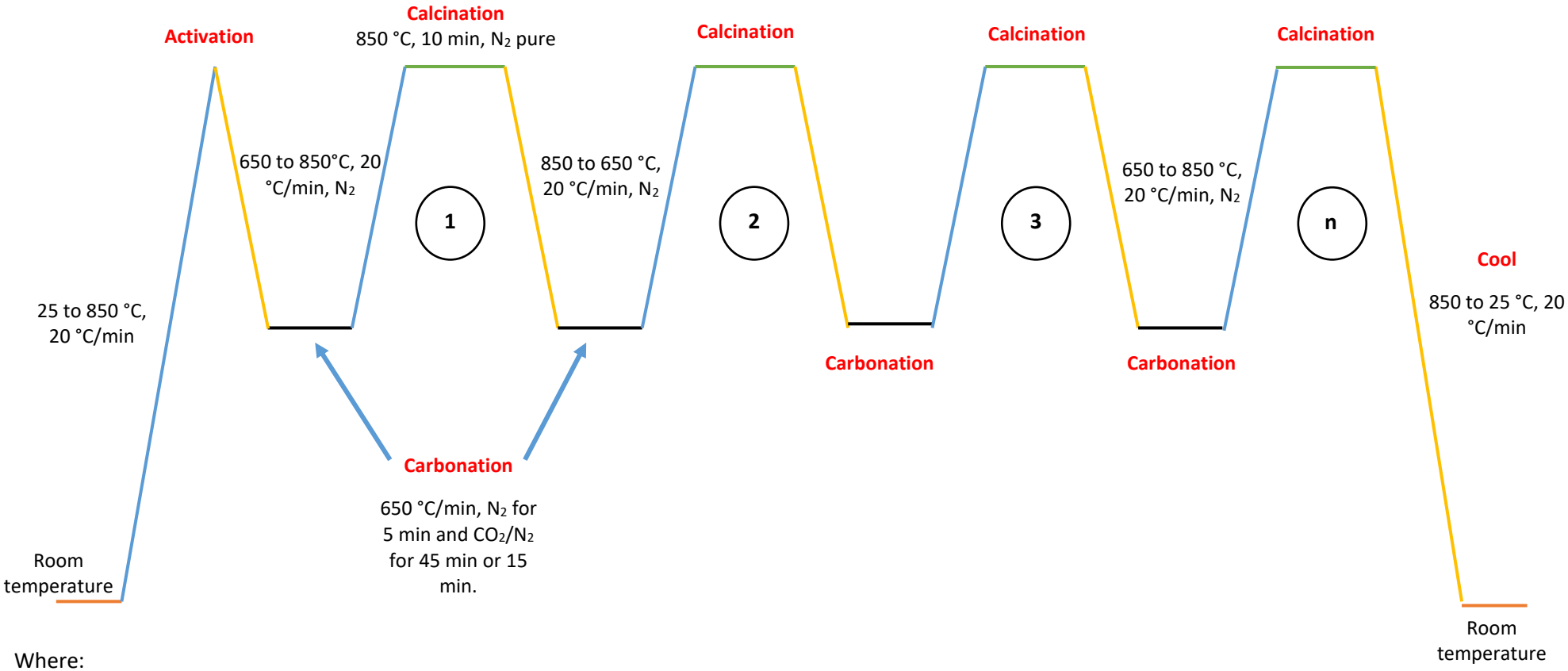

Where:

$n = \ number\ of\ cycles, \qquad n = \ 1, 2, 3, \ldots, n = 30$
$T_{min} = \ \ room\ temperature; T_{capture} = \ 650\ °C; T_{calcination} = \ 850\ °C$

Figure 5-1. TGA program used to evaluate the performance of CaO-saffil sorbents impregnated with diverse amounts of CaO.

water molecules adsorbed during sample storing storage are released. The second stage comprises a carbonation reaction performed at 650 °C for 45 min or 15 min in an atmosphere composed of 90% CO_2/10% N_2. This CO_2-rich mixture is used to reduce mass transfer limitations. The flow rate is fixed at 50 cm^3/min due to the university's health & safety policies. The third stage is associated with the reverse reaction: $CaCO_3$ to CaO. Upon completion of the capture process, the gaseous atmosphere is switched to N_2 and the temperature is increased to 850 °C at a rate of 20 °C/min and the dwell time used to reach the decarbonation is 10 min. To end the first cycle, the temperature decreases to 650 °C maintaining a pure N_2 flow (fourth stage). The remaining 29 cycles are carried out considering stages 2 to 4 under alike parameters and intervals.

5.2 CO_2 uptake capacity measurements

It has been widely documented that the CO_2 uptake capacity (also termed carrying capacity) in CaO particles occurs in two stages: a fast carbonation reaction on the available external surface of particles, followed by a slower diffusion-limited regime. This second stage consists of the diffusion of CO_2 through the $CaCO_3$ layer (30-50 nm thick, [301]) formed after 1-4 min of carbonation [225]. The reaction rate of the carbonation process is depended on operational parameters such as pressure and temperature [301, 302]. With respect to the reverse reaction $CaCO_3$ to CaO, CO_2 is released in a period of 2-6 min using temperatures above 800 °C.

A carbonation-decarbonation profile (1st cycle) presented in Figure 5-2 extracted from the multicycle TGA trial performed on the Ca-Sa-25%-WI sorbent (reference) reveals consistency with studies performed on natural or synthetic CaO-based sorbents documented by different authors. The two-stage sorption process of sorbents CaO/Sf-%-U and CaO/Sf-%-SH with CaO weight percentages of 25-5% were also consistent with the sample used as the reference (Figure 5-2).

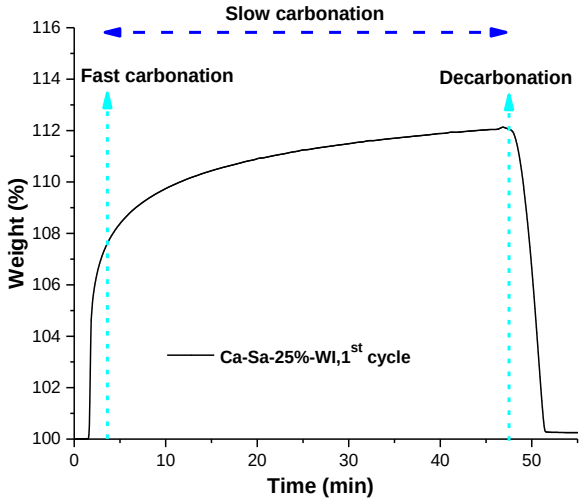

Figure 5-2. Typical carbonation-decarbonation cycle extracted from the multicycle TGA trial performed on the Ca-Sa-25%-WI sorbent. The carbonation reaction was carried out for 45 min at 650 °C, with decarbonation for 10 min at 850 °C.

Typical TGA sorption/desorption profiles of multicycle CO_2 sorption trials are shown in Figure 5-3. The curves of representative sorbents Ca-Sa-25%-WI, CaO/Sf-25%-U and CaO/Sf-25%-SH indicate mass changes as a function of the time. TGA results showed in Figure 5-3 reveals a drastic uptake decay over the course of 30 carbonation–decarbonation cycles. The loss of carrying capacity as the number of cycles proceed is associated with volumetric densification. The sintering, which produces the collapse of the network of pores (micro and meso pores), reduces the surface areas of the CO_2 sorbent (confirmed in section 5.3). On the basis of a wide number of investigations, the consensus indicates that the apparent densification of the CaO present in CaO-Saffil sorbents may occurs during the calcination stage as high temperatures are used to drive the reverse reaction $CaCO_3$ to CaO [303, 304]. Although in CaO-based sorbents formed by two or more metal oxides (supported sorbents) reported in the literature, microstructural changes produced by the mixture of phases also have a negative influence in the carrying capacity [303], this effect is negligible in CaO-Saffil sorbents because Saffil is thermally stable up to 1600 °C. Hence, the strong densification showed in 25 wt. % samples led to characterize them through conventional techniques such as scanning electron microscopy. A detailed analysis of

morphological and microstructural transformations on used samples is presented in section 5.3.

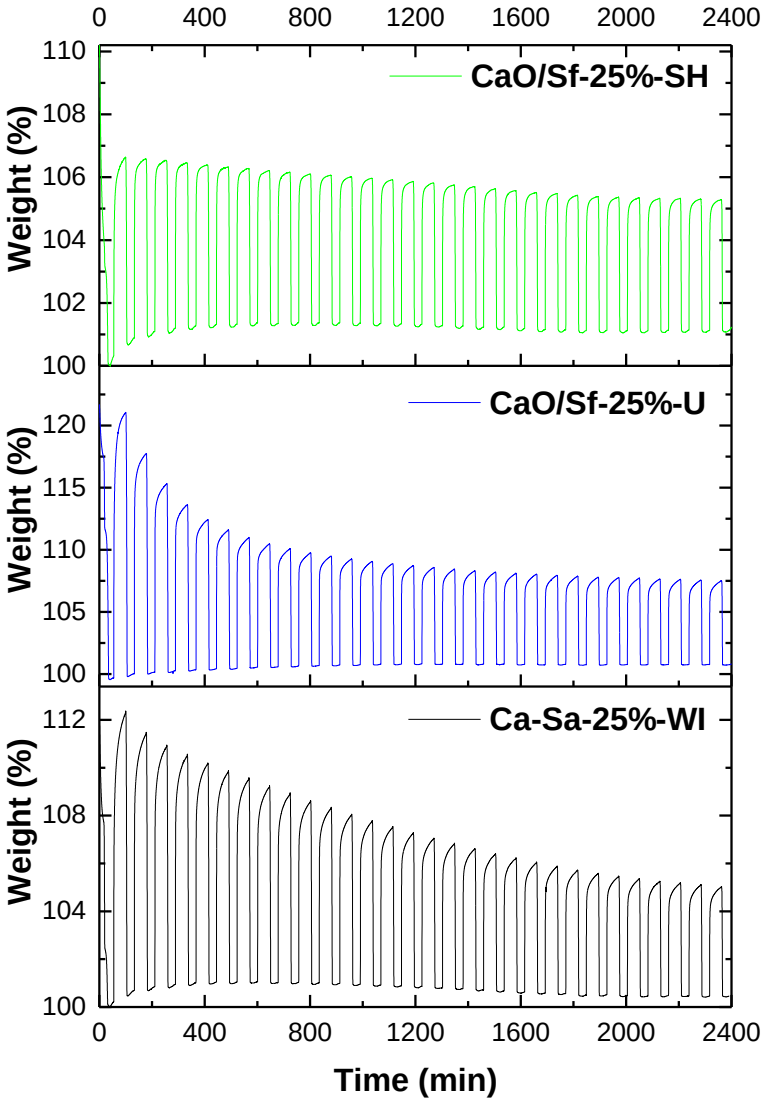

Figure 5-3. CO_2 sorption/desorption evolution of Ca-Sa-%-WI, CaO/Sf-%-U and CaO/Sf-%-SH sorbents impregnated with 25 wt. % of CaO. The TGA settings to conduct the carbonation stage were 650 °C in presence of a gaseous mixture composed of 90% CO_2 with N_2 balance and the decarbonation stage was carried out in pure N_2 at 850 °C.

5.2.1 Performance of Ca-Sa-%-WI sorbents in multicycle CO_2 capture trials

Multicycle CO_2 uptake capacities for the as-prepared sorbents are predicted on the basis of equation (5-1) presented below,

$$CC_N = \frac{(m_{f,N} - m_i)}{m_i} \quad (5\text{-}1)$$

where CC_N is the carrying capacity of the sorbent at cycle N, m_i is the mass of the sorbents post-activation, $m_{f,N}$ is the mass during the cycle, and the subscript N denotes the cycle being evaluated.

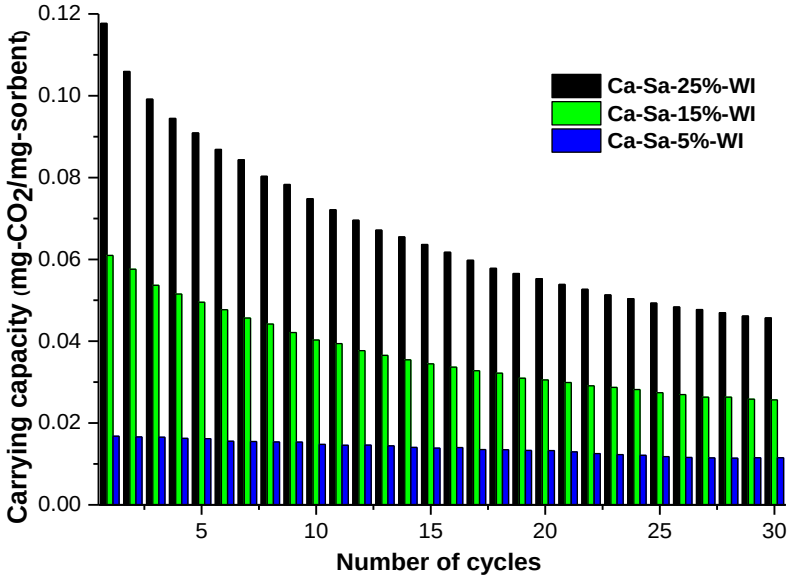

Figure 5-4. Carrying capacities for samples Ca-Sa-%-WI (25, 15 and 5 wt. % CaO) measured in the course of 30 carbonation-decarbonation cycles. The carbonation process is carried out for 45 min in presence of a CO_2-enriched gas mixture (90% CO_2/10% N_2).

The maximum capture capacities measured at cycle *N (1-30 cycles)* for the Ca-Sa-%-WI sorbent are shown in Figure 5-4. This bar plots exhibit initial uptake capacities of 0.118, 0.061 and 0.017 mg CO_2/mg Sorbent for the samples with CaO weight percentages of 25, 15 and 5 %, respectively (Figure 5-4). By cycle 30, circa 30% of CO_2 retention is lost by the Ca-Sa-5%-WI sorbent, whereas the sorbents with higher CaO loadings (Ca-Sa-25%-WI and Ca-Sa-15%-WI) had more drastic deteriorations in uptake capacity, namely ~60 and ~50%, respectively. Although the deactivation of the sorbent was committed as the amount of CaO deposited on Saffil supports increased, the capture capacity doubles or triples compared with the 5 wt. % sorbent. As a benchmark, multicycle uptake profile and carrying capacities of unsupported CaO (without Saffil supports) prepared using similar methodology is displayed in Figure 5-5. This multicycle TGA plot exhibit similar deactivation trend but

there is a slight difference in the deactivation performance of the unsupported CaO and the CaO-Saffil sorbents with active phase loadings of 15 and 25 wt. %. Hence, the major benefits of incorporating Saffil fibres as supports of CaO are exhibited in the Ca-Sa-5%-WI sorbent due to its great durability. The enhanced performance is distinguished in more detail through the bar plots shown in Figure 5-6 that summarizes the carrying capacity depletion in the course of 10, 20 and 30 cycles.

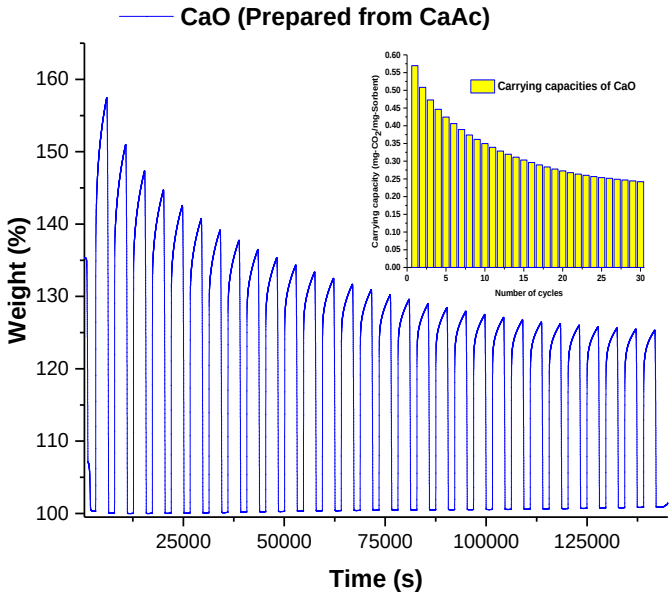

Figure 5-5. Multicycle TGA trial and uptake capacities of unsupported CaO prepared from calcium acetate under comparable methodology and conditions to Ca-Sa-%-WI sorbents.

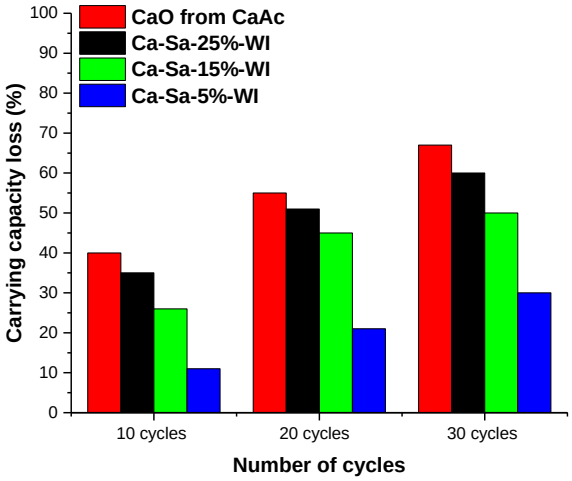

Figure 5-6. Comparison of the carrying capacity loss of Ca-Sa-%-WI sorbents with 5-25 wt. % in the course of 30 continuous carbonation-calcination cycles.

Figure 5-6 confirms that the 5 wt. % sample with the thinnest layer of nanoflakes has the best 30 cycles performance. The long-term durability is apparently produced by the distribution of tensile forces throughout the CaO coating. This effect is a consequence of the low thermal expansion coefficient of Saffil ceramic fibres compared to CaO (information provided by Saffil's supplier, UNIFRAX, UK). In addition, the low degradation of the cycled Ca-Sa-25%-WI sorbent is assumed to be of the substrate-clamping effect [305]. This effect increases the stability of the sorbent at high temperatures as it inhibits lateral shrinkage and reduces densification of the CaO nanoflakes [305]. This effect has been widely documented for ceramic materials in which a thin film of an element or compound is clamped on planar substrates. For CaO-Saffil Sorbents Ca-Sa-15%-WI and Ca-Sa-25%-WI with thicker CaO coatings, volumetric densification was more prominent after their exposure to CO_2 uptake cycles as clamping effect is effective in the proportion of CaO adjacent to the interface Saffil-Sorbent (SEM images of tested sorbents displayed in section 5.3.1). There would also be an important contribution in the carrying capacity depletion because of sintering on freestanding CaO aggregates observed in SEM images reported on section 4.2. The diagram presented in Figure 5-7 intuitively represent clamping of nanoflakes over the smooth surface of Saffil substrates.

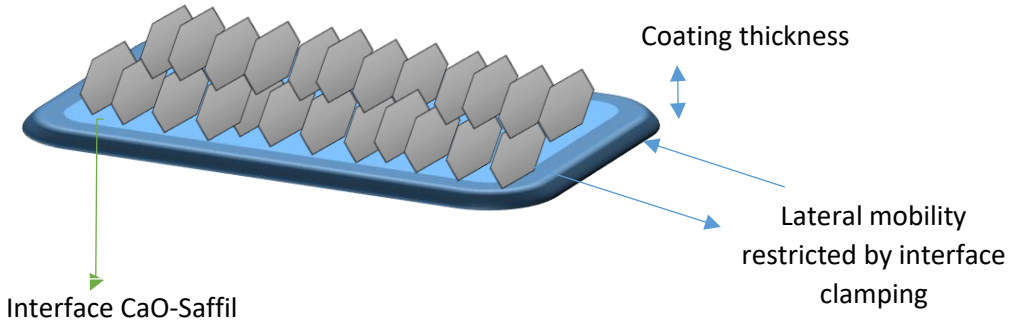

Figure 5-7. Mobility of CaO nanoflakes restricted by clamping effect. Thinner thicknesses increase effects of mechanical interface clamping.

5.2.1.1 Prediction of the residual reactivity for Ca-Sa-%-WI sorbents

The multicycle uptake results plotted in Figure 5-4 reveals that albeit the carrying capacity is near stable by the end of the carbonation-decarbonation trials, a portion of reactivity is still lost beyond cycle 30. Hence, there is an interest in predicting to what extent reactivity declines. In the literature, a wide range of models have been proposed to estimate sorbent degradation over a long sequence of thermal cycles. For example, Abanades et al. and Lysikov et al. proposed mathematical models to predict the residual reactivity for repeated recarbonation-calcination cycles. The semi-empirical conversion model (5-2) proposed by Abanades et al. results from a series of adaptations performed to a solid-state kinetic model (second-order process) for a catalyst deactivated by densification [299]. In equation (5-2), the conversion at cycle *N* is represented by X_n, X_r is the residual conversion and k is the deactivation constant. The k values are predicted by non-linear curve fitting. Furthermore, Lysikov et al. rearranged the equation (5-2) introduced by Abanades et al. and added a sintering exponent n that is intended to improve model fitting. Although the nomenclature of equation (5-3) was changed by the authors, the three fitting coefficients k, n and a_∞ are involved [196].

$$X_N = \frac{1}{\frac{1}{1 - x_r} + kN} + x_r \tag{5-2}$$

$$a_N = \frac{1 - a_\infty}{(1 + kN)^n} + a_\infty \tag{5-3}$$

In the attempt to predict the residual reactivity of the samples coated with 25 and 15 wt. % of CaO, equations (5-2) and (5-3) were fitted with experimental uptake curves. From the non-linear analysis, the correlation factors R^2 were below 0.92. As a result, a simple exponential-decay model derived from a first-order deactivation equation was suggested and used to correlate the thermal data. In the equation (5-4) that best correlate the multicycle recarbonation ($a_{cc,N}$), *N* is the cycle, K represents once more the decay constant, and a_r is the residual CO_2 uptake capacity ($N \rightarrow \infty$).

$$a_{cc,N} = a * e^{-kN} + a_r \quad (5\text{-}4)$$

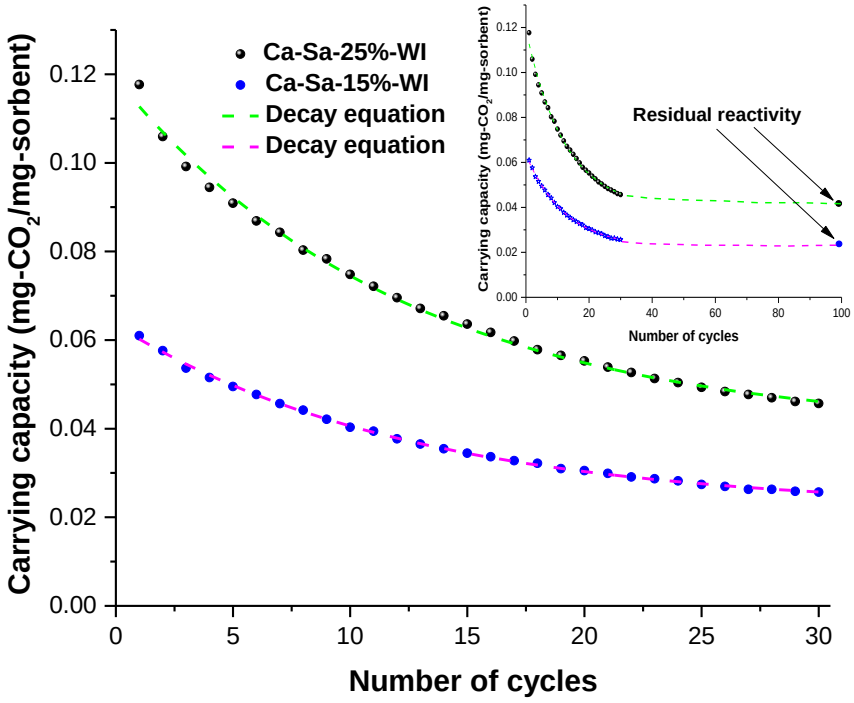

Figure 5-8. Residual reactivities of Ca-Sa-15%-WI and Ca-Sa-25%-WI predicted by fitting a decay equation on experimental TGA data. Modelling results show correlation factors R^2 > 0.995.

In the experimental carrying capacity curves shown in Figure 5-8, dashed lines correspond to the non-linear fit carried out. It can be discerned that there was a correspondence between the experimental curves of samples Ca-Sa-15%-WI and Ca-Sa-25%-WI and the model exponential decay model. Using equation (5-4), it was possible to perform the predictions with R^2 values >0.995. From the curve fitting analysis, comparable degradation rate constants (K) were determined for sorbents with 15 and 25 wt. %, namely 0.0809 and 0.08159, respectively. In relation to the residual capacities at $a_N \cong a_r$, the predicted values were 0.02191 and 0.03925 mg CO_2/mg sorbent, where the higher reactivity belongs to the sorbent Ca-Sa-%-WI impregnated with 25 wt.%. The study of residual reactivity was not conducted on Ca-Sa-5%-WI because the deactivation was much less severe Figure 5-4. By cycle 25, the carrying capacity was constant in 0.012 mg CO_2/mg Sorbent, so, this value is designated as its residual reactivity.

5.2.2 Performance of CaO/Sf-%-U and CaO/Sf-%-SH sorbents tested in multicycle capture trials.

The curves representing the changes in uptake capacity for sorbents CaO/Sf-%-U are exhibited in Figure 5-9. The carrying capacities in cycle 1 for sorbents CaO/Sf-%-U were 0.193, 0.113 and 0.0389 in mg CO_2/mg sorbent for loadings of 25, 15 and 5 wt. %, respectively. In terms of CO_2 capacity, enhanced performance was shown compared to Ca-Sa-%-WI sorbents. By correlating samples of similar CaO weight percentage of sorbents CaO/Sf-%-U and Ca-Sa-%-WI, improvements of ~38%, ~46% and~ 56% were observed between loadings of 25, 15 and 5 wt. %, respectively. This difference is attributed to increases in coating thicknesses, which according to estimations performed through the software “ImageJ”, raised by 9-10.5% with respect to Ca-Sa-%-WI sorbents (15 and 25 wt. %) (higher presence of aggregates in Ca-Sa-%-WI sorbents than in CaO/Sf-%-U sorbents). Although the outcomes presented for the three different CaO/Sf-%-U sorbents in Figure 5-9 revealed improved capture capacity, sharper deactivations occasioned by densification (as explained earlier) were also observed (>56%). After the 30 continuous carbonation-calcination cycles, the uptake capacities of CaO/Sf-%-U samples with weight percentages of 25, 15 and 5 decreased to 0.06, 0.04 and 0.0155 mg CO_2/mg Sorbents, respectively (Figure 5-9).

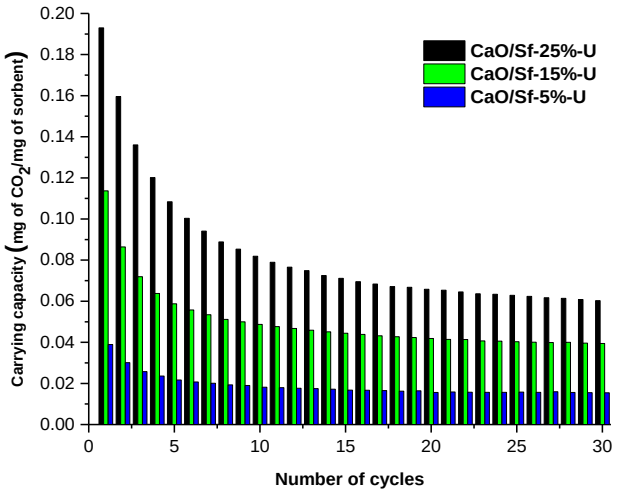

Figure 5-9. CO_2 carrying capacities over 30 continuous TGA cycles of CaO/Sf-%-U sorbents. Carbonation-calcination reactions were performed in 90% CO_2/10% N_2 and pure N_2, respectively.

Experimental measurements carried out over 30 TGA cycles revealed initial carrying capacity of 0.059, 0.036, and 0.028 mg CO_2/mg sorbent for the sorbents CaO/Sf-25%-SH, CaO/Sf-15%-SH and CaO/Sf-5%-SH, respectively (Figure 5-10). The relative decay throughout the multicycle trials was lower compared to Ca-Sa-%-WI and CaO/Sf-%-U, but the CO_2 uptake capacity was significantly lower, as would be expected given the heterogeneous distribution on Saffil and the morphology of the coating (as per discussed in section 4.2.1). By cycle 30, around 30% of reactivity was lost by the CaO/Sf-25%-SH, whereas the sorbents with lower loadings (15% and 5 wt. %) exhibited higher resistance to sintering with reactivity losses of 23% and 0%, respectively (Figure 5-10). It is imperative to indicate that the capture capacity of the 5% wt. % sorbent increased ~3% by cycle 30th. The opening of micropores on the surface of CaO particles, which were promoted by the high temperatures used to desorb the CO_2, apparently caused this slight augment (confirmed in section 5.3.2). The enhanced durability of samples CaO/Sf-%-SH was attributed to mechanical clamping effect (explained above) in conjunction to morphological and textural characteristics of the CaO coating.

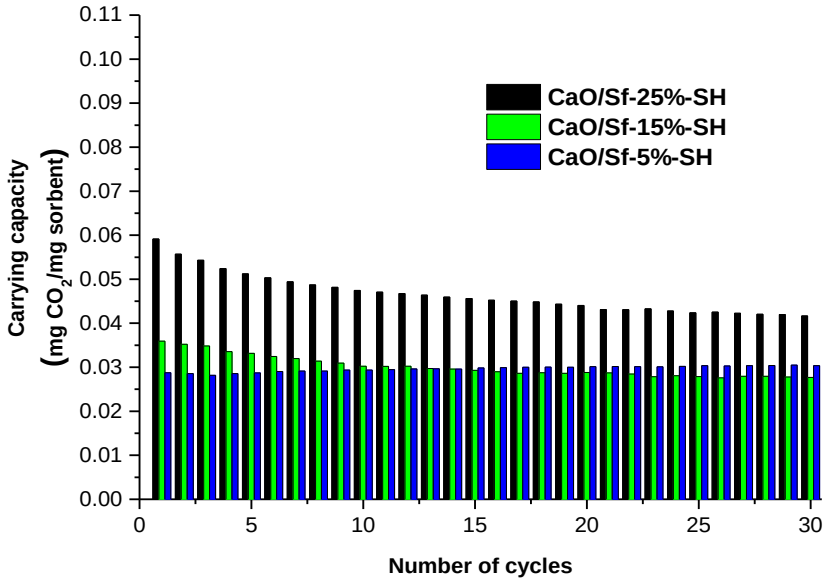

Figure 5-10. Performance of CaO/Sf-%-SH sorbents in which CaO was carbonated using a mixture composed by 90% of CO_2 balance N_2 for 45 min. The calcination reactions were attained in pure N_2 for 10 min.

The improved consistency in sorbent performance of the CaO/Sf-%-SH sorbents displayed in Figure 5-11 indicated a marked sintering inhibition

compared to the benchmark unsupported CaO (Figure 5-5). Although CO_2 experiments performed with carbonations slots of 45 min revealed modest carrying capacities in the family of CaO/Sf-%-SH sorbents, Figure 5-11 revealed an outstanding durability. A contributor of this low percentage of relative degradation was the absence of freestanding CaO particulate (identified by SEM), as previous investigations demonstrate that detached particulate also know as free standing agglomerates have a pronounced deactivation over multicycle recarbonation- decarbonation.

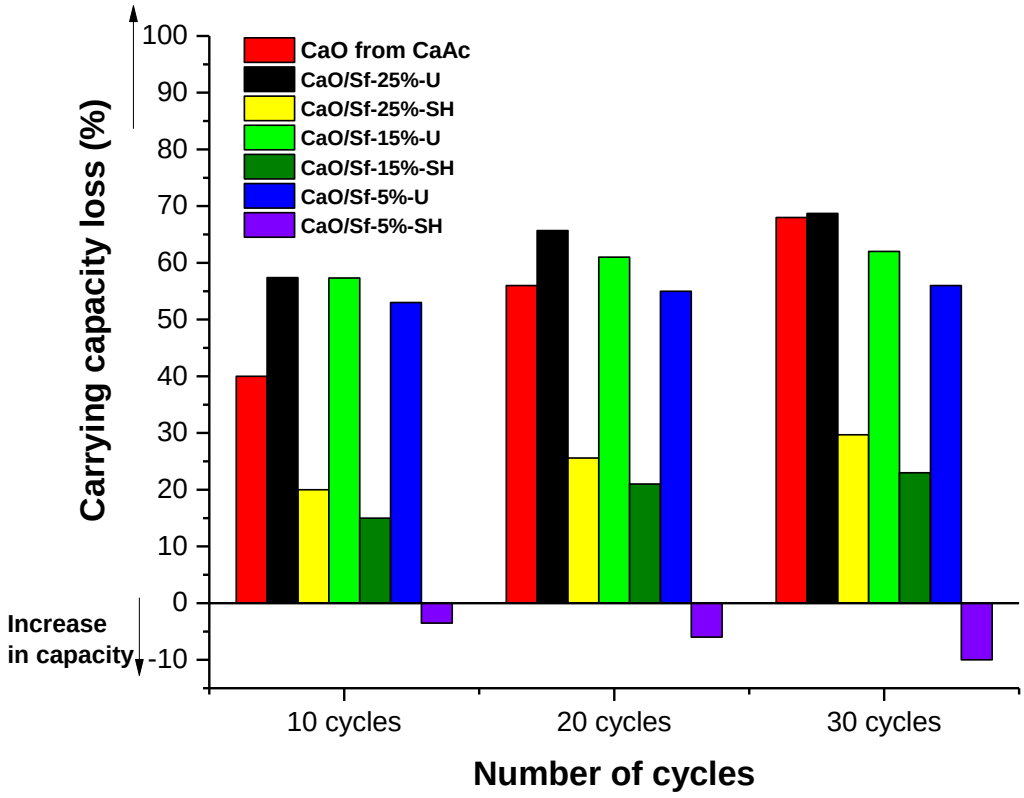

Figure 5-11. Experimental carrying capacity losses (%) of sorbents CaO/Sf-%-SH and CaO/Sf-%-U at cycle 10, 20 and 30; CaO was presented as a reference.

5.2.2.1 Residual carrying capacity analysis of CaO/Sf-%-U and CaO/Sf-%-SH sorbents

In the attempt to predict sorbent degradation over a large number of carbonation-decarbonation cycles, correlations (5-2) and (5-3) proposed by Abanades et al. and Lysikov et al. were fitted with the experimental data of

both CaO/Sf-%-U and CaO/Sf-%-SH sorbents. From the non-linear curve fitting regression, the correlation factors were below the margin or reliability (>0.95). According to the fitting parameters evaluated, comparable R^2 values were obtained for the sorbents Ca-Sa-%-WI with 15 and 25 wt. %, namely ~0.92. Accordingly, the exponential decay model represented by equation (5-4) was used to model the TGA data. Although the residual R^2 was ~0.94, a double exponential decay model was proposed to improve the correlation coefficient. In the literature, equation (5-5) has been used to describe physical or chemical phenomena described by a fast and a slow process of exponential decay trends (e.g. kinetics, biology, etc.) [181, 306]. As a result, its application was extrapolated to predict the residual reactivity of samples CaO/Sf-%-U and CaO/Sf-%-SH. In equation (5-5), the constants $k_{1,D}$ and $k_{2,D}$ represent the degradation rates of the fast and slow process, respectively. The term a_r is the residual carrying capacity, A_1 and A_2 are pre-exponential factors and $a_{cc,N}$ is maintained as the carrying capacity at cycle *N*.

$$a_{cc,N} = A_1 * e^{-k_{1,D}*N} + A_2 * e^{-k_{2,D}*N} + a_r \qquad (5\text{-}5)$$

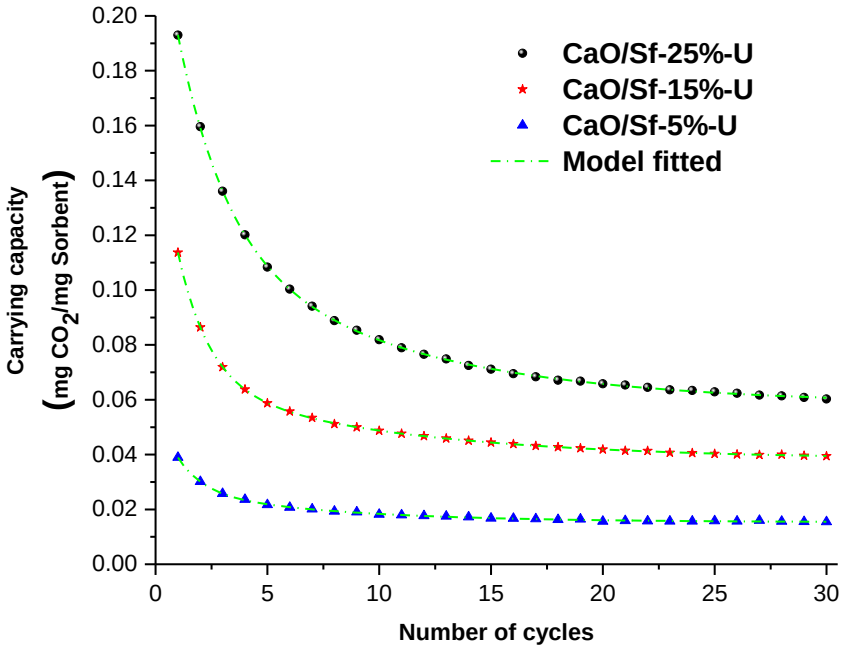

Figure 5-12. Residual reactivity analysis performed by fitting the double-exponential decay model to experimental carrying capacity data. R^2 values above 0.998 confirm the strong agreement with experimental data of CaO/Sf-%-U sorbents.

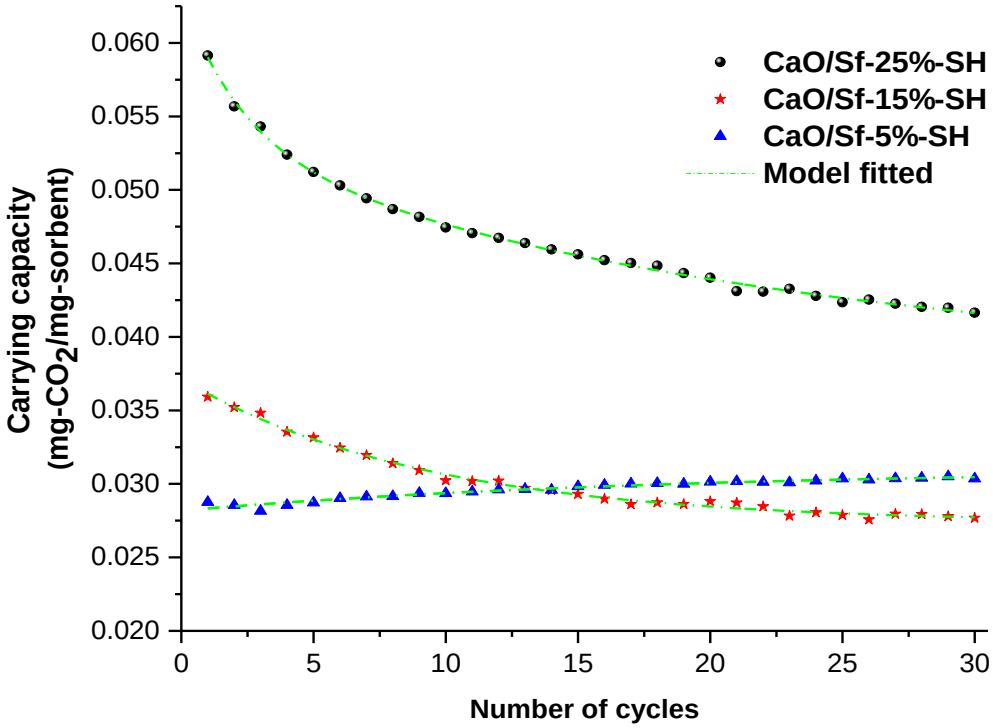

Figure 5-13. Non-linear curve fitting to predict the residual carbonation capacity of CaO/Sf-%-SH sorbents. R^2 values >0.998 are obtained by fitting the two-exponential model Dashed lines.

In the curves shown in Figure 5-12 and Figure 5-13, dashed lines correspond to curve fit implemented to the carrying capacity data. Both plots confirm the strong correlation between the two-phase decay model and the experimental carrying capacity data. Using equation (5-5), it was possible to achieve R^2 values >0.998. The deactivation parameters and residual reactivities calculated from the model fitting analysis are reported in Table 5-1. On the basis of the non-linear regression, the highest residual uptake capacities at $a_{CC,N} \approx a_r$ were 0.058 and 0.041 mg CO_2/mg Sorbent, where the uppermost capacities belong to sorbents CaO/Sf-25%-U and CaO/Sf-25%-SH sorbents, respectively. Based on the residual reactivies presented in Table 5-1, modelled sorbents presented a loss of uptake effectivity between 1.3-3.6%. This finding confirms that within the 30 carbonation-calcination trials, these sorbents reach almost constant carrying capacities.

Table 5-1. Deactivation rate constants ($k_{1,D}$ and $k_{2,D}$) and residual reactivities values predicted by fitting a double exponential decay model in experimental data.

Sorbent	Deactivation rate constant "$k_{1,D}$"	Deactivation rate constant "$k_{2,D}$"	Residual reactivity (mg CO_2/mg sorbent)
CaO from CaAc	0.317	0.148	0.202
CaO/Sf-25%-U	0.457	0.105	0.058
CaO/Sf-15%-U	0.704	0.109	0.038
CaO/Sf-5%-U	0.860	0.141	0.015
CaO/Sf-25%-SH	0.430	0.140	0.041
CaO/Sf-15%-SH	0.104	~$k_{1,D}$	0.027
CaO/Sf-5%-SH	-0.054	~$k_{1,D}$	0.031

The results reported in Table 5-1 show that rate constants $k_{1,D}$ and $k_{2,D}$ have reaction rate values with a trend $k_{1,D} > k_{2,D}$. This finding is consistent with results expected from the double exponential model: $k_{1,D}$ for the fast carrying capacity loss, whereas $k_{2,D}$ for the slow stage. As expected, $k_{1,D}$ values increased as the amount of CaO loaded decreases. This effect is caused as high contents (25 wt. % samples) loss porosity gradually as a function of the number of carbonation-calcination cycles, whilst in thinner coatings (15 wt. % and 5 wt. %), unstable pores collapse under a shorter time. Therefore, the residual reactivity in CO_2 sorbents loaded with CaO percentages below 25% is reached earlier than CaO/Sf-25%-U or CaO/Sf-25%-SH. The residual reactivity analysis indicates that carrying capacities were near constant after cycle 30, and thus, for practical purposes these values correspond to their uptake capacity.

5.2.3 Performance of CaO/Sf-%-Oct sorbents in multiple carbonation-decarbonation TGA cycles

The carrying capacity evolution over 30 recarbonation/decarbonation cycle of CaO/Sf-%-Oct sorbents with loadings of 5, 15 and 25 wt. % of the CaO in the presence of a CO_2-rich mixture (90% CO_2/10% N_2) are presented in Figure 5-14. The results shown in Figure 5-15 reveals that the capture process of CaO/Sf-%-Oct sorbents is also conducted in two stages: a rapid superficial

reaction with a >70% weight rise during the first minute, followed by a regime governed by diffusion. The analysis of cycle 1 and 30 reveals slight changes in the diffusion-limited regime throughout the uptake trials. By cycle 30, the CO_2 sorption is apparently completed in the 45 min of carbonation, whereas in cycle 1, diffusion is still in progress after alike carbonation time.

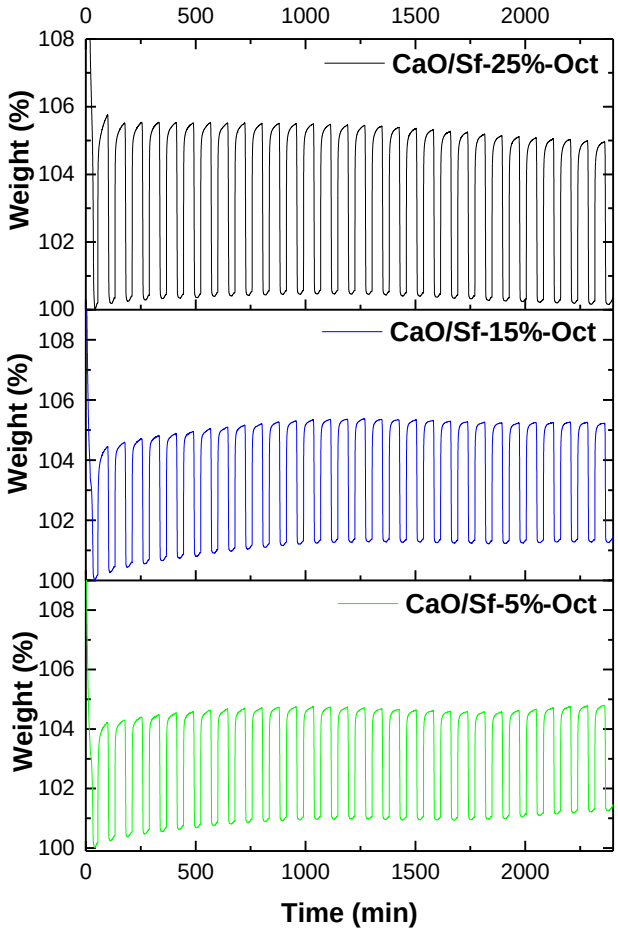

Figure 5-14. Multicycle TGA profiles of CaO/Sf-%-Oct sorbents carried out using a carbonation temperature of 650 °C for 45 min and a gaseous mixture composed by 90% CO_2 with N_2 as balance. The decarbonation stage involved 10 min dwell time at 850 °C.

The experimental carrying capacities for samples CaO/Sf-%-Oct with 25, 15 and 5 wt. % are exhibited in Figure 5-16. The multicycle TGA results showed that the maximum uptake capacities were observed in cycle 1, with 0.039, 0.042 and 0.056 mg CO_2/mg Sorbent for 5, 15 and 25 wt. % CaO loadings, respectively. Upon cycling the different CaO/Sf-%-Oct samples, ~13.5% was the highest relative uptake decay measured (Figure 5-16). The best performing sample over 30 cycles was CaO/Sf-5%-Oct, with an only ~5.7 %

reactivity decrease. The enhanced durability is attributed to the substrate clamping effect, homogeneous distribution of tensile forces through the interface CaO-Saffil and the octahedral morphology of the active phase. As anticipated, the octahedral shape of CaO particles contributes to inhibiting macroscopic strain (thermal expansion) stimulated by thermal stress, and thus, sintering on octahedral-like particle diminishes considerably [307]. Although the carrying capacity decay was low compared with Ca-Sa-%-WI, CaO/Sf-%-U, and CaO/Sf-%-SH samples, densification on unattached particles would also contribute on the deactivation (with a stronger effect in sorbents with high CaO loadings as per observed through the SEM image of Figure 4-11).

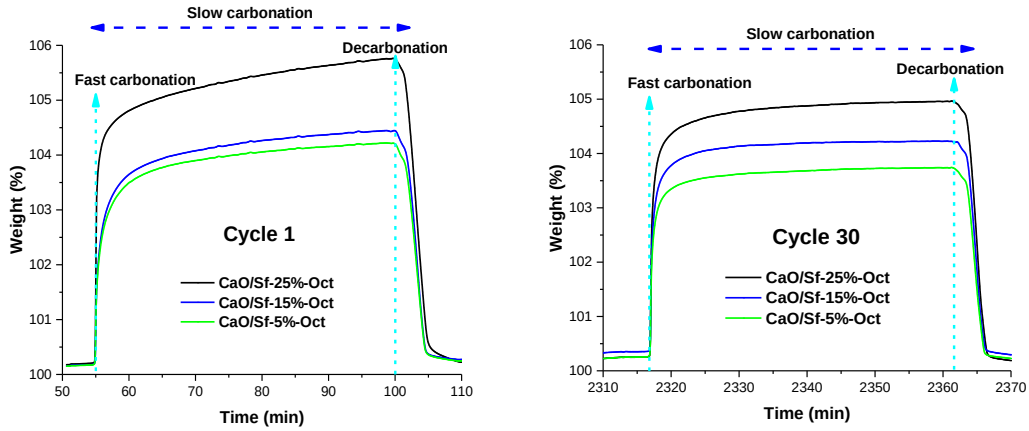

Figure 5-15. Isothermal carbonation-decarbonation TGA profiles of cycles 1 and 30 for the CaO/Sf-%-Oct sorbents (Carbonation, 650 °C in 90% CO_2; decarbonation, 850 °C in pure N_2).

According to the uptake capacities shown in Figure 5-16, residual reactivity in samples CaO/Sf-%-Oct was not predicted because the deactivation trend was less severe. The results showed that the capture capacities were stable after cycle 25 in ~0.048, ~0.039, and ~0.035 mg CO_2/ mg Sorbents for sorbents with 25, 15 and 5 wt. %, respectively, and thus, these values are associated with the residual capacities.

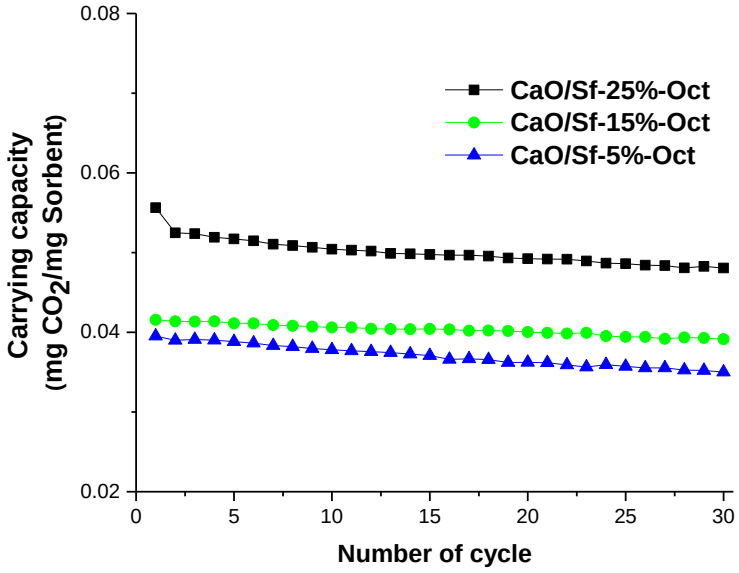

Figure 5-16. Carrying capacities of CaO/Sf-%-Oct sorbents estimated over 30 continuous uptake cycles.

5.2.4 Performance of CaO-Saffil sorbents in CO_2 capture cycles performed at shorter carbonation periods (15 min)

In the previous sections, results of performance and durability of CaO-Saffil sorbents tested over multicycle TGA trials using carbonation periods of 45 min were shown. However, in practical applications (large-scale chemical operations), a shorter carbonation time would be a more realistic benchmark as CaO-based sorbents have short contact times with CO_2 molecules [308, 309]. In theory, a fast carbonation would produce low degradation of sorbents in the course of the carbonation-decarbonation cycles.

On the basis of practical parameters, additional CO_2 uptake experiments were performed under narrower carbonation slots of 15 min but with comparable conditions to the 45 min experiments. Multicycle TGA data of the most representative CaO loading (25 wt. %) of the four families sorbents were used as a benchmark to study the effect of carbonation time (Figure 5-17). The results illustrate that there is a slight difference in capture capacity of sorbents Ca-Sa-%-WI, CaO/Sf-%-U, CaO/Sf-%-SH, and CaO/Sf-%-Oct tested over 45 min and 15 min. This is attributed to the weight percentage gained by the

diffusion-limited regime after the first 15 min of carbonation. According to the results, comparable sorption rates in both the chemical reaction and diffusion-controlled regime were observed compared to samples evaluated in 45 min. The fast carbonation involved ~ 70% mass gain in the first 2 min, followed by a slower diffusion process. In terms of durability, comparable deteriorations were predicted in samples Ca-Sa-25%-WI evaluated in 45 and 15 min, with ~60 and ~57% reactivity decays respectively. For CaO/Sf-25%-U sorbents performed with 15 min carbonation, ~60% deactivation over 30 cycles was measured. The relative reactivity decays of sorbents CaO/Sf-25%-SH and CaO/Sf-25%-Oct tested with carbonation slots of 15 min were ~10% and ~4%, respectively. Multicycle TGA trials revealed a slight difference of CaO-Saffil sorbents evaluates with carbonation periods of 45 min and 15 min. On the basis of other studies performed by other authors, it has been demonstrated that carbonation time had a minor impact on deactivation, and thus, consistent results of durability for both 15 and 45 min were found [188, 310].

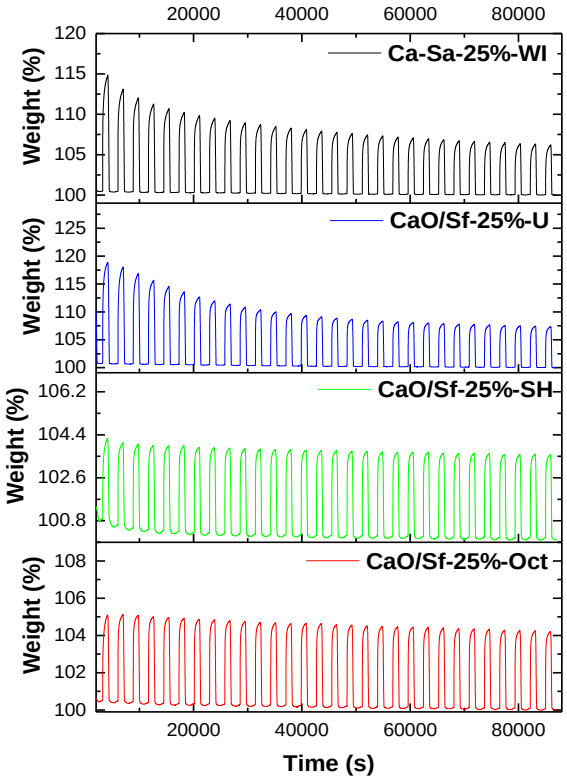

Figure 5-17. Multicycle TGA profiles of samples Ca-Sa-%-WI, CaO/Sf-%-U, CaO/Sf-%-SH, and CaO/Sf-%-Oct with loadings of 25 wt. % performed with 15 min carbonation and 10 min decarbonation. Operational parameters comparable with previous uptake experiments: carbonation stage carried out at 650 °C in presence of a gaseous mixture composed of 90% CO_2/10% N_2, followed by decarbonation at 850 °C in pure N_2.

5.3 Characterization of sorbents post CO_2 uptake trials

5.3.1 Morphological changes in Ca-Sa-%-WI sorbents derived from CO_2 uptake experiments

Multicycle carbonation-decarbonation tests performed to evaluate the performance of Ca-Sa-%-WI, CaO/Sf-%-U and CaO/Sf-%-SH sorbents revealed relative reactivity decays of ~23% to ~69% on samples with loadings of 15 and 25 wt. %. The effects of calcination temperature on the carrying capacity and durability of tested sorbents were examined using SEM technique. On the basis of high magnification SEM micrographs of the Ca-Sa-%-WI sorbent with a loading of 25 wt. %, microstructural transformations were observed in detached agglomerates (Figure 5-18-(a)-(b)). The surface morphology of freestanding particulates was rough and open pores were found. As expected, high calcination temperatures induced the loss of fine pores, whereas volumetric expansion, the formation of large cracks of 1-4 μm (Figure 5-18-(a)-(b)). These transformations on detached CaO particulate in CaO-Saffil sorbents, were comparable with microstructural changes (cracks of ~1 μm) on powder sorbents tested over 20 carbonation-calcination cycles reported by Fennel et al. [195]. In the research work of Lysikov et al., which was aimed to enhance the carrying capacity of CaO-based sorbents by studying the influence of the CaO precursor, comparable textural transformations with those of Figure 5-18-(a)-(b) were detected [196]. It must be mentioned that Lysikov et al. attributed multicycle densification to the high temperature, CaO precursor, and duration of decarbonation. It must be highlighted that the sample Ca-Sa-15%-WI had similar morphological changes with Ca-Sa-25%-WI as a result of densification.

High-magnification micrographs of examined sorbents type Ca-Sa-%-WI with loadings of 25, 15 and 5 wt. % are displayed in Figure 5-19–(c) to (f). Figure 5-19 also includes SEM images (a) and (b) associated with untested Ca-Sa-%-WI sorbents with 25 and 15 wt. % that will be used as a benchmark for discerning potential changes between sorbents evaluated in 30 cycles and untested ones. Although CO_2 capture trials carried out with carbonation times

of 15 min provided evidence on the deactivation of Ca-Sa-%-WI sorbents, SEM analysis confirms this robust deterioration is mainly associated with sintering of detached agglomerates (Figure 5-19–(c) to (f)). The improving residual capacity compared to CaO without Saffil is confirmed by the outstanding thermal stability displayed in CaO coatings (anticipated to arise as a result of mechanical clamping effect), which improved for thin coatings (Figure 5-19–(c) to (e)). Fibres of CaO-Saffil sorbents with loadings of 25, 15 and 5 wt. % scanned at high-magnification reveals that the distribution of nanoflakes over the Saffil surface allied with inter-flake distances reduced the sintering produced by volumetric changes in the reversible transformation of CaO to $CaCO_3$ (SEM images of panels (c) to (e) in Figure 5-19).

For the thinnest 5 wt. % coating, improved durability demonstrated in the course of multicycle carbonation-decarbonation cycles was consistent with enhanced resistance shown by nanoflakes in Figure 5-19-(e). Hence, the ~30% reactivity decay measured for the Ca-Sa-5%-WI sample, which were significantly low compared to ~60% decline on the sample 25 wt. %, is explained through the SEM micrograph of a fiber termination shown in Figure 5-19–(f). This image revealed a small area on the edge of a coated fibre in which nanoflakes presented lateral shrinkage, and thus, microstructural changes on the coatings.

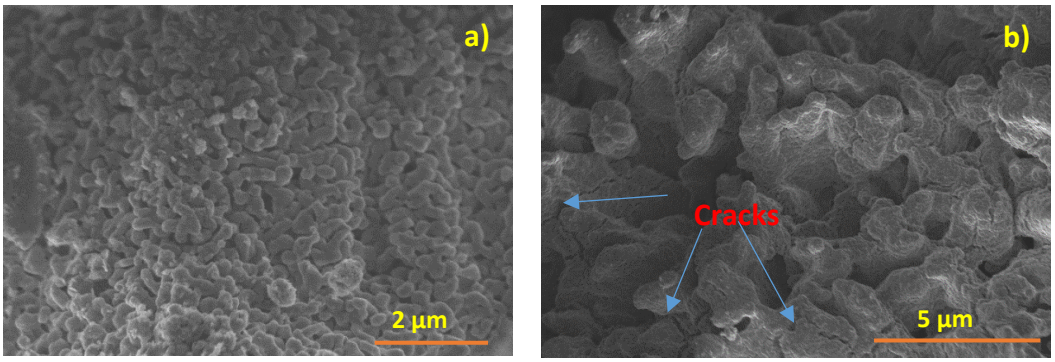

Figure 5-18. (a) High-magnification SEM images of CaO agglomerates and b) cracks of 1-4 µm formed on sintered CaO agglomerates.

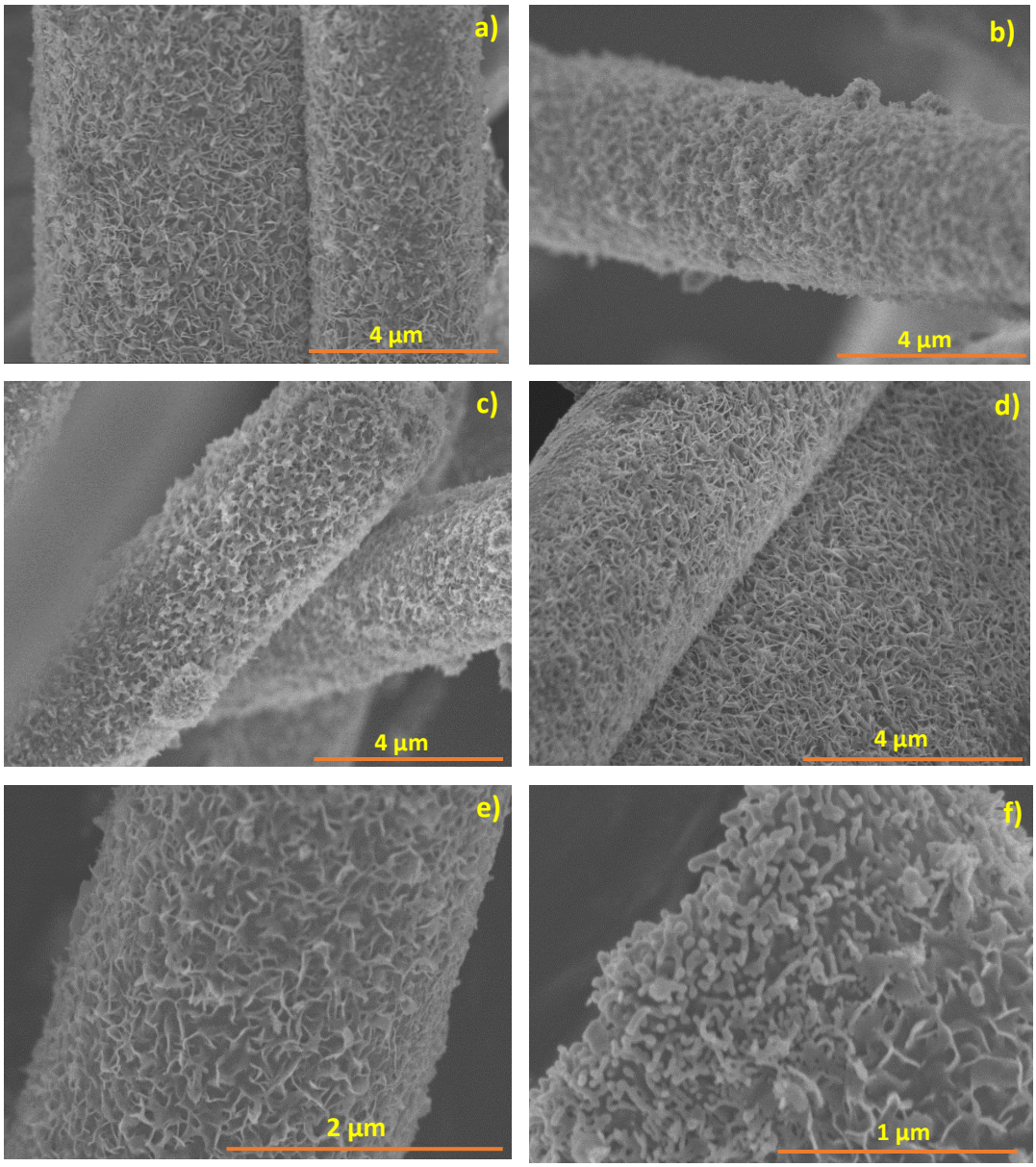

Figure 5-19. a) and b) SEM micrographs of untested Ca-Sa-%-WI sorbents with loadings of 25 and 15 wt. %, respectively. c), d) and e) Examined samples of Ca-Sa-%-WI sorbents with 25, 15 and 5 wt.% of CaO, respectively, and f) high-magnification image of the sample Ca-Sa-5%-WI with a coated area affected by sintering.

5.3.2 Morphological and microstructural changes in sorbents Ca-Sa-%-U and Ca-Sa-%-SH produced post multicycle trials

The effect of microstructural and morphological changes on the multicycle performance of CaO/Sf-%-U sorbents were examined using SEM (Figure 5-20 and Figure 5-21). Micrographs of CaO/Sf-25%-U samples registered before (Figure 5-20-(a)) and after (Figure 5-20-(b)) performing multicycle TGA trials allowed to discern densification on freestanding agglomerates caused by the

high temperature used to regenerate the active phase (unsupported CaO). According to the image presented on the panel (b) of Figure 5-20, in the course of 30 uptake cycles, freestanding particles lost both fine pores and surface roughness compared to fresh sorbents (Figure 5-20-(a)). These transformations visualized in the high-magnification image (b) associated with the spent sorbent confirm the high degree of sintering experienced (Figure 5-20-(b)). The scanned area confirmed severe structural shrinkage at the surface of the aggregates, with resulted in the formation of grains with sizes of ~100 nm and non-porous areas. Although the external surface is accessible for a fast reaction, sintering drastically limits the carrying capacity because this loss of small pores restrict the diffusion of CO_2 toward the bulk of the aggregates. In addition, densification also contribute in the decline of available active surface area. On the basis of the study reported by Manovic and Anthony, these textural changes are more pronounced at the surface of the particle compared to the interior because of surface thermal tension [311]. These results were similar in CaO agglomerates of the CaO/Sf-%-U sample with 15 wt. % coating. There would also be a minor contribution to performance decay because of densification on nanoflakes coatings (Figure 5-21).

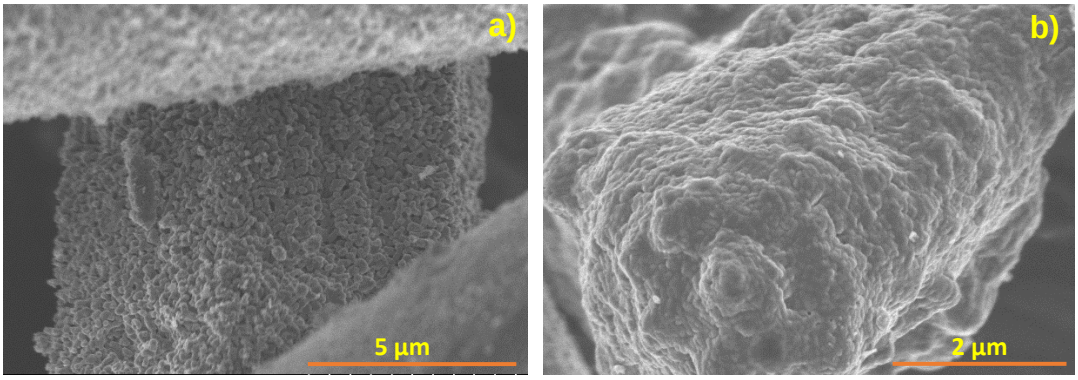

Figure 5-20. (a) and (b) High-magnification SEM micrographs of freestanding agglomerates before and after multicycle trials found in samples of the CaO/Sf-25%-U sorbent, respectively. CaO agglomerates present high degree of densification produced in the course of 30 carbonation-decarbonation cycles.

The SEM study carried out to confirm the benefits of substrate clamping effect on CaO/Sf-%-U sorbents is displayed in panels (a) to (d) of Figure 5-21. The presence of coatings with minimal sintering after 30 continuous uptake cycles

confirms a high thermal resistance, which in relation to detached agglomerates, was strongly improved by the incorporation of Saffil substrates (Figure 5-21-(a) to (c)).

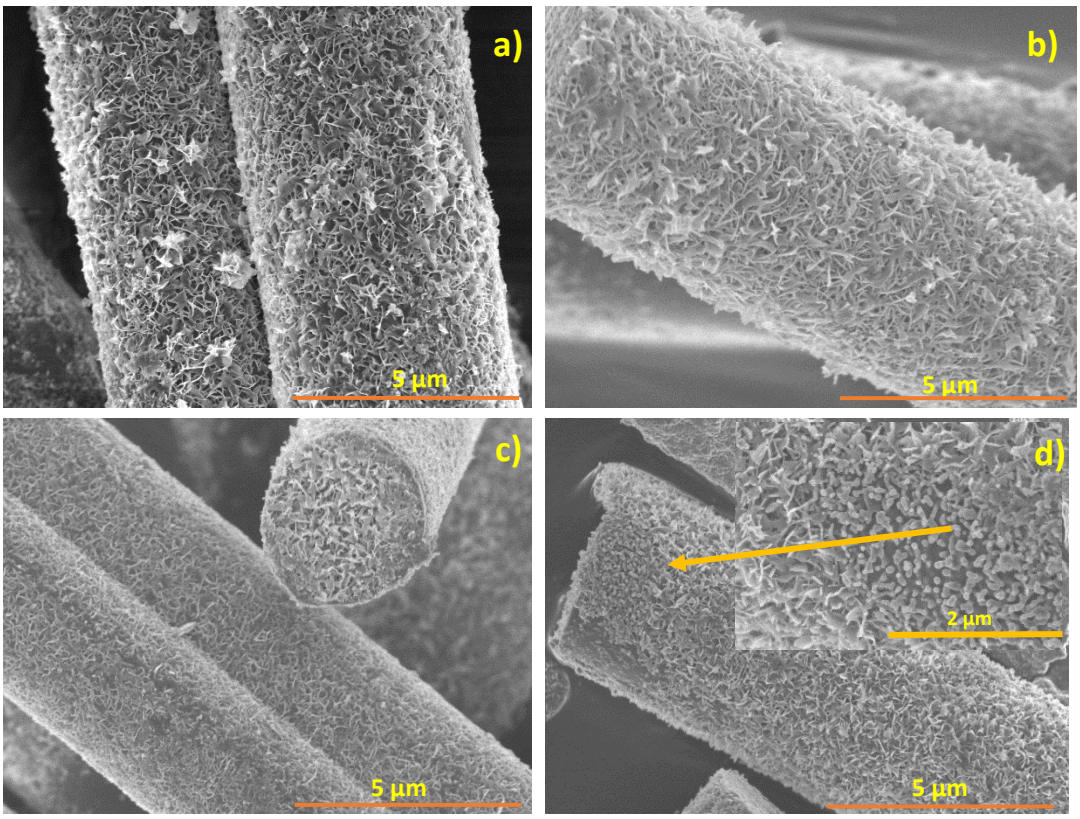

Figure 5-21. High-resolution SEM images registered after cycling the Ca-Sa-25%-U sorbent: a) Ca-Sa-25%-U s, b) Ca-Sa-15%-U, c) Ca-Sa-5%-U and d) coated fiber of the Ca-Sa-25%-U sample with sintered edges.

As mentioned before, the clamping effect is more effective on thin coatings, and thus, in samples with high loadings, there would be a higher probability of lateral shrinkage by the effect of the sintering. The vulnerability of thick coatings is exhibited in the high-resolution SEM micrograph of the CaO/Sf-25%-U sample shown in Figure 5-21-(d). This image illustrates fibre ends with a coated area of ~2.5 µm deteriorated by densification after 30 continuous uptake/desorption cycles. It must be mentioned that coated areas affected by sintering represented a small proportion of the fibre coating, and thus, the influence in the uptake capacity decline is much lower compared to detached aggregates. These results are consistent with studied samples of lower loadings, namely 15 and 5 wt. %. In summary, the SEM findings showed that

carrying capacity loss above 60% in CaO/Sf-%-U sorbents was produced by volumetric densification in freestanding CaO agglomerates as well as on coated areas, but in a minor proportion.

In relation to CaO/Sf-%-SH sorbents tested throughout 30 CO_2 sorption-desorption cycles, results of the microscopy characterization of samples with 25, 15 and 5 wt. % are shown in Figure 5-22. On the basis of multicycle carrying capacity results, capacity depletions below 30% in sorbents CaO/Sf-%-SH were attributed to sintering of micrometer particles (0.3-1 µm) deposited over the surface of Saffil fibres. Although these aggregates have a large area attached to the substrate, clamping effect benefits are lessened by the thickness of these agglomerates (Figure 5-22–(a) and (b)). As illustrated in SEM micrographs of panels (c) and (d), the number of agglomerates decreases as the weight percentage of CaO impregnated reduces, and thus, multicycle deterioration by sintering is also diminished. This is in conformity with lower deactivations measured for sorbents CaO/Sf-15%-SH and CaO/Sf-5%-SH compared to the sorbent CaO/Sf-25%-SH (Figure 5-22–(c) and (d)).

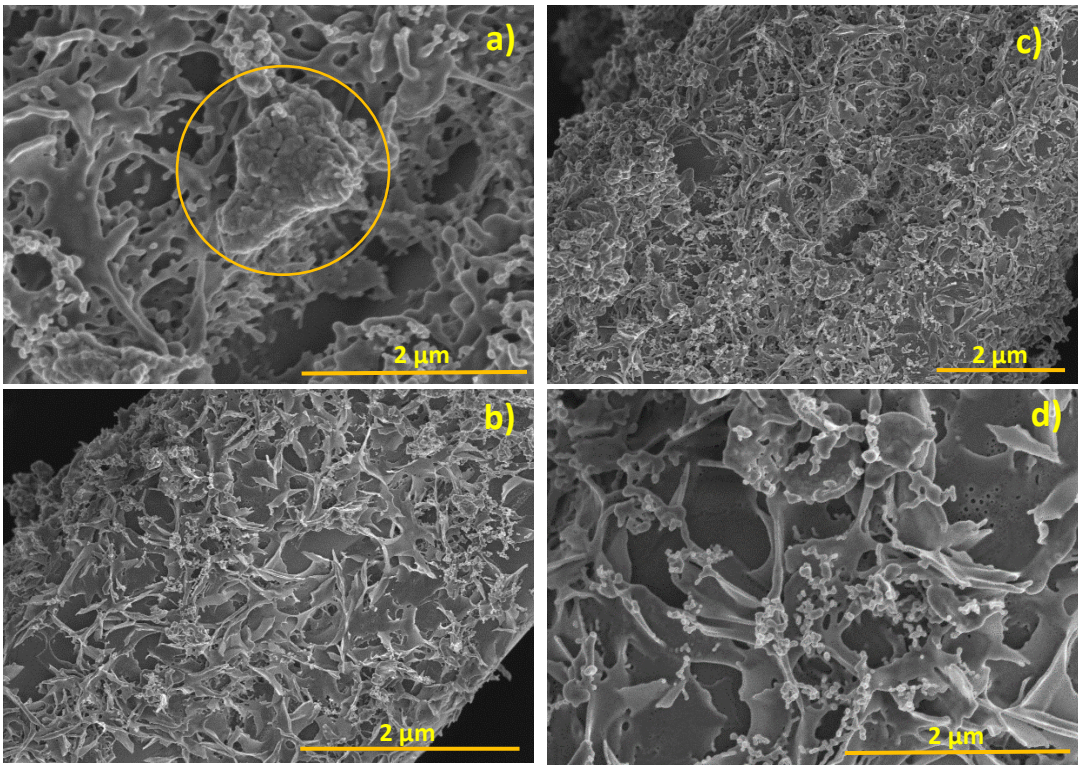

Figure 5-22. Morphological evolution of sorbents throughout 30 carbonation-decarbonation cycles: a) and b) SEM micrographs of the Ca-Sa-25%-SH sorbent collected at different magnifications, c) Ca-Sa-15%-SH sorbent and d) Ca-Sa-5%-SH sample.

5.3.3 Microstructural changes exhibited by CaO/Sf-%-Oct sorbents after multicycle CO_2 uptake tests

The low deactivation in CaO/Sf-%-Oct sorbents observed in the course of 30 carbonation-decarbonation cycles was also explained through high-resolution micrographs registered by SEM (Figure 5-23). Images displayed in panels (a) to (d) of sorbents with loadings of 25, 15 and 5 wt. % showed that CaO octahedra were highly resistant to sintering in the course of the 30 uptake/desorption trials. Although volume expansion due to the CaO-CO_2 reaction is significant, CaO octahedra remained without important morphological changes (Figure 5-23-(a) to (d)).

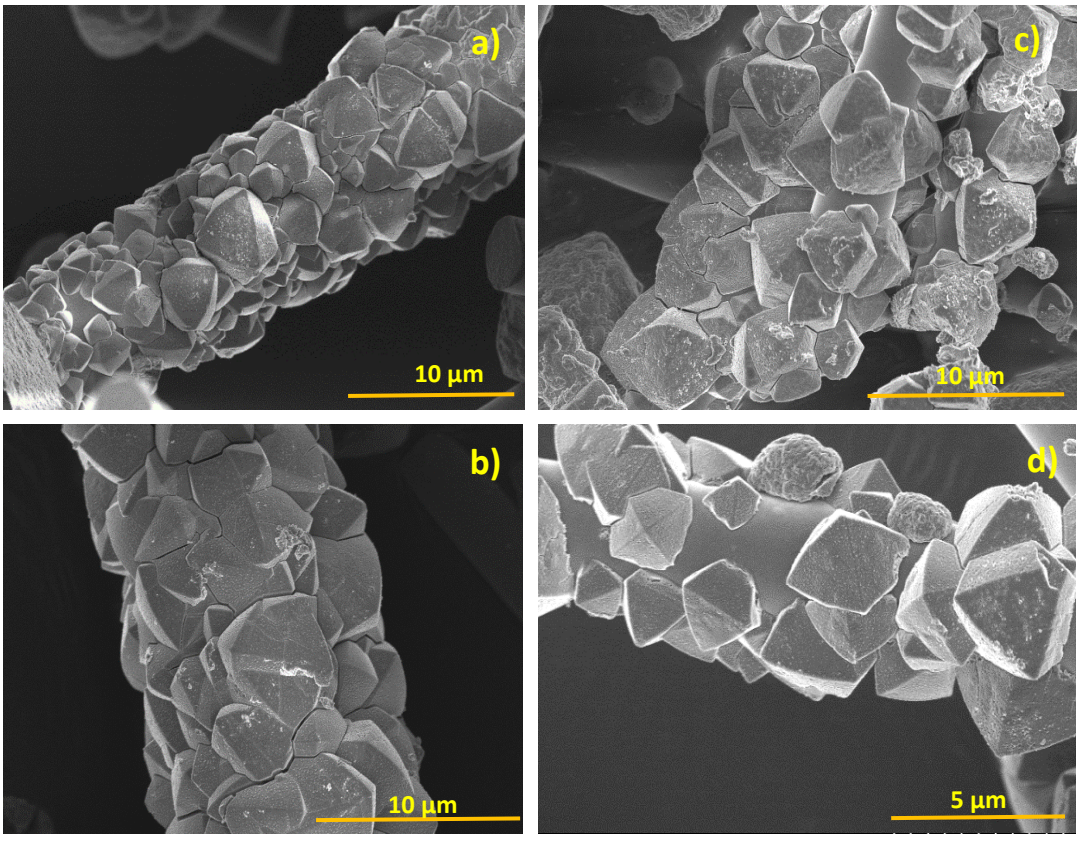

Figure 5-23. Sorbents tested in TGA carbonation-calcination cycles using carbonation times of 45 min in presence of a mixture composed of 90% CO_2/10% N_2: (a) and (b) CaO/Sf-25 %-Oct, (c) CaO/Sf-15 %-Oct, and (d) CaO/Sf-5 %-Oct.

High-magnification SEM images of cycled CaO/Sf-25%-Oct and CaO/Sf-15%-Oct samples shown that large cracks on the facets of the octahedral particles arose after the 30 carbonation-calcination cycles (Figure 5-24-(a), (b) and (c)). Although the cracks were propagated across the faces, octahedral particles

were not detached from the substrate because of the strong interfacial bond between CaO and Saffil. It is imperative to mention that octahedral particles with sizes above ~3 µm were more sensitive to changes in volume and high temperature. The SEM image of Figure 5-24-(c) confirms high thermal stability in small octahedral particles, which was apparently enhanced because of the minor shrinkage of Saffil at 850°C (as anticipated through technical information provided by the Saffil mat supplier, UNIFRAX). This SEM image also reveals aperture of fine pores arisen as a result of the “self-activation” phenomenon, which on the basis of documented investigations, was produced by the temperature to regenerate CaO [205].

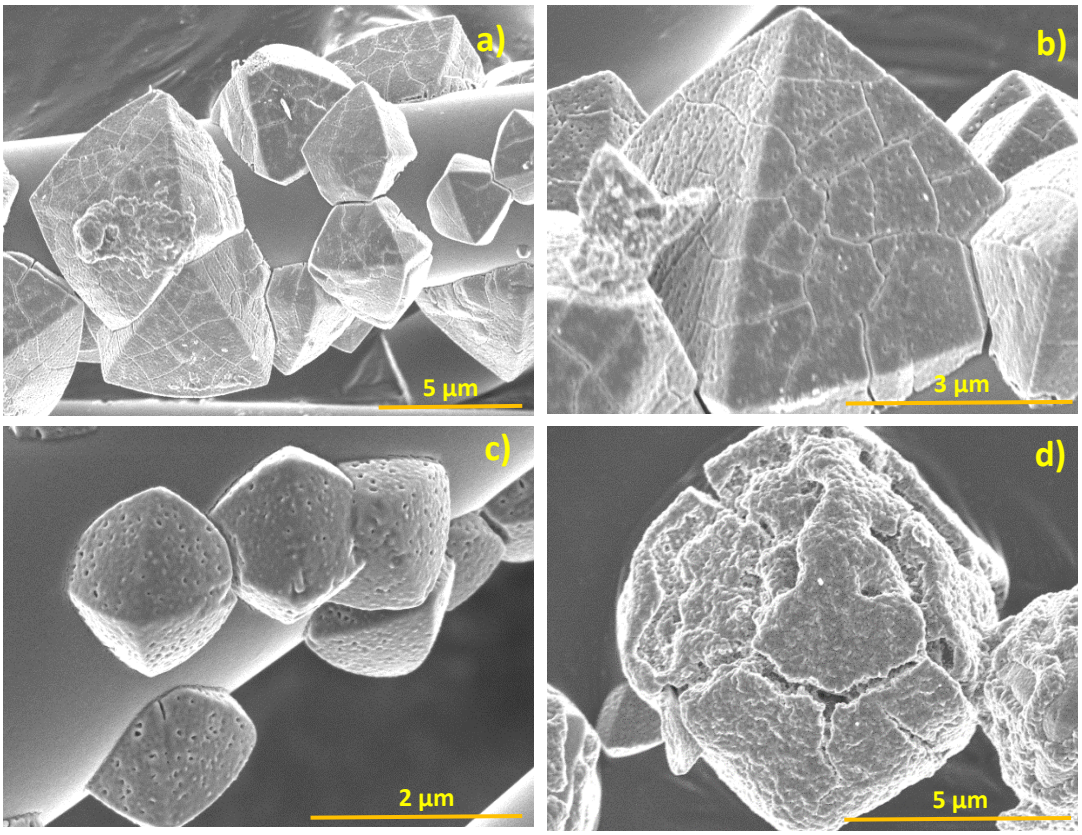

Figure 5-24. (a) and (b) SEM micrographs of CaO/Sf-25%-Oct and CaO/Sf-15%-Oct sorbent shown cracks formed throughout 30 uptake cycles, c) octahedra of ~2-3 µm with high-thermal stability and d) freestanding octahedron fractured by thermal stress.

Benefits of incorporate Saffil as a stabilizer of CaO are evident in the SEM image of the CaO/Sf-25%-Oct sample displayed in Figure 5-24-(d). This illustrates that without Saffil supports, thermal and mechanical stability of CaO octahedra reduced, and thus, fractures with different propagation sizes arise.

The detached octahedron presented on the SEM micrograph of Figure 5-24-(d), which has a cross-section dimension above ~6 µm, showed also strong deterioration by densification, and thus, loss of mesopores. Hence, it was confirmed that Saffil supports allied with clamping effect contributed to the increased mechanical resistance of octahedral particles.

On the basis of the SEM study, multicycle deactivations of ~5.7%-13% measured in CaO/Sf-%-Oct samples was mainly attributed to sintering of freestanding octahedra and in minor proportion, on CaO octahedra clamped over Saffil fibres. The results indicate that the CaO/Sf-5%-Oct sorbent had a lower relative decay over 30 cycles because of a smaller presence of freestanding octahedra. It must be mentioned that albeit the sintering produces a decline in the capture capacity of these unattached octahedra, the large cracks minimise this impact by allowing a faster diffusion of CO_2 towards the interior of the particle as well as maximizing the available surface area.

5.3.4 Performance of CaO-Saffil sorbents compared to other leading CaO-based CO_2 sorbents reported in the literature

Carbonation-calcination TGA experiments of CaO-Saffil sorbents revealed that the highest capture capacity was ~0.06 mg CO_2/mg Sorbent in the CaO/Sf-25%-U sorbent over 30 continuous cycles whilst the CaO/Sf-5%-Oct sorbent had the lowest degradation with only ~5.7%. Although the maximum uptake capacities in CaO-Saffil samples with 25 wt. % were apparently modest, they still comparable with residual capacities of 0.055-0.063 mg CO_2/mg Sorbent of natural CaO-based sorbents with high percentages of CaO (results of samples tested in a wide range of parameters) [225]. In terms of carrying capacity, albeit Ca-Sa-25%-WI and CaO/Sf-%-U sorbents had significant deactivations, >10% reactivity compared to natural CaO (>85% degradation) was enhanced by incorporating Saffil fibres as supports of CaO. As discussed early, the presence of Saffil supports improve the thermal and mechanical stability of CaO by promoting a uniform distribution of tensile forces throughout the interface CaO-Saffil. In addition, Saffil substrates

contribute with the clamping effect in which lateral shrinkage of CaO is avoided by restricting densification.

In the literature, nano CaO/Al_2O_3 sorbent have been documented as one of the most promising sorbents for CO_2 capture applications at high temperature [312]. Although the $CaO/ Ca_{12}Al_{14}O_{33}$ sorbent has an outstanding performance, its synthesis comprises a very complex methodology in which a mixture of aluminium sol, hexametaphosphate and nano calcium carbonate are blended to form an active powder. This co-existing $CaO\text{-}Ca_{12}Al_{14}O_{33}$ (mayenite) phases formed retained ~67% of capacity in the course of 50 carbonation-decarbonation performed under comparable conditions to CaO-Saffil sorbents tested in this work [312]. This durability was similar to the Ca-Sa-5%-WI sorbent but lower in relation with CaO/Sf-%-SH and CaO/Sf-%-Oct samples with 25, 15 and 5 wt. %. The CO_2 uptake analysis carried out over 25 uptake cycles revealed that synthetic $CaO/Ca_{12}Al_{14}O_{33}$ is able to capture ~0.2 mg CO_2/mg Sorbent and preserve this performance for the first 12 cycles [312]. The 75-85% CaO loadings permitted for greater capture capacity than CaO-Saffil sorbents tested in the current investigation.

Multicycle durability of CaO-Saffil sorbents was also comparable with other synthetic CaO-based sorbents prepared with La_2O_3 or Ca_2MnO_4 co-existing phases. TGA carbonation-calcination experiments indicate that carrying capacities of sorbents $CaO:La_2O_3$ and $CaO:Ca_2MnO_4$ decay >50% during 30 cycles, but maintains a downward trend as cycles proceed [313]. By cycle 100, more than 74% of uptake capacity was lost by both sorbents. Although this sorbent retained 0.2 ± 0.02 mg CO_2/mg Sorbent, which is much higher because of the higher CaO contents (composition: 80% CaO/ 20% support), their durability was overcome by the Ca-Sa-5%-WI sample and CaO/Sf-%-SH and CaO/Sf-%-Oct sorbents with 5-25 wt. %. In terms of simplicity of preparation, CaO-Saffil sorbents were prepared using conventional routes with very direct methodologies that implied a limited number of steps and operation units, whilst powder composites $CaO:La_2O_3$ and $CaO:Ca_2MnO_4$ by an expensive process and with high technological requirements as is the sol-gel method (synthesis conditions). On the same bases of simplicity, synthesis flexibility of CaO-Saffil sorbents compared to other documented sorbents

obtained under strict, complex and expensive methods as is flame spray pyrolysis suggest that CaO-Saffil sorbents are worthy of further development [314]. Comparison to other alternative CO_2 sorbents are accessible in refs [304, 315]

5.4 Conclusion

Study of performance and durability of CaO-Saffil sorbents was carried out in the present chapter. The carbonation/calcination TGA experiments aimed to determine the carrying capacity of the as-prepared sorbents were performed using carbonation slots of 45 or 15 min (benchmark to demonstrate potential for industrial applications), whilst decarbonation for 10 min. The carbonation-decarbonation reactions were performed in 90% CO_2/10% N_2 and pure N_2, respectively.

In terms of multicycle performance, the greatest carrying capacities were obtained in CaO-Saffil sorbents with CaO loadings of 25 wt. %. According to measurements of cycle 1, sorbents Ca-Sa-25%-WI and CaO/Sf-25%-U exhibited initial uptake capacities of 0.118 and 0.19 mg CO_2/mg Sorbent, respectively, but declined to ~0.05 and ~0.06 mg CO_2/mg Sorbent after 30 carbonation-decarbonation cycles. These results indicate that the high capture capacity observed in sorbents densely coated with 15-25 wt. % compromised ~50-68% of durability. The 5 wt. % CaO loading produced the lowest reactivity decay in multicycle uptake experiments, with a ~30% deterioration in the course of 30 continuous cycles. Although the Ca-Sa-5%-WI sorbent have extended stability compared to unsupported CaO (80-85% capacity decay), its residual carrying capacity was modest, namely ~0.012 mg CO_2/mg Sorbent. In relation to sorbents CaO/Sf-%-SH and CaO/Sf-%-Oct, 25 wt. % loadings were the best performing with initial capture capacities of 0.059 and 0.056 mg CO_2/mg Sorbent, respectively. By cycle 30, these sorbents retained more than 70% of carrying capacity, but despite enhanced stability, their residual reactivity is below sorbents Ca-Sa-25%-WI and CaO/Sf-25%-U. Although consistency with sorbents loaded in lower CaO amounts was seen,

this improved durability advocate that these type of sorbents are worthy of further development.

The SEM study confirmed that degradation over 30 carbonation-calcination cycles in sorbents Ca-Sa-%-WI and CaO/Sf-%-U with loadings 15 and 25 wt. % was produced by volumetric densification on freestanding agglomerates and in much less proportion on the CaO coatings. The improved consistency in sorbent performance of samples with loadings of 5 % was attributed to the improved effects of mechanical clamping and inhibition of sintering. These benefits were confirmed in CaO/Sf-%-SH and -Oct sorbents as deactivation was substantially improved by clamping the CaO or CaO octahedra on Saffil supports. In the particular case of CaO/Sf-%-Oct sorbents, octahedral morphology tailored contributed to improving the mechanical stability of CaO. In addition, the concept of using loosely entwined fibres to reduce the contact between adjacent fibres coated with CaO, and thus, maximize the interaction CO_2-CaO was apparently successful due to the improvement in multicycle durability. The results obtained in this chapter suggest that these as–prepared sorbents are promising candidates for their future implementation in SESR.

Chapter 6 Kinetic Study of the Carbonation Reaction in CaO-based Sorbents

This chapter presents a detailed kinetic study of the carbonation reaction on CaO-Saffil sorbents prepared by wet impregnation and precipitation methods. The thermo-kinetic analysis was conducted using the isothermal method. The trials were performed in a TGA apparatus within a temperature range of 550 to 625 °C. The rate constants were estimated by fitting conventional solid-state kinetic equations and a double exponential model over conversion curves predicted on the basis of isothermal data. The activation energies (kJ/mol) for both the chemical reaction and diffusion-controlled regime were determined applying the linear form of the Arrhenius equation. The kinetic study concludes evaluating the feasibility of the isothermal method by comparing the activation energies measured for the CaO-Saffil sorbents and other CaO-based sorbents reported in the literature.

6.1 Solid-state kinetic models for non-catalytic solid-gas reactions

A kinetic study of thermally controlled reactions in solid phase is performed here using well-established reaction models that fit experimental data conducted under isothermal or non-isothermal conditions. The governing kinetic equation that describe the disappearance of reactants and evolution of products is the differential expression presented in (6-1),

$$\frac{d\alpha}{dt} = k(T)f(\alpha)h(P) \qquad (6\text{-}1)$$

Where α is the fractional conversion of the reacting solid, $d\alpha/dt$ is the isothermal reaction rate, $k(T)$ is the temperature-dependent rate constant, $h(P)$ is a function that indicate pressure dependence (fundamentally based or empirical), and $f(\alpha)$ is also a function but corresponds to a reaction model that represents a particular process observed during the thermal

conversion [316]. The different behaviours described by the mathematical functions $f(\alpha)$ are: shrinking core (geometrical contraction models), intraparticle diffusion resistance (diffusion models), nucleation-growth processes, and distributed reactivity (reaction-order models). Other alternative models that can describe nucleation-growth mechanisms are Avrami-Erofeyev and Prout-Tompkins [316].

The solid-state kinetic models established to help interpreting the behaviour of an uncatalyzed reaction are categorized as acceleratory, deceleratory, linear and sigmoidal. In general terms, in the acceleratory models, as the reaction proceeds, the reaction rate ($d\alpha/dt$) increases. It must be pointed out that these trends are infrequent. In the deceleratory kinetic models, the reaction rate declines as a function of the reaction progress. In the case of sigmoidal models, they are composed of first, an acceleratory phase, followed by a deceleratory phase [317, 318].

The interest in evaluating the temperature dependence in reactions performed over solids materials leads the use of semi-empirical expressions like the Arrhenius equation (6-2):

$$k(T) = A * \exp^{(-E/RT)} \tag{6-2}$$

E = Apparent Activation energy

A = pre-exponential factor

R = gas constant

Although the Arrhenius expression has been disapproved of from the physical perspective by authors such as Garn [319], numerous theoretical studies and physical interpretations have demonstrated its suitability to gas-solid reactions. In the particular case of defining the temperature dependence in the thermal decomposition of solids, the Arrhenius equation has been a reliable path to describe physically such processes [318].

A major concern in the evaluation and interpretation of E and A comes from the source of data acquisition. Nowadays, available conventional techniques such as differential scanning calorimetry (DSC) and thermogravimetric

analysis (TGA)) lack the capability in identifying the elementary reactions taking place. Hence, the kinetics parameters estimated using thermal analysis methods provide a global rate for the ensemble of reaction intermediates not considered. Thus, the Arrhenius constants and activation energies are considered effective only when the prediction is complemented with supplementary data [318, 320]. On the basis of TGA data, the fractional conversion α is given by the formula (6-3):

$$\propto = \frac{m_{in} - m_t}{m_{in} - m_f} \tag{6-3}$$

where m_{in} and m_f are the initial and final weight of the sample, whilst m_t corresponds to the current weight at time t. In the attempt of developing expressions for identifying kinetic rate constants, a non-isothermal method that implies heating samples at constant rates was proposed. Based on this concept, a transformation of equation (6-1) was performed. The term $d\alpha/dt$ was substituted by $d\alpha/dT$ as shown in equation (6-4):

$$\frac{d\alpha}{dT} = \frac{d\alpha}{dt}\frac{dt}{dT} \tag{6-4}$$

The term $d\alpha/dT$ represents the non-isothermal reaction rate, $d\alpha/dt$ is the conventional isothermal reaction rate and dT/dt corresponds to the heating rate that can be substituted by β. Setting those variables in equation (6-1) and incorporating (6-2), the result is the expression displayed below (equation (6-5)),

$$\frac{d\alpha}{dT} = \frac{A}{\beta} e^{(-E/RT)} f(\alpha) \tag{6-5}$$

Equation (6-5) gives the differential form of the non-isothermal rate law. Rearranging and integrating equations (6-1) and (6-5) give rise to rate law expressions applicable to isothermal and non-isothermal processes ((6-6) and (6-7)) respectively. The term $g(\alpha)$ is the integral reaction model and is defined by the equation (6-8).

$$g(\alpha) = Ae^{(-E/RT)}t \qquad \text{(Isothermal)} \tag{6-6}$$

$$g(\alpha) = \frac{A}{\beta}\int_0^T e^{(-E/RT)}dT \qquad \text{(non-isothermal)} \tag{6-7}$$

$$g(\alpha) = \int_0^\alpha \frac{d\alpha}{f(\alpha)} \tag{6-8}$$

The main assumption when including equation (6-5) into (6-6) is the reaction kinetics of that the conversion from reactants to products is not affected by the change of experimental conditions from isothermal to non-isothermal. Evidently, this mathematical inference can be reasonable for reactions with a single step, whereas those with many steps carry additional implications [317].

Non-isothermal methods conducted by thermal techniques have been gaining relevance as they have the capability to address problems arising from data acquisition under isothermal conditions. For instance, in so called isothermal conditions, there is the inevitable non-isothermal lapse before reaching the optimal temperature fixed for the analysis, this may result in a partial conversion of the sample being tested. Therefore, these early transformations most probably affect the kinetic parameters subsequently calculated in so called isothermal conditions. This effect may be more prominent in measurements conducted over samples exposed to high temperatures. In the isothermal experiments of the kinetic study on the as-prepared sorbents, any potential transformation during the non-isothermal lapse was minimized by means of the TGA instrument utilized. More details are presented in the section concerning the experimental setup.

In regards to the estimation of the Arrhenius parameters, kinetic parameters calculated on the basis of isothermal and non-isothermal data regularly present inconsistencies with each other [318]. A foundation of this disagreement is the selection of a proper model able to describe the shape of the conversion vs. temperature curves resulting from experimental isothermal data (Table 6-1 includes algebraic $f(\alpha)$ and $g(\alpha)$ equations used for model fitting). The complexity of a reaction mechanism also contributes to inconsistencies due to parallel reactions despite model-fitting methods only being able to extract one set of rate parameters [321]. Thus, the nature of

these methods restricts their application for the study of an overall process in which the reconstruction of the reaction mechanism is not a priority. Although there are exceptions in which the Arrhenius parameters obtained from non-isothermal TGA data are in agreement with the values extracted from isothermal data, they could be the result of a fortuitous analysis [318].

With regards to isoconversional methods, despite having been designed on the basis of mechanistic assumptions, they exclude the use of solid-state kinetic models (termed also as model-free methods) to predict the kinetic parameters. Isoconversional methods were proposed in the 70's and authors such a Friedman, Ozawa, Flynn, Wall contributed substantially in the development of the differential method or with informative discussions related to the integral method [316, 317, 321].

Table 6-1. Solid-state kinetic models with integral/differential algebraic expressions for functions $\boldsymbol{f(\alpha)}$ and $\boldsymbol{g(\alpha)}$ [321-323].

Name of the Model	Differential form $\boldsymbol{f(x) = \frac{1}{k}\frac{d\alpha}{dt}}$	Integral form $\boldsymbol{g(x) = kt}$
Nucleation Models including sigmoidal rate equations		
Power law (P2)	$2\alpha^{1/2}$	$\alpha^{1/2}$
Power law (P3)	$3\alpha^{2/3}$	$\alpha^{1/3}$
Power law (P4)	$4\alpha^{3/4}$	$\alpha^{1/4}$
Avrami-Erofeyev (A2)	$2(1-\alpha)\left[-\ln(1-\alpha)^{1/2}\right]$	$[-\ln(1-\alpha)]^{1/2}$
Avrami-Erofeyev (A3)	$3(1-\alpha)\left[-\ln(1-\alpha)^{2/3}\right]$	$[-\ln(1-\alpha)]^{1/3}$
Avrami-Erofeyev (A4)	$4(1-\alpha)\left[-\ln(1-\alpha)^{3/4}\right]$	$[-\ln(1-\alpha)]^{1/4}$
Prout-Tompkins (B1)		$\ln[\alpha/(1-\alpha)] + c^{a}$
Geometrical Contraction Models		
Contracting area (R2)	$2(1-\alpha)^{1/2}$	$1-(1-\alpha)^{1/2}$
Contracting volume (R3)	$3(1-\alpha)^{2/3}$	$1-(1-\alpha)^{1/3}$
Diffusion models		
1-D diffusion (D1)	$1/(2\alpha)$	α^{2}
1-D diffusion (D2)	$-[1/\ln(1-\alpha)]$	$\left((1-\alpha)\ln(1-\alpha)\right)+\alpha$
1-D diffusion-Jander (D3)	$\left[3(1-\alpha)^{2/3}\right]/\left[2(1-(1-\alpha)^{1/3})\right]$	$(1-(1-\alpha)^{1/3})^{2}$
Ginstling-Brounshtein (D4)	$3/\left[2((1-\alpha)^{-1/3}-1)\right]$	$1-\left(\frac{2}{3}\right)\alpha-(1-\alpha)^{1/3}$
Reaction-Order Models (Chemical process)		
Zero-order (F0/R1)	1	α
1st-order (F1)	$(1-\alpha)$	$-\ln(1-\alpha)$
2nd –order (F2)	$(1-\alpha)^{2}$	$[1/(1-\alpha)]-1$
3rd-order (F3)	$(1-\alpha)^{3}$	$(1/2)[(1-\alpha)^{-2}-1]$

The application of isoconversional method implies to examine specimens within a wide range of temperature programs, which in other words means recording thermal data from experiments conducted at different heating rates. The aim is the stimulation of changes in fractional conversion (α) and activation energies (*E*) to get access to the kinetic parameters of each step in complex reactions [318]. Certainly, the kinetics committee for performing kinetic computation on thermal analysis data (ICTAC) support the estimation of the activation energy by the iterative methods proposed in this work [324, 325].

6.2 Kinetic analysis of the carbonation reaction based on thermogravimetric data

6.2.1 Isothermal measurements during the carbonation stage

The kinetic study related to the carbonation reaction was conducted using thermogravimetric measurements obtained by a Mettler Toledo DSC/TGA system. Isothermal data obtained between 550 to 625 °C with increments of 25 °C is used to determine the rate constants (*k*) and Arrhenius parameters (E and A). The CO_2 atmosphere utilized to perform the carbonation reaction on the specimens of interest is composed of 90% CO_2 with the balance of N_2. A high concentration of CO_2 is used to avoid mass transfer limitations as the reaction rate of the heterogeneous systems relies on the transport of the gas phase through the solid [326]. The flow rate in all isothermal experiments is fixed at 50 cm^3/min. In order to provide a general overview of the program designed for performing the carbonation experiments, Figure 6-1 is incorporated. Based on the scheme, the as-prepared sorbents are initially subjected to an activation process achieved at 850 °C under a heating rate of 20°C/min. Upon desorption of water molecules and other undesirable compounds causing slaking of CaO, the temperature decreases (550-625 °C) to initiate the carbonation reaction. At this point, the N_2 feed is switched to the gaseous mixture CO_2/N_2 keeping the same flowrate. Finally, the sample is cooled in pure N_2 until it reaches room temperature after 1 h of carbonation.

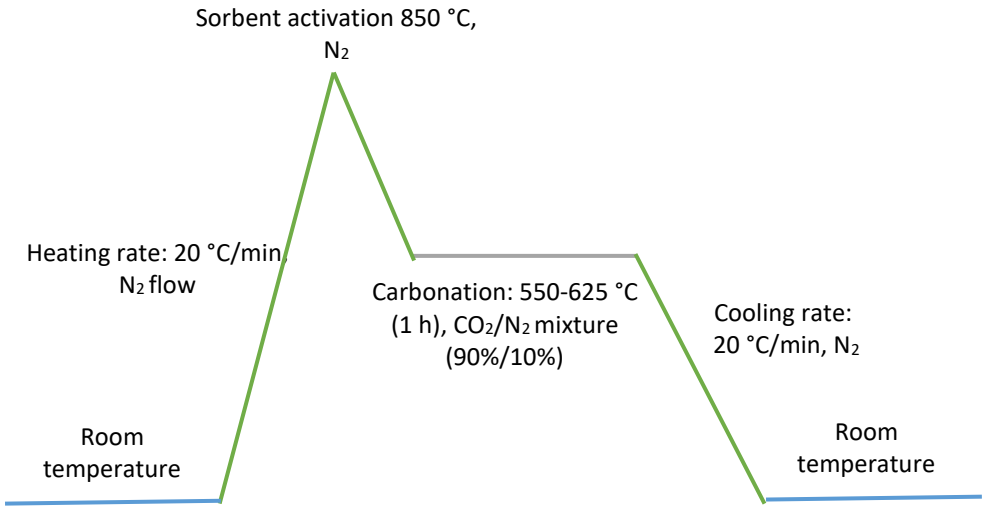

Figure 6-1. TGA program developed to perform the CO_2-CaO reaction. The isothermal experiments cover the temperature range of 550 to 625 °C using a carbonation period of 1h.

6.2.2 Determination of the kinetic parameters for the carbonation reaction using isothermal data

According to section 6.1, one of the major concerns in the determination of the kinetic parameters through the isothermal method is the time needed to reach the temperature chosen for the isothermal experiment. During this dynamic period, the reactant might present a partial transformation [317]. This problem becomes more evident when high-temperatures are required to conduct the study of a particular reaction. Apparently, it would be a limitation for the kinetic analysis related to the carbonation and calcination reactions. However, the TGA apparatus used to run the isothermal trials allows minimizing this issue due to being equipped with a system that permits a very fast switch from an inert gas flow to a reactive atmosphere. For the carbonation reaction, the activation of the sorbent is performed using pure N_2, so, no reactions will take place during the sorbent's activation period (Figure 6-1). Therefore, the isothermal method can be a reliable approach for the calculation of the kinetic parameters. In relation to the calcination reaction, this problem intensifies because it requires both higher temperatures and a previous carbonation of the sorbent. More details associated with the thermo-

kinetic study for the decomposition of the $CaCO_3$ phase to CaO, releasing CO_2, are provided in Chapter 7.

To estimate the kinetic parameters by the isothermal method, conversion (α) vs time (min) curves are needed. Figure 6-2 shows typical conversion curves plotted from TGA carbonation experiments performed on the sample Ca-Sa-25%-WI at temperatures between 550-625 °C. This sample is used as a reference since its counterparts with lower mass percentages (15 and 5 wt. %) displayed a similar behaviour. The TGA conversion curves show the dependence between the conversion of CaO and sorption temperature. Figure 6-2 reveals that the carbonation rate is rapid at low conversions (0-~0.4); this range corresponds to the transformation of CaO to $CaCO_3$ on the surface of the particles. In the thermal range of 550-625 °C, a fast chemical reaction is maintained but a marked dependence with the temperature is observed at conversions above 0.4 (diffusion-controlled regime). The curves confirm the extent of conversion is favoured as the temperature increases. Furthermore, Figure 6-2 shows that the chemical reaction regime governs at conversions below ~0.4 whilst the diffusion-limited regime dominates above 0.4. A similar behaviour is exhibited by the sorbent Ca-Sa-%-WI coated with 5 wt.% for which the carbonation process has a very rapid sorption stage followed by a slow region with a marked dependence of the temperature (Figure 6-3). The conversion trend observed in Ca-Sf-%-WI sorbents is in agreement with previous studies of non-catalysed CO_2 chemisorption performed using CaO particles [327].

Based on the exponential trend observed in the conversion (α) curves recorded for the Ca-Sa-%-WI sorbent, solid-state kinetic models such as nucleation, geometrical contraction, diffusion and reaction-order were initially used for predicting the rate constants. When fitting the isothermal data on the mathematical models, a low correlation was obtained ($R^2 < 0.91$). In the attempt to find a mathematical model that best described the behaviour of the sorbents prepared via wet impregnation, a double exponential model was therefore proposed (equation (6-9)). In theory, this model considers that the carbonation reaction consists of two global reaction steps: 1) a chemisorption produced by the forward reaction between CO_2 molecules and the surface of

the CaO; and 2) a carbonation reaction impeded by the diffusion barrier for the CO_2 to cross before reaching and reacting with CaO, caused by the formation of a $CaCO_3$ product shell over the external surface of CaO particles. The diffusion of CO_2 through the carbonate layer is taken as an assumption since the two-steps are expressed in the power of the exponents in equation (6-9) where the conversion curves are apparently the sum of an initial very fast process followed by a slow one.

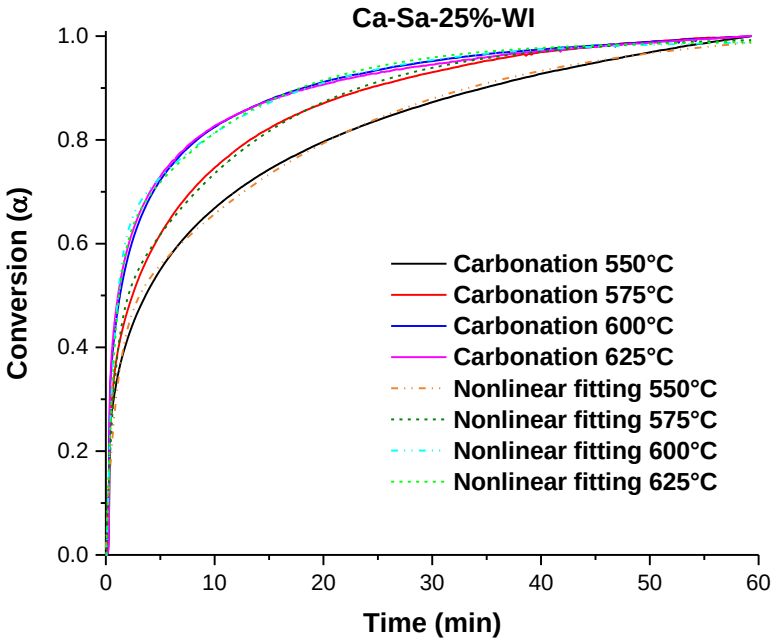

Figure 6-2. TGA experiments presenting α vs time (min) data collected over 60 min of carbonation. Different temperatures were fixed to perform the CO_2 uptake on the sorbents Ca-Sa-25%-WI at isothermal conditions. Nonlinear fitting curves use Equation 6-8.

$$y = A \cdot exp^{-k_1 t} + B \cdot exp^{-k_2 t} + C \qquad (6\text{-}9)$$

In equation (6-9), C is the y-intercept constant, y represents the conversion (α), t is the carbonation time, *A* and *B* are pre-exponential factors related to the intervals that control the capture process. k_1 and k_2 correspond to the exponential constants for the CO_2 sorption on the particle surface and the constant of the diffusion of CO_2 through the $CaCO_3$ layer formed during the capture process, respectively..

Table 6-2. Kinetic parameters obtained by fitting a double exponential model of Equation 6-8 in the conversion curves of Ca-Sa-%-WI sorbents obtained by TGA. Both chemical reaction and the diffusion-controlled regimes were estimated simultaneously.

Ca-Sa-25%-WI						
T(°C)	**k_1 (s^{-1})**	**k_2 (s^{-1})**	**A**	**B**	**C**	**R^2**
550	0.021	0.0012	-0.4278	-0.5841	1.0241	0.995
575	0.023	0.0013	-0.4701	-0.5518	0.9992	0.996
600	0.024	0.0013	-0.4169	-0.6056	0.9910	0.993
625	0.025	0.0014	-0.3893	-0.6648	0.9911	0.991
Ca-Sa-15%-WI						
T(°C)	**k_1 (s^{-1})**	**k_2 (s^{-1})**	**A**	**B**	**C**	**R^2**
550	0.024	0.0016	-0.91541	-0.21538	0.9935	0.992
575	0.025	0.0020	-0.85015	-0.2013	0.9624	0.959
600	0.028	0.0032	-0.8845	-0.27943	1.0147	0.993
625	0.029	0.0043	-0.71656	-0.38105	1.0060	0.996
Ca-Sa-5%-WI						
T(°C)	**k_1 (s^{-1})**	**k_2 (s^{-1})**	**A**	**B**	**C**	**R^2**
550	0.009	0.0007	-0.5396	-0.4994	1.0583	0.999
575	0.013	0.0011	-0.5369	-0.4494	0.9895	0.996
600	0.019	0.0016	-0.53401	-0.4425	0.9947	0.993
625	0.025	0.0021	-0.6853	-0.3682	0.9914	0.993

Dashed lines in Figure 6-2 and Figure 6-3 in conjunction with the correlations factors R^2> 0.956 reported in Table 6-2 confirm that the double exponential model of Equation (6-9) produced a good fit over the isothermal data recorded in the interval of temperature under study (550-625 °C). The reliability provided by the proposed model allowed the calculation of the rate constants for the chemical reaction (k_1) and diffusion-controlled regimes (k_2) and the pre-exponential factors *A* and *B*. The results displayed in Table 6-2 show that k_1 values were one order of magnitude greater than rate constants k_2. This gap indicates that carbonation process initiates on the surface of the solid, then, the CO_2 diffuses through the $CaCO_3$ layer towards the interior of the particle. Although isothermal curves of the Ca-Sa-15%-WI sample are omitted, k_1 and k_2 values presented in Table 6-2 confirm a similar behaviour.

On the basis of the rate constants values measured, the overall sorption process was limited by diffusion.

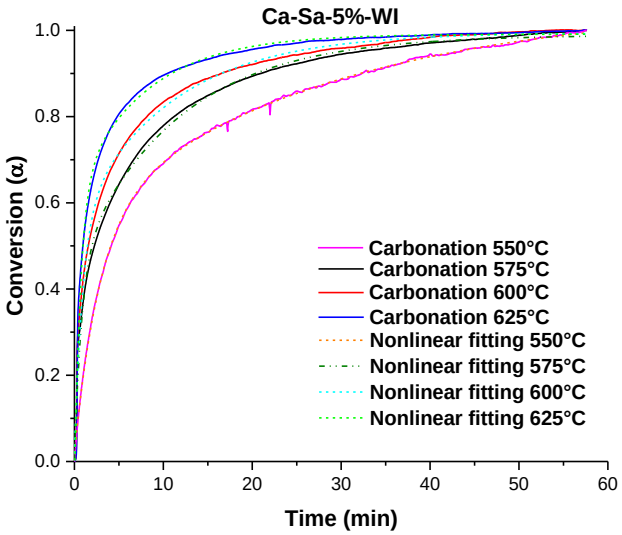

Figure 6-3. Conversion data related to the carbonation reaction performed on the Ca-Sa-5%-WI sorbent under isothermal regime using different temperature ranging from 550 to 625 °C. Nonlinear fitting curves use Equation 6-8.

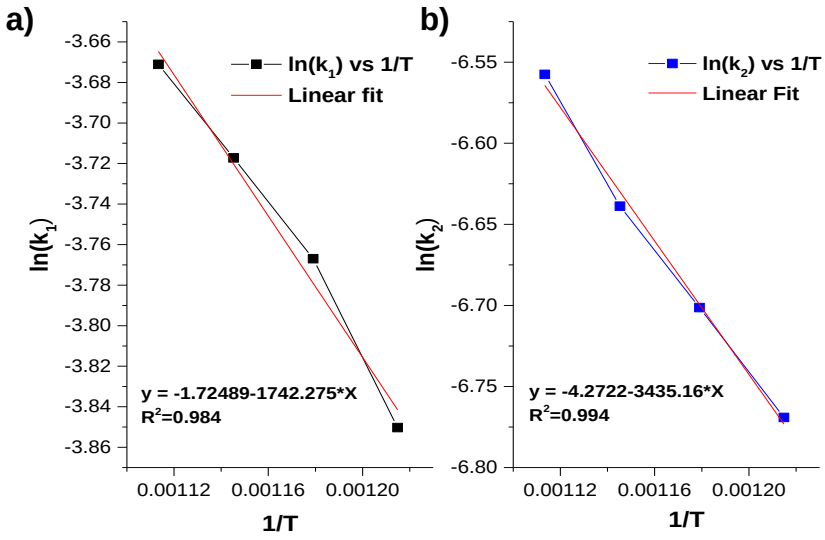

Ca-Sa-25%-WI (chemical reaction regime) Ca-Sa-25%-WI (diffusion regime)

Figure 6-4. Arrhenius plots used for determination of activation energies *E* and the pre-exponential factors *A* in the sorbents Ca-Sa-25%-WI for both chemical reaction (a) and diffusion-controlled regime (b). The straight lines were obtained from a linear fitting performed on k_1 and k_2 values estimated on the bases of the double exponential model in a temperature range of 550-625 °C.

The activation energies for the carbonation reaction of Ca-Sa-%-WI sorbents were calculated using Arrhenius plots. The logarithm (*ln(k)*) of kinetic constants k_1 and k_2 against the inverse of the temperatures *(1/T)* gave rise to straight lines (Figure 6-4). In the equations derived from the linear regression (*y = m*x + b* - equation (6-10)), the y-intercept corresponds to *ln(A)* and the gradient equals - *E/R* . As this regression analysis provided correlation coefficients >0.95 for k_1 and k_2 constants, the double exponential model (equation (6-9)) was confirmed as a viable model in the range of temperature selected for the kinetic study.

$$\ln k = \ln(A, B) - \frac{E}{RT} \qquad (6\text{-}10)$$

Where:

K = rate constants k_1 or k_2

A, *B* = pre-exponential factors of either chemical reaction or diffusion- limited regime.

Table 6-3. Summary of activation energies (rounded values) for the rate constants k_1 and k_2 in both chemical reaction and diffusion-limited regimes.

Sorbent	Activation Energy (kJ/mol) Chemical Reaction	Activation Energy (kJ/mol) Diffusion-limited regime
Ca-Sa-25%-WI	15	29
Ca-Sa-15%-WI	15	80
Ca-Sa-5%-WI	85	85

The activation energies estimated for sorbents prepared via wet impregnation using Arrhenius plots are reported in Table 6-3. It must be highlighted that there is a strong dependence of sorption with increments in temperature as it was observed a jump in the activation energy of the chemical reaction regime of the Ca-Sa-5%-WI sorbent compared with Ca-Sa-15%-WI and Ca-Sa-25%-WI. This effect can be explained through the collision theory as the probability of interaction CO_2-CaO decreases as the content of CaO decreases, and thus, it will be reflected in a slower reaction rate. The energies for both chemical reaction and diffusion regimes were in the range of carbonation energies reported for other CaO-based sorbents in the literature, namely between 9-

239 kJ/mol [328]. The *E* (kJ/mol) values associated with the chemical reaction regime are comparable with activation energies predicted by Abanades and Gupta et al. for limestone [329, 330]. For the diffusion-controlled regime, the activation energies for Ca-Sa-%-WI were below those calculated in the kinetic study conducted by Bhatia-Perlmutter and Gupta-Fan for CaO prepared via calcination of Lime [193, 330]. The open structure of the catalytic grade Saffil mat conformed by cavities and the network of mesopores are likely explanation of the energy difference. Although the effect of morphology on the reaction kinetics does not draw consensus among researchers, the peculiar morphology tailored for CaO (nanoflakes) could also influence the activation energy values.

Conversion curves obtained from carbonation trials on CaO/Sf-25%-U and CaO/Sf-25%-SH samples (sorbents used as reference) using isothermal programs (550-625 °C) are displayed in Figure 6-5 and Figure 6-6, respectively. A trend analogous to that obtained for the Ca-Sa25%-WI sorbents led to also propose the double-exponential equation (6-9) as the kinetic model for predicting the kinetic constants of the families of sorbents prepared by precipitation with urea or NaO as the precipitant agent. The curves derived from the non-linear regression performed through equation (6-9) are displayed also in Figure 6-5 and Figure 6-6 (dashed lines). The trend of conversion curves plotted for the CaO/Sf-25%-U sorbents indicates that the superficial carbonation occurs also at low conversions, thus, the diffusion limited conversion stage governs the overall CO_2 sorption process. The dependence on temperature is evident, the highest the temperature, the faster the carbonation. This assertion is confirmed through the values for k_1 and k_2 estimated by curve fitting (Table 6-4); both constants increase as the temperature rise. It must be highlighted that sorbents coated with 15 and 5 wt. % of CaO exhibited a similar behaviour. Hence, their conversion curves with non-linear fitting integrated are not shown from the current section and are relocated into Appendix A.

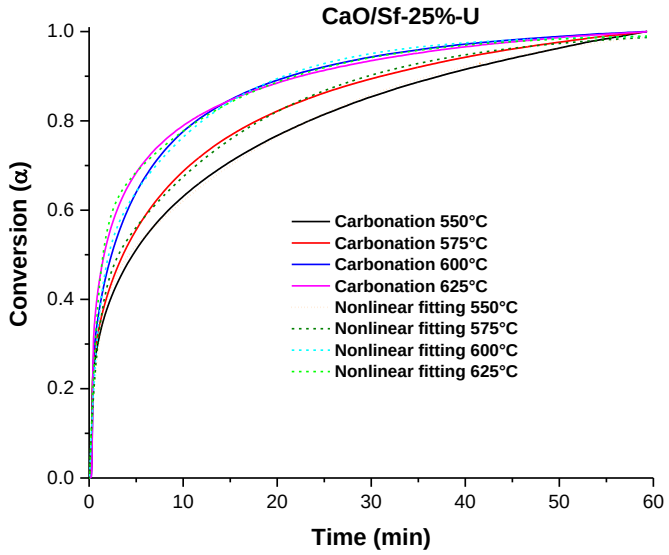

Figure 6-5. Carbonation conversions of CaO/Sf-25%-U sorbents obtained under isothermal conditions in a temperature range of 550 to 625 °C. Nonlinear fitting curves used Equation 6-8.

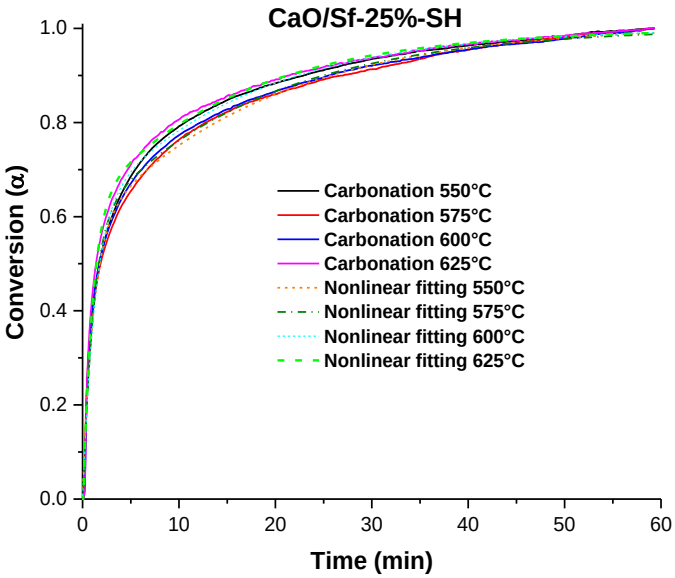

Figure 6-6. Carbonation conversions estimated for the CaO/Sf-25%-SH sorbent tested isothermally under a CO_2-enriched atmosphere and in a temperature interval of 550 to 625 °C. Nonlinear fitting curves used Equation 6-8.

The conversion curves obtained for the sample CaO/Sf-25%-SH show very similar carbonation profiles (Figure 6-6). The thermal data reveals that in the range of 550 to 625 °C, the temperature has a similar effect on the carbonation rate for both the chemical reaction and the diffusion-limited process. Their rate

constants k_1 and k_2 calculated on the basis of equation (6-9) and also reported in Table 6-4 confirm the temperature effect. Minor changes in k_2 mean a slight increase in CO_2 sorption rate in the regime governed by diffusion. In the case of CaO/Sf-%-SH with CaO loads of 15 and 5 wt. % (Figure 6-7) the temperature had a stronger effect on the diffusion-limited stage. The reaction rate in this regime was slower at 550 °C but as the temperature rose up to 625 °C, the diffusion of CO_2 toward the interior of the particle was accelerated. The effect of temperature is analysed in more detail after the estimation of the activation energies (E in kJ/mol) through Arrhenius plots and the linear equation (6-10)).

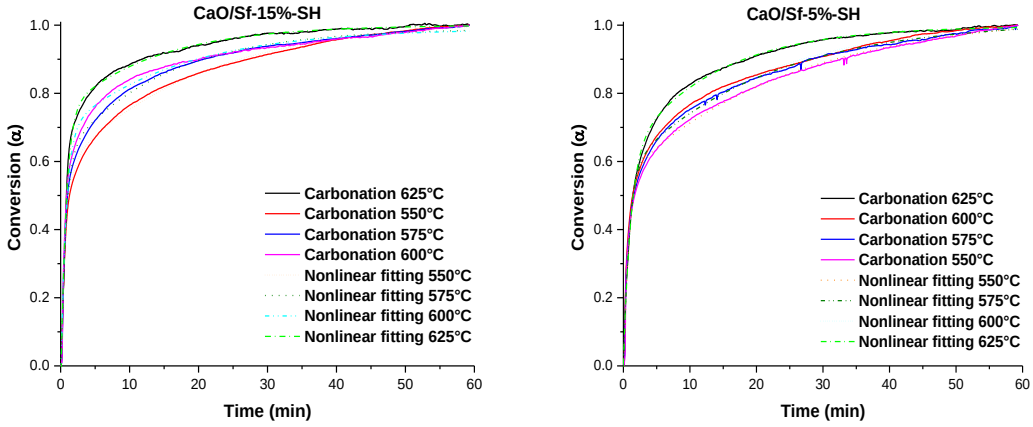

CaO/Sf-15%-SH CaO/Sf-5%-SH

Figure 6-7. Evolution in the carbonation conversion of CaO/Sf-%-SH sorbents loaded with 15 and 5 wt. %. Isothermal data used to predict the Arrhenius parameters in a temperature range of 550 to 625 °C. Nonlinear fitting curves use equation 6-8 (dashed lines).

Arrhenius plots plotted on the basis of rate constants of the CaO/Sf-25%-U sorbent are shown in Figure 6-8. The suitability of the proposed kinetic model was once more confirmed by the good linearity obtained when the Arrhenius equation (6-10) was applied. In addition, the correlation factors R^2 above 0.97 permits to conjecture that the estimations of the activation energy are reliable. It is noteworthy to mention that consistent values of *E* (kJ/mol) are calculated for samples CaO/Sf-%-U with 15 and 5 wt. % CaO; the linear regressions

show correlations R^2 above 0.97. Full particulars of the mathematical analysis of their Arrhenius plots are found in Appendix A.

Table 6-4. Rate constants (k_1 and k_2), pre-exponential factors (A and B) and correlation factors (R^2) predicted by fitting the double exponential model into the isothermal data acquired for Ca-Sa-%-U and Ca-Sa-%-SH sorbents.

Ca-Sa-25%-U						
T(°C)	**k_1 (s^{-1})**	**k_2 (s^{-1})**	**A**	**B**	**C**	**R^2**
550	0.02246	0.00102	-0.49365	-0.52267	1.00002	0.995
575	0.02466	0.00108	-0.51759	-0.51998	1.00104	0.995
600	0.02755	0.00118	-0.69106	-0.37976	0.99086	0.995
625	0.03127	0.00129	-0.79194	-0.34862	0.99085	0.989
Ca-Sa-15%-U						
T(°C)	**k_1 (s^{-1})**	**k_2 (s^{-1})**	**A**	**B**	**C**	**R^2**
550	0.02246	0.001020	-0.49365	-0.52267	1.00002	0.995
575	0.02446	0.001084	-0.51759	-0.51998	1.00104	0.995
600	0.02700	0.001159	-0.69106	-0.37976	0.99086	0.996
625	0.03127	0.001216	-0.79194	-0.34862	0.99085	0.989
Ca-Sa-5%-U						
T(°C)	**k_1 (s^{-1})**	**k_2 (s^{-1})**	**A**	**B**	**C**	**R^2**
550	0.01358	0.00084	-0.34246	-0.56719	1.02208	0.999
575	0.01860	0.00109	-0.4419	-0.56989	1.00822	0.997
600	0.02545	0.00144	-0.52036	-0.52143	0.99454	0.996
625	0.02947	0.00199	-0.66558	-0.40966	0.9903	0.992
Ca-Sa-25%-SH						
T(°C)	**k_1 (s^{-1})**	**k_2 (s^{-1})**	**A**	**B**	**C**	**R^2**
550	0.01548	0.00092	-0.55801	-0.44382	1.00759	0.996
575	0.01753	0.00095	-0.6065	-0.42555	1.00173	0.997
600	0.02121	0.00103	-0.60128	-0.40469	1.0014	0.998
625	0.02545	0.00106	-0.66027	-0.38543	0.9991	0.996
Ca-Sa-15%-SH						
T(°C)	**k_1 (s^{-1})**	**k_2 (s^{-1})**	**A**	**B**	**C**	**R^2**
550	0.02232	0.00086	-0.62802	-0.43895	1.01451	0.997
575	0.02306	0.00103	-0.69107	-0.37976	0.99089	0.995
600	0.02430	0.00115	-0.75524	-0.3069	0.99028	0.990
625	0.02545	0.00127	-0.83676	-0.26205	1.00066	0.996
Ca-Sa-5%-SH						
T(°C)	**k_1 (s^{-1})**	**k_2 (s^{-1})**	**A**	**B**	**C**	**R^2**
550	0.01532	0.00067	-0.5974	-0.4797	1.03406	0.997
575	0.01889	0.00079	-0.58147	-0.4411	1.01299	0.996
600	0.02296	0.00098	-0.58727	-0.4308	1.02203	0.995
625	0.02545	0.00126	-0.61086	-0.38285	0.99754	0.998

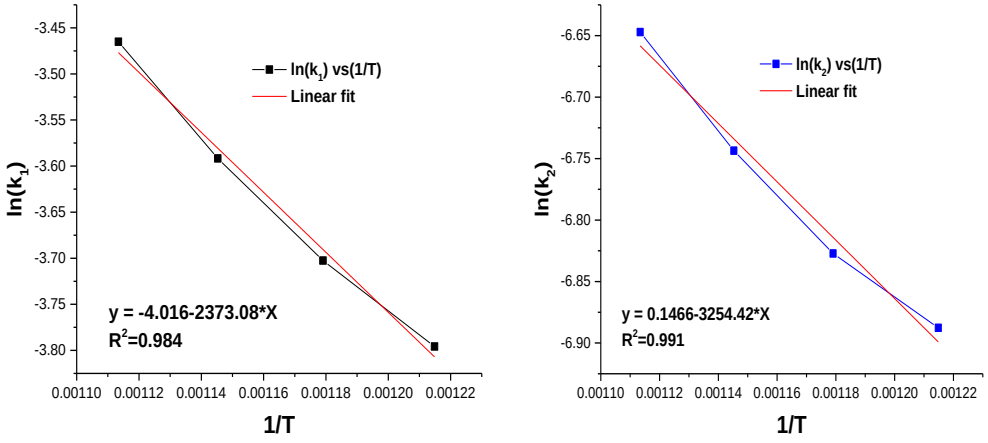

a) CaO/Sf-25%-U (chemical reaction regime)

b) CaO/Sf-25%-U (diffusion regime)

Figure 6-8. Arrhenius plots of the two different CO_2 sorption processes existing in the CaO/Sf-25%-U sorbent: a) direct reaction on the CaO surface and b) reaction controlled by diffusion of CO_2 through the external $CaCO_3$ layer.

Activation energies of sorbents CaO/Sf-%-U determined using the linearized Arrhenius equation (6-10) are reported in Table 6-5. In the particular case of the sorbent coated with 25 wt. %, the energies assessed for the chemical reaction and diffusion-controlled regime agreed with values of the sample Ca-Sa-25%-WI. The energetic analogy is attributed to the microstructural, morphological and texture resemblance between both families of sorbents. For the samples with the lowest CaO loads CaO/Sf-5%-U and Ca-Sa-5%-WI, the energy requirements to initiate the chemisorption of CO_2 differ widely, namely from ~14-19 kJ/mol to ~60-84 kJ/mol. The sharp increase can be explained by the collision theory, the smaller the active surface area for the collision of CO_2 molecules with CaO, the slower the rate of carbonation. Thus, a lower activation energy is required for those CaO-Saffil sorbents with higher loads of active phase. Despite the rise in *E* (kJ/mol) values, the energies calculated for CaO/Sf-%-U and Ca-Sa-%-WI sorbents were within the range of others available in the literature for CaO obtained from a natural or synthetic source using isothermal and non-isothermal methods [331].

Table 6-5. Activation energies (rounded values) of samples CaO/Sf-%-U for the chemical reaction and diffusion-limited regime estimated on the basis of Arrhenius plots.

Sorbent	Activation Energy E (kJ/mol) Chemical reaction	Activation Energy E (kJ/mol) Diffusion-controlled regime
CaO/Sf-25%-U	20	25
CaO/Sf-15%-U	20	27
CaO/Sf-5%-U	59	72

The activation energies of CaO/Sf-%-SH sorbents loaded with 25, 15 and 5 wt. % of CaO calculated for the fast and slow CO_2 sorption process are reported in Table 6-6. Plots for CaO/Sf-%-SH sorbents with contents of CaO below 25 wt. % are not shown but their linear regression of the reactions rate constants produced R^2 values within a very acceptable window (>0.95). The corresponding set of straight lines for samples CaO/Sf-15%-SH and CaO/Sf-5%-SH derived from the Arrhenius behaviour can be seen in Appendix A.

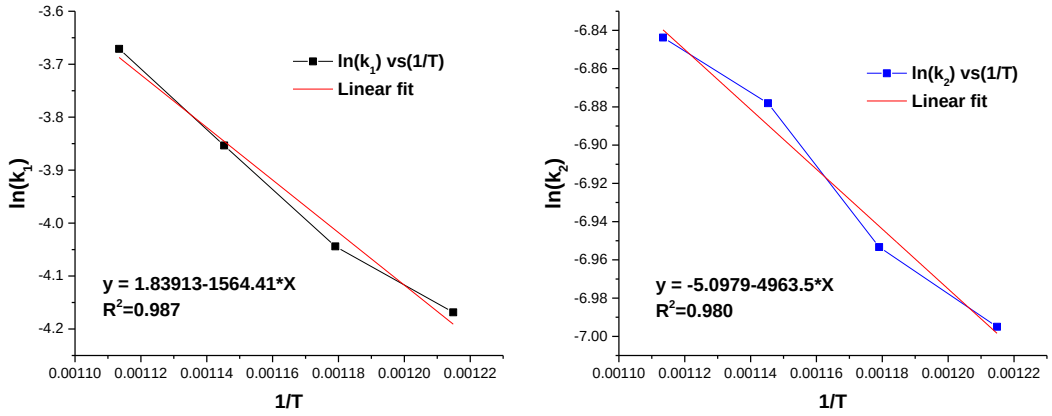

a) CaO/Sf-25%-SH (chemical reaction) b) CaO/Sf-25%-SH (diffusion regime)

Figure 6-9. Arrhenius plots used to predict the activation energies of carbonation in samples CaO/Sf-25%-SH. Correlation factors R^2 above 0.980 were obtained through the curve fitting analysis.

The E (kJ/mol) values reported for the CaO/Sf-%-SH sorbents gave similar energy requirements compared to those of Ca-Sf-%-WI and CaO/Sf-%-U to initiate superficial conversion of CaO to $CaCO_3$. In relation to the regime governed by diffusion, the activation energies presented a rise merely attributed to the sorbents' morphology as well as their disordered network of pores. Evidently, reaction rate was affected due to CO_2 having a slower

diffusion toward the interior of the unstructured CaO supported over Saffil supports.

Table 6-6. Activation energies (rounded values) of the CaO/Sf-%SH sorbents obtained for the carbonation reaction.

Sorbent	Activation Energy *E* (kJ/mol) Chemical Reaction	Activation Energy *E* (kJ/mol) Diffusion-limited regime
CaO/Sf-25%-SH	13	42
CaO/Sf-15%-SH	11	31
CaO/Sf-5%-SH	42	52

Lastly, the CaO/Sf-%Oct sorbents were kinetically studied following the sequential methodology: isothermal experiments → conversion curves → kinetic constants/pre-exponential factors → activation energies. The conversion curves of the sample CaO/Sf-25%-Oct (reference) shown in Figure 6-10 reveals that the carbonation on the octahedral particles of CaO had the same sorption pattern than in previously studied CaO-Saffil sorbents, namely a rapid carbonation process followed by a slow diffusion controlled one. However, major differences because of changes in the physical properties (morphology and texture) were observed in the reaction rates and fractional conversion of CaO. The thermal history in the carbonation curves of the CaO/Sf-25%-Oct sorbent confirms a very fast sorption during the first 1-2.5 min of carbonation (temperature dependent). This rapid superficial reaction allows conversion fractions to reach above 0.7 (in contrast to 0.4 in the previously studied samples), whereas the unreacted region of the curves is due to the diffusion regime.

The very good correlation factors (>0.97) acquired from the non-linear curve fitting carried out over thermal data of the sample CaO/Sf-25%-Oct confirmed the accuracy of equation (6-9) in modelling the carbonation reaction (dashed lines in Figure 6-10). A summary of the rate constants k_1 and k_2, pre-exponential factors and correlation R^2 values for the sorbents CaO/Sf-%-Oct loaded with CaO weight percentages of 25, 15 and 5 are reported in Table 6-7. The rate constants for the superficial carbonation of the reference sample CaO/Sf-25%-Oct are greater compared to those in sorbents coated with nanoflakes, which means a more rapid reaction rate for the temperature range

under study (550-625 °C). The k_1 values seemed right due to the presence of minimal restrictions for driving the direct interaction between the CO_2 molecules and the smooth faces of the CaO octahedra. In the diffusion-controlled region, the 25 wt. % sorbent presented slow sorption that speed up as the temperature of the trial increased. The shapes of the conversion curves shown in Figure 6-10 give evidence that the rate-limiting step for the global CO_2 uptake process is diffusion. This inference is confirmed with the rate constants values calculated; k_1 is one or even two orders of magnitude above k_2 (Table 6-7). Concerning CaO/Sf-%-Oct sorbent loaded with 15 and 5 wt. %, their thermal histories show similarity with the sample CaO/Sf-25%-Oct. Therefore, isothermal curves related to the carbonation of CaO/Sf-15%-Oct and CaO/Sf-5%-Oct sorbents are presented in Appendix A.

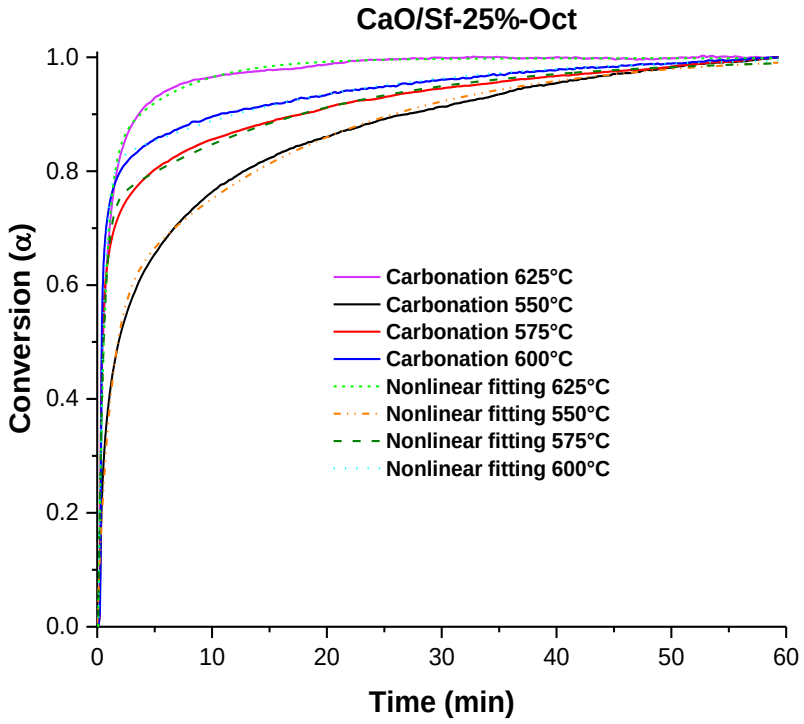

Figure 6-10. Conversion vs time plot of the CaO/Sf-25%-Oct sorbent. The data acquisition is performed through a TG program designed to drive the carbonation reaction under isothermal conditions in a range of temperatures of 550-625 °C. Nonlinear fitting curves used equation 6-8.

Table 6-7. Rate constants k_1 and k_2, pre-exponential factors and correlation factors derived from fitting the double exponential model of equation 6-8 into the isothermal conversion curves of CaO/Sf-%-Oct sorbents.

Ca-Sa-25%-Oct						
T(°C)	**k_1 (s^{-1})**	**k_2 (s^{-1})**	**A**	**B**	**C**	**R^2**
550	0.01547	0.00088	-0.55801	-0.44382	1.00759	0.996
575	0.02043	0.00098	-0.89101	-0.26562	0.99916	0.986
600	0.02545	0.00111	-1.01911	-0.19438	1.00259	0.977
625	0.02982	0.00130	-0.93703	-0.18494	0.99824	0.990
Ca-Sa-15%-Oct						
T(°C)	**k_1 (s^{-1})**	**k_2 (s^{-1})**	**A**	**B**	**C**	**R^2**
550	0.01731	0.00110	-0.59483	-0.38208	0.99922	0.995
575	0.02073	0.00130	-0.61783	-0.4251	0.99407	0.995
600	0.02430	0.00145	-0.6388	-0.38712	0.99002	0.994
625	0.02755	0.00166	-0.70372	-0.35209	0.98853	0.992
Ca-Sa-5%-Oct						
T(°C)	**k_1 (s^{-1})**	**k_2 (s^{-1})**	**A**	**B**	**C**	**R^2**
550	0.02035	0.00102	-0.68317	-0.36237	1.00077	0.993
575	0.02205	0.00110	-0.68251	-0.34733	0.99659	0.995
600	0.02395	0.00120	-0.74182	-0.31712	0.99172	0.992
625	0.02545	0.00131	-0.77027	-0.29851	0.99632	0.993

The determination of the kinetic triplet ends the calculation of the activation energies for the CO_2-CaO reaction on the CaO/Sf%-Oct sorbents. The linear fitting analysis performed on the Arrhenius plots of the reference sample (25 wt. % of CaO) reveals correlation factors R^2> 0.98 (Figure 6-11). The good linearity predicted through the Arrhenius model reassert the benefits of using the double exponential equation as the model to assess the carbonation reaction. The $ln(k_{1,2})$ values dispersed close to the straight line predicted from the linear regression is consistent for both the chemical reaction and diffusion-controlled regimes. The activation energies (E (kJ/mol)) predicted for the samples CaO/Sf%-Oct with 25. 15 and 5 wt. % of CaO are reported in Table 6-8.

Based on predicted *E* values, the sorbent with 25 wt. % had the highest activation energies in the chemical reaction and diffusion controlled regimes with ~31.7 kJ/mol and ~54 kJ/mol respectively. The activation energies of the CaO/Sf-%-Oct sorbents presented fluctuations as the amount of CaO

deposited declined. These changes indicate the reliance of the kinetic parameters to slight variations in the morphology and texture (surface area and pore size and volume distribution). It is worth mentioning that the *E* values predicted for the CaO/Sf-%-Oct sorbents were within the range of activation energies reported in the literature for other CaO-based sorbents [331].

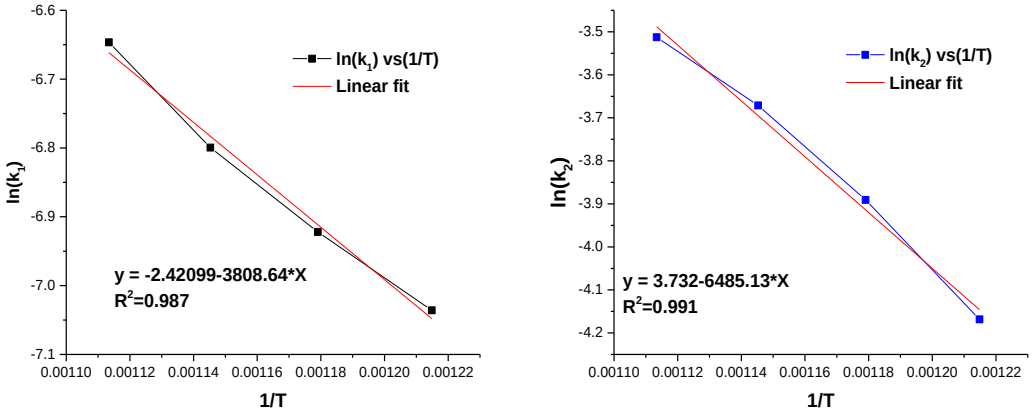

a) CaO/Sf-25%-Oct (chemical reaction regime)

b) CaO/Sf-25%-Oct (diffusion controlled regime)

Figure 6-11. Arrhenius plots for the prediction of activation energies using rate constants k_1 and k_2 obtained from the application of the double exponential model (equation 6-8) on TGA experimental data.

Table 6-8. Summary of activation energies (rounded values) for the chemical reaction and diffusion-controlled regimes calculated for the CO_2-CaO reaction CaO/Sf-%-Oct sorbents through linear regression in Arrhenius plots.

Sorbent	Activation Energy E (kJ/mol) Chemical Reaction	Activation Energy E (kJ/mol) Diffusion-limited Regime
CaO/Sf-25%-Oct	32	54
CaO/Sf-15%-Oct	31	38
CaO/Sf-5%-Oct	19	21

6.3 Conclusion

In this chapter, the carbonation kinetics of Ca-Sa-%-WI, CaO/Sf-%-U, CaO/Sf-%-SH and CaO/Sf-%-Oct sorbents coated with 5, 15 and 25 wt. % of CaO were investigated. The experiments were conducted isothermally in a

window of temperature from 550 to 625 °C under a CO_2-rich atmosphere composed of 90% CO_2/10% N_2. Conventional solid-state models were used to estimate the kinetic parameters. The curves fitting analysis over the experimental conversion data revealed meaningless kinetic constants (correlation factors below 0.95). Hence, a double exponential model able to predict simultaneously the kinetic constants for the chemical reaction and diffusion-controlled regimes was proposed.

The non-lineal regressions performed on the basis of the model proposed gave correlations R^2 above 0.98 for all the as-prepared sorbents. This goodness of fit was observed for both the fast and slow CO_2 sorption regimes. In terms of the kinetic constants, k_1 (chemical reaction) showed values one or even two orders of magnitude above k_2 (diffusion controlled reaction). The gap between k_1 and k_2 confirmed that the carbonation has as a rate-limiting step the “diffusion” controlled reaction. In relation to the activation energies, the apparent activation energy values (*E*) for the CO_2 sorbents with flake-like structure (Ca-Sa-%-WI and CaO/Sf-%-U) rose as the amount of CaO reactant decreased. Apparently, the morphology and coating thicknesses had a strong influence in both superficial and inner carbonation. Conversely, in sorbents CaO/Sf-%-Oct, the activation energies for the diffusion-limiting regime increased as a function of the remaining CaO amount. These energy changes were attributed to the network of narrow cavities inherent of the octahedral particles.

The *E* values predicted were within the range of activation energies reported in the literature for other natural and synthetic CaO-based sorbents. This similarity confirmed the suitability of the isothermal method to predict apparent kinetic parameters for the carbonation process. Evidently, the double exponential model played an important role in the accuracy of the kinetic study carried out.

Chapter 7 Thermo-Kinetic Study of the Calcination Reaction in CaO-based Sorbents

In the current chapter, a thermo-kinetic study aimed at predicting kinetic parameters of the decarbonation (calcination) reaction in CaO-Saffil sorbents is presented. The estimation of rate constants (*k)* are carried out using conventional methods: 1) isothermal method and 2) isoconversional also termed “model-free methods”. The activation energies are calculated applying the linear form of the Arrhenius equation on rate constants predicted under isothermal conditions or using different heating rates. Finally, the suitability of the methodologies used to estimate the kinetic parameters is confirmed by comparing the values of CaO-Saffil sorbents and others reported by different authors.

7.1 Estimation of the kinetic parameters of the calcination reaction using isothermal data

In the literature, a vast number of investigations has been driven to predict kinetic parameters associated with both carbonation and calcination reactions performed using CaO-rich compounds. Most of the current publications motivated to study the thermo-kinetic behaviour of CaO-based sorbents have utilized naturally sourced CaO such as limestone, magnesite and dolomite. Natural CO_2 sorbents have caught the attention of authors because of their abundance on nature and low cost compared to synthetic CaO-based sorbents [331, 332]. In the particular case of limestone, kinetic studies have been carried out under a wide range of process variables such as carbonation-calcination temperatures, different times of the reactions, heating rates, particle sizes and different CO_2 partial pressures. From the analysis of the effect of the aforementioned variables on kinetics, conflicting results have caused difficulties to conciliate a conclusion of their real influence. Furthermore, there is not a concise evidence of how the morphology influences the reaction rates. Thus, differences in morphology and texture of CaO-Saffil sorbents compared to conventional CaO-based sorbents

(powders) motivated this work to carry out the thermo-kinetic study of sorbents Ca-Sa-%-WI, CaO/Sf-%-U, CaO/Sf-%-SH and CaO/Sf-%-Oct sorbents with loadings of 25, 15 and 5 wt. % during the calcination reaction.

7.1.1 Isothermal experiments for the kinetic analysis of the decomposition reaction on CaO-Saffil sorbents

Isothermal experiments performed to predict kinetic parameters of the conversion of $CaCO_3$ to CaO followed a methodology analogous to that of the isothermal trials for evaluating the kinetic triplet of the carbonation reaction on CaO-Saffil sorbents (section 6.2.1). The study started with a fast activation step meant to release water molecules or any other contaminant bonded over the surface of CaO. Subsequently, the temperature was decreased from 850°C to 650 °C to perform the carbonation step using a CO_2-rich gaseous mixture (90% CO_2/10% N_2) for 1 h. Lastly, the flow was switched to N_2 to initiate the isothermal decomposition of $CaCO_3$. On the basis of previous works reported by various authors, optimal decomposition temperatures chosen to perform the kinetic study were 680, 700, 720 and 740 °C [333]. Thermal conditions to attain a favorable thermodynamic for decarbonation of $CaCO_3$ were also taken into consideration to select this optimal range of temperatures.

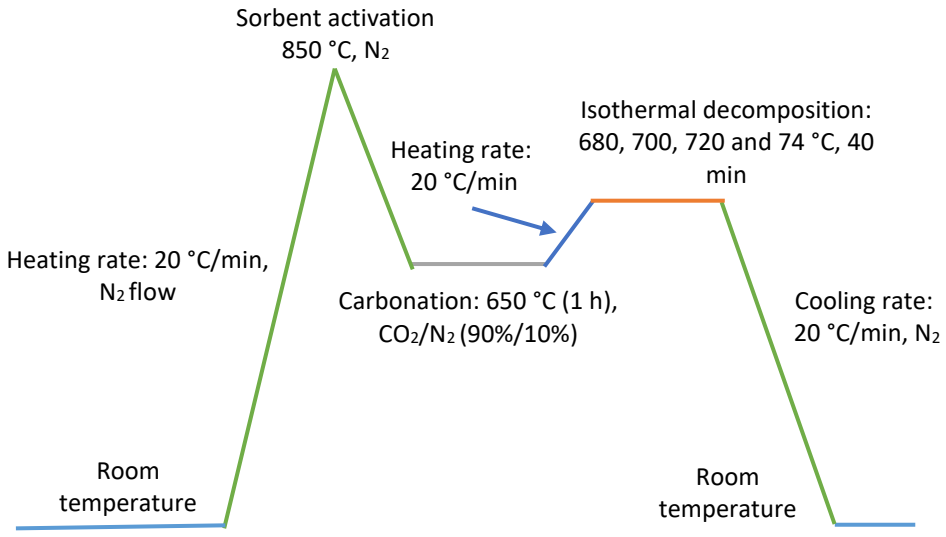

Figure 7-1 . Experiments for the prediction of kinetic parameters of the thermal decomposition of $CaCO_3$ in CaO-Saffil sorbents.

As mentioned in Chapter 6, an undesired effect in isothermal experiments is data acquisition of the dynamic stage in which the sorbent is heated up until it reaches the temperature set to perform the decomposition reaction. Thus, in order to address this issue, the gaseous mixture composed of 90% CO_2/10% N_2 was maintained until the beginning of the decomposition process. Then, the flow was swapped to 100% N_2 to trigger the isothermal decomposition. After 40 min of decarbonation, the TGA experiment concluded with cooling the sample dynamically at a rate of 20 °C/min. Parameters and time intervals are specified in the diagram presented in Figure 7-1.

7.1.2 Calculation of kinetic parameters using solid state reaction models applied to isothermal data

The kinetic parameters of Ca-Sa-%-WI, CaO/Sf-%-U, CaO/Sf-%-SH and CaO/Sf-%-Oct sorbents were predicted by correlating conventional solid-state reaction models (Table 6-1) with the experimental data obtained using isothermal conditions. Although section 6.1 mentioned drawbacks of the isothermal method, the kinetics committee for performing kinetic computation on thermal analysis data (ICTAC) validated its application. From the technical point of view, improving data collection is achieved by using the Mettler Toledo TGA. This system, which is equipped with a gas box that allows a fast process for swapping TGA atmospheres (from 90% CO_2/10% N_2 to pure N_2), reduces the loss of conversion data in the dynamic regime prior to thermal decomposition (between 650 °C to temperature selected for decomposition).

Kinetic parameters including apparent activation energies are compared with kinetic triplets predicted using the non-isothermal method (section 7.2) and validated through other values documented in the literature for natural or synthetic CaO-based sorbents. Although no agreement is expected on kinetic parameters predicted from isothermal and non-isothermal methods, the results must be coherent with each other.

7.1.2.1 Prediction of kinetic parameters of the decarbonation reaction of Ca-Sa-%-WI sorbents using isothermal data

The thermo-kinetic study of the decarbonation reaction of Ca-Sa-%-WI sorbents using isothermal method is shown in the current section. On the basis of the methodology presented in Figure 7-1, isothermal TGA curves collected in temperatures between 680 to 740 °C were treated and transformed to normalized conversion curves). The results of the Ca-Sa-25%-WI sorbent used as a reference revealed that the decomposition reaction followed a different mechanism compared to the carbonation reaction (Figure 7-2). According to the conversion curves of the 25 wt. % sorbent, a sigmoid (also termed S-shape curve) behaviour was observed. This decomposition trend is confirmed by the sequence of activities described below:

1. An initial period in which the context of the desorption process developed.
2. Conversion experienced a sharp growth that reflected a fast CO_2 desorption.
3. A transition between a fast and maturity of the desorption process.
4. Desorption rate decreased and became steady upon completion of the decarbonation of $CaCO_3$.

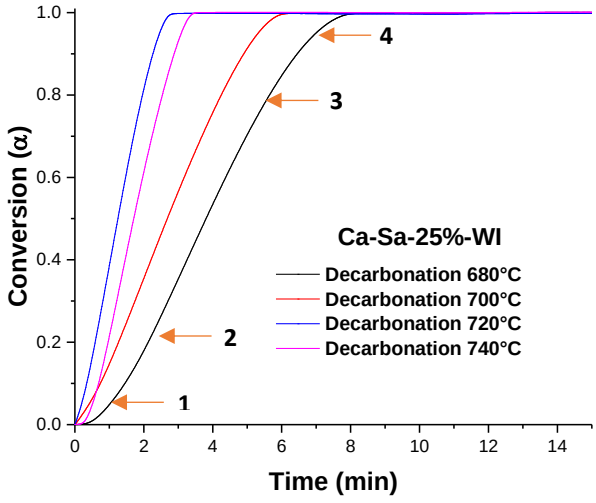

Figure 7-2. Normalised conversion curves of the decarbonation reaction of the Ca-Sa-25%-WI sorbent. The decomposition analysis was conducted upon completion of the carbonation process reached at 650 °C for 60 min using a CO_2 enriched flow (90% CO_2/10% N_2).

The kinetic parameters were predicted by fitting solid-state reaction models with the experimental curves. The ideal model must be able to describe the decomposition reaction to any progress of conversion. The solid-state models for non-catalysed solid-gas reactions were Power law (P1, P2 and P3), Evrami-Erofeyev (A2, A3 and A4), Prout-Tompkins (B1), 3-D diffusion-Jander (D3) and reaction order models (1^{st}–F1, 2^{nd}–F2 and 3^{rd}–F3) (Table 6-1). As a benchmark, the thermal decomposition curves and model fitting curves obtained at 680, 700, 720 and 740 °C for the carbonated Ca-Sa-25%-WI sorbent are shown in Figure 7-3.

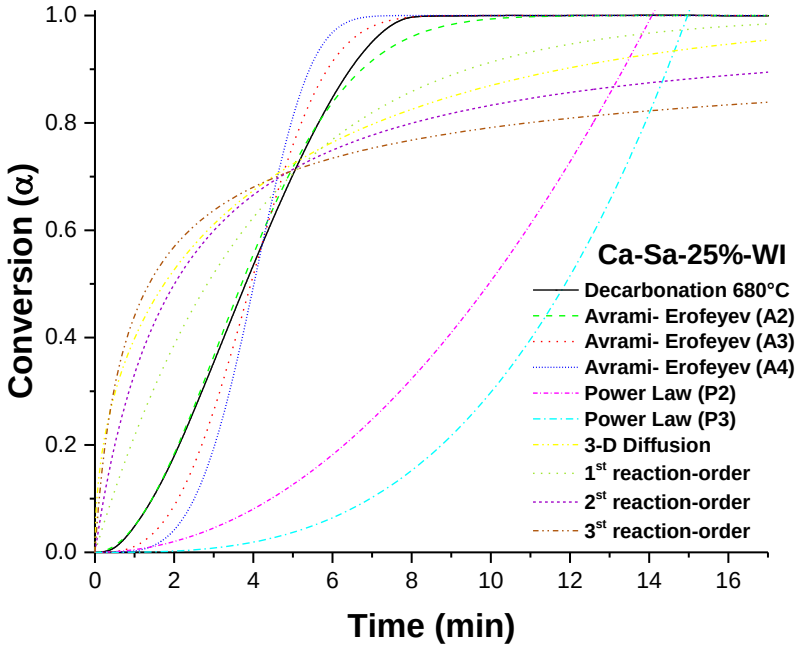

Figure 7-3. Solid-state models fitted with the TGA curve of the Ca-Sa-25%-WI sorbent registered under isothermal conditions in 680-740 °C range in pure N_2.

The results exhibited in Figure 7-3 reveal that some particular algebraic expressions result in a closer fit with the experimental data of the Ca-Sa-25%-WI sorbent decomposed isothermally. For instance, although the 3-D diffusion model was proposed as a candidate to describe the carbonation process, this model was far from describing the mechanism of CO_2 desorption of this sample. Leading a similar fitting analysis but using nucleation models such as Power Law equations P2 and P3 (Table 6-1), the nonlinear fit exhibited low correlation with the isothermal data (Figure 7-3). Certainly, the convex trend

of modelled functions P2 and P3 gave an initial regime of slow desorption of CO, followed by a regime of fast desorption of exponential growth (second and third order). According to the curves obtained by fitting reaction-order models, the results showed that equations F1, F2 and F3 were useful for describing decomposition reactions with a very rapid initial loss of CO_2, followed by a deceleratory stage of slow reaction rate. The non-linear curve fitting analysis also revealed that for $\alpha > 0.5$, the reaction rate had an exponential trend away from the behaviour observed in the experimental data. Thus, reaction-order integral functions were not able to describe the decomposition process in Ca-Sa-%-WI sorbent.

In the attempt to find an appropriate model, nucleation models proposed by Avrami-Erofeyev were correlated with the α vs. time decomposition curve of the Ca-Sa-25%-WI sorbent. The results shown in Figure 7-3 reveal that Avrami-Erofeyev models A2-A4 satisfied the trend of the sigmoidal-shaped curve [334]. On the basis of correlations performed using Avrami's functions, there was one with a better approximation with the experimental data of the 25 wt. % sample. From Figure 7-3, the A2 model exhibited the best approximation with the α vs. time curve obtained from isothermal data collected at 680°C. In the singular case of A3 and A4, their trends would fit sigmoidal curves in which the decarbonation had faster reaction rates. Therefore, models A3 and A4 were more appropriate for transformations with quicker acceleratory and deceleratory stages. Consequently, the curve fitting results confirm that A2 was the most adequate algebraic expression to describe the decomposition trend of the Ca-Sa-25%-WI sorbent. However, it must be highlighted that for $\alpha > 0.83$, the desorption reaction had a quicker deceleratory period compared to the modelled A2 curve. The experimental curve indicated a rapid decarbonation prolonged until conversions above 0.9. Despite this small variation of the TGA conversion curve and the predicted A2 line, excellent correlation coefficients $R^2 > 0.998$ were reached.

According to the curve fitting analysis of the Ca-Sa-25%-WI sorbent, the good correlation obtained by the Avrami-Erofeyev An models (nucleation and nuclei growth models) can be explained through the physical properties of the sorbent studied Ca-Sa-%-WI. The nucleation, which is the formation of the

new CaO phase, was performed at specific reactive points over the lattice of the sorbent. This assumption was fulfilled by the presence of nanoflakes that act as nucleation sites.

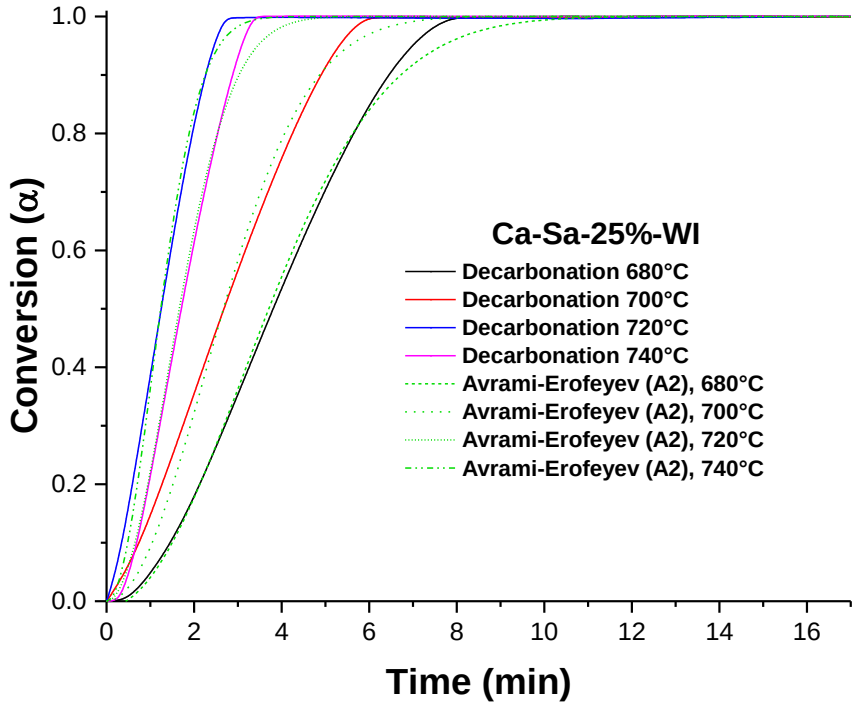

Figure 7-4. α vs. time plots of the thermal decomposition of the $CaCO_3$ phase in the carbonated sorbent Ca-Sa-25%-WI. The different TGA data came from experiments performed isothermally in temperatures between 680 to 740 °C.

Experimental α vs. time curves of thermal decomposition reactions of the Ca-Sa-25%-WI sorbent carried out at 680, 700, 720 and 740 °C are shown in Figure 7-4. According to the sigmoidal-shaped α-time curves, reaction rates had a strong dependence on temperature. This effect is confirmed by increments observed in the slope of isothermal conversion curves. Therefore, the experimental curves indicate that the higher the temperature the faster the release of CO_2. This is consistent with a predictable kinetic effect in which temperature promotes faster reaction rates. The results of fitting the nucleation model A2 with experimental data of the 25 wt. % sample demonstrate that the nucleation-growth model A2 (dashed lines) describe with accuracy decomposition reactions in the window of temperature used to perform the isothermal experiments (Figure 7-4). The consistency of this

model is supported by correlation coefficient values ranging from 0.995-0.997 (Table 7-1).

Table 7-1. Kinetic parameters predicted using the well-known nucleation model Avrami-Erofeyev A2 that describes decomposition processes with a sigmoid trend.

Ca-Sa-25%-WI			Ca-Sa-15%-WI			Ca-Sa-5%-WI		
T(°C)	k (s^{-1})	R^2	T(°C)	k (s^{-1})	R^2	T(°C)	k (s^{-1})	R^2
680	0.02477	0.995	680	0.00699	0.997	680	0.00974	0.996
700	0.03325	0.998	700	0.00856	0.982	700	0.01438	0.984
720	0.05345	0.997	720	0.01173	0.987	720	0.01839	0.998
740	0.07415	0.996	740	0.01809	0.971	740	0.02357	0.996

Sorbents Ca-Sa-%-WI with loadings of 15 and 5 wt. % were also fitted with the Avrami-Erofeyev (A2). The R^2 coefficients ranging of 0.97 - 0.998 ratified A2 as the optimum solid-state model to evaluate the kinetics of decomposition of Ca-Sa-15%-WI and Ca-Sa-5%-WI sorbents. Details of these curve fittings are shown in Appendix B.

Rate constants of Ca-Sa-%-WI sorbents estimated through the application of the solid-state model A2 for non-catalysed systems are reported in Table 7-1. Analogies of kinetic parameters were found in sorbents loaded with 5-25 wt. %. In terms of rate constants (k), the higher the temperature of the isothermal TGA experiments, the greater the rate constants. This effect was coherent with the kinetic theory for which, as was mentioned before, rate constant increases as the temperature goes up. This effect was observed in all Ca-Sa-%-WI sorbents with the different loadings.

The procedure to predict activation energies of Ca-Sa-%-WI sorbents maintained a similar sequence compared to calculations carried out in section 6.2.2, this is, Arrhenius plots ($ln(k)$ vs $1/T$) → linear fitting on the basis of Arrhenius equation → activation energies. For instance, application of the linearized expression (6-10) with the Arrhenius plot for the Ca-Sa-25%-WI sorbent displayed in Figure 7-5 gives as a result the term E/R (slope of the correlated line). Certainly, the E value is obtained after multiplying the slope

by the gas constant 8.314 J mol^{-1} K^{-1}. The linear fit carried out on the rate constants predicted through the Avrami-Erofeyev A2 model, which were consistent as anticipated, revealed a correlation factor of 0.991. According to this mathematical analysis, the minimum energy (E) required to drive the transformation of $CaCO_3$ to CaO was 151 kJ/mol.

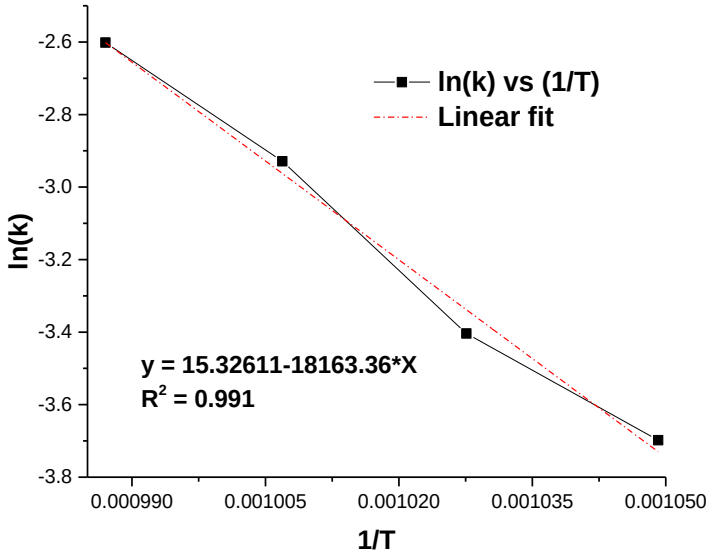

Figure 7-5. Arrhenius plot used to predict the activation energy of the decarbonation reaction of the Ca-Sa-25%-WI sorbent. The rate constants displayed in the plot belong to temperatures of 680, 700, 720 and 740 °C.

As the results of linear fitting to predict the activation energies of Ca-Sa-%-WI sorbents with loadings of 15 and 5 wt. % revealed correlation constants >0.98, Arrhenius plots of sorbents Ca-Sa-15%-WI and Ca-Sa-5%-WI were omitted in this section but incorporated into Appendix B. The summary of activation energies calculated for sorbents prepared via wet impregnation are reported in Table 7-2.

Table 7-2. Activation energies (rounded values) of Ca-Sa-%-WI sorbents with loadings 25, 25 and 5 wt. % predicted on the basis of rate constants in isothermal TGA runs.

Sorbent	Activation Energy *E* (kJ/mol) of the decomposition reaction
Ca-Sa-25%-WI	151
Ca-Sa-15%-WI	127
Ca-Sa-5%-WI	116

The thermo-kinetic study conducted of Ca-Sa-%-WI sorbents suggests that differences in activation energies of the decomposition reaction are intrinsically related with the presence of freestanding aggregates in samples with 15 and 25 wt. %. The discrepancy of E values discerned in Table 7-2 were attributed to the presence of detached aggregates in sorbents with loadings above 15 wt. %. Apparently, large $CaCO_3$ particles required higher energy to release CO_2 from the bulk, and thus, there was an important increase in the activation energy of Ca-Sa-%-WI sorbents with 15 and 25 wt. % compared to the Ca-Sa-5%-WI sorbent.

The activation energy values of the decomposition stage of Ca-Sa-%-WI sorbents predicted using isothermal method were comparable to energies reported in the literature. Comparisons to a full range of activation energies of natural and synthetic calcium-rich compounds are available in Table 2 of reference [331]. On the basis of these kinetic studies performed by various authors, CaO-based CO_2 sorbents (powders) had activation energies ranging between 91.7 kJ/mol to 212 kJ/mol, which were coherent with the values reported in Table 7-2.

7.1.2.2 Kinetic parameters of the decomposition reaction of CaO/Sf-%-U sorbents predicted using isothermal TGA data

In order to determine the kinetic parameters of the decarbonation reaction of CaO/Sf-%-U sorbents, different solid-state rate expressions were fitted once again with isothermal TGA data. As a benchmark, the kinetic study for the CaO/Sf-25%-U sorbent, representing the behaviour of sorbents with loadings of 15 and 5 wt. %, is shown in the current section. The experimental TGA data that exhibit the decarbonation profile of the 25 wt. % loading are displayed in Figure 7-6. This plot illustrates that the decomposition of $CaCO_3$ was slower compared to its equivalent (Ca-Sa-25%-WI sorbents) prepared by wet impregnation. A preliminary evidence of a slower desorption rate is discerned in the time required to reach the full transformation of $CaCO_3$ to CaO (Figure 7-6). The results indicate that a decarbonation delay compared to Ca-Sa-25%-WI occurs in all temperatures tested. For instance, there is a notorious delay

of 2 min for the curve of CaO/Sf-25%-U recorded at 680 °C. Although this lag varied from temperature to temperature, the gap persisted.

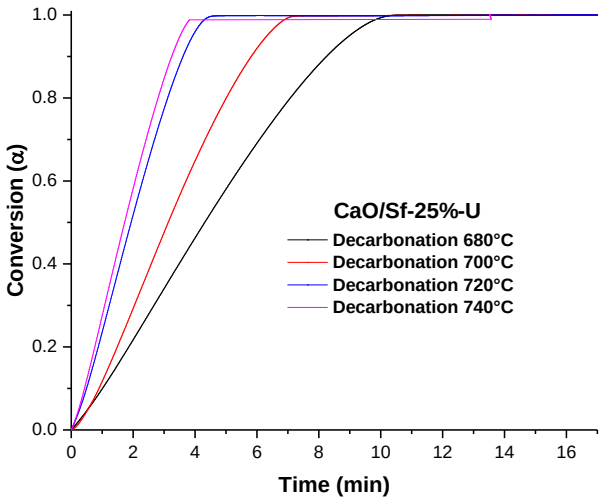

Figure 7-6. α vs. time curves plotted based on the data released by the isothermal heating programs created to perform the decomposition of CaO/Sf-25%-U at different temperature.

In the attempt to predict the rate constants of the decarbonation reaction of the CaO/Sf-25%-U sorbent, reaction expressions of nucleation, diffusion and reaction-order models were fitted to the experimental data. The results indicate that the 3-D diffusion, reaction-order rate of 1st, 2nd, and 3rd order, and power law P2 and P3 models were unable to describe the decarbonation reaction experienced in the CaO/Sf-25%-U (Figure 7-7). Although Avrami-Erofeyev models (A3) and (A4) were algebraic functions that had a good approximation to the experimental data, both nucleation models would fit better in reactions that commence and end with slower decomposition rates. For instance, the transformation of $CaCO_3$ to CaO in the 25 wt. % sample had a rapid start at low conversions ($0.1 \geq \alpha \geq 0$), the slope of the exponential zone ($0.9 \geq \alpha > 0.1$) had moderate reaction rates and the deceleratory region slowed down for a longer time compared to simulated curves by Avrami-Erofeyev models A3 and A4. Thus, curve fitting analysis demonstrates that A2 expression better defined the calcination process in the sorbent CaO/Sf-25%-U.

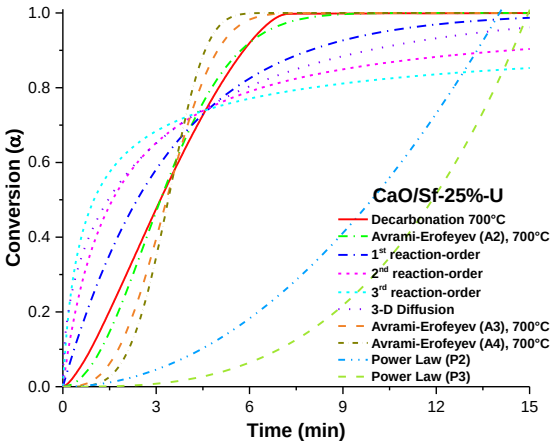

Figure 7-7. Solid-state rate expressions fitted to isothermal data of the decarbonation reaction of the CaO/Sf-25%-U sorbent**.** This conversion curve α vs. time was obtained at 700 °C (selected for illustrative purposes).

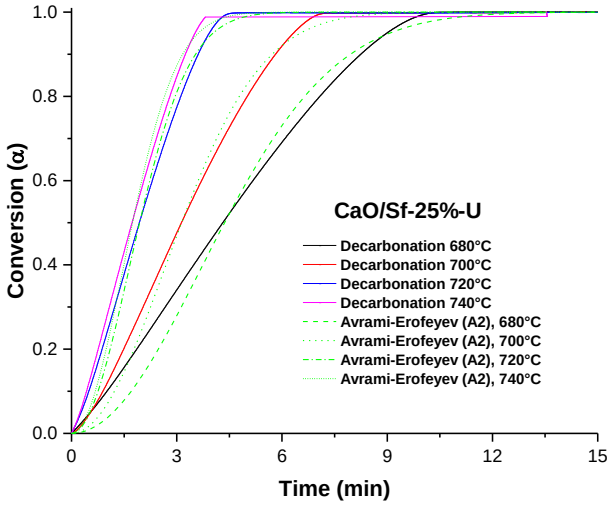

Figure 7-8. Avrami-Erofeyev A2 model correlated with experimental α vs. time curves of the CaO/Sf-25%-U sorbent obtained isothermally at 680, 700, 720 and 740 °C.

The results of fitting Avrami-Erofeyev A2 model with isothermal TGA data of CaO/Sf-25%-U samples collected at 680, 700, 720 and 740 °C are shown in Figure 7-8. The correlation coefficients obtained of the non-linear regression were above 0.98 for all temperatures predicted. This suggests that the A2 expression described properly the mechanism of the decomposition of the CaO/Sf-25%-U sorbent. On the basis of curves of sorbents with loadings of 15 and 5 wt. %, similar R^2 values were estimated. The rate constants and R^2

values predicted for the different CaO/Sf-%-U sorbent are reported in Table 7-3.

Table 7-3. Rate constants and correlation factors R^2 calculated by fitting Avrami-Erofeyev (A2) nucleation model with α-time curves of the isothermal decomposition of CaO/Sf-%-U sorbents.

CaO/Sf-25%-U			CaO/Sf-15%-U			CaO/Sf-5%-U		
T(°C)	k (s^{-1})	R^2	T(°C)	k (s^{-1})	R^2	T(°C)	k (s^{-1})	R^2
680	0.01434	0.989	680	0.03537	0.997	680	0.03482	0.997
700	0.01913	0.995	700	0.04608	0.997	700	0.04472	0.997
720	0.03416	0.994	720	0.07921	0.997	720	0.06284	0.998
740	0.04763	0.993	740	0.10223	0.998	740	0.08731	0.998

An overview of the procedure used to predict the activation energies of CaO/Sf-%-U sorbents is observed through calculations performed with rate constants of the CaO/Sf-25%-U sorbent. The Arrhenius plot that displays the natural logarithm of those reaction rate constants predicted for the 25 wt. % sorbents against the inverse of the temperature are presented in Figure 7-9. The R^2 coefficients >0.982 obtained of the linear fitting indicates that kinetics constants predicted on the basis of correlation of the A2 model with isothermal data were coherent. Despite a slight deviation of the simulated line compared to the graph produced by the kinetic constants was observed, activation energies predicted had a trivial error.

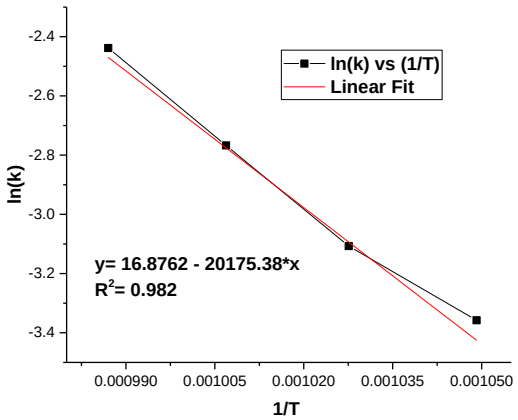

Figure 7-9. Arrhenius Equation correlated with experimental data. The red straight line provides the slope from which the activation energy of the CaO/Sf-25%-U sorbents was predicted from isothermal decomposition.

The activation energies predicted for the CaO/Sf-%-U sorbents by means of Arrhenius plots are reported in Table 7-4. Although Arrhenius plots of sorbents CaO/Sf-15%-U and CaO/Sf-5%-U were not displayed in the current section, their correlation factors measured (>0.967) were within allowable limits, namely above 0.95. According to the activation energies predicted, a downward trend was found as the loadings of CaO decreased. These results were parallel with those obtained for Ca-Sf-%-WI. Apparently, this trend is attributed to changes morphology and porosity, which as observed in sections 4.3-4.6, varied significantly between highest and lowest CaO loadings. For instance, 25 and 15 wt. % have nanoflakes and agglomerates, whilst the 5 wt. % sample does not have freestanding particulate matter. In terms of textural properties, the surface area decreased in the sequence 25 wt. %> 15 wt. % > 5 wt. %. Hence, the increase in the minimum energy for performing desorption of CO_2 could be apparently justified by changes of surface area and the presence of detached agglomerates.

Table 7-4. Activation energies (rounded values) of CaO/Sf-%-U sorbents calculated on the basis of kinetic constants derived from fitting the A2 model with isothermal experimental TGA.

Sorbent	Activation Energy *E* (kJ/mol) $CaCO_3$ decomposition
CaO/Sf-25%-U	168
CaO/Sf-15%-U	143
CaO/Sf-5%-U	128

The results of *E* listed in Table 7-4 showed strong agreement with activation energies of other CaO-based sorbents reported by different authors in the literature. It is worth mentioning that the comparison was performed with a full range of alternative natural and synthetic sorbents and for which activation energies were predicted using a broad range of solid-state model expressions. For instance, in the kinetic study carried out by Guler et al. and Borgwardt using natural CaO [335, 336], activation energies of 200 kJ/mol of the decarbonation reaction were obtained. According to Table 7-4, there was a decrease in the energy barrier to be overcome to release CO_2 and these

changes might be associated with: 1) differences in morphology and porosity, 2) method used to collect data and 3) solid-state model and numerical method used to correlate with experimental data.

7.1.2.3 Kinetic study of the decarbonation reaction of CaO/Sf-%-SH sorbents through the isothermal method

The thermo-kinetic study related to the decarbonation reaction of CaO/Sf-%-SH sorbents is presented in the course of this section. The evolution of the CO_2 desorption reactions of the 25 wt. % sample (sorbent used as a benchmark) tested isothermally at 680, 700, 720, and 740 °C is exhibited in the plot of Figure 7-10. These conversion curves, which displayed an S-shape, had a decarbonation pathway with different behaviour at low conversion ($\alpha < 0.1$) compared to sorbents Ca-Sa-%-WI and CaO/Sf-%-U. Despite their analogy observed in the trend of the acceleratory and deceleratory regime ($0.1< \alpha < 1$), the main differences found were: 1) the time taken to reach decomposition was longer for CaO/Sf-%-SH sorbents and 2) in the initial period of the decarbonation reaction, conversion did not follow an exponential trend. In terms of the decarbonation time (Figure 7-10), the CaO/Sf-25%-SH sorbent showed a slower decarbonation in contrast with sorbents Ca-Sa-25%-WI and CaO/Sf-25%-U. For instance, at 680 °C, the transformation of $CaCO_3$ to CaO took ~11 min to complete, whilst sorbents Ca-Sa-%-WI and CaO/Sf-%-U with 25 wt. % took ~7.7 and ~9.8 min respectively. This dephasing was apparently induced by the textural characteristics of CaO/Sf-25%-SH, namely a network of narrow pores that would have slowed down the release of CO_2. For the reaction rate at low conversions ($0.1 \geq \alpha \geq 0$), the insert added to the α vs. time plot of Figure 7-10 confirms the atypical evolution of the conversion. This linear and sloped decomposition trend was attributed to a fast desorption of CO_2 on the most exposed $CaCO_3$ that is coating Saffil fibres.

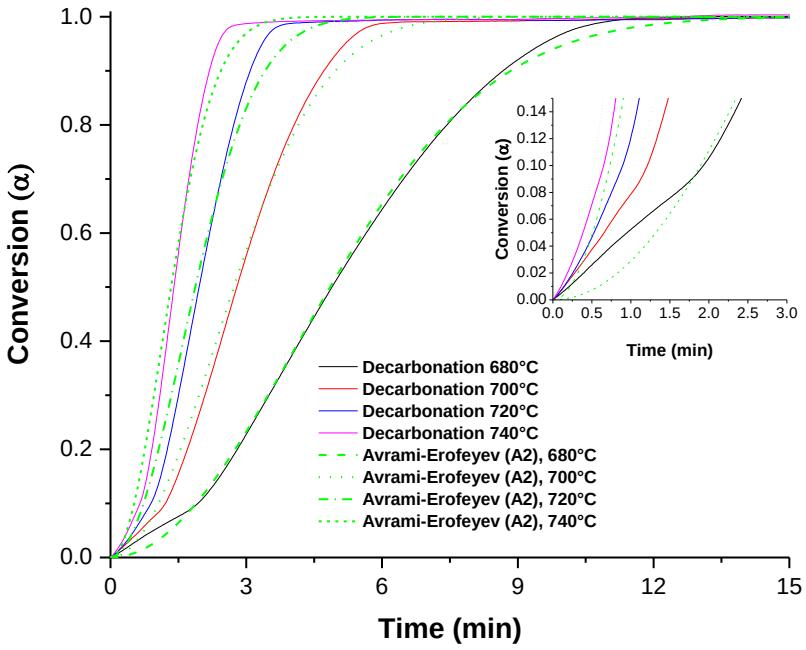

Figure 7-10. Experimental α vs. time curves of the CaO/Sf-25%-SH sorbent plotted on the basis of experimental data registered at isothermal conditions. Avrami-Erofeyev (A2) model was used to predict the rate constants.

On the basis of the sigmoidal trend of the decomposition curves of the CaO/Sf-25%-SH sorbent and also of samples with 5 and 15 wt. % loadings (curves reported in Appendix B), the determination of kinetic constants was carried out by Avrami-Erofeyev A2. The curve fitting analysis with models such as power law (P1, P2 and P3), diffusion and reaction-order models was eluded because of previous correlation results of sorbents Ca-Sa-%-WI and CaO/Sf-%-U exhibited in Figure 7-3 and Figure 7-7. The results reported in Table 7-5 confirm a positive non-linear relationship of the A2 model with conversion curves registered at the different temperatures. The correlation coefficients calculated for the CaO/Sf-%-SH samples with 5-15 wt. % loadings above 0.986 confirm acceptability of the A2 expression. Although the simulated curves had a good correlation between $0.1 \leq \alpha \leq 0.9$, A2 curves were out of phase with experimental points at conversions below 0.1 and above 0.9 (Figure 7-10). As discussed above, the heterogeneity of the CaO coating and the characteristics of the pores (narrow pores) produced slight variations of simulated curves with TGA conversion curves. The kinetic constants and R^2

coefficients predicted on the basis of the A2 expression are reported in Table 7-5.

Table 7-5. Summary of rate constants obtained from α vs. time plots of isothermal decomposition of the CaO/Sf-%-SH sorbents. The model fitted with experimental data to predict *k* values was Avrami-Erofeyev A2.

CaO/Sf-25%-SH			CaO/Sf-15%-SH			CaO/Sf-5%-SH		
T(°C)	k (s^{-1})	R^2	T(°C)	k (s^{-1})	R^2	T(°C)	k (s^{-1})	R^2
680	0.02678	0.999	680	0.02094	0.998	680	0.02167	0.999
700	0.03751	0.997	700	0.03097	0.993	700	0.03135	0.998
720	0.05455	0.994	720	0.04864	0.998	720	0.03922	0.995
740	0.09713	0.993	740	0.08150	0.986	740	0.04743	0.988

The prediction of the activation energies of CaO/Sf-%-SH sorbents was carried out using the kinetic constants reported in Table 7-5. As a benchmark, the Arrhenius plot traced with rate constants *k* of the CaO/Sf-%-SH sorbent with 25 wt. %, correlated using the linearized Arrhenius equation (6-10), is shown in Figure 7-11. The correlation coefficient 0.978 indicates the coherence of kinetic constants predicted through the A2 model with experimental data. As expected, comparable results were found in sorbents with 15 and 5 wt. %, thus, their Arrhenius plots with linear fitting analysis integrated were added in Appendix B.

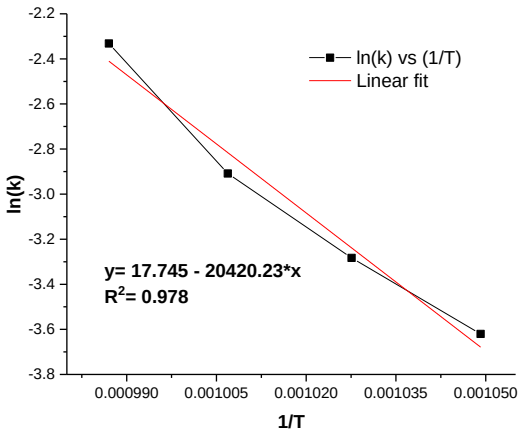

Figure 7-11. Arrhenius plot used to predict the activation energy of the isothermal decomposition of the CaO/Sf-25%-SH sorbent. The reaction rate coefficients were obtained of the mathematical fitting of the Avrami-Erofeyev model A2 with experimental conversion curves

The activation energies of CaO/Sf-%-SH predicted through the mathematical regression using the linear expression proposed by Arrhenius are reported in Table 7-6. Contrary to sorbents Ca-Sa-%-WI and CaO/Sf-%-U, random activation energies values suggest inhomogeneity of the coatings. The formation of CaO aggregates on the surface of Saffil would probably participate in non-trend activation energies observed in Table 7-6.

Table 7-6. Activation energies of isothermal decomposition of CaO/Sf-%-SH sorbents calculated on the basis of isothermal data.

Sorbent	Activation Energy *E* (kJ/mol) $CaCO_3$ decomposition reaction
CaO/Sf-25%-SH	171
CaO/Sf-15%-SH	182
CaO/Sf-5%-SH	103

7.1.2.4 Prediction of Kinetic parameters of the decarbonation reaction of CaO/Sf-%-Oct sorbents using the isothermal method

In the current section, thermo-kinetic study of the decomposition of $CaCO_3$ to CaO of CaO/Sf-Oct sorbents were performed. As a benchmark, the kinetic study of the CaO/Sf-25%-Oct sorbent, which encompasses the prediction of the kinetic parameters, is shown below. The α vs. time curves of the 25 wt. % samples obtained of isothermal experiments driven with decomposition temperatures in the range of 680–740 °C are shown in Figure 7-12. These conversion plots illustrate that the time to attain a full decomposition varies considerably between 680°C and 740 °C, namely ~9 min and >3 min, respectively. This difference suggests that the decarbonation reaction, which is thermally activated, is very sensitive to changes in temperature (Figure 7-12). As expected, the thermodynamics of the decomposition reaction (endothermic) is favoured at high temperatures.

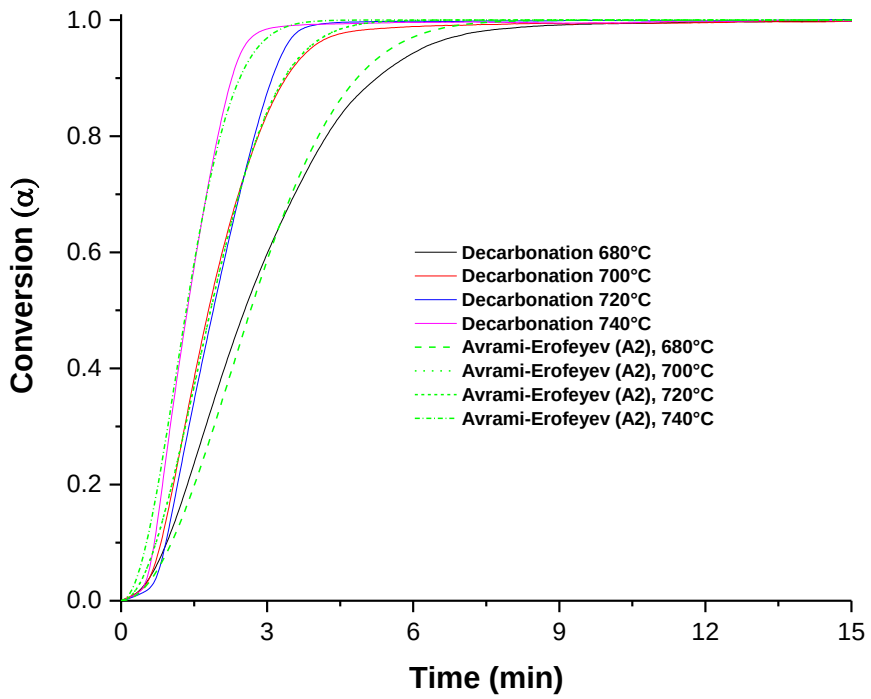

Figure 7-12. Decomposition curves of the CaO/Sf-25%-Oct sorbent with fitting analysis performed by using the Avrami-Erofeyev (A2) model. The dashed lines represent the simulated isothermal decomposition reactions at temperatures of 680, 700, 720 and 740 °C.

The experimental α vs. time curves of the CaO/Sf-25%-Oct sorbent reveal also a sigmoidal decomposition trend compared to sorbents Ca-Sa-%-WI, CaO/Sf-%-U and CaO/Sf-%-SH. This comparable behaviour leads to avoid fitting models such as diffusion and reaction-order, and thus, concentrate the curve analysis on the Avrami-Erofeyev A2 model. This algebraic expression correlated with experimental TGA data gave R^2 coefficients above 0.996. Accordingly, the A2 nucleation model was a reliable expression to simulate the decomposition reaction progress and obtain the kinetic parameters. The rate constants and correlation coefficients predicted through model fitting with isothermal TGA data of CaO/Sf-%-Oct sorbents with 5-25 wt. % loadings are reported in Table 7-7. In terms of the rate constants of CaO-Saffil sorbents with octahedral particles deposited over Saffil supports, their values had the same order of magnitude of the sorbents evaluated so far. These results indicate coherence between the kinetic A2 model and experimental data, which have been predicted for the decomposition reaction under isothermal conditions. As a reference, α vs. time plots of sorbents CaO/Sf-15%-Oct and CaO/Sf-5%-Oct were incorporated in Appendix B.

Table 7-7. Reaction rate constants and R^2 coefficients calculated for the CaO/Sf-%-Oct sorbents loaded with 5, 15 and 25 wt. %. The calculation was carried out using Avrami-Erofeyev (A2) model that is regularly used for decomposition processes.

CaO/Sf-25%-Oct			CaO/Sf-15%-Oct			CaO/Sf-5%-Oct		
T(°C)	k (s^{-1})	R^2	T(°C)	k (s^{-1})	R^2	T(°C)	k (s^{-1})	R^2
680	0.02678	0.996	680	0.03032	0.996	680	0.03032	0.992
700	0.03454	0.999	700	0.03803	0.999	700	0.03718	0.999
720	0.03933	0.996	720	0.05894	0.996	720	0.05692	0.997
740	0.05321	0.996	740	0.07442	0.996	740	0.07442	0.993

The Arrhenius plot of the CaO/Sf-25%-Oct sorbent used to demonstrate the suitability of the methodology applied to predict kinetic constants with experimental data is shown in Figure 7-13. Although the reaction rate constant obtained at 720°C was slightly out of phase, the linear regression revealed an acceptable correlation factor of 0.977. This deviation, which produces only an error of ±5 % in conversion with respect to the linear trend predicted, is caused by the proximity of experimental data registered at 700 and 720°C. Details of the linear fitting analysis performed on Arrhenius plots of sorbents CaO/Sf-%-Oct with loadings of 15 and 5 wt. % used to calculate the activation energies are shown in Appendix B.

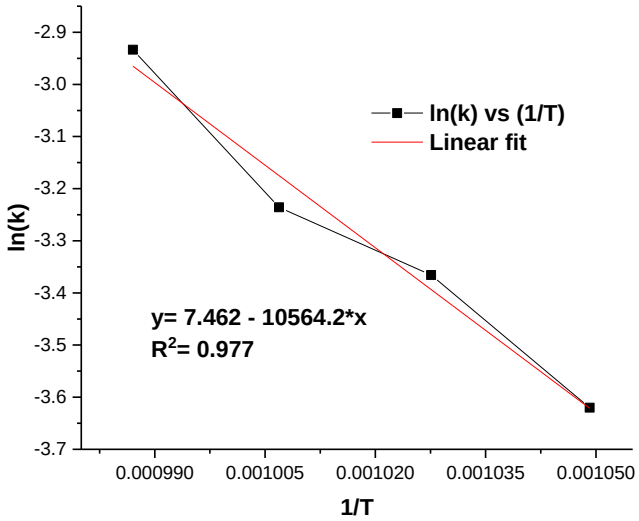

Figure 7-13. Arrhenius plot of the logarithm of the reaction rate constants against the inverse of the temperature. The rate constants correspond to decarbonation experiments performed on CaO/Sf-25%-Oct at 680, 700, 720, and 740 °C under isothermal conditions.

The activation energies *E* predicted for the CaO/Sf-%-Oct sorbents are reported in Table 7-8. The results indicate a strong dependence with the loading percentage, the higher the amount of CaO, the higher the activation energy. Compared to sorbents Ca-Sa-%-WI and CaO/Sf-%-U, the activation energies of the CaO/Sf-%-Oct samples had a different behaviour. The energy barrier needed to undertake the decarbonation reaction did not rely on the octahedral morphology as was understood in the sorbents mentioned above, but textural properties seem to have a strong influence. As confirmed in section 4.6.3, the CaO/Sf-25%-Oct sorbent exhibited the largest pore radius (3.28 nm), and thus, its network of pores, which are classified in the range of mesoporosity, permitted the transformation of $CaCO_3$ with lower energy requirements. Hence, the results exhibited in Table 7-8 suggest the activation energy of CO_2 desorption decreased as the pore radii in the CaO/Sf-%-Oct sorbents increased [337]. This can be explained by considering that the CO_2 would be released faster from the bulk of the octahedra to the exterior though bigger pores.

Table 7-8. Activation energies calculated on the basis of reaction rate constants obtained by fitting the Avrami-Erofeyev (A2) equation with isothermal decomposition experimental TGA data.

Sorbent	Activation Energy *E* (kJ/mol) $CaCO_3$ decomposition	Pore radius (nm)
CaO/Sf-25%-Oct	88	3.28
CaO/Sf-15%-Oct	126	2.4
CaO/Sf-5%-Oct	125	2.17

7.2 Kinetic study of the decomposition reaction in CaO-based CO_2 sorbents performed under non-isothermal conditions

The thermo-kinetic analysis of the decarbonation reaction performed on sorbents Ca-Sa-%-WI, CaO/Sf-%-U, CaO/Sf-%-SH and CaO/Sf-%-Oct using the isothermal method allied with results of alternative CaO-based sorbents demonstrate that several factors influence on the activation energy values

(sections 7.1-7.1.2). For instance, the morphology of the CaO, textural properties (specific surface area, pore size and pore volume), the method used for heating the sample under study (isothermal), TGA's furnace atmosphere, etc. are factors that may promote variations on the apparent activation energy *E*. This evidence suggests leading to study the kinetics of the transformation of $CaCO_3$ to CaO through an alternative TGA method such as the non-isothermal method in which dynamic heating conditions are used.

The procedure followed to perform the non-isothermal measurement of the decarbonation reaction is illustrated in Figure 7-14. The thermal TGA program designed to conduct the non-isothermal analysis encompassed three main stages: 1) activation of the CaO-Saffil sorbents, 2) carbonation reaction using optimal conditions (temperature and time) predicted through the multicycle CO_2 sorption/desorption trials (section 5.2) and 3) decarbonation reaction. More details related to the stages immersed in the non-isothermal experiments are displayed in Figure 7-14.

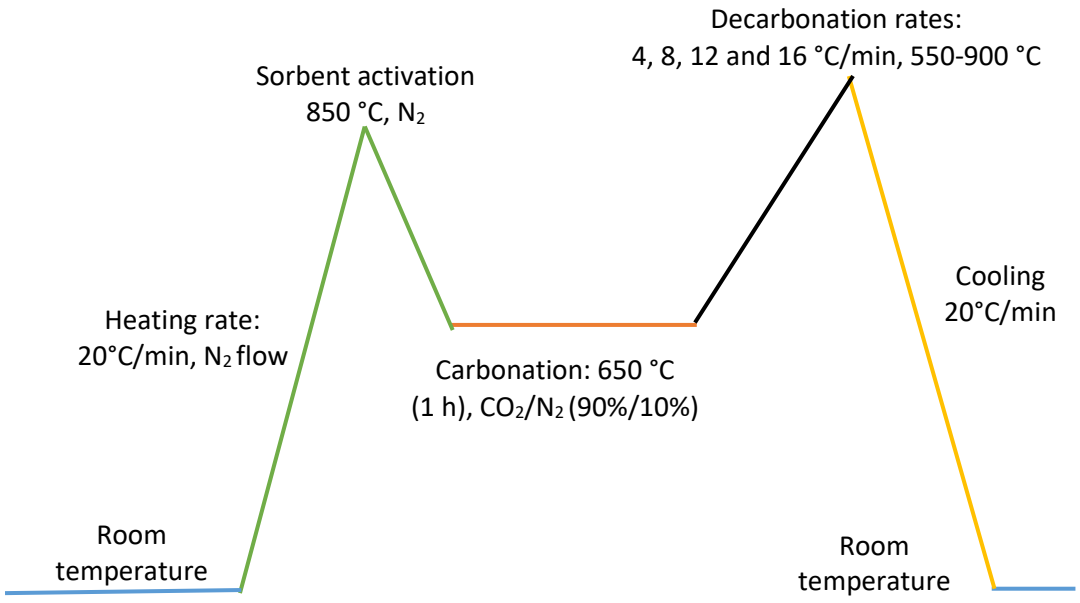

Figure 7-14. Sequence of non-isothermal experiments performed at different calcination rates and in a temperature range of 550 to 900°C. The thermal decomposition begins after exposing the CaO-Saffil sorbents to a carbonation process for 1 h at 650 °C.

According to the diagram of Figure 7-14, samples of CaO-Saffil sorbents prepared through wet impregnation and precipitation method were initially activated at 850 °C in pure N_2 (1^{st} stage). Subsequently, the sorbents were carbonated for 1h using an atmosphere enriched with CO_2, namely composed of 90% CO_2 with N_2 as balance (2^{nd} stage). Then, the decomposition data were recorded as soon as a gas box (integrated to the TGA Mettler Toledo system) swapped CO_2/N_2 to just N_2, but preserving a flow rate of 50 cm^3/min (3^{rd} stage). The TGA program was planned to monitor the thermal history of the decarbonation reactions performed at heating rates of 4, 8, 12 and 16 °C/min while these rates were selected on the basis of research works reported by various authors [322, 338] as well as a wide spectrum of reaction rates would provide more evidence of the mutual dependence between the fractional conversion and temperature (slow and fast desorption rates). In terms of the temperature range for the dynamic decomposition stage, the analysis started and ended at 550°C and 900°C, respectively. The amount of sample used to perform the different TGA analysis was ~15 mg. An overview of the procedure for data collections described above is displayed in Figure **7-14**.

7.2.1 Thermo-kinetic analysis: prediction of kinetic parameters using isoconversional methods

In the introductory section of Chapter 6, a detailed discussion of solid-state models used to predict the kinetic parameters of non-catalysed reactions was presented. These algebraic expressions, which can be applied to study the decomposition of a two-phase system (solid-gas reaction, equation (7-1)), are founded on mechanistic assumptions. Although the models implemented sometimes are to some extent unrealistic, a doubt exists whether these mathematical equations are able to predict thermo-kinetic properties of experimental data collected under certain conditions such as temperature and time. In theory, the reliability of the isothermal method is restricted to one step reactions. These limitations lead to use isoconversional methods, which in addition to being capable of addressing complex reactions that involve multiple steps, requires minimal a priori information.

$$A_{(solid)} \rightarrow B_{(Solid)} + C_{(gas)} \quad (7\text{-}1)$$

Table 7-9. Different well-known isoconversional methods used to predict the activation energy of the decomposition reaction [322].

Method	Equation	
Ozawa-Flynn–Wall method	$\ln(\beta) = ln\frac{0.0048\,A\,E}{g(\alpha)R} - 1.0516\frac{E}{RT}$	(7-2)
Friedman method	$\ln\left(\frac{d\alpha}{dt}\right)_{\alpha,i} = \ln\left(\beta\frac{d\alpha}{dT}\right)_{\alpha,i} = ln[f(\alpha)A\,] - \frac{E}{RT}$	(7-3)
Coats-Redfern method	$\ln\frac{g(\propto)}{T^2} = ln\left[\frac{AR}{\beta E}\right] - \frac{E}{RT}$	(7-4)
Kissinger-Akahira-Sunose method	$\ln\frac{\beta_i}{T_{\alpha,i}^2} = ln\frac{A_\alpha R}{g(\alpha)E_\alpha} - \frac{E_\alpha}{RT_{\alpha,i}}$	(7-5)

Where:

$\boldsymbol{\beta = \frac{dT}{dt} = constant\ rate\ of\ temperature\ change}$ *(heating rate)*
$\boldsymbol{g(\alpha)}$
$\boldsymbol{= function\ depended\ on\ conversion\ mechanism\ and\ mathematical\ model}$
$\boldsymbol{\alpha = conversion}$
$\boldsymbol{T = temperature}$
$\boldsymbol{E = activation\ energy}$
$\boldsymbol{R = ideal\ gas\ constant}$
$\boldsymbol{A = pre - exponentioal\ factor}$

Nowadays, various isoconversional models concentrated in the study the kinetics of decomposition reactions are available in the literature [339]. Two of the most widely used methods used for thermal data correlation are the Ozawa-Flynn–Wall (OFW) and Friedman methods. The OFW model also termed as “integral isoconversional method” was the first method for non-isothermal data treatment [339]. Friedman, who reported the second method, defined its expression as a differential isoconversional method because the plots used for performing the mathematical analysis involved mass loss

curves obtained by applying the first derivate. The Ozawa's method has a more generalized approach to be a real model-free method, whilst Friedman built his model opened to reactions of *n*-order in which solid-state rate expressions could be fitted [340, 341]. The equations proposed by OFW and Friedman are reported in Table 7-9 [322].

Authors such as Kissinger-Akahira-Sunose (KAS) and Coats-Redfern performed adjustments to model-free methods for predicting activation energies of the decomposition of materials using non-isothermal data [259, 342, 343]. In the particular case of the KAS method, its expression was built on the basis of the concept of reduced time (integral of Arrhenius exponential over time) introduced by the Ozawa's kinetic model. For the Coats and Redfern method, this is an integral expression in which an asymptotic approximation is used to find a solution for the thermal degradation of the sample being study. The mathematical expressions proposed by Kissinger-Akahira-Sunose and Coats-Redfern are also reported in Table 7-9.

7.2.1.1 Kinetic study of the decarbonation reaction of sorbents Ca-Sa-%-WI, CaO/Sf-%-U, CaO/Sf-%-SH and CaO/Sf-%-Oct using the Ozawa-Flynn–Wall method

For the prediction of kinetic parameters through the isoconversional method proposed by Ozawa-Flynn–Wall, mass loss data obtained at different heating rates and temperatures in TGA are required. This non-isothermal data, which are correlated with the OFW expression, are converted to reaction rates. The result of treating experimental data of the decomposition process is activation energies, which are useful to determine the reaction mechanism. According to the Kinetics Committee of the International Confederation for Thermal Analysis and Calorimetry (ICTAC), isoconversional methods are a reliable technique to predict the kinetic parameters through data obtained from techniques based on the thermal analysis. Therefore, the thermo-kinetic study presented in this section was carried out on the basis of TGA experiments.

The iterative method proposed by Ozawa-Flynn–Wall to calculate the activation energies and frequency factors is run through equation (7-2) shown

in Table 7-9. For a reliable analysis, the method is applied in a range of conversions of 0.1 to 0.9. In addition, this method must be correlated with experimental data obtained from at least three different heating rates to predict activation energies with minimal errors. The apparent activation energies (*E)* and pre-exponential factors (*A*) values were calculated correlating equation (7-2) with plots of logarithms of heating rates *ln(β)* against the inverse of temperature (*1/T*). As expected, experimental conversion curves were the starting point for the prediction of the kinetic parameters. As a benchmark, α vs. temperature plots of CaO-Saffil sorbents recorded in dynamic heating profiles (4, 8. 12 and 16 °C/min) are displayed in Figure 7-15.

The conversion plots shown in Figure 7-15 indicated that the faster the heating rate, the greater was the dephasing towards higher decomposition temperatures. Although this effect is common in the non-isothermal method, double Y-axis plots would add important information of the mutual dependence of conversion, time, and temperature. The α-temperature (°C) vs time (min) plots of sorbents Ca-Sa-25%-WI and CaO/Sf-25%-Oct used as references (Figure 7-16) reveal that the decarbonation reaction begun within shorter periods at higher heating rates. Evidently, low heating rates prolonged the decomposition reaction but reduced the temperature in which the CO_2 was released.

The OFW plots were used to calculate the activation energy of the decomposition of $CaCO_3$ to CaO in CaO-Saffil sorbents with 25 wt. % and are displayed in Figure 7-17. The set of straight lines observed in these plots provide activation energy values for a conversion range $0.1 \leq \alpha \leq 0.9$ ($\alpha = x$ in all plots). The results indicate that the dependence of *ln(β)* with *1/T* is linear. The association of the lines plotted with the OFW equation (7-2) provides $1.052 * E/(RT)$ (lines slope) values, which through separating variables, activation energies ($E = 1.052 * R$) are obtained. The activation energies *E (kJ/mol)* of the thermal decarbonation of sorbents Ca-Sa-25%-WI, Ca-Sa-15%-WI, and Ca-Sa-5%-WI predicted for each conversion (α) are reported in Table 7-10. The apparent activation energy *E* of the desorption reaction corresponded to the statistical mean value predicted for the conversion range of 0.1-0.9.

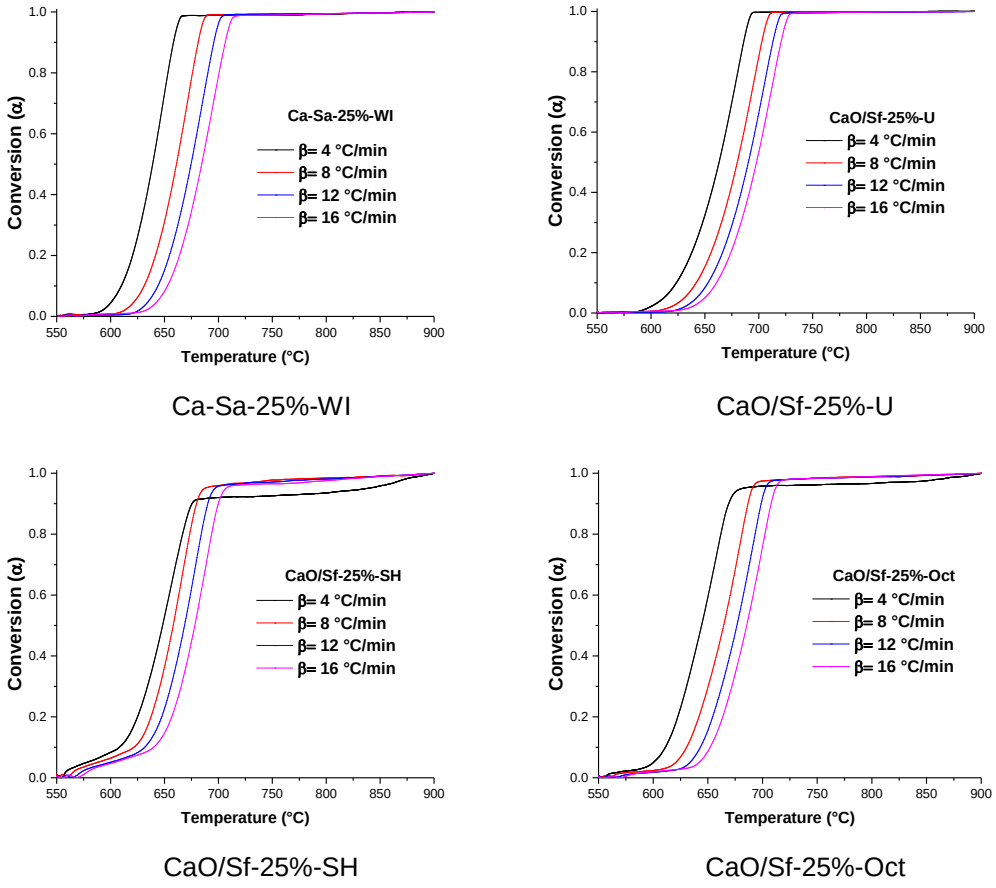

Figure 7-15. α vs. temperature plots of the decomposition reaction of CaO-Saffil sorbents with 25 wt. % loadings obtained under non-isothermal conditions. The dynamic analysis was conducted in a temperature range of 550 to 900°C using heating rates (β) of 4, 8, 12 and 16 °C/min.

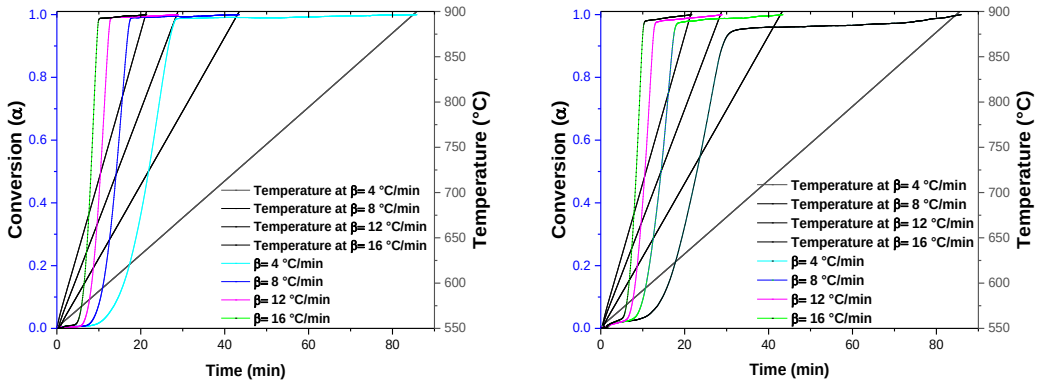

Figure 7-16. Double-Y plots of sorbents Ca-Sa-25%-WI (a) and CaO/Sf-25%-Oct (b) used to understand the effect of the heating rate with temperature-conversion-time.

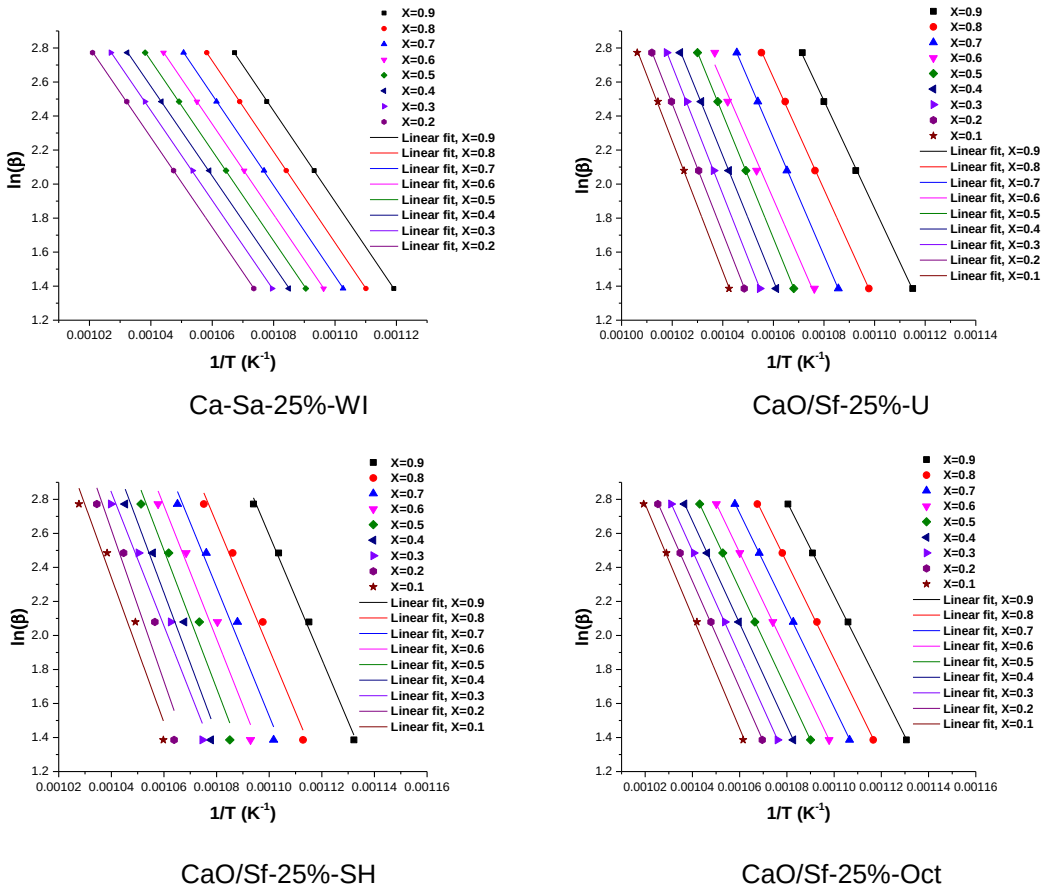

Figure 7-17. ln(β) vs. *1/T* plots used to predict the activation energies of the thermal decomposition of CaO-Saffil sorbents with loadings of 25 wt. % under non-isothermal conditions (x in plots represent α values).

The activation energies of CaO-Saffil sorbents with loadings of 25 wt. % reported in Table 7-10, which were used as a benchmark, reveal slight variations of ±5 kJ/mol. The results indicate that *E* values correspond to the decomposition of the $CaCO_3$ phase in a single step. This effect is confirmed through the plot *E* (kJ/mol) against conversion degree (α) of the Ca-Sa-25%-WI sorbent used as a reference (Figure 7-18) because the straight line situated in ~208 kJ/mol showed dispersion of energies close to the median, and thus, the reaction mechanism only implies the forward reaction of $CaCO_3$ to CaO without intermediate stages.

Table 7-10. Relationship between the activation energy (*E*, kJ/mol) and the conversion degree (α) exhibited through calculations performed by using the Ozawa-Flynn-Wall expression (equation 7-2).

Conversion (α)	*E* (kJ/mol)	Conversion (α)	*E* (kJ/mol)	Conversion (α)	*E* (kJ/mol)
Ca-Sa-25%-WI		**Ca-Sa-15%-WI**		**Ca-Sa-5%-WI**	
0.9	210	0.9	202	0.9	193
0.8	211	0.8	198	0.8	196
0.7	211	0.7	196	0.7	197
0.6	210	0.6	193	0.6	197
0.5	210	0.5	193	0.5	197
0.4	210	0.4	193	0.4	196
0.3	201	0.3	196	0.3	198
0.2	209	0.2	200	0.2	200
0.1	202	0.1	-	0.1	203
Average =	208		196		197

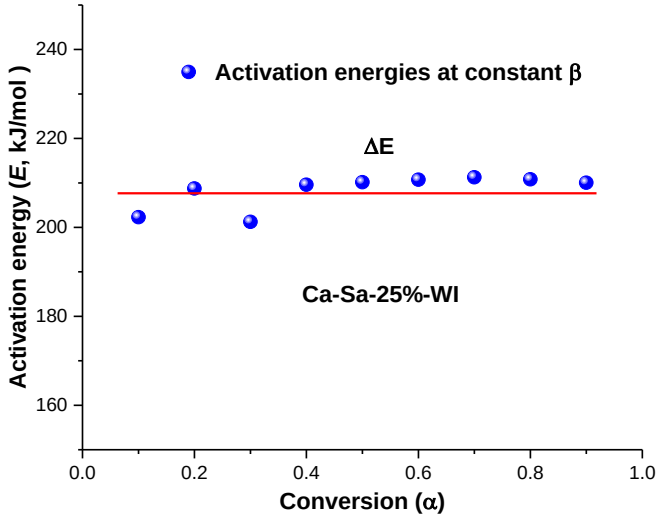

Figure 7-18. Activation energies estimated for the non isothermal decomposition of Ca-Sa-25%-WI sorbent at different conversions degrees by means of the OFW method. The red line represent the statistical mean.

On the basis of activation energies predicted for sorbents CaO/Sf-%-U, CaO/Sf-%-SH and CaO/Sf-%-Oct with their different loadings (5, 15 and 25 wt. %) using the OFW method (plots added into Appendix C), similar ±5 kJ/mol deviations from the statistical mean value were found compared to Ca-Sa-%-WI sorbents. The apparent *E* values calculated for the decomposition of the sorbents mentioned above in the conversion range of 0.1-0.9 are reported in

Table 7-11. Although important differences were found among the global activation energies of CaO-Saffil sorbents, these energies required to trigger CO_2 desorption were found to be within the range of other *E* values of alternative CaO-based sorbents reported by various authors [331, 332]. Based on findings of different research works [344], three processes would potentially produce changes in the thermal behaviour of the decomposition reaction, and thus, on the activation energies: 1) heat transfer to the reaction interface, 2) chemical reaction itself and 3) CO_2 diffusion through the outer CaO layer formed. For sorbents Ca-Sa-25%-WI and CaO/Sf-25%-U, the substantial raise in the activation energy compared to their analogous with 15 and 5% loadings can be attributed to the presence of freestanding agglomerates in which the desorption of CO_2 was limited by diffusion. As expected, detached particulates lose surface area and pores as a result of sintering, and thus, overall reaction rate decreases, whilst the activation energy increases. Compared to freestanding agglomerates, the thermal resistance of nanoflake promoted a rapid decomposition rate with activation energies similar compared to other good-performing CaO-based sorbents of refs [344] and [345].

As expected, inconsistencies of activation energies predicted using isothermal data (A2 model) with non-isothermal method (OFW) were found. These differences in activation energies for CaO-Saffil sorbents were appreciated through the ranges of activation energies of 88-181 kJ/mol and 190-313 kJ/mol predicted by using A2 and OFW models, respectively. A potential cause is the isothermal method itself, as the transformation of $CaCO_3$ to CaO could start before attaining the temperatures settled to perform the isothermal experiments, namely 680, 700, 720 and 740°C. Although this effect was minimized by using the Mettler Toledo TGA/DSC system, the prediction of the activation energies using isothermal data could entail inconsistencies compared to non-isothermal data. The selection of an appropriate reaction model to be correlated with isothermal data, which for complex reactions is a tricky task, plays also an important role in the discrepancies. For instance, in CaO-Saffil sorbents studied through the isothermal method, Avrami-Erofeyev (A2) and (A3) showed good fitting with experimental data, but the correlation coefficients in conjunction with the expertise of the researcher allowed

performing an adequate selection of a solid-state rate expression. Consequently, a more reliable activation energy values were determined.

Table 7-11. Activation energies of non-isothermal decomposition of sorbents CaO/Sf-%-U, CaO/Sf-%-SH and CaO/Sf-%-Oct obtained using the isoconversional method proposed by OFW.

	Sorbents		
	CaO/Sf-25%-U	**CaO/Sf-15%-U**	**CaO/Sf-5%-U**
	E (kJ/mol)	*E* (kJ/mol)	*E* (kJ/mol)
Average =	282	191	202
	Sorbents		
	CaO/Sf-25%-SH	**CaO/Sf-15%-SH**	**CaO/Sf-5%-SH**
	E (kJ/mol)	*E* (kJ/mol)	*E* (kJ/mol)
Average =	313	244	279
	Sorbents		
	CaO/Sf-25%-Oct	**CaO/Sf-15%-Oct**	**CaO/Sf-5%-Oct**
	E (kJ/mol)	*E* (kJ/mol)	*E* (kJ/mol)
Average =	236	219	215

7.2.1.2 Kinetic study of the decarbonation process of CaO-Saffil sorbents through the Friedman method

The Friedman method results from arrangements performed on equation (7-6) defined below. This resulting equation, which is also reported in Table 7-9, presents several advantages compared to other isoconversional methods. For instance, Friedman's equation (7-3) is applicable to a wide range of temperatures and applies to linear positive heating rates. However, for the application of mathematical expression proposed by Friedman, non-isothermal mass loss data collected from the thermogravimetry analysis must be transformed to a differential form. This data manipulation is performed through an advanced software that allows calculating derivative ($d\alpha/dt$) of the input data (conversion data), but this procedure frequently generates noise. Although there are tools to reduce the noise of the derivative, in samples with noisy conversion data, noise would still be a great disadvantage. In this work, amplified noise produced from the numerical differentiation of non-isothermal

TGA data were diminished by signal processing technique such as smoothing. Accordingly, this mathematical treatment contributed to reducing dragging a systematic error throughout the kinetic study driven by using the Friedman method.

$$\frac{d \propto}{dt} = A * e^{\frac{-E}{RT}} * f(\propto) \qquad (7\text{-}6)$$

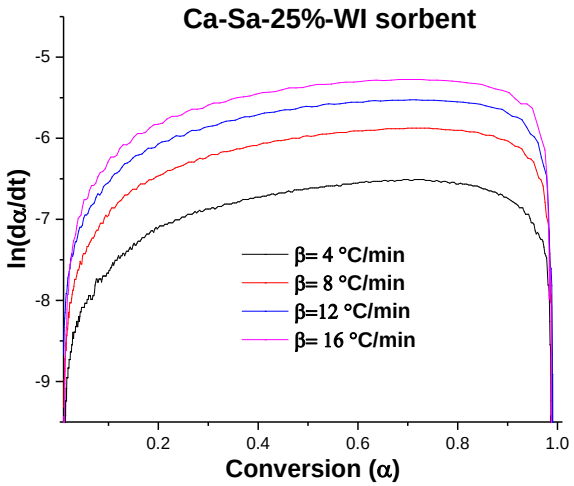

Figure 7-19. Normalized *dα/dt* vs. conversion (α) curves for the decomposition of the Ca-Sa-25%-WI sorbent obtained from a numerical differentiation through the Originpro software. The *dα/dt* values were predicted for heating rates of 4, 8, 12 and 16 °C/min.

As a benchmark, a conventional numerical differentiation analysis performed on the normalized conversion (α) vs time (min) curves of the decomposition of the sorbent Ca-Sa-25%-WI is shown in Figure 7-19. The curves reveal that the noise produced through the differentiation process was effectively reduced by the smoothing technique. Consequently, signal processing of ln(*dα/dt)* - (α) data enhanced the reliability of kinetic parameter predictions of the thermal decomposition reaction.

The plot exhibited in Figure 7-19 suggest that the transformation of $CaCO_3$ to CaO was accomplished in a single step. The regular trend of the curves obtained in the conversion range of 0.1< α <0.9, which does not show apparent deviations, excluded any possibility of a mechanism with two or more reactions. In the case of Ca-Sa-%-WI sorbents with 15 and 5 wt. % loadings

and sorbents CaO/Sf-%-U, CaO/Sf-%-SH and CaO/Sf-%-Oct, their ln(*dα/dt)* vs. (α) plots were incorporated into Appendix C because they showed similar decomposition patterns compared to the reference Ca-Sa-25%-WI.

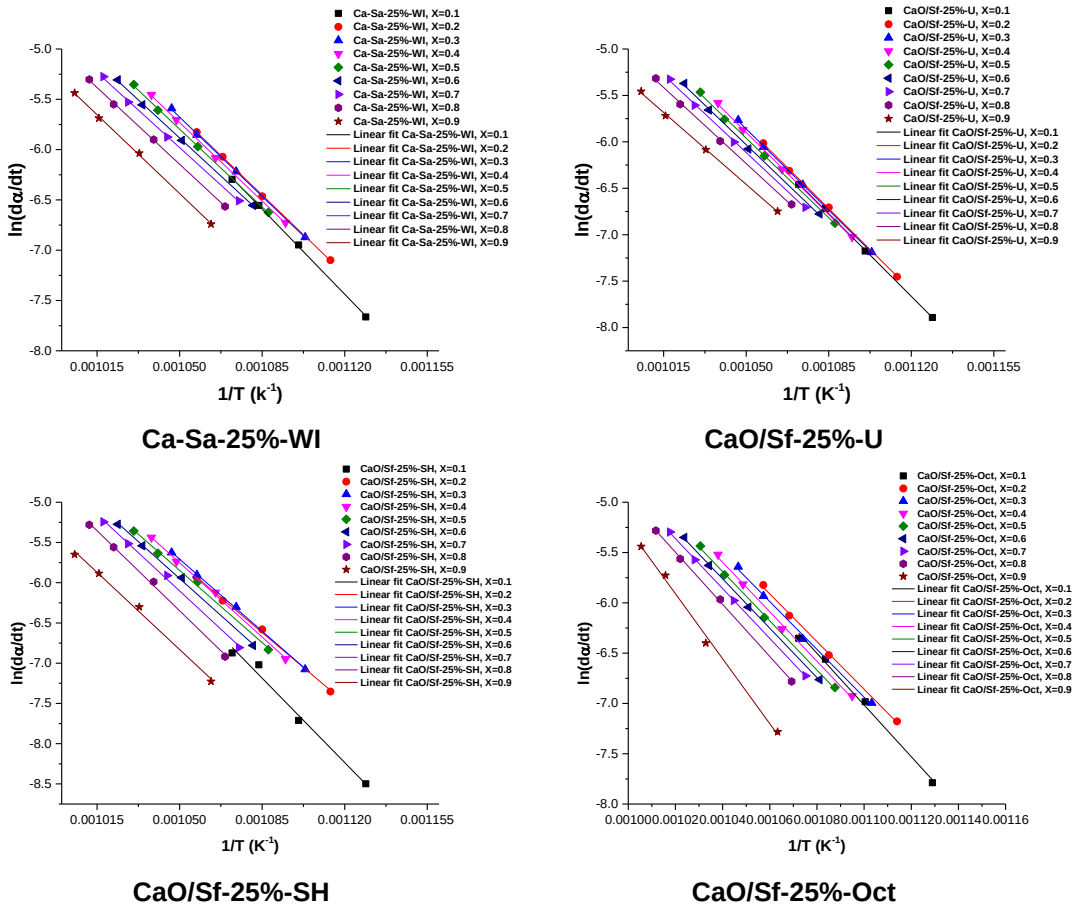

Figure 7-20. Friedman *ln(dα/dt*) vs. *1/T* plots of non-isothermal decomposition of CaO-Saffil sorbents loaded with 25 wt.% of CaO. The points in each straight line are associated with the *dα/dt* values at particular conversions, namely from 0.1 to 0.9 (x in plots represent α values).

Friedman plots, which show the intrinsic relation of $\ln(d\alpha/dt)$ and *1/T* (K^{-1}) in sorbents Ca-Sa-25%-WI, CaO/Sf-25%-U, CaO/Sf-25%-SH and CaO/Sf-25%-Oct, are displayed in Figure 7-20. The numerical differentiation carried out with non-isothermal TGA data confirmed good correlations as the dispersion of $\ln(d\alpha/dt)$ values obtained in the conversion range of 0.1 to 0.9 remained on phase. The coherence observed between Friedman plots and differentiation data allowed predicting activation energies. In relation to the calculation procedure, *E* values are predicted from the slope of the lines $\ln(d\alpha/dt)$ vs *1/T*. The results of the Ca-Sa-25%-WI sorbent used as a reference revealed deviations of activation energy below 6% with respect to

the mean *E*= 184.5 kJ/mol (Figure 7-21). This dispersion of E (kJ/mol) values, collected at different conversion degrees, indicates again the lack of an additional chemical reaction during the decomposition time (no significant increments or reductions on the activation energies observed).

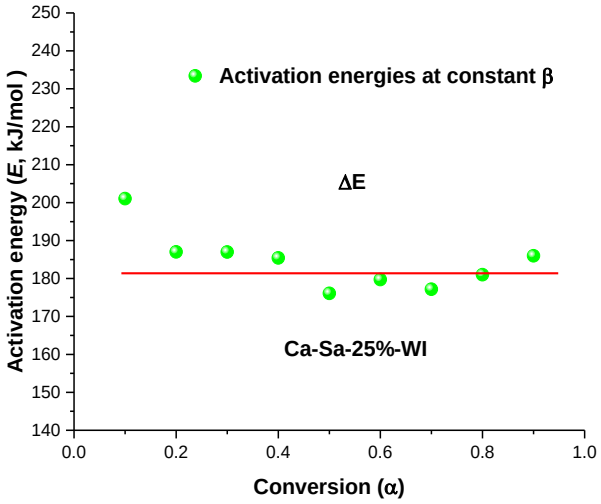

Figure 7-21. Activation energies predicted for the thermal decomposition of Ca-Sa-25%-WI sorbents by Friedman method (equation 7-3)

On the basis of activation energies calculated using Friedman plots (attached in Appendix C) for sorbents prepared via wet impregnation loaded with 15 and 5 wt. % CaO and those prepared by precipitation using urea and NaOH as precipitants (CaO/Sf-%-U, CaO/Sf-%-SH and CaO/Sf-%-Oct), similar decarbonation mechanisms were observed. The dispersion of activation energy values was not that important to consider the existence of a stepped process with two or more kinetics constants. It is worth mentioning that at low and high conversions (α: >0.1 and >0.9), activation energies fluctuated around the mean. According to the numerical data treatment (differentiation of the conversion curves), these fluctuations were attributed to amplified noise. Although data obtained by applying the first derivate on normalized conversion curves were treated with the smoothing signal processing tool of the OriginPro software suit, noise produced at conversions <0.1 and >0.9 generated inaccurate results. Hence, Friedman's method would provide more stable activation energy results in the conversion range of 0.1≤ α ≤0.9.

The global activation energies of Ca-Sa-%-WI, CaO/Sf-%-U, CaO/Sf-%-SH and CaO/Sf-%-Oct predicted from the slopes of the Friedman plots *ln(dα/dt*) vs *1/T* are reported in Table 7-12. The predicted activation energies indicate that the highest barrier to initiate the decomposition of the $CaCO_3$ is manifested by CaO/Sf-%-SH sorbents. Although these results are consistent with predictions of OFW method, there is discrepancy in the *E* values calculated between the OFW and Friedman methods.

Table 7-12. Activation energies predicted for the non isothermal decarbonation reaction of sorbents Ca-Sa-%-WI, CaO/Sf-%-U, CaO/Sf-%-SH and CaO/Sf-%-Oct through the isoconversional method proposed by Friedman.

		Sorbents	
Ca-Sa-25%-WI		**Ca-Sa-15%-WI**	**Ca-Sa-5%-WI**
	E (kJ/mol)	*E* (kJ/mol)	*E* (kJ/mol)
Average =	185	197	196
		Sorbents	
CaO/Sf-25%-U		**CaO/Sf-15%-U**	**CaO/Sf-5%-U**
	E (kJ/mol)	*E* (kJ/mol)	*E* (kJ/mol)
Average =	202	179	186
		Sorbents	
CaO/Sf-25%-SH		**CaO/Sf-15%-SH**	**CaO/Sf-5%-SH**
	E (kJ/mol)	*E* (kJ/mol)	*E* (kJ/mol)
Average =	223	201	241
		Sorbents	
CaO/Sf-25%- Oct		**CaO/Sf-15%- Oct**	**CaO/Sf-5%-Oct**
	E (kJ/mol)	*E* (kJ/mol)	*E* (kJ/mol)
Average =	214	204	198

For the Ca-Sa-%-WI sorbents, consistent measurements were obtained, but contrasting activation energy values were observed in sorbents CaO/Sf-%-U and CaO/Sf-%-Oct. An apparent justification of this discrepancy is the numerical differentiation applied to determine *dα/dt*. As observed in *dα/dt* vs. *α* curves of the Ca-Sa-25%-WI sorbent used as a benchmark (Figure 7-19), although the amplitude of the noise was attenuated drastically, there were oscillations mostly in low and high conversions. This noise was equally intense within the conversion intervals from 0 - 0.2 and 0.85 - 1 regardless the heating rates *β* (°C/min) used to record the non-isothermal data. This effect persisted in all sorbents CaO/Sf-%-U, CaO/Sf-%-SH and CaO/Sf-%-Oct, and plots of *E*

against *α* allowed discerning these abrupt activation energy changes for the conversion intervals of 0 - 0.2 and 0.85 – 1 (results incorporated in Appendix C). Although in theory and practice, the kinetic parameters of decomposition of CaO-Saffil sorbents obtained on the basis of non-isothermal data are inconsistent, their activation energies calculated were within the range of other decarbonation energies of other alternative CaO-based sorbents reported by various authors [322, 331].

7.2.1.3 Kinetic study of the decarbonation reaction of CaO-Saffil sorbents by using non-isothermal data and the Kissinger-Akahira-Sunose method

As has been seen so far, isoconversional methods are a powerful tool to study the kinetics due to the mutual dependence of *E* (kJ/mol) with conversion extend α and decomposition temperature. The Ozawa-Flynn-Wall and Friedman methods have shown being a convenient approach to determine the activation energies of CaO-Saffil sorbents, but more evidence should be obtained to discard any drastic energetic variation, thus, Kissinger-Akahira-Sunose (KAS) method was also evaluated. The mathematical model, kinetic parameters and constants involved in the expression proposed by Kissinger et al. is showed in Table 7-9 and rewritten in equation (7-7). For the KAS method, the kinetic parameters are predicted through plots $ln(\beta/T^2)$ against $1/T$ obtained by varying heating rates (β= 4. 8, 12 and 16 °C/min). The slope and intercept of straight lines traced in a conversion range of 0.1-0.9 correspond to activation energies and pre-exponential factors respectively.

$$\ln\frac{\beta_i}{T_{\alpha,i}^2} = ln\frac{A_\alpha R}{g(\alpha)E_\alpha} - \frac{E_\alpha}{RT_{\alpha,i}} \qquad (7\text{-}7)$$

As a benchmark, plots $ln(\beta/T^2)$ against $1/T$ also termed “KAS plots” of sorbents Ca-Sa-25%-WI, CaO/Sf-25%-U, CaO/Sf-25%-SH and CaO/Sf-25%-Oct are shown in Figure 7-22. The KAS plot of the Ca-Sa-25%-WI sample, which were used as a reference to describe the procedure to predict the activation energies at different conversions, showed the coherence of non-isothermal

data with the kinetic KAS model. The activation energies calculated in the conversion interval of 0.1-0.9 are displayed in Figure 7-23. The dispersion of E values, which had a maximum deviation of 4.5% from the mean (red line), confirmed the good correlation. Accordingly, the prediction of the global activation energy by the KAS method was a consistent approach to study the kinetics of the decomposition of Ca-Sa-25%-WI.

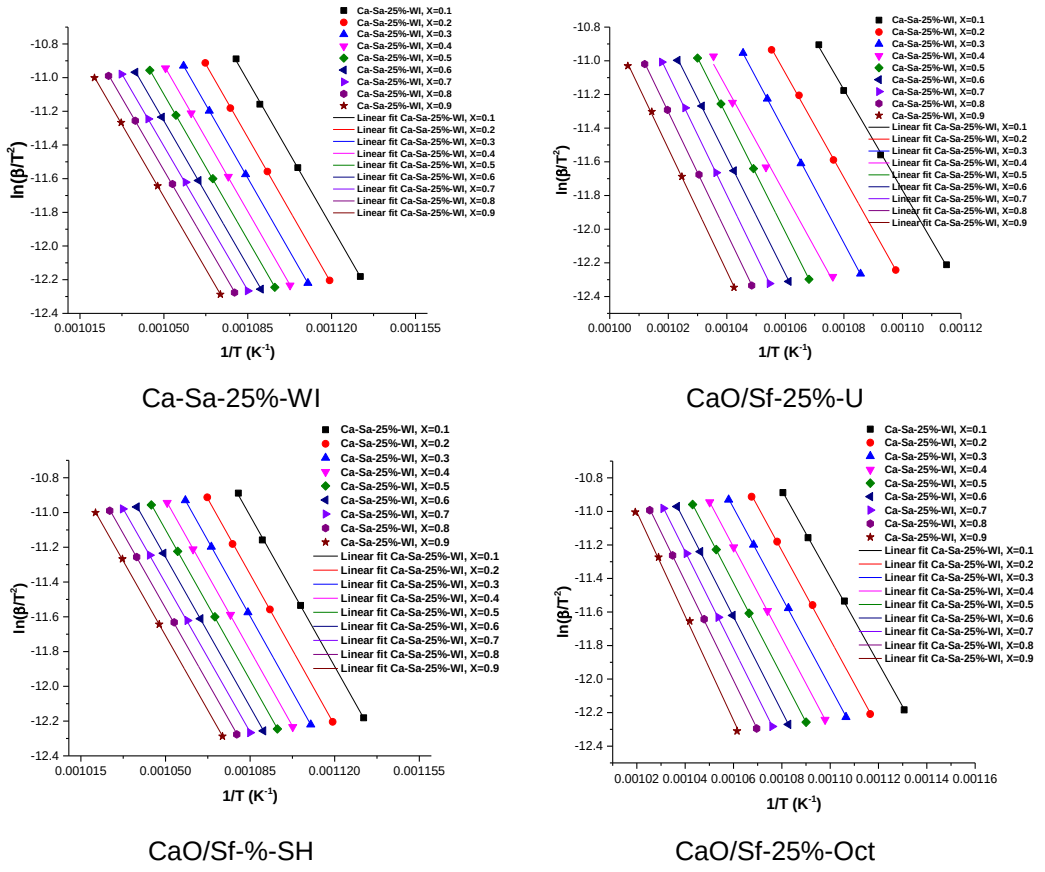

Figure 7-22. KAS plots of CaO-Saffil sorbents with loadings of 25 wt. % for the non-isothermal decarbonation reaction (x in plots represent α values).

On the basis of the results of apparent activation energies calculated for Ca-Sa-25%-WI sorbent, which had almost constant values over the conversions range of 0.1-0.9 (Figure 7-23), suggests that the decomposition reaction was carried out in a single step [317, 338, 346]. For sorbents Ca-Sa-%-WI with 15 and 5 wt. % of CaO, albeit greater instability of the activation energies was found (Figure 7-24), the variations are not important to consider a reaction mechanism controlled by two or more reactions. In the case of sorbents CaO/Sf-%-U, CaO/Sf-%-SH and CaO/Sf-%-Oct impregnated with 5-25 wt. %,

the activation energies calculated by means of the KAS method revealed very similar trends compared to Ca-Sa-%-WI samples, namely apparent energies in phase with the mean and a one-step reaction mechanism. This consistency was documented in plots $ln(\beta/T^2)$ vs. $1/T$ and E vs. α of CaO-Saffil sorbents prepared through precipitation (-U, -SH and -Oct) added into Appendix C

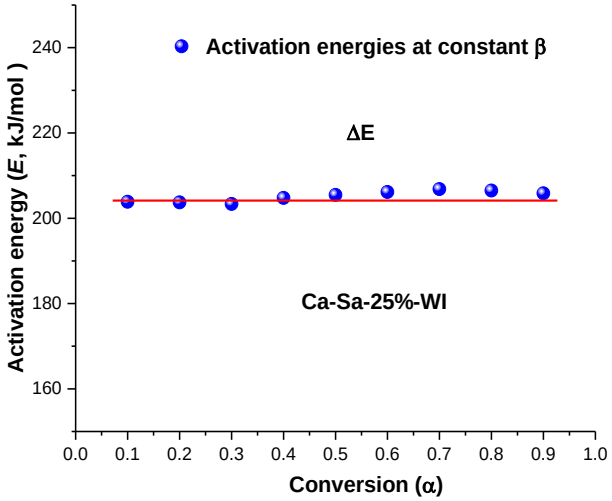

Figure 7-23. Activation energies predicted for the decomposition of Ca-Sa-25%-WI sorbent using the KAS method. The red line in a horizontal position represents the mean.

The global activation energies predicted for all CaO-Saffil sorbents with loadings of 25, 15 and 5 wt. % through the KAS expression are reported in Table 7-13. Comparable activation energies obtained by Kissinger's method with values predicted by the integral method proposed by OFW were observed. Although variation in the activation energy values predicted from integral and differential isoconversional expressions are common, the KAS method yielded activation energies within the same range of those estimated by the Friedman method even when this differential method carried the systematic error caused by amplified noise produced throughout the numerical differentiation ($d\alpha/dt$) of experimental conversion curves (see section 7.2.1.2). As expected, the integral isoconversional method of KAS resulted in a reliable approach to estimate activation energies.

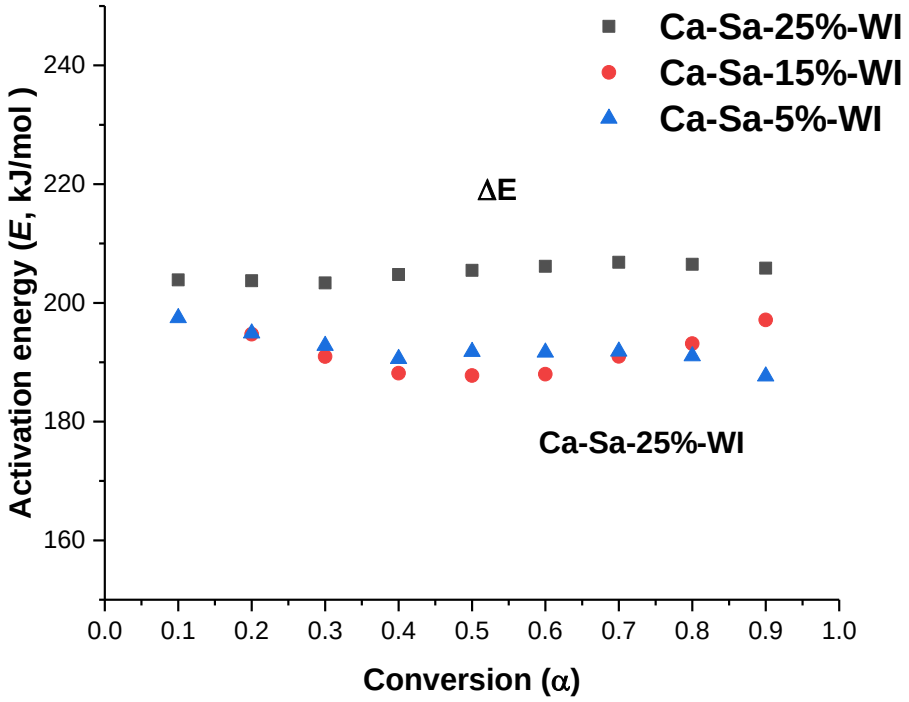

Figure 7-24. Plots *E* (kJ/mol) vs conversion (α) of Ca-Sa-%-WI sorbents loaded with 25, 15 and 5 wt. % of CaO. Stable values *E* in the range 0.1 ≤ α ≤ 0.9 suggest a decomposition reaction carried out in a single step.

Table 7-13. Activation energies of decomposition of sorbents Ca-Sa-%-WI, CaO/Sf-%-U, CaO/Sf-%-SH and CaO/Sf-%-Oct with 25, 15 and 5 wt. % predicted by means of the KAS method.

		Sorbents	
Ca-Sa-25%-WI		**Ca-Sa-15%-WI**	**Ca-Sa-5%-WI**
	E (kJ/mol)	*E* (kJ/mol)	*E* (kJ/mol)
Average =	205	170	192
		Sorbents	
CaO/Sf-25%-U		**CaO/Sf-15%-U**	**CaO/Sf-5%-U**
	E (kJ/mol)	*E* (kJ/mol)	*E* (kJ/mol)
Average =	280	185	197
		Sorbents	
CaO/Sf-25%-SH		**CaO/Sf-15%-SH**	**CaO/Sf-5%-SH**
	E (kJ/mol)	*E* (kJ/mol)	*E* (kJ/mol)
Average =	205	241	278
		Sorbents	
CaO/Sf-25%- Oct		**CaO/Sf-15%- Oct**	**CaO/Sf-5%-Oct**
	E (kJ/mol)	*E* (kJ/mol)	*E* (kJ/mol)
Average =	232	218	211

7.2.1.4 Kinetic study of Ca-Sa-%-WI, CaO/Sf-%-U, CaO/Sf-%-SH and CaO/Sf-%-Oct by the Coats-Redfern method

In the preceding sections, integral and differential isoconversional methods such as OFW, Friedman, and KAS have demonstrated capabilities to predict activation energies of the decarbonation reaction of CaO-Saffil sorbents. The last method proposed not only to predict the activation energies but also to ratify the *E* (kJ/mol) calculated so far, was the isoconversional method proposed by Coats and Redfern. This method is a reliable non-isothermal thermoanalytical rate measurement to calculate kinetic parameters. On the basis of studies reported by various authors, this integral method has proved effective in conduct kinetic studies related to the decomposition and dehydration of a wide range of sorbents in solid phase [343, 347]. The determination of the kinetic parameters by the Coast-Redfern method is performed through equation (7-4) shown below (also reported in Table 7-9):

$$\ln \frac{g(\propto)}{T^2} = ln\left[\frac{AR}{\beta E}\right] - \frac{E}{RT} \qquad (7\text{-}4)$$

where, the term $g(\propto)$ is the integral function that best describes the conversion trend of the decarbonation reaction. As expected, this mathematical function is basically a kinetic model that corresponds to a solid-state reaction mechanism. *R* is the ideal gas constant in J mol^{-1} K^{-1}, *T* corresponds to the absolute temperature and *β* denotes the heating rates used in the non-isothermal TGA experiments.

The calculation of the kinetic parameters relies on an integral expression that must be selected again. This $g(\propto)$ function allow building plots $\ln(g(\propto)/T^2)$ vs. 1/*T*, where straight lines, which are produced at constant heating rates, permit the estimation of apparent activation energies *E* (kJ/mol) and pre-exponential factors *A* (s^{-1}). Unlike OFW, Friedman and KAS methods, the Coats-Redfern model strongly depends on an algebraic expression that fittingly describes the mechanism of decomposition of the carbonated sorbent being studied.

As a benchmark, Coats-Redfern $ln(g(\propto)/T^2)$ vs 1/*T* plots of sorbents Ca-Sa-%-WI, CaO/Sf-%-U, CaO/Sf-%-SH and CaO/Sf-%-Oct loaded with 25 wt. %, used to exemplify the methodology followed to predict the kinetic parameters, are shown in Figure 7-25. The presence of the integral function $g(\propto)$ involves not only searching for an algebraic expression that describes the decomposition reaction but also correlating this function with experimental data to obtain the kinetic parameters. According to the kinetic study performed with isothermal TGA data shown in section 7.1.2, the decomposition reactions with S-shape (sigmoidal) are appropriately described by nucleation and nuclei growth $g(\propto)$ functions. Certainly, among the sigmodal rate equations also termed "nucleation models" available to describe the decomposition trend of the CaO-Saffil sorbents, Avrami-Erofeyev (A2) and (A3) stand out.

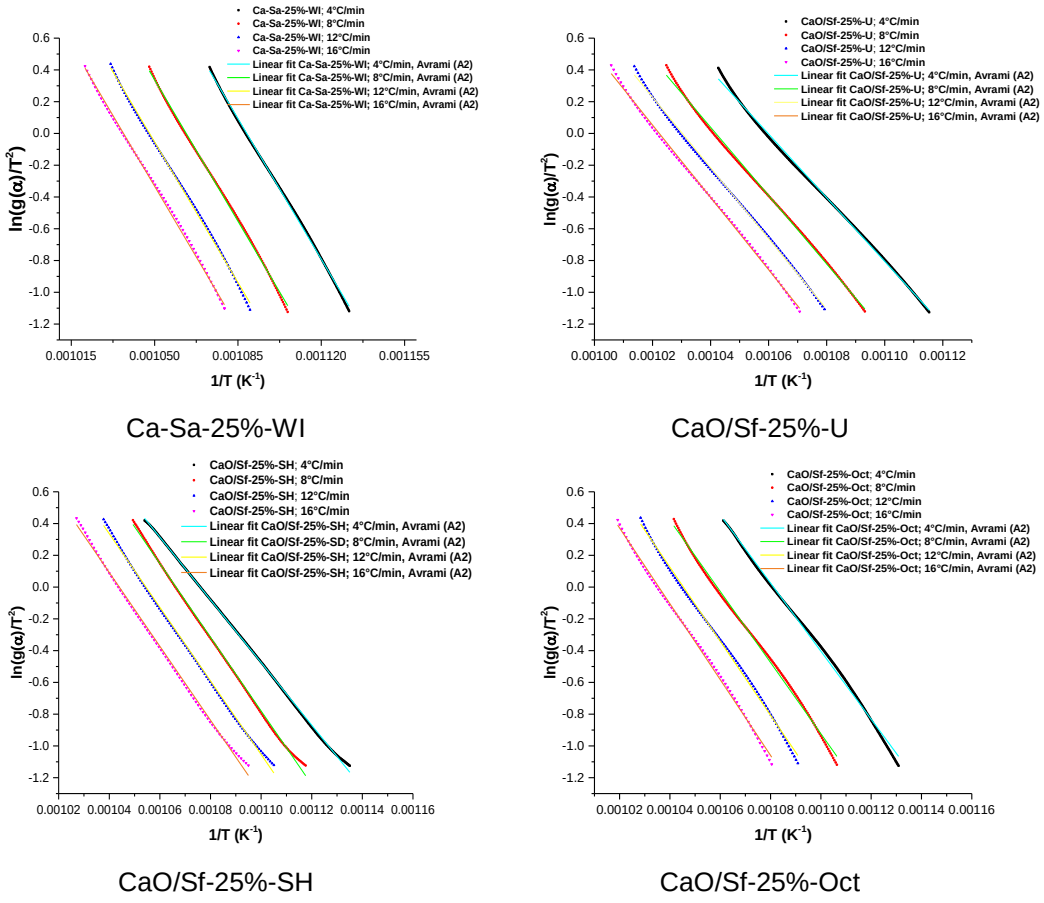

Figure 7-25. Plots $\ln(g(\propto)/T^2)$ against *10³/T* generated to estimate the activation energy for the non isothermal decarbonation reaction. The plots based on non-isothermal data related to sorbents Ca-Sa-25%-WI, CaO/Sf-25%-U, CaO/Sf-25%-SH and CaO/Sf-25%-Oct were fitted with the Avrami-Erofeyev A2 model.

As an inherent part of the procedure to predict the kinetic parameters, Avrami-Erofeyev models were incorporated into the left side term $ln(g(\propto)/T^2)$ of the Coats-Redfern equation (7-4). Then, the calculations on conversion (α) vs. time (min) data using $g(\propto)$ equal to [*-ln(1-α)$^{1/2}$*] and [*-ln(1-α)$^{1/3}$*] for A2 and A3 models respectively, diagonal lines were obtained. Lastly, the best fitting model was selected on the basis of the correlation coefficients calculated (>0.95).

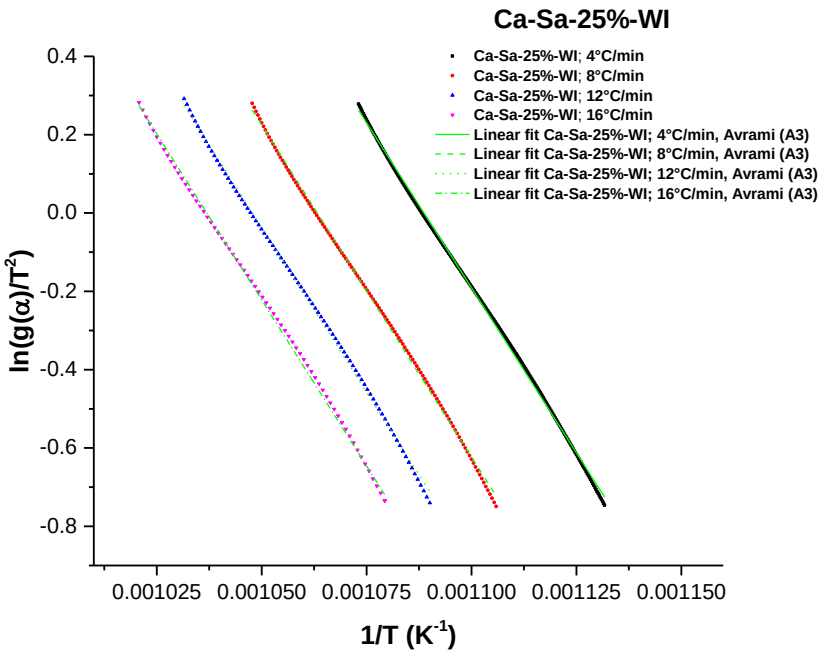

Figure 7-26. Coats-Redfern plot of the Ca-Sa-25%-WI sorbent: the ordinate axis is represented by the term "$\ln(g(\propto)/T^2)$", the integral function *g(α)* corresponds to the model Avrami-Erofeyev A3 and diagonal lines are associated with different heating rates used**.**

Coats-Redfern plots of the Ca-Sa-25%-WI sorbent (reference) with integrated Avrami-Erofeyev A3 model on term $ln(g(\propto)/T^2)$ are displayed in Figure 7-26. Dotted and solid lines correspond to experimental and simulated data obtained for heating rates of 4, 8, 12 and 16 °C/min in the interval of temperature of 550 to 900 °C. Although R^2 coefficients, which were calculated through the linear fitting analysis carried out on the Ca-Sa-25%-WI sorbent using A3 model, were above 0.95. The Avrami-Erofeyev A2 was also evaluated into the Coats-Redfern equation to select the most accurate

function. The correlation of A3 and A2 models with experimental non-isothermal data yielded very reliable R^2 values, but an improved correlation was discerned by using Avrami's model A2. As a reference, Cost and Redfern plots of sorbents CaO/Sf-25%-U, CaO/Sf-25%-SH and CaO/Sf-25%-Oct generated by using A2 model are shown in Figure 7-25. The R^2 values above 0.99 obtained by the non-linear fitting analysis confirmed that the A2 model was an apt model to calculate the activation energies of the decarbonation process of CaO-Saffil sorbents.

Activation energies of Ca-Sa-%-WI sorbents (reference) calculated on the basis of the Coats-Redfern expression are listed in plots *E* vs. *β* (°C/min) displayed in Figure 7-27. The *E* values obtained for sorbents prepared through wet impregnation were within the range of 204-225 kJ/mol. As expected, the results were consistent with activation energies calculated through the OFW, Friedman and KAS methods. In addition, lack of sharp increases of activation energies collected at different heating rates suggested that a one-step decomposition reaction.

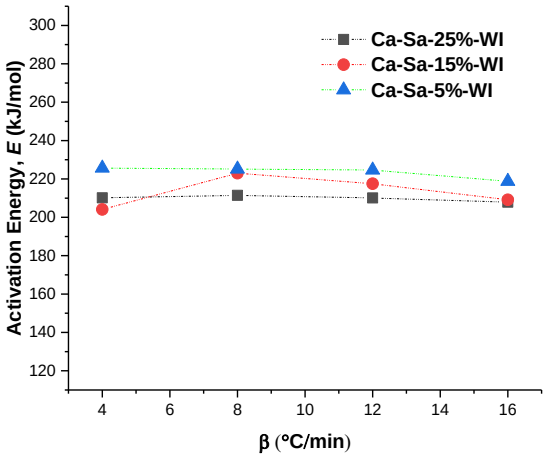

Figure 7-27. Activation energies of decomposition of sorbents Ca-Sa-%-WI obtained from Coats-Redfern plots. The four *E* values corresponds to activation energies for non-isothermal experiments carried out at 4, 8, 12 and 16 °C/min.

The activation energies calculated following the methodology described in the course of the present section are reported in Table 7-14. Although activation energy values calculated for the Ca-Sa-%-WI sorbent using Coast-Redfern method were comparable with OFW, Friedman, KAS results, in the case of

sorbents CaO/Sf-%-U, CaO/Sf-%-SH and CaO/Sf-%-Oct, their predicted *E* values were inferior. However, despite this difference, their *E* values were equivalent to other CaO-based sorbents reported in the literature [343, 347]. For instance, the activation energies of the decomposition of calcium carbonate predicted theoretically and experimentally (E^e (kJ/mol)) in refs [348] and [322] had values that varied from 133.5- 325 kJ/mol, and thus, were coherent with *E* (kJ/mol) values of CaO-Saffil sorbents.

Table 7-14. Activation energies of the non-isothermal decomposition reaction of sorbents Ca-Sa-%-WI, CaO/Sf-%-U, CaO/Sf-%-SH and CaO/Sf-%-Oct obtained by using the Coats-Redfern method and A2 model.

Sorbents			
Ca-Sa-25%-WI		**Ca-Sa-15%-WI**	**Ca-Sa-5%-WI**
β (°C/min)	*E* (kJ/mol)	*E* (kJ/mol)	*E* (kJ/mol)
4	210	204	226
8	211	223	225
12	210	218	225
16	208	209	218
Average =	210	213	224
Sorbents			
CaO/Sf-25%-U		**CaO/Sf-15%-U**	**CaO/Sf-5%-U**
β (°C/min)	*E* (kJ/mol)	*E* (kJ/mol)	*E* (kJ/mol)
4	167	185	219
8	179	180	213
12	190	180	216
16	189	154	218
Average =	181	175	216
Sorbents			
CaO/Sf-25%-SH		**CaO/Sf-15%-SH**	**CaO/Sf-5%-SH**
β (°C/min)	*E* (kJ/mol)	*E* (kJ/mol)	*E* (kJ/mol)
4	164	168	177
8	193	182	224
12	193	191	234
16	193	188	232
Average =	186	182	217
Sorbents			
CaO/Sf-25%- Oct		**CaO/Sf-15%- Oct**	**CaO/Sf-5%-Oct**
β (°C/min)	*E* (kJ/mol)	*E* (kJ/mol)	*E* (kJ/mol)
4	178	158	155
8	186	168	159
12	193	170	161
16	198	174	163
Average =	189	168	160

A comparative of activation energies predicted for the Ca-Sa-%-WI sorbents through the diverse isoconversional methods used in section 7.2, is shown in Figure 7-28. These sorbents were once again selected as a reference because they provide an overview of the effect of the isoconversional methods on the estimation of activation energies. The activation energies obtained by OFW, Friedman, KAS and Coats-Redfern methods, which are represented by specific symbols displayed in Figure 7-28, had activation energies ranging between 170-225 kJ/mol. Although the discrepancy of one method compared to the other was perceptible, investigations such as those conducted by Kumar et al., Niu et al., Ramezani et al. and Georgieva et al. confirmed that the estimations performed in this research are in context with *E* values reported up to date [322, 331, 338, 349].

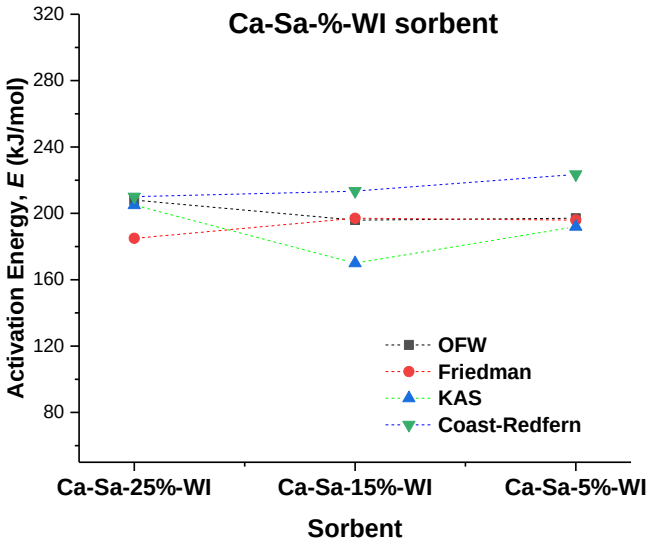

Figure 7-28. Activation energies of decomposition of Ca-Sa-%-WI sorbents with loadings of 25, 15 and 5 wt. % predicted through OFW, Friedman, KAS and Coats-Redfern isoconversional methods.

7.2.1.5 Comparison of Activation energies predicted from isothermal method and isoconversional methods

Certainly, the activation energies of the decomposition process predicted by model-free methods present inconsistencies compared to the isothermal method (Figure 7-29). As indicated in section 6.1, the pathway followed to

acquire data in non-catalysed solid-state reactions play an important role on the predicted kinetic parameters. Despite the Mettler Toledo TGA being able to narrow down errors produced in the dynamic lapse, the contribution is still apparent on the activation energy values predicted through the isothermal method. Although the CO_2 flow fed into the TGA was maintained up to attain the temperatures fixed to decompose the CaO-Saffil sorbents, the decomposition reaction could start before recording data. Thermal data, which were unrecorded during the start of transformation of $CaCO_3$ to CaO, apparently yielded lower activation energies compared to energies calculated by isoconversional methods.

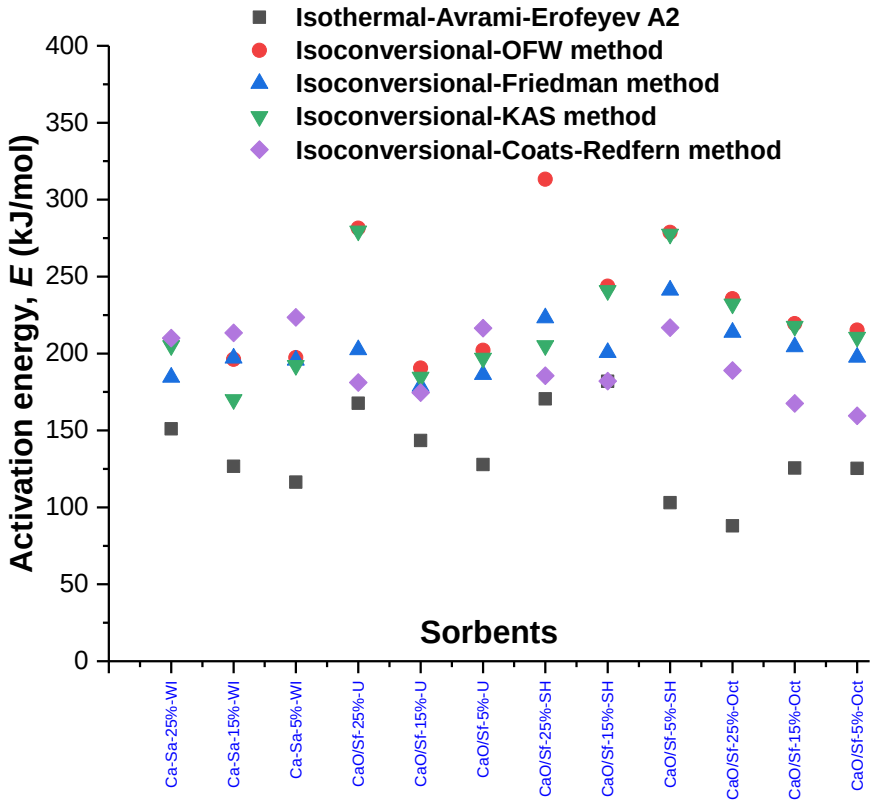

Figure 7-29. Plot *E (kJ/mol)* vs Sorbents reporting all activation energies estimated by using isothermal and non-isothermal sorbents decomposition TGA data. *E (kJ/mol)* values using isothermal conditions were acquired by Avrami-Erofeyev A2 model, whilst *E (kJ/mol) values* predicted through dynamic heating tests were estimated by means of isoconversional methods such as OFW, Friedman, KAS, and Coats-Redfern.

Given the dissimilarity between activation energies of sorbents decomposition predicted from isothermal and non-isothermal data, a multistep scheme of decomposition may have been considered as a presumable contributor.

However, *E* vs. α plots of OFW, Friedman, KAS and Coats-Redfern methods refuted this hypothesis because the variations in activation energies derived from the isoconversional methods were not as significant to indicate a kinetic mechanism that involved two or more reactions. On the basis of research work reported by Wang et al., successive reactions (multistep decomposition) with coexistence of a metastable CaO* phase are most probable under higher vacuum conditions, and thus, this particular condition could lead to obtaining higher activation energies for the decarbonation reaction [189, 350].

Although isothermal data permitted to distinguish the effect of the textural properties over the energy requirements to initiate the desorption of CO_2, the dispersion of activation energy values estimated through the four isoconversional methods did not allow to attribute the dependence of *E* with respect to the physicochemical properties of the sorbents. Consequently, a direct correlation between variations of activation energy and inherent properties of the sorbent was not confirmed.

In terms of *E* values obtained for the decarbonation reaction of CaO-Saffil sorbents with solid-state reaction models (Avrami-Erofeyev A2) and isoconversional models (OFW, Friedman, KAS and Coast-Redfern) compared to energies available in the literature, Figure 7-29 situates the activation energies in the range of other reported by various authors, namely, $134 \leq E\ (kJ/mol) \leq 325$ [322, 348].

7.3 Conclusion

In Chapter 7, a thermo-kinetic study of the decarbonation reaction $CaCO_{3(s)} \rightarrow CaO_{(s)} + CO_{2\,(g)}$ of the CaO-Saffil sorbents was carried out. The prediction of kinetic parameters was performed using two types of thermal methods to a more reliable analysis: isothermal and non-isothermal methods. For the prediction of reaction rate constants of sorbents Ca-Sa-%-WI, CaO/Sf-%-U, CaO/Sf-%-SH and CaO/Sf-%-Oct using isothermal TGA data, non-catalytic solid-state models such as power law, reaction-order, diffusion and Avrami-Erofeyev were proposed. The curve fitting analysis suggested that the Avrami-

Erofeyev A2 model best correlated with the sigmoidal shape of isothermal decomposition conversion curves. Rate constants were then used in Arrhenius plots (*ln(k)* vs. *1/T*), and through the linearized Arrhenius equation, the activation energies were predicted.

The thermo-kinetic analysis of the transformation of $CaCO_3$ to CaO which were performed on the basis of non-isothermal TGA data, used isoconversional mathematical models to predict the kinetic parameters. These model-free methods allowed calculating rate constants, activation energy and pre-exponential factors from alterations produced on the conversion rates by the effect of varying heating rates in a fixed interval of temperature. The isoconversional models, which are also recommended by the kinetics Committee ICTAC, used to predict the kinetic parameters, were Ozawa-Flynn–Wall, Friedman, Kissinger-Akahira-Sunose, and Coats-Redfern.

In relation to desorption rates of CaO-Saffil sorbents, isothermal experiments revealed that a fast decarbonation are attained under higher temperatures (>720 °C). The results indicated that the full thermal decomposition of CaO-Saffil sorbents was achieved in 2-3 min (in the most favorable temperature), and thus, this rapid CO_2 release was attributed to the CaO morphologies and textural properties of the different families of sorbents. In the particular case of sorbents coated with nanoflakes, the homogeneous distribution of nanoflakes in conjunction with the separation flake-to-flake contributed to the enhanced decarbonation rate. For CaO/Sf-%-Oct sorbents, the rate of the thermal decarbonation was favoured also at temperatures >680 °C. According to their conversion curves, comparable desorption times were observed for CaO/Sf-%-Oct sorbents, namely, 2-3 min. Despite the octahedra having a dense structure, the CO_2 was rapidly released from the layer of $CaCO_3$. This result suggested that the high thermal stability of CaO/Sf-%-Oct sorbents allied with textural properties (SSA and PS) promote the rapid decarbonation.

In terms of the activation energies, a discrepancy of values reported by isothermal and isoconversional methods was discerned. The *E* values of the decarbonation reaction of CaO-Saffil sorbents predicted using isothermal data in a temperature window of 680 – 740 °C were within the range of 85-175 kJ/mol, whilst they ranged from 152-310 kJ/mol by means of model-free

methods. This inconsistency was apparently produced during isothermal data collections for the non-catalysed decomposition reaction. However, despite *E* values predicted by isoconversional models mostly greater compared to those obtained using the isothermal method, the reliability of predictions was supported through the good linearity calculated when solid-state reaction models and isoconversional models were fitted, namely correlation coefficients $R^2 > 0.95$. The consistency of the methodology used to predict *E* was also confirmed by considering other activation energies of natural or synthetic CaO-based sorbents reported by various authors ($134 \leq E\ (kJ/mol) \leq 325$).

The energetic requirements to start with the decarbonation reaction allied with the rapid decomposition rates observed in Ca-Sa-%-WI, CaO/Sf-%-U, CaO/Sf-%-SH and CaO/Sf-%-Oct suggest that these type of fibrous sorbents are worthy of application for CO_2 removal in sorption enhanced steam reforming processes.

Chapter 8 Conclusions & Future Recommendations

8.1 Conclusions

In this work, synthetic CaO-based CO_2 sorbents with enhanced performance and resistance to high-temperature to applications in sorption-enhanced steam reforming process were conceived. Conventional methods such as wet impregnation and precipitation allowed to support CaO on Saffil fibres where this refractory support was used as a manner to increase thermal resistance to high temperatures of the active phase. Multicycle sorption/desorption trials in presence of a CO_2-rich atmosphere (90%CO_2/N_2) highlighted stability gained by the presence of Saffil supports. Additionally, benefits of using a fibrous sorbent with an open structure (entwined fibres with cavities that improve transit of gases whilst reduces pressure drops) and benefits coming from the morphologies adopted by CaO (nanoflakes or octahedral) were stand out through the kinetic analysis performed for sorption/desorption reactions. Conclusions associated with the synthesis of CaO-Saffil sorbents, performance and durability in multicycle CO_2 uptake tests of the as-prepared sorbents and evaluation of kinetic parameters through isothermal and non-isothermal methods are presented below.

8.2 Preparation of CaO-based CO_2 sorbents with enhanced thermal and mechanical properties

CaO-Saffil CO_2 sorbents with tailored textural and morphological properties were successfully synthesised by modified wet impregnation and precipitation methods without adding tensoactive agents (promoters of direct formation of crystal with different shapes). Parameters such as stirring, the temperature to evaporate the excess of solvent, ageing time and content of CaO precursor dissolved demonstrated to play a critical factor in loading notional CaO contents between 5 to 25 wt. %. Optimized synthesis conditions allowed to deposit amounts of active phase close to those proposed (confirmed by XRF

technique). Despite the simplicity of the wet impregnation method, which implies attraction forces between the CaO precursor and Saffil supports, was possible to form coatings with uniformly dispersed nanoflakes on the surface of the refractory support. However, in Ca-Sa-%-WI sorbents with loadings of 15 and 25 wt. % CaO, SEM revealed the formation of freestanding agglomerates outside Saffil supports.

Precipitation method via urea, which was used as a way to diminish the formation of detached aggregates whilst improve deposition of CaO on Saffil fibres, demonstrated being an effective method not only to improve deposition of active phase on the surface of the support but also textural properties (porosity and surface area). By analysing fiber terminations, thicker coatings in CaO/Sf-%-U sorbents with CaO weight percentages of 15 and 25% compared with Ca-Sa-%-WI sorbents with equivalent CaO contents were measured (~9.5 - 10% thickness increase). This raise, which was attributed to a more controlled and homogeneous deposition of CaO over the Saffil fibres surface, was promoted by slow urea hydrolysis produced at 85°C.

For CaO-based sorbents prepared via precipitation with NaOH as the precipitant agent, very basic pH (>12) produced a spontaneous deposition that drives to the formation of amorphous CaO over the support surface. However, varying ageing times and pH, drastic changes in morphology arose, namely CaO octahedra. Although nucleation-growth mechanisms aimed to rationalize the formation of CaO octahedra were proposed, the factual pathway is vague, and thus, it is worthy of further investigation.

8.3 Carrying capacity and durability of CaO-Saffil sorbents

Multicycle carbonation-decarbonation trials, which were performed in 90 CO_2/10% N_2 with carbonation times of 45 min or 15 min at 650 °C and calcination at 850 °C in pure N_2, exhibited that sorbents CaO/Sf-%-U have higher CO_2 uptake capacities compared with sorbents Ca-Sa-%-WI, CaO/Sf-%-SH and CaO/Sf-%-Oct. In loadings of 25 wt. % CaO, urea-prepared sorbents attained initial capture capacities of 0.193 mg CO_2 per mg sorbent, whilst sorbents -WI, -SH and -Oct had uptake capacities of 0.118, 0.059 and

0.048 mg CO_2/mg Sorbent, respectively. Comparable trends were found in CaO-Saffil sorbents with lower loadings (15 and 5 wt. %). For the lowest loading of 5 wt. %, modest initial carrying capacities were registered, namely, 0.017, 0.039, 0.028 and 0.035 for Ca-Sa-%-WI, CaO/Sf-%-U, CaO/Sf-%-SH and CaO/Sf-%-Oct, respectively.

In the course of 30 carbonation-decarbonation cycles, trials performed with carbonation periods of 45 minutes revealed that CaO/Sf-%-U sorbents had a more severe degradation compared to sorbents Ca-Sa-%-WI, CaO/Sf-%-SH and CaO/Sf-%-Oct. The 25 wt. % sample showed the highest reactivity loss among CaO/Sf-%-U sorbents, with ~70% decline. In the case of sorbents Ca-Sa-25%-WI and CaO/Sf-25%-SH, carrying capacity deteriorations were ~60% and 30%, respectively. TGA trials revealed improved consistency in sorbents CaO/Sf-25%-Oct, with an only ~13% decay in uptake capacity. In samples with 5 wt. %, although modest carrying capacities were obtained, durability was significantly enhanced by the incorporation of Saffil. On the basis of the residual reactivity study performed to CaO-Saffil sorbents with loadings of 5, 15 and 25 wt. %, the nonlinear fit of exponential and double exponential decay models with experimental data demonstrated a strong correlation (R^2 >0.95). Residual reactivities predicted confirmed that the capture capacities presented minimal degradation beyond cycle 30, namely below ~3.5%.

In terms of durability, uptake-calcination trials demonstrated extended durability of CaO-Saffil sorbents compared to unsupported CaO. This improving resistance, more evident for sorbents with the lowest CaO loading (5 wt. %), was attributed to a low CaO densification diminished by the incorporation of the low-density mat of catalytic grade Saffil. The incorporation of Saffil supports improved the thermal stability of CaO loaded over the surface of the support through the improved effect of mechanical clamping as well as the distribution of tensile forces imparted along the CaO-Saffil interface. The clamping effect, which diminishes lateral shrinkage of CaO, was weaker for higher loadings because of a smaller proportion of the coating is exposed to interfacial clamping. As a result, volumetric densification was more intense in CaO-Saffil sorbents with 25 and 15 wt. % CaO after 30 CO_2 uptake cycles.

Morphologies adopted by CaO (nanoflakes or octahedra) demonstrated improved durability in relation to unsupported CaO. High-magnification SEM micrographs corroborated that nanoflakes deposited over Saffil had low volumetric densification after 30 continuous cycles but the biggest contribution to the loss of >50% of carrying capacity in sorbents Ca-Sa-%-WI and CaO/Sf-%-U with loadings of 25 and 15 wt. % was mostly produced by sintering on freestanding CaO particulate. In the particular case of CaO/Sf-%-SH, in which the presence of detached CaO particulate was minimal, deteriorations below 30% also highlighted the importance of mechanical clamping in the decline of densification.

For CaO/Sf-%-Oct sorbents with 5-25 wt. % loadings, thermal stability was increased but at the cost of modest carrying capacities. The highest reactivity decay observed was ~13.5% for the 25 wt. % sample, whilst 0.048 mg CO_2/mg Sorbents was the maximum uptake capacity reached after 30 cycles in the CaO/Sf-25%-Oct sorbent. Although volumetric changes generated in the forward and reverse reaction $CaO + CO_2 \leftrightarrow CaCO_3$ produced transverse cracks on octahedra, mechanical clamping effect inhibited particulate detachment and densification, and thus, severe deactivation of CaO/Sf-%-Oct sorbents.

8.4 Evaluation of kinetic parameters via isothermal and non-isothermal methods

The thermo-kinetic study for the carbonation process conducted using isothermal data collected in a TGA system in a temperature range 500-625 °C under an enriched-CO_2 atmosphere (90% CO_2/N_2) permitted successfully estimate the kinetic triplet (rate constants, activation energies and pre-exponential factors). The conversion curves of the carbonation process of CaO-Saffil sorbents revealed that the reaction is developed in two stages; a fast chemical surface reaction followed by a slow diffusion-controlled stage. The fast process, which takes place on the external surface of CaO, formed a layer of carbonate ($CaCO_3$). For the slow stage, the CO_2 diffuses towards the unreacted CaO zone (interior of the particle). Therefore, the carbonation rate

is restricted by the access of CO_2 through the product layer of $CaCO_3$ that covered the network of pores.

Conventional solid-state kinetic models were unable to predict CO_2 sorption behaviour but instead, a double exponential model effectively allowed simultaneously the prediction of the kinetic constants of both chemical reaction (k_1) and diffusion-limited regime (k_2). The predicted kinetic constants showed k_1 greater in an order of magnitude compared to k_2, which confirmed that diffusion is the limiting process in the uptake of CO_2 at higher temperature.

Activation energies *E* of the carbonation reaction of CaO-Saffil sorbents, which were calculated on the basis of the Arrhenius equation, showed differences. These variations were associated with the CaO morphology, thicknesses of the CaO layer and the inherent textural properties. The *E* values of 11-59 kJ/mol were obtained for the chemical reaction and of 20-84 kJ/mol for the diffusion-controlled regime. This suggested that the energies required to perform the transformation of CaO to $CaCO_3$ in the Saffil fibre-supported CaO sorbents were comparable to other *E* values of CaO-based sorbents reported in the literature by various authors.

Kinetic parameters of the decarbonation of $CaCO_3$ to CaO of the CaO-Saffil sorbents were successfully estimated by isothermal and isoconversional methods. Rate constants of decomposition curves obtained from isothermal data were satisfactorily estimated by Avrami-Erofeyev A2 model, whereas Arrhenius equation allowed estimating activation energies (*E*). For non-isothermal data, *E* values were accurately calculated on the basis of isoconversional models proposed by Ozawa-Flynn–Wall, Friedman, Coats-Redfern and Kissinger-Akahira-Sunose

E values derived from isothermal and non-isothermal methods presented inconsistencies attributed to the route followed for data collection. Activation energies predicted by isoconversional models ranged between 152 to 310 kJ/mol, whilst through isoconversional methods, from 85 to 175 kJ/mol. Despite discrepancies, *E* values were in context with activation energies reported in the literature for other CaO-based sorbents (including limestone). The reliability of the predictions was also confirmed through correlation coefficients R^2 above 0.985 obtained for both isothermal and non-isothermal

data. Kinetic parameters estimated through isoconversional expressions also presented differences among them. The Friedman method showed greater inconsistencies due to the nature of the calculations, namely, data treatment by numerical differentiation. Signals at low conversions produced noise that systematically amplified the error in the global activation energies predicted. Although differentiated data were mathematically treated (noise smoothing) to diminish discrepancies, noise at low conversions ($\alpha < 0.2$) was evident.

According to activation energy values calculated for both the carbonation and decarbonation reactions allied with the CO_2 sorption-desorption times, it is concluded that CaO-Saffil sorbents are kinetically comparable with the best performing sorbents reported in the literature, and thus, these CaO-Saffil sorbents are worthy of further development.

8.5 Future work

The preparation of novel CaO-based CO_2 sorbents incorporating Saffil fibre as supports provided a clear evidence of the possibility to synthesize solid sorbents with enhanced durability. However, performance decay produced by effect of sintering is still a challenge to overcome. To cope with this problem, as a future work, it is considered examining alternative methods to reach CaO loadings above 25 wt. % over the periphery of Saffil sorbents. For instance, methods such as the sol-gel and hydrothermal are proposed to enhance interfacial deposition of CaO precursors over Saffil supports. These nucleation/growth-based methods apparently offers the scope for increasing CaO loadings by improve the axial growth of nanoflakes. In addition, a sequential deposition of CaO, which involves the formation of a multilayer coating, could contribute in reducing or avoiding formation of detached CaO particulate matter. In the attempt to reach improved deposition, an acid pre-treatment to Saffil fibres in order to increase surface roughness, which in turn would promote higher deposition of CaO active phase is also proposed as future work.

In the case of sorbents with CaO of octahedral morphology, a detailed study to understand both the mechanism of formation and octahedral shape adopted will be conducted. This investigation will encompass different stages:

1) Experimental: CaO-Saffil sorbents will be prepared using precipitation method via NaOH varying pH, temperature, ageing time and CaO content. The idea behind it is to figure out the influence of the driving force that potentially can modify the nucleation and growth process of octahedral particles, namely supersaturation. Information related to this state of instability would contribute to determining the spontaneity of the nucleation process as well as the influence of the mother liquor (solvent) in crystallinity of particles formed by Ostwald ripening.
2) Characterization of the as-prepared sorbents: to discern structural and morphological changes produced through modifying synthesis parameters, each material will be examined by means of SEM. This analysis will be also performed in dried and calcined samples to track the morphological evolution of crystals prior to and after the transformation from precursor to CaO. Characterization also includes XRD technique that will contribute to phases identification. This technique will also allow detecting polymorphism, which in metal oxides, would produce drastic variations in the morphology of particles because of the crystalline nature of each polymorph.
3) Decomposition of sorbent precursor in situ: thermal decomposition of the CaO precursor can be an important factor in the formation of octahedral particles as recrystallization could take place not only at high temperatures but also in the course of drying the wet material obtained after steps ageing and rinsing. Therefore, XRD coupled with a hot stage system would permit to monitor the crystallographic evolution of a wet sample of CaO-Saffil in a range of temperature from room temperature up to 850 °C. This analysis will be a strong foundation to support the hypothesis associated with polymorphism, recrystallization during the decomposition stage or any effect produced by the solvent or precipitant agent.

As a future work, viable routes to increase porosity in octahedral crystals of CaO will be analysed. An enhancement in the textural properties of the CaO would contribute to increasing the carrying capacity while improving the sorption rate. The initial proposal is the use of anionic surfactants that will allow generating mesopores with a bimodal pore size distribution after the thermal decomposition of these organic compounds. Open pores would promote a faster diffusion of CO_2 toward the bulk of the octahedra. As a result, the reactions rates of CaO/Sf-%-Oct sorbents will be favoured.

Carrying capacity measurements of CaO-Saffil sorbents in 30 carbonation-calcination cycles demonstrated that beyond cycle 30, uptake capacities have a minimal decline, but albeit mathematical models proposed apparently provided good approximations of the reactivity loss, TGA trials with 50-100 cycles would provide a more realistic thermal behaviour of CaO-Saffil sorbents.

CO_2 removal in a vessel containing a steam reforming catalyst and a sorbent denotes a challenge not only to finding the optimal operational parameters and distribution of both solid materials, but also the performance of the sorbent itself. Although TGA permitted to measure the CO_2 uptake capacities of CaO-Saffil sorbents, an atmosphere with reactive gases such as water vapour and fuel (methane, shell gas or tail gas) would give rise to a more representative analysis of the behaviour of the sorbents. Hence, the thermo-kinetic study of sorption-desorption of CO_2 in presence of a solid catalyst is also expected to be conducted for further research. The kinetic parameters obtained from the kinetic study will be used to predict the performance of CaO-Saffil sorbents at different conditions using software such as Aspen Plus and gPROMS.

It is also planned to prepare of bi-functional solid materials with tailored morphologies in which catalyst and sorbent are coated simultaneously over Saffil fibres through wet dissolved solutions. The benefit of loading both oxides over the same surface is to provide a more homogeneous distribution of active materials along the bed of the fixed bed reactors. Thus, well-distributed active reaction sites for fuel transformation and in situ CO_2 removal would promote higher yield and purity in a system with smaller dimensions.

Finally, the CaO-Saffil sorbents synthesized in this work were designed for pre-combustion capture purposes, but their scope might go beyond that, for instance in more complex, hybrid processes as the sorption-enhanced chemical looping reforming process (SECLR). However, some features must be provided to the sorbents for a successful application in this particular chemical process. For instance, tailoring the materials in pellets to increase the mechanical resistance and diminishing attrition. These adaptations are also contemplated as future work.

References

1. Mitchell, J.F., *The "greenhouse" effect and climate change.* Reviews of Geophysics, 1989. 27(1): p. 115-139.
2. Fleming, J.R.J.E., *Joseph Fourier, the 'greenhouse effect', and the quest for a universal theory of terrestrial temperatures.* 1999. 23(2): p. 72-75.
3. Wallington, T.J., et al., *Greenhouse gases and global warming.* Environ Ecol Chem, 2009. 1: p. 36.
4. Change, I.P.O.C., *Climate change 2007: The physical science basis.* Agenda, 2007. 6(07): p. 333.
5. Statistics, I., *CO_2 emissions from fuel combustion-highlights.* IEA, Paris http://www. iea. org/co2highlights/co2highlights. pdf. Cited July, 2011.
6. Orr, J.F.M., *CO_2 capture and storage: are we ready?* Energy & Environmental Science, 2009. 2(5): p. 449.
7. Ren, P., *Renewables 2015 global status report.* REN21 Secretariat: Paris, France, 2015.
8. Sawin, J.L., et al., *Renewables 2017 Global Status Report.* 2013.
9. Pachauri, R.K., et al., *Climate change 2014: synthesis report. Contribution of Working Groups I, II and III to the fifth assessment report of the Intergovernmental Panel on Climate Change*. 2014: IPCC.
10. D'Alessandro, D.M., B. Smit, and J.R. Long, *Carbon dioxide capture: prospects for new materials.* Angew Chem Int Ed Engl, 2010. 49(35): p. 6058-82.
11. Yamasaki, A., *An overview of CO_2 mitigation options for global warming-Emphasizing CO_2 sequestration options.* Journal of Chemical Engineering of Japan, 2003. 36(4): p. 361-375.
12. Yang, H., et al., *Progress in carbon dioxide separation and capture: A review.* Journal of Environmental Sciences, 2008. 20(1): p. 14-27.
13. Olivier, J.G., J.A. Peters, and G. Janssens-Maenhout, *Trends in global CO_2 emissions 2012 report.* 2012.
14. Haman, K. and E. Stiever, *Literature Review of Hydrogen Production, Storage.* Distribution, and Utilization Technologies, 2007.
15. Van der Hoeven, M., *CO_2 emissions from fuel combustion–highlights.* IEA Statistics, 2011.
16. Leonardo Beltran, C.C., Jose Marial Valenzuela, Moises Dvila, Vicente Arevalo, Oscar Jimenez, Erik Medina, Oscar Cuevas, Hector Ortega, *Atlas de Almacenamiento Geologico de CO_2, Mexico.* Federal Government Journal 2012: p. 44.
17. Department of Energy, D.o.e.a.n.r., Mexican Petroleum, National Comission of Electricity, Mario Molina Centre, National Politecnic Institute, National Autonomous University of Mexico, *Map of the technology route of CCUS in Mexico.* Federal Government Journal, 2014: p. 31.
18. Change, I.C., *The physical science basis. Contribution of working group I to the fifth assessment report of the intergovernmental panel on climate change*. 2013, USA: Cambridge University Press.
19. Administration, N.A.a.S., *"NASA Science: Earth Science Missions.* Internet Archive, 2017.
20. Thomas DeMichelePublished - December 1, *Humans Impact Climate Change* 2015.
21. Agency, U.S.E.P., *Potential Climate Change Impacts* 2017.
22. Karmalkar, A.V. and R.S. Bradley, *Consequences of global warming of 1.5 °C and 2 °C for regional temperature and precipitation changes in the contiguous United States.* PloS one, 2017. 12(1): p. e0168697.

23. Yin, Y., D. Ma, and S. Wu, *Climate change risk to forests in China associated with warming.* Scientific reports, 2018. 8(1): p. 493.
24. Venkataramanan, M., *Causes and effects of global warming.* Indian Journal of Science and Technology, 2011. 4(3): p. 226-229.
25. Meyssignac, B. and A. Cazenave, *Sea level: a review of present-day and recent-past changes and variability.* Journal of Geodynamics, 2012. 58: p. 96-109.
26. Wang, J. and B. Chameides, *Global Warming's Increasingly Visible Impacts*. 2005: Environmental Defense.
27. Liverman, D.M. and K.L. O'Brien, *Global warming and climate change in Mexico.* Global Environmental Change, 1991. 1(5): p. 351-364.
28. Ministry of Environment and Natural Resources, N.I.o.E.a.C.C., *Mexico's Climate Change Mid-Century Strategy.* 2016.
29. Vecchi, G., *Precipitation change in Mexico.* Geophysical Fluid Dynamics Laboratory, National Oceanic and Atmospheric Administration, 2010-2018.
30. Wilder, M., et al., *Adapting across boundaries: climate change, social learning, and resilience in the US–Mexico border region.* Annals of the Association of American Geographers, 2010. 100(4): p. 917-928.
31. Harrison, J., *New Report Outlines Current, Future Impacts of Climate Change.* University Communications, The University of Arizona, 2009.
32. Haszeldine, R.S., et al., *Negative emissions technologies and carbon capture and storage to achieve the Paris Agreement commitments.* Phil. Trans. R. Soc. A, 2018. 376(2119): p. 20160447.
33. Allen, M.R., et al., *Warming caused by cumulative carbon emissions towards the trillionth tonne.* Nature, 2009. 458(7242): p. 1163.
34. Matthews, H.D., et al., *Focus on cumulative emissions, global carbon budgets and the implications for climate mitigation targets.* Environmental Research Letters, 2018. 13(1): p. 010201.
35. IEA, *Technology roadmap: carbon capture and storage.* 2013, Paris, France: IEA: p. 63.
36. Leung, D.Y.C., G. Caramanna, and M.M. Maroto-Valer, *An overview of current status of carbon dioxide capture and storage technologies.* Renewable and Sustainable Energy Reviews, 2014. 39: p. 426-443.
37. Agency, I.E., *Global Energy & CO_2 Status Report: 2017.* IEA publications & data, 2017.
38. Conti, J., et al., *International Energy Outlook 2016 With Projections to 2040*. 2016, USDOE Energy Information Administration (EIA), Washington, DC (United States). Office of Energy Analysis.
39. Agency, I.E., *World Energy Balances 2017: An Overview.* IEA publications & data, World Energy Statistics 2017, 4 August 2017.
40. Rodríguez-Mosqueda, R. and H. Pfeiffer, *Thermokinetic analysis of the CO_2 chemisorption on Li_4SiO_4 by using different gas flow rates and particle sizes.* The Journal of Physical Chemistry A, 2010. 114(13): p. 4535-4541.
41. Agency, U.S.E.P., *Natural Gas Issues and Trends.* U.S. Environmental Protection Agency, 2010.
42. (EPA), E.P.A., *Cleaned-Up Coal and Clean Air: Facts About Air Quality and Coal-Fired Power Plants*, in *Environmental Protection Agency*. 2017: U.S.
43. Association, N.G.S. *Natural Gas and Technology*. 2014 2014 [cited 2018; 2011-2014:[Available from: http://naturalgas.org/environment/naturalgas/.
44. l'énergie, A.i.d., *Energy Technology Perspectives 2008: Scenarios & Strategies to 2050: in Support of the G8 Plan of Action*. 2008: OECD/IEA.
45. Lipponen, J., et al., *The IEA CCS technology roadmap: one year on.* Energy Procedia, 2011. 4: p. 5752-5761.
46. Phaal, R., *Foresight Vehicle technology roadmap-technology and research directions for future road vehicles.* UK Department of Trade and Industry, URN, 2002. 2: p. 933.

47. Tomei, J., *Planning for a transition to a hydrogen economy: a review of roadmaps.* UKSHEC Working Paper, 2009(2).
48. Gibbins, J., et al., *Electric vehicles for low-carbon transport.* Proceedings of the Institution of Civil Engineers-Energy, 2007. 160(4): p. 165-173.
49. Ogden, J.M., *Hydrogen: The fuel of the future?* 2002.
50. Balat, M., *Potential importance of hydrogen as a future solution to environmental and transportation problems.* International Journal of Hydrogen Energy, 2008. 33(15): p. 4013-4029.
51. Sherif, S.A., F. Barbir, and T.N. Veziroglu, *Towards a Hydrogen Economy.* The Electricity Journal, 2005. 18(6): p. 62-76.
52. Dougherty, W., et al., *Greenhouse gas reduction benefits and costs of a large-scale transition to hydrogen in the USA.* Energy Policy, 2009. 37(1): p. 56-67.
53. Corneil, H.G. and F.J. Heinzelmann, *Hydrogen in Oil Refinery Operations.* 1980. 116: p. 67-94.
54. Bachman, J.E. *Electrolysis*. Nuclear Generation 2010; Available from: https://wiki.uiowa.edu/display/greenergy/Electrolysis.
55. Ball, M. and M. Wietschel, *The future of hydrogen – opportunities and challenges ☆.* International Journal of Hydrogen Energy, 2009. 34(2): p. 615-627.
56. Riis, T., et al., *Hydrogen production and storage—R&D priorities and gaps.* International Energy Agency Hydrogen Coordination Group Hydrogen Implementing Agreement, 2006.
57. Haryanto, A., et al., *Current status of hydrogen production techniques by steam reforming of ethanol: a review.* Energy & Fuels, 2005. 19(5): p. 2098-2106.
58. Sørensen, B., *Hydrogen and fuel cells: emerging technologies and applications*. 2011: Academic Press.
59. Lamy, C., *From hydrogen production by water electrolysis to its utilization in a PEM fuel cell or in a SO fuel cell: Some considerations on the energy efficiencies.* International Journal of Hydrogen Energy, 2016. 41(34): p. 15415-15425.
60. Kalamaras, C.M. and A.M. Efstathiou, *Hydrogen Production Technologies: Current State and Future Developments.* Conference Papers in Energy, 2013. 2013: p. 1-9.
61. Styring, P., et al., *Carbon Capture and Utilisation in the green economy*. 2011: Centre for Low Carbon Futures New York.
62. Boot-Handford, M.E., et al., *Carbon capture and storage update.* Energy Environ. Sci., 2014. 7(1): p. 130-189.
63. Haszeldine, R.S., *Carbon capture and storage: how green can black be?* Science, 2009. 325(5948): p. 1647-1652.
64. Institute, G.C., *Geological CO_2 storage.* 2013. Carbon capture, use and storage (CCUS).
65. Metz, B., et al., *IPCC, 2005: IPCC special report on carbon dioxide capture and storage. Prepared by Working Group III of the Intergovernmental Panel on Climate Change.* Cambridge, United Kingdom and New York, NY, USA, 2005. 442.
66. Kuramochi, T., et al., *Comparative assessment of CO_2 capture technologies for carbon-intensive industrial processes.* Progress in energy and combustion science, 2012. 38(1): p. 87-112.
67. Rubin, E.S., C. Chen, and A.B. Rao, *Cost and performance of fossil fuel power plants with CO_2 capture and storage.* Energy policy, 2007. 35(9): p. 4444-4454.
68. Cuéllar-Franca, R.M. and A. Azapagic, *Carbon capture, storage and utilisation technologies: a critical analysis and comparison of their life cycle environmental impacts.* Journal of CO_2 Utilization, 2015. 9: p. 82-102.
69. Markewitz, P., et al., *Worldwide innovations in the development of carbon capture technologies and the utilization of CO_2.* Energy & environmental science, 2012. 5(6): p. 7281-7305.

70. Brinckerhoff, P., *Accelerating the uptake of CCS: industrial use of captured carbon dioxide.* Global CCS Institute, 2011: p. 260.
71. Figueroa, J.D., et al., *Advances in CO_2 capture technology—The U.S. Department of Energy's Carbon Sequestration Program.* International Journal of Greenhouse Gas Control, 2008. 2(1): p. 9-20.
72. Wall, T.F., *Combustion processes for carbon capture.* Proceedings of the Combustion Institute, 2007. 31(1): p. 31-47.
73. Salkuyeh, Y.K. and T.A.A. II, *Co-Production of Olefins, Fuels, and Electricity from Conventional Pipeline Gas and Shale Gas with Near-Zero CO_2 Emissions. Part I: Process Development and Technical Performance.* Energies, 2015. 8(5): p. 3739-3761.
74. Bougie, F. and X. Fan, *Analysis of the Regeneration of Monoethanolamine Aqueous Solutions by Microwave Irradiation.* Energy Procedia, 2017. 142: p. 3661-3666.
75. Thiruvenkatachari, R., et al., *Post combustion CO_2 capture by carbon fibre monolithic adsorbents.* Progress in Energy and Combustion Science, 2009. 35(5): p. 438-455.
76. Lee, S.-Y. and S.-J. Park, *A review on solid adsorbents for carbon dioxide capture.* Journal of Industrial and Engineering Chemistry, 2015. 23: p. 1-11.
77. Abu-Zahra, M.R., et al., *CO_2 capture from power plants: Part I. A parametric study of the technical performance based on monoethanolamine.* International Journal of Greenhouse gas control, 2007. 1(1): p. 37-46.
78. Gibbins, J. and H. Chalmers, *Carbon capture and storage.* Energy Policy, 2008. 36(12): p. 4317-4322.
79. Herzog, H. and D. Golomb, *Carbon capture and storage from fossil fuel use.* Encyclopedia of energy, 2004. 1(6562): p. 277-287.
80. Kanniche, M., et al., *Pre-combustion, post-combustion and oxy-combustion in thermal power plant for CO_2 capture.* Applied Thermal Engineering, 2010. 30(1): p. 53-62.
81. Ogden, J.M., *Review of small stationary reformers for hydrogen production.* Report to the international energy agency, 2001(609).
82. Rostrup-Nielsen, J.R. and J. Sehested, *Steam reforming for hydrogen. The process and the mechanism.* Fuel Chemistry Division Preprints, 2003. 48(1): p. 218-219.
83. Iulianelli, A., et al., *Advances on methane steam reforming to produce hydrogen through membrane reactors technology: A review.* Catalysis Reviews, 2016. 58(1): p. 1-35.
84. Holladay, J.D., et al., *An overview of hydrogen production technologies.* Catalysis Today, 2009. 139(4): p. 244-260.
85. Barelli, L., et al., *Hydrogen production through sorption-enhanced steam methane reforming and membrane technology: A review.* Energy, 2008. 33(4): p. 554-570.
86. Nieva, M.A., et al., *Steam-methane reforming at low temperature on nickel-based catalysts.* Chemical Engineering Journal, 2014. 235: p. 158-166.
87. Assabumrungrat, S., J. Phromprasit, and A. Arpornwichanop, *Fuel Processing Technologies for Hydrogen Production from Methane.* Engineering Journal, 2012. 16(2): p. 1-4.
88. Van Beurden, P., *On the catalytic aspects of steam-methane reforming.* Energy Research Centre of the Netherlands (ECN), Technical Report I-04-003, 2004.
89. RJ, B.S., M. Loganathan, and M.S. Shantha, *A review of the water gas shift reaction kinetics.* International Journal of Chemical Reactor Engineering, 2010. 8(1).
90. Bustamante, F., et al., *Kinetic study of the reverse water gas shift reaction in high-temperature, high pressure homogeneous systems.* Fuel Chem. Div. Preprints, 2002. 47: p. 663-664.
91. Hla, S., et al., *Kinetics of high-temperature water-gas shift reaction over two iron-based commercial catalysts using simulated coal-derived syngases.* Chemical Engineering Journal, 2009. 146(1): p. 148-154.

92. Li, D., Y. Nakagawa, and K. Tomishige, *Methane reforming to synthesis gas over Ni catalysts modified with noble metals.* Applied Catalysis A: General, 2011. 408(1-2): p. 1-24.
93. Rhodes, C., et al., *Promotion of Fe_3O_4/Cr_2O_3 high temperature water gas shift catalyst.* catalysis communications, 2002. 3(8): p. 381-384.
94. Brunetti, A., E. Drioli, and G. Barbieri, *Medium/high temperature water gas shift reaction in a Pd–Ag membrane reactor: an experimental investigation.* RSC Advances, 2012. 2(1): p. 226-233.
95. Song, C., et al., *Optimization of steam methane reforming coupled with pressure swing adsorption hydrogen production process by heat integration.* Applied energy, 2015. 154: p. 392-401.
96. Tavan, Y., S.H. Hosseini, and M. Olazar, *A note on an integrated process of methane steam reforming in junction with pressure-swing adsorption to produce pure hydrogen: mathematical modeling.* Industrial & Engineering Chemistry Research, 2015. 54(51): p. 12937-12947.
97. Sircar, S. and T.C. Golden, *Purification of Hydrogen by Pressure Swing Adsorption.* Separation Science and Technology, 2000. 35(5): p. 667-687.
98. *Van Beurden, P., 2004. On the catalytic aspects of steam-methane reforming. Energy Research Centre of the Netherlands (ECN), Technical Report I-04-003.*
99. Rollinson, Andrew N., V. Dupont, G. L. Rickett, and Martyn V. Twigg. "Hydrogen production by catalytic steam reforming of urea." In *5th International Ege Energy Symposium and Exhibition, Denizli (Turkey), 27th to 30th June*. 2010.
100. Rollinson, A.N., et al. *Hydrogen production by catalytic steam reforming of urea*. in *5th International Ege Energy Symposium and Exhibition, Denizli (Turkey), 27th to 30th June*. 2010.
101. Udengaard, N.R., *Hydrogen production by steam reforming of hydrocarbons.* Preprint Papers-American Chemical Society, Division of Fuel Chemistry, 2004. 49: p. 906-907.
102. Murata, K., et al., *Hydrogen production from steam reforming of hydrocarbons over alkaline-earth metal-modified Fe-or Ni-based catalysts.* Energy & fuels, 2004. 18(1): p. 122-126.
103. Fahim, M.A., T.A. Al-Sahhaf, and A. Elkilani, *Fundamentals of petroleum refining*. 2009: Elsevier.
104. Rostrup-Nielsen, J.R., T.S. Christensen, and I. Dybkjaer, *Steam reforming of liquid hydrocarbons*, in *Studies in Surface Science and Catalysis*. 1998, Elsevier. p. 81-95.
105. Neiva, L.S., *A Study on the Characteristics of the Reforming of Methane: A Review.* Brazilian Journal of Petroleum and Gas, 2010: p. 119-127.
106. Wu, H., et al., *Ni-Based Catalysts for Low Temperature Methane Steam Reforming: Recent Results on Ni-Au and Comparison with Other Bi-Metallic Systems.* Catalysts, 2013. 3(2): p. 563-583.
107. Balat, M. and N. Ozdemir, *New and renewable hydrogen production processes.* Energy sources, 2005. 27(13): p. 1285-1298.
108. Sheet, H.F., *Hydrogen Production–Steam Methane Reforming (SMR).* New York State Energy Research and Development Authority, New York, 2005.
109. Freitas, A.C. and R. Guirardello, *Thermodynamic analysis of methane reforming with CO_2, CO_2+ H_2O, CO_2+ O_2 and CO_2+ air for hydrogen and synthesis gas production.* Journal of CO_2 utilization, 2014. 7: p. 30-38.
110. Harrison, D.P., *Sorption-Enhanced Hydrogen Production: A Review.* Industrial & Engineering Chemistry Research, 2008. 47(17): p. 6486-6501.
111. Ding, Y., and E. Alpay. "Adsorption-enhanced steam–methane reforming."*Chemical Engineering Science*, no. 18 (2000): 3929-3940.

112. García-Lario, A.L., G.S. Grasa, and R. Murillo, *Performance of a combined CaO-based sorbent and catalyst on H_2 production, via sorption enhanced methane steam reforming.* Chemical Engineering Journal, 2015. 264: p. 697-705.
113. Iliuta, I., H.R. Radfarnia, and M.C. Iliuta, *Hydrogen Production by Sorption-Enhanced Steam Glycerol Reforming: Sorption Kinetics and Reactor Simulation.* AIChE Journal, 2013. 59(6): p. 2105-2118.
114. Cotton, A., K. Patchigolla, and J.E. Oakey, *Overview of, and Experimental Methodology for, Sorption Enhanced Hydrogen Production.* Energy Procedia, 2013. 37: p. 2232-2244.
115. Lopes, F.V.S., C.A. Grande, and A.E. Rodrigues, *Activated carbon for hydrogen purification by pressure swing adsorption: Multicomponent breakthrough curves and PSA performance.* Chemical Engineering Science, 2011. 66(3): p. 303-317.
116. Lee, C.H., S. Mun, and K.B. Lee, *Application of multisection packing concept to sorption-enhanced steam methane reforming reaction for high-purity hydrogen production.* Journal of Power Sources, 2015. 281: p. 158-163.
117. Dou, B., et al., *Solid sorbents for in-situ CO_2 removal during sorption-enhanced steam reforming process: A review.* Renewable and Sustainable Energy Reviews, 2016. 53: p. 536-546.
118. Solieman, A.A.A., et al., *Calcium oxide for CO_2 capture: Operational window and efficiency penalty in sorption-enhanced steam methane reforming.* International Journal of Greenhouse Gas Control, 2009. 3(4): p. 393-400.
119. Martavaltzi, C.S. and A.A. Lemonidou, *Hydrogen production via sorption enhanced reforming of methane: Development of a novel hybrid material—reforming catalyst and CO_2 sorbent.* Chemical Engineering Science, 2010. 65(14): p. 4134-4140.
120. Sisinni, M., et al., *Hydrogen-Rich Gas Production by Sorption Enhanced Steam Reforming of Woodgas Containing TAR over a Commercial Ni Catalyst and Calcined Dolomite as CO_2 Sorbent.* Energies, 2013. 6(7): p. 3167-3181.
121. Johnsen, K., et al., *Sorption-enhanced steam reforming of methane in a fluidized bed reactor with dolomite as -acceptor.* Chemical Engineering Science, 2006. 61(4): p. 1195-1202.
122. Ding, Y. and E. Alpay, *Adsorption-enhanced steam–methane reforming.* Chemical Engineering Science, 2000. 55(18): p. 3929-3940.
123. Han, C. and D.P. Harrison, *Simultaneous shift reaction and carbon dioxide separation for the direct production of hydrogen.* Chemical Engineering Science, 1994. 49(24): p. 5875-5883.
124. Hufton, J., S. Mayorga, and S. Sircar, *Sorption-enhanced reaction process for hydrogen production.* American Institute of Chemical Engineers. AIChE Journal, 1999. 45(2): p. 248.
125. Mayorga, S.G., et al., *Sorption enhanced reaction process for production of hydrogen. Phase 1 final report*. 1997, ; Air Products and Chemicals, Inc., Allentown, PA (United States). p. Medium: ED; Size: 59 p.
126. Shokrollahi Yancheshmeh, M., H.R. Radfarnia, and M.C. Iliuta, *High temperature CO_2 sorbents and their application for hydrogen production by sorption enhanced steam reforming process.* Chemical Engineering Journal, 2016. 283: p. 420-444.
127. Tomishige, K., et al., *Comparative study between fluidized bed and fixed bed reactors in methane reforming combined with methane combustion for the internal heat supply under pressurized condition.* Applied Catalysis A: General, 2002. 223(1): p. 225-238.
128. Trimm, D.L., *Catalysts for the control of coking during steam reforming.* Catalysis Today, 1999. 49(1): p. 3-10.
129. Eigenberger, G., *Ullmann Encyclopedia of Industrial Chemistry, Fixed Bed Reactors, vol*. 1992, B4.

130. Jing, Q., et al., *Comparative study between fluidized bed and fixed bed reactors in methane reforming with CO_2 and O_2 to produce syngas.* Energy Conversion and Management, 2006. 47(4): p. 459-469.
131. Warnecke, R., *Gasification of biomass: comparison of fixed bed and fluidized bed gasifier.* Biomass and bioenergy, 2000. 18(6): p. 489-497.
132. Hu, B. and H. Zhai, *The cost of carbon capture and storage for coal-fired power plants in China.* International Journal of Greenhouse Gas Control, 2017. 65: p. 23-31.
133. Singh, U. and A.B. Rao, *Integrating SO_2 and NO_x control systems in Indian coal-fired power plants.* Decision, 2015. 42(2): p. 191-209.
134. Yu, K.M., et al., *Recent advances in CO_2 capture and utilization.* ChemSusChem, 2008. 1(11): p. 893-9.
135. Fan, X., *Post-Combustion Carbon Capture.* Handbook of Clean Energy Systems, 2015.
136. Wang, Q., et al., *CO_2 capture by solid adsorbents and their applications: current status and new trends.* Energy Environ. Sci., 2011. 4(1): p. 42-55.
137. Yong, Z., V. Mata, and A.r.E. Rodrigues, *Adsorption of carbon dioxide at high temperature—a review.* Separation and purification technology, 2002. 26(2-3): p. 195-205.
138. Granite, E.J. and T. O'Brien, *Review of novel methods for carbon dioxide separation from flue and fuel gases.* Fuel Processing Technology, 2005. 86(14-15): p. 1423-1434.
139. Lu, X. and H. Xiao, *A review on CO_2 sorbents*. Vol. 42. 2015. 50-57.
140. Condon, J., *Surface Area and Porosity Determinations by Physisorption*. 2006.
141. IUPAC. 2016; Available from: *http://old.iupac.org/reports/2001/colloid_2001/manual_of_s_and_t/node16.html*
142. Bong Lee, K., et al., *Reversible Chemisorbents for Carbon Dioxide and Their Potential Applications*. Vol. 47. 2008.
143. Webb, P.A., *Introduction to chemical adsorption analytical techniques and their applications to catalysis.* Micromeritics Instrument Corp. Technical Publications, 2003.
144. Keskes, E., C. S. Adjiman, and A. Galindo, *A Physical Absorption Process for the Capture of CO_2 from CO_2-Rich Natural gas Streams*. 2008.
145. Auroux, A., *Calorimetry and Thermal Methods in Catalysis*. 2013.
146. Thommes, M., *Physical Adsorption Characterization of Nanoporous Materials.* Chemie Ingenieur Technik, 2010. 82(7): p. 1059-1073.
147. Adamson, A.W. and A.P. Gast, *Physical chemistry of surfaces*. 1997: Wiley.
148. Lennard-Jones, J.E., *Processes of adsorption and diffusion on solid surfaces.* Transactions of the Faraday Society, 1932. 28(0): p. 333-359.
149. Lowell, S., et al., *Characterization of Porous Solids and Powders: Surface Area, Pore Size and Density*. 2006: Springer Netherlands.
150. Theocharis, C.R., *The Measurement of Mesoporosity*, in *Multifunctional Mesoporous Inorganic Solids*. 1993, Springer. p. 3-18.
151. Sreenivasulu, B., et al., *Development Trends in Porous Adsorbents for Carbon Capture.* Environ Sci Technol, 2015. 49(21): p. 12641-61.
152. Chang, F., et al., *Microporous and mesoporous materials for gas storage and separation: a review.* Asia-Pacific Journal of Chemical Engineering, 2013. 8(4): p. 618-626.
153. Kumar, S. and S.K. Saxena, *A comparative study of CO_2 sorption properties for different oxides.* Materials for Renewable and Sustainable Energy, 2014. 3(3).
154. Li, J., et al., *Selective preparation of biomass-derived porous carbon with controllable pore sizes toward highly efficient CO_2 capture.* 2019. 360: p. 250-259.
155. Wang, J., et al., *Recent advances in solid sorbents for CO_2 capture and new development trends.* Energy & Environmental Science, 2014. 7(11): p. 3478-3518.
156. Singh, R., et al., *High temperature materials for CO_2 capture.* Energy Procedia, 2009. 1(1): p. 623-630.

157. Duan, Y., D. Luebke, and H. Henry Pennline, *Efficient Theoretical Screening of Solid Sorbents for CO_2; Capture Applications.* International Journal of Clean Coal and Energy, 2012. 01(01): p. 1-11.
158. Zhang, B., Y. Duan, and K. Johnson, *Density functional theory study of CO_2 capture with transition metal oxides and hydroxides.* J Chem Phys, 2012. 136(6): p. 064516.
159. Duan, Y. and D.C. Sorescu, *CO_2 capture properties of alkaline earth metal oxides and hydroxides: A combined density functional theory and lattice phonon dynamics study.* J Chem Phys, 2010. 133(7): p. 074508.
160. Nakagawa, K. and T. Ohashi, *A novel method of CO_2 capture from high temperature gases.* Journal of the Electrochemical Society, 1998. 145(4): p. 1344-1346.
161. Kato, M., et al., *Novel CO_2 Absorbents Using Lithium-Containing Oxide.* International Journal of Applied Ceramic Technology, 2005. 2(6): p. 467-475.
162. Ida, J.-i. and Y.S. Lin, *Mechanism of High-Temperature CO_2 Sorption on Lithium Zirconate.* Environmental Science & Technology, 2003. 37(9): p. 1999-2004.
163. Ida, J.-i., R. Xiong, and Y.S. Lin, *Synthesis and CO_2 sorption properties of pure and modified lithium zirconate.* Separation and Purification Technology, 2004. 36(1): p. 41-51.
164. Fauth, D.J., et al., *Eutectic salt promoted lithium zirconate: Novel high temperature sorbent for CO_2 capture.* Fuel Processing Technology, 2005. 86(14-15): p. 1503-1521.
165. Xiao, Q., et al., *Citrate route to prepare K-doped Li_2ZrO_3 sorbents with excellent CO_2 capture properties.* Chemical Engineering Journal, 2011. 174(1): p. 231-235.
166. Pannocchia, G., et al., *Experimental and Modeling Studies on High-Temperature Capture of CO_2 Using Lithium Zirconate Based Sorbents.* Industrial & Engineering Chemistry Research, 2007. 46(21): p. 6696-6706.
167. 加藤雅礼 and 中川和明, *New Series of Lithium Containing Complex Oxides, Lithium Silicates, for Application as a High Temperature CO_2 Absorbent.* Journal of the Ceramic Society of Japan (日本セラミックス協会学術論文誌), 2001. 109(1275): p. 911-914.
168. Xiong, R., J. Ida, and Y.S. Lin, *Kinetics of carbon dioxide sorption on potassium-doped lithium zirconate.* Chemical Engineering Science, 2003. 58(19): p. 4377-4385.
169. Wang, K., et al., *High temperature capture of CO_2 on lithium-based sorbents from rice husk ash.* J Hazard Mater, 2011. 189(1-2): p. 301-7.
170. Kato, M., et al., *Pre-combustion CO_2 capture using ceramic absorbent and methane steam reforming*, in *Greenhouse Gas Control Technologies 7*. 2005, Elsevier Science Ltd: Oxford. p. 1897-1899.
171. Rusten, H.K., et al., *Hydrogen Production by Sorption-Enhanced Steam Methane Reforming Using Lithium Oxides as CO_2-Acceptor.* Industrial & Engineering Chemistry Research, 2007. 46(25): p. 8729-8737.
172. Xu, H., et al., *Effect of the Particle Size of Quartz Powder on the Synthesis and CO_2 Absorption Properties of Li_4SiO_4 at High Temperature.* Industrial & Engineering Chemistry Research, 2013. 52(5): p. 1886-1891.
173. Barraza Jiménez, D., et al., *Kinetic study and modeling of the high temperature CO_2 capture by Na_2ZrO_3 solid absorbent.* International Journal of Hydrogen Energy, 2013. 38(5): p. 2557-2564.
174. López-Ortiz, A., et al., *Novel Carbon Dioxide Solid Acceptors Using Sodium Containing Oxides.* Separation Science and Technology, 2005. 39(15): p. 3559-3572.
175. Ochoa-Fernández, E., et al., *Effects of steam addition on the properties of high temperature ceramic CO_2 acceptors.* Journal of Environmental Engineering, 2009. 135(6): p. 397-403.
176. Jakobsen, J.P. and E. Halmøy, *Reactor modeling of sorption enhanced steam methane reforming.* Energy Procedia, 2009. 1(1): p. 725-732.

177. Guzman-Velderrain, V., et al., *Synthesis, Characterization and Evaluation of SodiumDoped Lithium Zirconate as a High Temperature CO_2 Absorbent.* Journal of New Materials for Electrochemical Systems, 2008. 11(2): p. 131.
178. Santiago-Torres, N., I.C. Romero-Ibarra, and H. Pfeiffer, *Sodium zirconate (Na_2ZrO_3) as a catalyst in a soybean oil transesterification reaction for biodiesel production.* Fuel Processing Technology, 2014. 120: p. 34-39.
179. Martínez-dlCruz, L. and H. Pfeiffer, *Microstructural Thermal Evolution of the Na_2CO_3 Phase Produced during a Na_2ZrO_3–CO_2 Chemisorption Process.* The Journal of Physical Chemistry C, 2012. 116(17): p. 9675-9680.
180. Pfeiffer, H., E. Lima, and P. Bosch, *Lithium–Sodium Metazirconate Solid Solutions, $Li_{2-x}Na_xZrO_3$ ($0 \le x \le 2$): A Hierarchical Architecture.* Chemistry of Materials, 2006. 18(11): p. 2642-2647.
181. Radfarnia, H.R. and M.C. Iliuta, *Application of surfactant-template technique for preparation of sodium zirconate as high temperature CO_2 sorbent.* Separation and Purification Technology, 2012. 93: p. 98-106.
182. Zhao, T., et al., *Preparation and High-Temperature CO_2 Capture Properties of Nanocrystalline Na_2ZrO_3.* Chemistry of Materials, 2007. 19(13): p. 3294-3301.
183. Pfeiffer, H., et al., *Thermal Behavior and CO_2 Absorption of $Li_{2-x}Na_xZrO_3$ Solid Solutions.* Chemistry of Materials, 2007. 19(4): p. 922-926.
184. Li, B., et al., *Advances in CO_2 capture technology: A patent review.* Applied Energy, 2013. 102: p. 1439-1447.
185. Barin, I. and G. Platzki, *Thermochemical data of pure substances*. Vol. 304. 1989: Wiley Online Library.
186. Silaban, A. and D. Harrison, *High temperature capture of carbon dioxide: characteristics of the reversible reaction between $CaO_{(s)}$ and $CO_{2(g)}$.* Chemical Engineering Communications, 1995. 137(1): p. 177-190.
187. Valverde, J.M. and S. Medina, *Crystallographic transformation of limestone during calcination under CO_2.* Physical Chemistry Chemical Physics, 2015. 17(34): p. 21912-21926.
188. Barker, R., *The reversibility of the reaction $CaCO_3 \rightleftarrows CaO + CO_2$.* Journal of applied Chemistry and biotechnology, 1973. 23(10): p. 733-742.
189. Maciejewski, M. and A. Reller, *How (un) reliable are kinetic data of reversible solid-state decomposition processes?* Thermochimica Acta, 1987. 110: p. 145-152.
190. Sun, P., et al., *The effect of CaO sintering on cyclic CO_2 capture in energy systems.* AIChE Journal, 2007. 53(9): p. 2432-2442.
191. Alvarez, D. and J.C. Abanades, *Determination of the Critical Product Layer Thickness in the Reaction of CaO with CO_2.* Industrial & Engineering Chemistry Research, 2005. 44(15): p. 5608-5615.
192. Wu, Y., et al., *Morphological Changes of Limestone Sorbent Particles during Carbonation/Calcination Looping Cycles in a Thermogravimetric Analyzer (TGA) and Reactivation with Steam.* Energy & Fuels, 2010. 24(4): p. 2768-2776.
193. Bhatia, S. and D. Perlmutter, *Effect of the product layer on the kinetics of the CO_2-lime reaction.* AIChE Journal, 1983. 29(1): p. 79-86.
194. Manovic, V., et al., *Influence of calcination conditions on carrying capacity of CaO-based sorbent in CO_2 looping cycles.* Fuel, 2009. 88(10): p. 1893-1900.
195. Fennell, P.S., et al., *The effects of repeated cycles of calcination and carbonation on a variety of different limestones, as measured in a hot fluidized bed of sand.* Energy & Fuels, 2007. 21(4): p. 2072-2081.
196. Lysikov, A.I., A.N. Salanov, and A.G. Okunev, *Change of CO_2 carrying capacity of CaO in isothermal recarbonation− decomposition cycles.* Industrial & Engineering Chemistry Research, 2007. 46(13): p. 4633-4638.

197. Broda, M., et al., *Effect of pelletization and addition of steam on the cyclic performance of carbon-templated, CaO-based CO_2 sorbents.* Environ Sci Technol, 2014. 48(9): p. 5322-8.
198. Li, Y., et al., *Modified CaO-based sorbent looping cycle for CO_2 mitigation.* Fuel, 2009. 88(4): p. 697-704.
199. Sun, R., et al., *Enhancement of CO_2 capture capacity by modifying limestone with propionic acid.* Powder Technology, 2013. 233: p. 8-14.
200. Li, Y., et al., *Cyclic CO_2 Capture Behavior of Limestone Modified with Pyroligneous Acid (PA) during Calcium Looping Cycles.* Industrial & Engineering Chemistry Research, 2011. 50(17): p. 10222-10228.
201. Radfarnia, H.R. and M.C. Iliuta, *Limestone Acidification Using Citric Acid Coupled with Two-Step Calcination for Improving the CO_2 Sorbent Activity.* Industrial & Engineering Chemistry Research, 2013. 52(21): p. 7002-7013.
202. Li, Y.J., et al., *CO_2 Capture Using CaO Modified with Ethanol/Water Solution during Cyclic Calcination/Carbonation.* Chemical Engineering & Technology, 2008. 31(2): p. 237-244.
203. Manovic, V. and E.J. Anthony, *Steam Reactivation of Spent CaO-Based Sorbent for Multiple CO_2 Capture Cycles.* Environmental Science & Technology, 2007. 41(4): p. 1420-1425.
204. Zeman, F., *Effect of steam hydration on performance of lime sorbent for CO_2 capture.* International Journal of Greenhouse Gas Control, 2008. 2(2): p. 203-209.
205. Manovic, V. and E.J. Anthony, *Thermal Activation of CaO-Based Sorbent and Self-Reactivation during CO_2 Capture Looping Cycles.* Environmental Science & Technology, 2008. 42(11): p. 4170-4174.
206. Wang, S., et al., *Enhanced CO_2 adsorption capacity and stability using CaO-based adsorbents treated by hydration.* AIChE Journal, 2013. 59(10): p. 3586-3593.
207. Valverde, J.M., P.E. Sanchez-Jimenez, and L.A. Perez-Maqueda, *High and stable capture capacity of natural limestone at Ca-looping conditions by heat pretreatment and recarbonation synergy.* Fuel, 2014. 123: p. 79-85.
208. Rong, N., et al., *Steam hydration reactivation of CaO-based sorbent in cyclic carbonation/calcination for CO_2 capture.* Energy & Fuels, 2013. 27(9): p. 5332-5340.
209. Ridha, F.N., et al., *Pelletized CaO-based sorbents treated with organic acids for enhanced CO_2 capture in Ca-looping cycles.* International Journal of Greenhouse Gas Control, 2013. 17: p. 357-365.
210. Champagne, S., et al., *Influence of Steam Injection during Calcination on the Reactivity of CaO-Based Sorbent for Carbon Capture.* Industrial & Engineering Chemistry Research, 2013. 52(6): p. 2241-2246.
211. Ridha, F.N., et al., *Assessment of limestone treatment with organic acids for CO_2 capture in Ca-looping cycles.* Fuel Processing Technology, 2013. 116: p. 284-291.
212. Chen, H., C. Zhao, and Y. Yang, *Enhancement of attrition resistance and cyclic CO_2 capture of calcium-based sorbent pellets.* Fuel Processing Technology, 2013. 116: p. 116-122.
213. Coppola, A., et al., *Reactivation by water hydration of the CO_2 capture capacity of a calcium looping sorbent.* Fuel, 2014. 127: p. 109-115.
214. Valverde, J.M., et al., *Role of Looping-Calcination Conditions on Self-Reactivation of Thermally Pretreated CO_2 Sorbents Based on CaO.* Energy & Fuels, 2013. 27(6): p. 3373-3384.
215. Grasa, G., et al., *Determination of CaO Carbonation Kinetics under Recarbonation Conditions.* Energy & Fuels, 2014. 28(6): p. 4033-4042.
216. Valverde, J.M., P.E. Sanchez-Jimenez, and L.A. Perez-Maqueda, *Effect of Heat Pretreatment/Recarbonation in the Ca-Looping Process at Realistic Calcination Conditions.* Energy & Fuels, 2014. 28(6): p. 4062-4067.

217. Ertl, G., H. Knözinger, and J. Weitkamp, *Handbook of Heterogeneous Catalysis*. 2008. 1-2497.
218. Li, Z.-s., et al., *Synthesis, experimental studies, and analysis of a new calcium-based carbon dioxide absorbent.* Energy & Fuels, 2005. 19(4): p. 1447-1452.
219. Li, Z.-s., N.-s. Cai, and Y.-y. Huang, *Effect of preparation temperature on cyclic CO_2 capture and multiple carbonation− calcination cycles for a new Ca-based CO_2 sorbent.* Industrial & Engineering Chemistry Research, 2006. 45(6): p. 1911-1917.
220. Zhou, Z., et al., *Synthesis of CaO-based sorbents through incorporation of alumina/aluminate and their CO_2 capture performance.* Chemical Engineering Science, 2012. 74: p. 172-180.
221. Koirala, R., G.K. Reddy, and P.G. Smirniotis, *Single Nozzle Flame-Made Highly Durable Metal Doped Ca-Based Sorbents for CO_2 Capture at High Temperature.* Energy & Fuels, 2012. 26(5): p. 3103-3109.
222. LTD, S., *SAFFIL.* Product information sheet, 2013: p. 17.
223. UNIFRAX, *SAFFIL: Fiber, Blanket, Mat and Felt products.* Product information sheet, 2013. Form C-1700: p. 1-4.
224. Campanati, M., G. Fornasari, and A. Vaccari, *Fundamentals in the preparation of heterogeneous catalysts.* Catalysis Today, 2003. 77(4): p. 299-314.
225. Valverde, J.M., *Ca-based synthetic materials with enhanced CO_2 capture efficiency.* Journal of Materials Chemistry A, 2013. 1(3): p. 447-468.
226. Nouri, S. and H. Ebrahim, *Effect of sorbent pore volume on the carbonation reaction in lime with CO_2.* Brazilian Journal of Chemical Engineering, 2016. 33(2): p. 383-389.
227. Blamey, J., et al., *On steam hydration of CaO-based sorbent cycled for CO_2 capture.* Fuel, 2015. 150: p. 269-277.
228. Perego, C. and P. Villa, *Catalyst preparation methods.* Catalysis Today, 1997. 34(3-4): p. 281-305.
229. Baiker, A., et al., *Handbook of Heterogeneous Catalysis.* Ertl, G., Knözinger, H., Weitkamp, J., Eds, 1997: p. 2422.
230. Schwarz, J.A., C. Contescu, and A. Contescu, *Methods for preparation of catalytic materials.* Chemical Reviews, 1995. 95(3): p. 477-510.
231. Marcilly, C., *La préparation des catalyseurs. Première partie: Germination et croissance des particules. Importance de la sursaturation du milieu.* Revue de l'Institut français du pétrole, 1984. 39(2): p. 189-208.
232. Naplocha, K. and K. Granat, *The structure and properties of hybrid preforms for composites.* Journal of Achievements in Materials and Manufacturing Engineering, 2007. 22(2): p. 35-38.
233. Fultz, B. and J. Howe, *Diffraction and the X-Ray Powder Diffractometer.* 2013: p. 1-57.
234. Lavina, B., P. Dera, and R.T. Downs, *Modern X-ray Diffraction Methods in Mineralogy and Geosciences.* Reviews in Mineralogy and Geochemistry, 2014. 78(1): p. 1-31.
235. Waseda, Y., E. Matsubara, and K. Shinoda, *X-ray diffraction crystallography: introduction, examples and solved problems*. 2011: Springer Science & Business Media.
236. Das, R., E. Ali, and S.B. Abd Hamid, Current applications of X-ray powder diffraction-a review. Reviews on Advanced Materials Science, 2014. 38(2).
237. Dann, S.E., *Reactions and characterization of solids*. Vol. 2. 2000: Royal Society of Chemistry.
238. Chauhan, A., *Powder XRD Technique and its Applications in Science and Technology.* Journal of Analytical & Bioanalytical Techniques, 2014. 5(6).
239. Tilley, R.J., *Crystals and crystal structures*. 2006: John Wiley & Sons.
240. Skoog, D.A., F.J. Holler, and S.R. Crouch, *Principles of instrumental analysis*. 2007: Thomson Brooks/Cole.
241. DARC, S.L.o.t.P., *X-Ray Diffraction (XRD).* 2016.

242. Sirdeshmukh, D.B., L. Sirdeshmukh, and K. Subhadra, *Diffraction of Radiation by Crystals (Principles and Experimental Methods)*, in *Atomistic Properties of Solids*. 2011, Springer. p. 115-164.
243. Fultz, B. and J.M. Howe, *Transmission electron microscopy and diffractometry of materials*. 2012: Springer Science & Business Media.
244. Bilton, M., A. Brown, and S. Milne. *Investigating the optimum conditions for the formation of calcium oxide, used for CO_2 sequestration, by thermal decomposition of calcium acetate*. in *Journal of Physics: Conference Series*. 2012. IOP Publishing.
245. Materials, R.I.f., *D8 Advance - X-ray diffraction system.*
246. Knözinger, H. and K. Kochloefl, *Heterogeneous catalysis and solid catalysts.* Ullmann's Encyclopedia of Industrial Chemistry, 2003.
247. Klobes, P., K. Meyer, and R.G. Munro, *Porosity and specific surface area measurements for solid materials.* 2006.
248. Sing, K.S., *Reporting physisorption data for gas/solid systems with special reference to the determination of surface area and porosity (Recommendations 1984).* Pure and Applied Chemistry, 1985. 57(4): p. 603-619.
249. Thommes, M., et al., *Physisorption of gases, with special reference to the evaluation of surface area and pore size distribution (IUPAC Technical Report).* Pure and Applied Chemistry, 2015. 87(9-10): p. 1051-1069.
250. Gregg, S.J., K.S.W. Sing, and H. Salzberg, *Adsorption surface area and porosity.* Journal of The Electrochemical Society, 1967. 114(11): p. 279C-279C.
251. Storck, S., H. Bretinger, and W.F. Maier, *Characterization of micro-and mesoporous solids by physisorption methods and pore-size analysis.* Applied Catalysis A: General, 1998. 174(1): p. 137-146.
252. Neimark, A.V., P.I.J.M. Ravikovitch, and M. Materials, *Capillary condensation in MMS and pore structure characterization.* 2001. 44: p. 697-707.
253. Leng, Y., *Materials characterization: introduction to microscopic and spectroscopic methods*. 2009: John Wiley & Sons.
254. Vernon-Parry, K., *Scanning electron microscopy: an introduction.* III-Vs Review, 2000. 13(4): p. 40-44.
255. CCWJ, C.C.f.W.J., *Microscopy.* 2016.
256. Shindo, D. and T. Oikawa, *Energy Dispersive X-ray Spectroscopy*, in *Analytical Electron Microscopy for Materials Science*. 2002, Springer. p. 81-102.
257. Wang, J., et al., *Enhanced stability of CaO and/or La_2O_3 promoted Pd/Al_2O_3 egg-shell catalysts in partial oxidation of methane to syngas.* Molecules, 2013. 18(7): p. 8289-97.
258. Prime, R.B., et al., *Thermogravimetric analysis (TGA).* Thermal analysis of polymers: Fundamentals and applications, 2009: p. 241-317.
259. Coats, A. and J. Redfern, *Thermogravimetric analysis. A review.* Analyst, 1963. 88(1053): p. 906-924.
260. Gabbott, P., *Principles and applications of thermal analysis*. 2008: John Wiley & Sons.
261. Gaisford, S., V. Kett, and P. Haines, *Principles of thermal analysis and calorimetry*. 2016: Royal society of chemistry.
262. Potts, P.J., *A handbook of silicate rock analysis*. 2012: Springer Science & Business Media.
263. Jung, Y.-S., et al., *A highly active Ni-Al_2O_3 catalyst prepared by homogeneous precipitation using urea for internal reforming in a molten carbonate fuel cell (MCFC): Effect of the synthesis temperature.* International Journal of Hydrogen Energy, 2010. 35(20): p. 11237-11244.
264. Qin, H., et al., *Application of urea precipitation method in preparation of advanced ceramic powders.* Ceramics International, 2015. 41(9): p. 11598-11604.
265. Tang, Z.-X., et al., *Preparation of nano-CaO using thermal-decomposition method.* Materials Letters, 2008. 62(14): p. 2096-2098.

266. Roy, A. and J. Bhattacharya, *Synthesis of $Ca(OH)_2$ nanoparticles by wet chemical method.* Micro & Nano Letters, 2010. 5(2): p. 131.
267. Niu, S., et al., *Thermogravimetric analysis of the relationship among calcium magnesium acetate, calcium acetate and magnesium acetate.* Applied Energy, 2010. 87(7): p. 2237-2242.
268. Gallala, W., et al., *Factors influencing the reactivity of quicklime.* Construction Materials, 2008. 161(1): p. 25.
269. Balzar, D., *X-ray diffraction line broadening: modeling and applications to high-Tc superconductors.* Journal of research of the National Institute of Standards and Technology, 1993. 98(3): p. 321.
270. Song, J., et al., *Soft Zr-doped TiO_2 Nanofibrous Membranes with Enhanced Photocatalytic Activity for Water Purification.* Scientific Reports, 2017. 7.
271. Nguyen, P.T., et al., *On the cavitation-like pore blocking in ink-bottle pore: evolution of hysteresis loop with neck size.* The Journal of Physical Chemistry C, 2013. 117(10): p. 5475-5484.
272. Reichenbach, C., et al., *Cavitation and pore blocking in nanoporous glasses.* Langmuir, 2011. 27(17): p. 10699-10704.
273. Thommes, M. and K.A. Cychosz, *Physical adsorption characterization of nanoporous materials: progress and challenges.* Adsorption, 2014. 20(2-3): p. 233-250.
274. Cychosz, K.A., et al., *Recent advances in the textural characterization of hierarchically structured nanoporous materials.* Chemical Society Reviews, 2017. 46(2): p. 389-414.
275. Coasne, B., *Multiscale adsorption and transport in hierarchical porous materials.* New Journal of Chemistry, 2016. 40(5): p. 4078-4094.
276. Watanabe, M., *Sample preparation for X-ray fluorescence analysis IV. Fusion bead method—part 1 basic principals.* English version, 2015: p. 12.
277. Gaigneaux, E., et al., *Scientific Bases for the Preparation of Heterogeneous Catalysts: Proceedings of the 9th International Symposium Louvain-la-Neuve, Belgium, September 10-14, 2006*. Vol. 162. 2006: Elsevier.
278. Rodriguez-Navarro, C., E. Hansen, and W.S.J.J.o.t.A.C.S. Ginell, *Calcium hydroxide crystal evolution upon aging of lime putty.* 1998. 81(11): p. 3032-3034.
279. Burlakov, V., et al., *Reversing Ostwald Ripening.* arXiv preprint arXiv:1412.6280, 2014.
280. Voorhees, P.W., *Ostwald ripening of two-phase mixtures.* Annual Review of Materials Science, 1992. 22(1): p. 197-215.
281. Voorhees, P.W., *The theory of Ostwald ripening.* Journal of Statistical Physics, 1985. 38(1): p. 231-252.
282. Marqusee, J. and J. Ross, *Theory of Ostwald ripening: Competitive growth and its dependence on volume fraction.* The Journal of chemical physics, 1984. 80(1): p. 536-543.
283. Helbig, U., *Growth of calcium carbonate in polyacrylamide hydrogel: Investigation of the influence of polymer content.* Journal of Crystal Growth, 2008. 310(11): p. 2863-2870.
284. Hlaing, N.N., et al., *Sol–gel hydrothermal synthesis of microstructured CaO-based adsorbents for CO_2 capture.* RSC Advances, 2015. 5(8): p. 6051-6060.
285. Zhao, Z., et al., *Surfactant-assisted solvo-or hydrothermal fabrication and characterization of high-surface-area porous calcium carbonate with multiple morphologies.* Microporous and Mesoporous Materials, 2011. 138(1-3): p. 191-199.
286. Koczkur, K.M., et al., *Polyvinylpyrrolidone (PVP) in nanoparticle synthesis.* Dalton Transactions, 2015. 44(41): p. 17883-17905.
287. Zhao, J., et al., *From solid-state metal alkoxides to nanostructured oxides: a precursor-directed synthetic route to functional inorganic nanomaterials.* Inorganic Chemistry Frontiers, 2015. 2(3): p. 198-212.

288. Henrist, C., et al., *Morphological study of magnesium hydroxide nanoparticles precipitated in dilute aqueous solution.* Journal of Crystal Growth, 2003. 249(1-2): p. 321-330.
289. Tobler, D.J., et al., *Effect of pH on amorphous calcium carbonate structure and transformation.* Crystal Growth & Design, 2016. 16(8): p. 4500-4508.
290. Samanta, A., et al., *Synthesis of nano calcium hydroxide in aqueous medium.* Journal of the American Ceramic Society, 2016. 99(3): p. 787-795.
291. Aquilano, D., et al., *Three study cases of growth morphology in minerals: Halite, calcite and gypsum.* Progress in Crystal Growth and Characterization of Materials, 2016. 62(2): p. 227-251.
292. Theocharis, C.R., et al., *Control of the morphology of crystalline calcium hydroxide.* Molecular Crystals and Liquid Crystals Science and Technology. Section A. Molecular Crystals and Liquid Crystals, 2001. 356(1): p. 205-214.
293. Rodriguez-Navarro, C., K. Elert, and R. Ševčík, *Amorphous and crystalline calcium carbonate phases during carbonation of nanolimes: implications in heritage conservation.* CrystEngComm, 2016. 18(35): p. 6594-6607.
294. Ruiz-Agudo, E.n., et al., *Dissolution and carbonation of portlandite [$Ca(OH)_2$] single crystals.* Environmental science & technology, 2013. 47(19): p. 11342-11349.
295. Chang, R., et al., *Calcium carbonate precipitation for CO_2 storage and utilization: a review of the carbonate crystallization and polymorphism.* Frontiers in Energy Research, 2017. 5: p. 17.
296. Sarkar, A. and S. Mahapatra, *Mechanism of unusual polymorph transformations in calcium carbonate: Dissolution-recrystallization vs additive-mediated nucleation.* Journal of Chemical Sciences, 2012. 124(6): p. 1399-1404.
297. Cullity, B.D., S.R. Cullity, and S. Stock, *Elements of X-ray Diffraction*. 2001.
298. Monson, P.A., *Understanding adsorption/desorption hysteresis for fluids in mesoporous materials using simple molecular models and classical density functional theory.* Microporous and Mesoporous Materials, 2012. 160: p. 47-66.
299. Grasa, G.S. and J.C. Abanades, *CO_2 capture capacity of CaO in long series of carbonation/calcination cycles.* Industrial & Engineering Chemistry Research, 2006. 45(26): p. 8846-8851.
300. Florin, N. and P. Fennell, *Synthetic CaO-based sorbent for CO_2 capture.* Energy Procedia, 2011. 4: p. 830-838.
301. Grasa, G., et al., *Application of the random pore model to the carbonation cyclic reaction.* AIChE Journal, 2009. 55(5): p. 1246-1255.
302. Choi, S., J.H. Drese, and C.W. Jones, *Adsorbent materials for carbon dioxide capture from large anthropogenic point sources.* ChemSusChem, 2009. 2(9): p. 796-854.
303. Manovic, V. and E.J. Anthony, *Screening of binders for pelletization of CaO-based sorbents for CO_2 capture.* Energy & Fuels, 2009. 23(10): p. 4797-4804.
304. Hu, Y., et al., *Screening of inert solid supports for CaO-based sorbents for high temperature CO_2 capture.* Fuel, 2016. 181: p. 199-206.
305. St, D. and M. Johansson, *Properties of powder coatings in load carrying construction.* Journal of Coatings Technology and Research, 2005. 2(6): p. 473-481.
306. Qi, Z., et al., *Analysis of CO_2 sorption/desorption kinetic behaviors and reaction mechanisms on Li_4SiO_4.* AIChE Journal, 2013. 59(3): p. 901-911.
307. Böhm, H.J. and A. Rasool, *Effects of particle shape on the thermoelastoplastic behavior of particle reinforced composites.* International Journal of Solids and Structures, 2016. 87: p. 90-101.
308. Lu, A.-H. and G.-P. Hao, *Porous materials for carbon dioxide capture.* Annual Reports Section" A"(Inorganic Chemistry), 2013. 109: p. 484-503.
309. Zhao, M., et al., *Durability of CaO–$CaZrO_3$ sorbents for high-temperature CO_2 capture prepared by a wet chemical method.* Energy & Fuels, 2014. 28(2): p. 1275-1283.

310. Alonso, M., et al., *Undesired effects in the determination of CO_2 carrying capacities of CaO during TG testing.* Fuel, 2014. 127: p. 52-61.
311. Manovic, V. and E.J. Anthony, *Sintering and formation of a nonporous carbonate shell at the surface of CaO-based sorbent particles during CO_2-capture cycles.* Energy & Fuels, 2010. 24(10): p. 5790-5796.
312. Wu, S.F., et al., *Properties of a nano CaO/Al_2O_3 CO_2 sorbent.* Industrial & Engineering Chemistry Research, 2008. 47(1): p. 180-184.
313. Luo, C., et al., *Effect of support material on carbonation and sulfation of synthetic CaO-based sorbents in calcium looping cycle.* Energy & Fuels, 2013. 27(8): p. 4824-4831.
314. Koirala, R., et al., *Effect of zirconia doping on the structure and stability of CaO-based sorbents for CO_2 capture during extended operating cycles.* The Journal of Physical Chemistry C, 2011. 115(50): p. 24804-24812.
315. Salaudeen, S.A., B. Acharya, and A. Dutta, *CaO-based CO_2 sorbents: A review on screening, enhancement, cyclic stability, regeneration and kinetics modelling.* Journal of CO_2 Utilization, 2018. 23: p. 179-199.
316. Burnham, A.K., *Global chemical reaction kinetics of fossil fuels*. 2017: Springer.
317. Vyazovkin, S. and C.A. Wight, *Isothermal and non-isothermal kinetics of thermally stimulated reactions of solids.* International Reviews in Physical Chemistry, 1998. 17(3): p. 407-433.
318. Vyazovkin, S. and C.A. Wight, *Isothermal and nonisothermal reaction kinetics in solids: in search of ways toward consensus.* The Journal of Physical Chemistry A, 1997. 101(44): p. 8279-8284.
319. Garn, P.D., *Kinetics of thermal decomposition of the solid state: II. Delimiting the homogeneous-reaction model.* Thermochimica Acta, 1990. 160(2): p. 135-145.
320. Vyazovkin, S., *Some basics en route to isoconversional methodology*, in *Isoconversional Kinetics of Thermally Stimulated Processes*. 2015, Springer. p. 1-25.
321. Khawam, A. and D.R. Flanagan, *Solid-state kinetic models: basics and mathematical fundamentals.* The journal of physical chemistry B, 2006. 110(35): p. 17315-17328.
322. Georgieva, V., L. Vlaev, and K. Gyurova, *Non-isothermal degradation kinetics of $CaCO_3$ from different origin.* Journal of Chemistry, 2012. 2013.
323. Vyazovkin, S., et al., *ICTAC Kinetics Committee recommendations for collecting experimental thermal analysis data for kinetic computations.* Thermochimica Acta, 2014. 590: p. 1-23.
324. Dickinson, C. and G. Heal, *A review of the ICTAC kinetics project, 2000: Part 2. Non-isothermal results.* Thermochimica Acta, 2009. 494(1): p. 15-25.
325. Dickinson, C. and G. Heal, *A review of the ICTAC Kinetics Project, 2000: Part 1. Isothermal results.* Thermochimica Acta, 2009. 494(1): p. 1-14.
326. Klaewkla, R., M. Arend, and W.F. Hoelderich, *A review of mass transfer controlling the reaction rate in heterogeneous catalytic systems*, in *Mass Transfer-Advanced Aspects*. 2011, InTech.
327. Broda, M., R. Pacciani, and C.R. Müller, *CO_2 capture via cyclic calcination and carbonation reactions*, in *Porous Materials for Carbon Dioxide Capture*. 2014, Springer. p. 181-222.
328. Sreenivasulu, B., et al., *Thermokinetic Investigations of High Temperature Carbon Capture Using a Coal Fly Ash Doped Sorbent.* Energy & Fuels, 2017. 31(6): p. 6320-6328.
329. Abanades, J.C., *The maximum capture efficiency of CO_2 using a carbonation/calcination cycle of $CaO/CaCO_3$.* Chemical Engineering Journal, 2002. 90(3): p. 303-306.
330. Gupta, H. and L.-S. Fan, *Carbonation− calcination cycle using high reactivity calcium oxide for carbon dioxide separation from flue gas.* Industrial & Engineering Chemistry Research, 2002. 41(16): p. 4035-4042.

331. Ramezani, M., et al., *Determination of Carbonation/Calcination Reaction Kinetics of a Limestone Sorbent in low CO_2 Partial Pressures Using TGA Experiments.* Energy Procedia, 2017. 114: p. 259-270.
332. Rashidi, N.A., M. Mohamed, and S. Yusup, *The kinetic model of calcination and carbonation of Anadara Granosa.* International Journal of Renewable Energy Research, 2012. 2(3): p. 497-503.
333. Antzara, A., et al., *Thermodynamic analysis of hydrogen production via chemical looping steam methane reforming coupled with in situ CO_2 capture.* International Journal of Greenhouse Gas Control, 2015. 32: p. 115-128.
334. Brown, M.E., D. Dollimore, and A.K. Galwey, *Reactions in the solid state*. Vol. 22. 1980: Elsevier.
335. Guler, C., D. Dollimore, and G.R. Heal, *The investigation of the decomposition kinetics of calcium carbonate alone and in the presence of some clays using the rising temperature technique.* Thermochimica Acta, 1982. 54(1): p. 187-199.
336. Borgwardt, R.H., *Calcination kinetics and surface area of dispersed limestone particles.* AIChE Journal, 1985. 31(1): p. 103-111.
337. Li, X., et al., *Effects of pore sizes of porous silica gels on desorption activation energy of water vapour.* Applied Thermal Engineering, 2007. 27(5-6): p. 869-876.
338. Kumar, D., S.C. Maiti, and C. Ghoroi, *Decomposition kinetics of $CaCO_3$ dry coated with nano-silica.* Thermochimica Acta, 2016. 624: p. 35-46.
339. Mamleev, V., et al., *Three model-free methods for calculation of activation energy in TG.* Journal of thermal analysis and calorimetry, 2004. 78(3): p. 1009-1027.
340. Friedman, H.L. *Kinetics of thermal degradation of char-forming plastics from thermogravimetry. Application to a phenolic plastic*. in *Journal of Polymer Science: Polymer Symposia*. 1964. Wiley Online Library.
341. Ozawa, T., *Estimation of activation energy by isoconversion methods.* Thermochimica Acta, 1992. 203: p. 159-165.
342. Kissinger, H.E., *Reaction kinetics in differential thermal analysis.* Analytical chemistry, 1957. 29(11): p. 1702-1706.
343. Coats, A.W. and J. Redfern, *Kinetic parameters from thermogravimetric data.* Nature, 1964. 201(4914): p. 68.
344. Rodriguez-Navarro, C., et al., *Thermal decomposition of calcite: Mechanisms of formation and textural evolution of CaO nanocrystals.* American Mineralogist, 2009. 94(4): p. 578-593.
345. Sanders, J. and P. Gallagher, *Kinetic analyses using simultaneous TG/DSC measurements.* Journal of thermal analysis and calorimetry, 2005. 82(3): p. 659-664.
346. Venkatesh, M., P. Ravi, and S.P. Tewari, *Isoconversional kinetic analysis of decomposition of nitroimidazoles: Friedman method vs Flynn–Wall–Ozawa method.* The Journal of Physical Chemistry A, 2013. 117(40): p. 10162-10169.
347. Ninan, K., K. Krishnan, and V. Krishnamurthy, *Kinetics and mechanism of thermal decomposition of insitu generated calcium carbonate.* Journal of thermal analysis, 1991. 37(7): p. 1533-1543.
348. L'vov, B.V., *Mechanism and kinetics of thermal decomposition of carbonates.* Thermochimica Acta, 2002. 386(1): p. 1-16.
349. Niu, S., et al., *Thermogravimetric analysis of the decomposition characteristics of two kinds of calcium based organic compounds.* Powder technology, 2011. 209(1-3): p. 46-52.
350. Wang, D., et al., *An investigation of the decomposition mechanism of calcium carbonate.* Metalurgija, 2017. 56(1-2): p. 9-12.

List of Publications and Conferences

A list of publications and conferences attended during the consummation of the present research is showed below. The contribution of the PhD's candidate in highlighted in the description of the events and research works.

Articles

- **Sergio Ramirez-Solis,** S. Milne and V. Dupont. Preparation and Evaluation of CaO-based CO_2 Sorbents Deposited on Saffil Fibre Supports. Energy & Fuels, 2018.

Presentations

- **S. Ramirez-Solis**, R. Bloom, J. Spragg, S. Milne, T. Mahmud and V. Dupont. Sorption Enhanced Chemical Looping Steam Reforming: current projects at The University of Leeds. IEAGHG's 7th High Temperature Solid Looping Cycles Network (HTSLCN), Lulea, Sweden, 2017 (Oral presentation).
- **S. Ramirez-Solis,** S. Milne and V. Dupont. High-temperature CO_2 Sorption using Sintering-Resistant CaO/Saffil Fibres Sorbents Prepared by Precipitation Method. UKCCSRC Autumn 2017 Biannual, University of Sheffield, UK, 2017 (Oral and poster presentation).
- **S. Ramirez-Solis,** S. Milne and V. Dupont. CO_2 sorption CaO/Saffil Fibres sorbents prepared by precipitation via urea. The role of universities in helping to meet future energy challenges. University of Leeds, UK, 2017 (Poster presentation).
- **S. Ramirez-Solis,** S. Milne and V. Dupont. High-temperature CO_2 sorption by CaO-based sorbents using Saffil Ceramic fibres as a substrate. UKCCSRC Network Conference Cambridge, University of Cambridge, UK, 2018 (Poster presentation).
- **S. Ramirez-Solis,** S. Milne and V. Dupont. CaO-based sorbents with enhanced thermal stability for High-Temperature CO_2 Uptake. UKCCSRC: Supporting CCUS Implementation Through Innovation, University of Sheffield, UK, 2018 (Poster presentation).

It must be confirmed that the candidate is a primary author for the publication and led experimental work and writing up of the publication. In addition, the candidate was first author from oral presentations and posters presented in Congresses. The research work published was co-supervised, discussed and proofread by Dr Valerie Dupont and Dr Steven J. Milne.

Appendix A

Kinetic study for the carbonation reaction using the isothermal method

CO_2 conversion curves used to predict the kinetic parameters using isothermal TGA data for the family of sorbents CaO/Sf-%-U, CaO/Sf-%-SH loaded with 25, 15 and 5 wt. % of CaO as the active phase. These curves also comprise those sorbents CaO/Sf-%-Oct with same contents of CaO (5-25 wt. %).

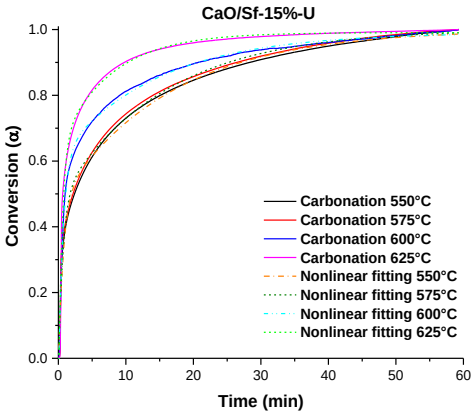

a) Ca-Sa-15%-U

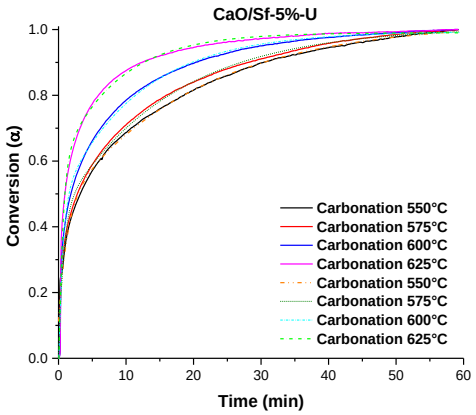

b) Ca-Sa-5%-U

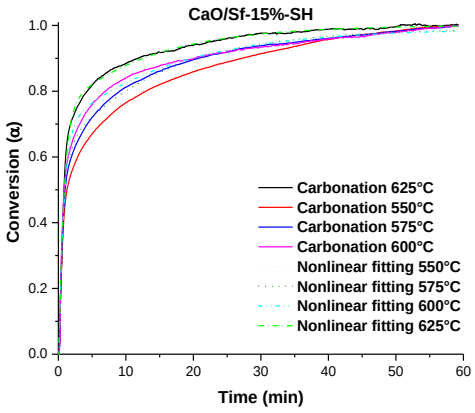

c) CaO/Sf-15%-SH

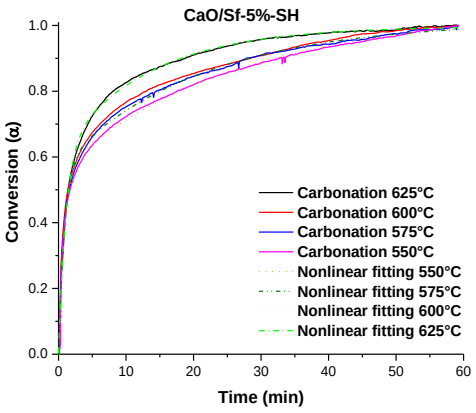

d) CaO/Sf-5%-SH

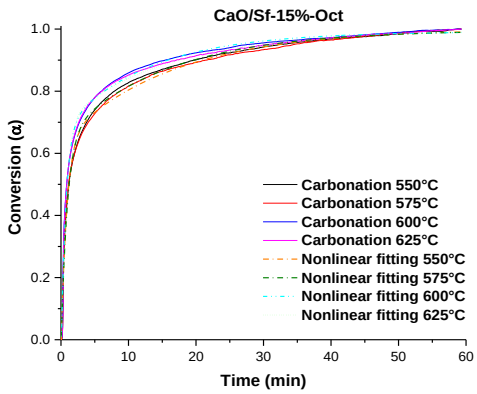

e) CaO/Sf-15%-Oct

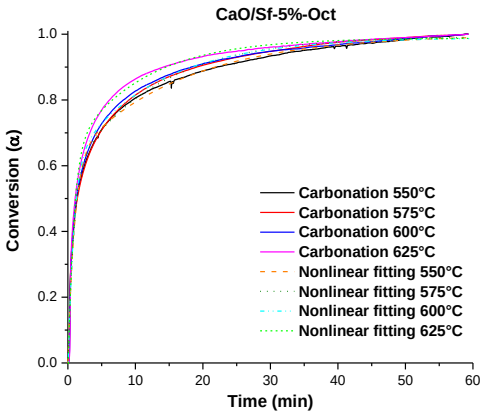

f) CaO/Sf-5%-Oct

Arrhenius plots of sorbents Ca-Sa-%-WI, Ca-Sa-%-WI, CaO/Sf-%-U and CaO/Sf-%-SH used for the estimation of activation energies (kJ/mol) from rate constants values obtained from the application of Avrami-Erofeyev A2 model into conversion (α) vs time (min) curves (temperature range 550-625°C). The *E* values are predicted for both chemical reaction and diffusion-controlled regime.

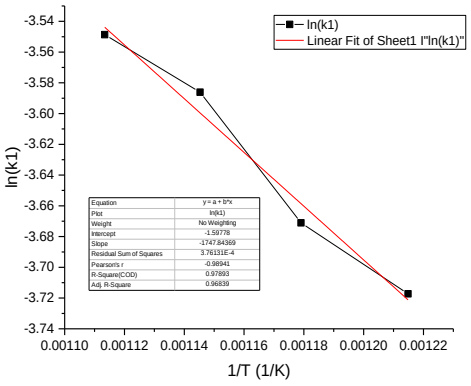

a) Ca-Sa-15%-WI (chemical reaction)

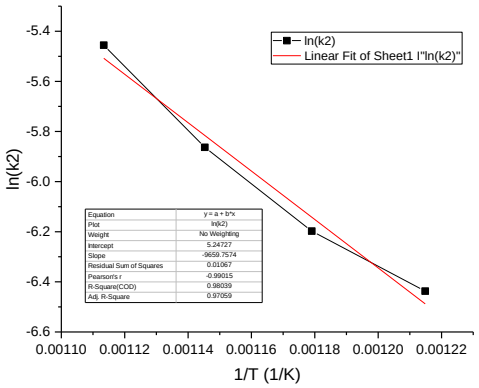

b) Ca-Sa-15%-WI (Diffusion)

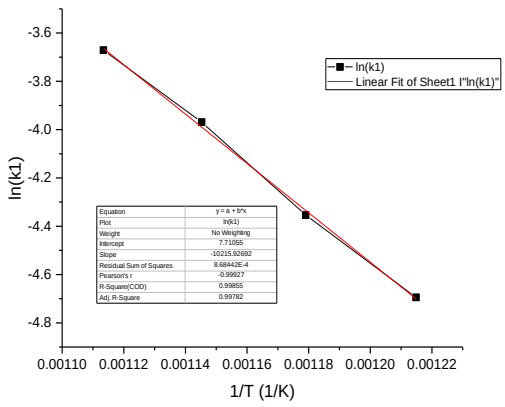

c) Ca-Sa-5%-WI (chemical reaction)

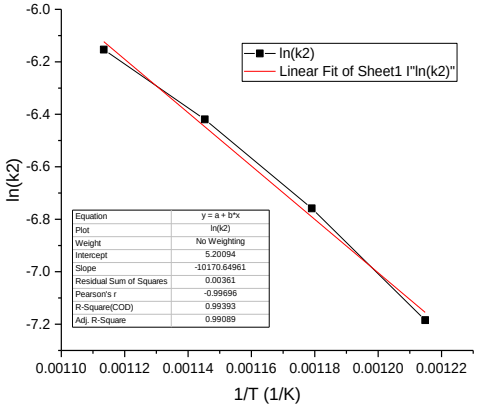

d) Ca-Sa-5%-WI (Diffusion)

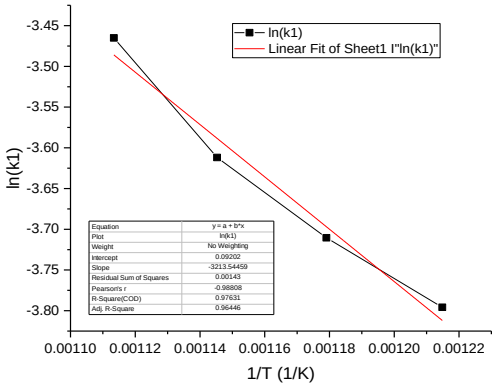

e) Ca-Sa-15%-U (chemical reaction)

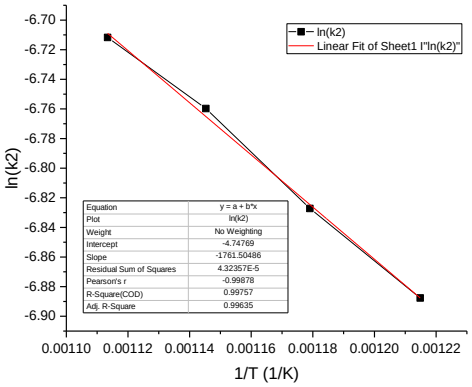

f) Ca-Sa-15%-U (Diffusion)

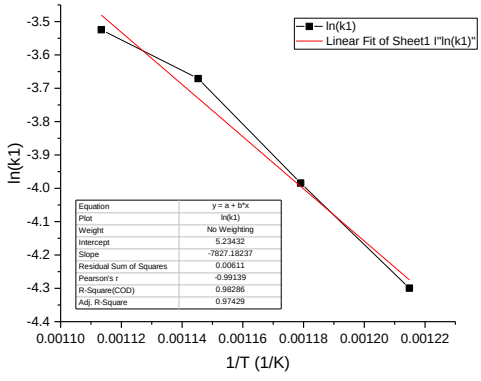

g) Ca-Sa-5%-U (chemical reaction)

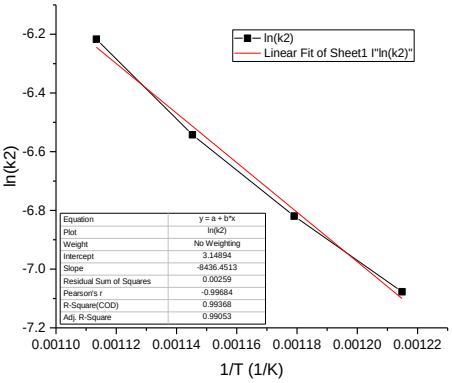

h) Ca-Sa-5%-U (Diffusion)

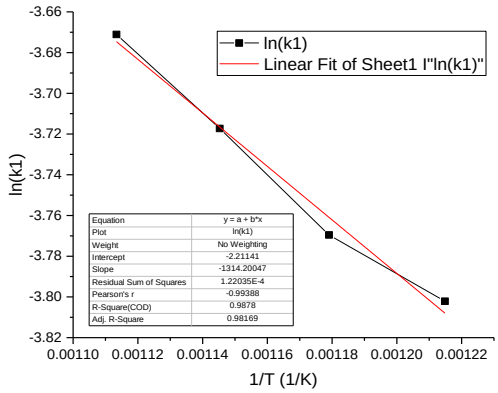

i) Ca-Sa-15%-SH (chemical reaction)

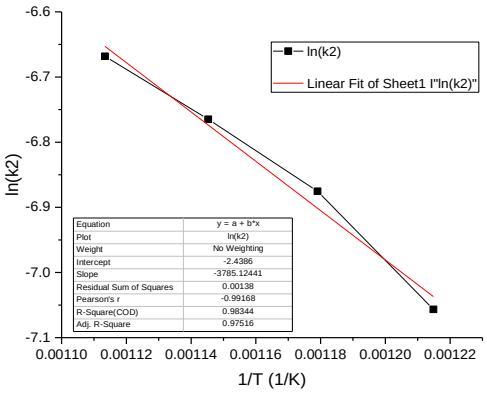

j) Ca-Sa-15%-SH (Diffusion)

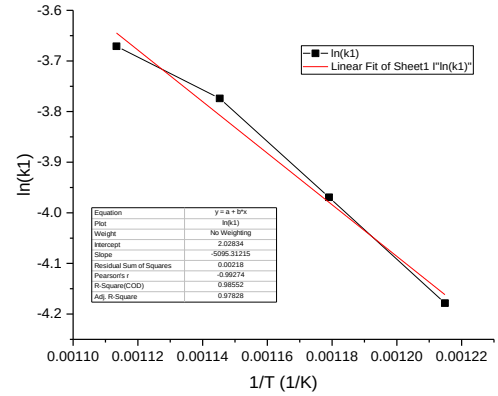

k) Ca-Sa-5%-SH (chemical reaction)

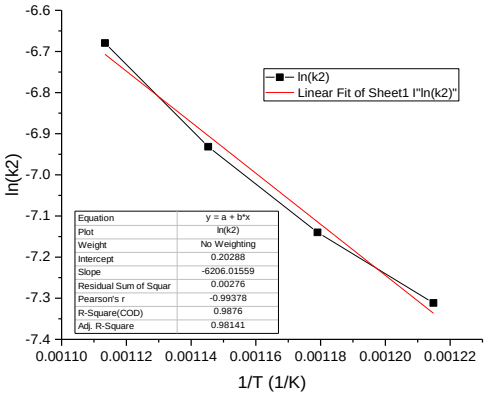

l) Ca-Sa-5%-SH (Diffusion)

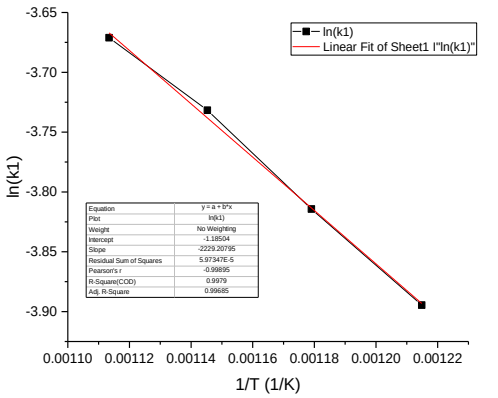

m) Ca-Sa-15%-Oct (chemical reaction)

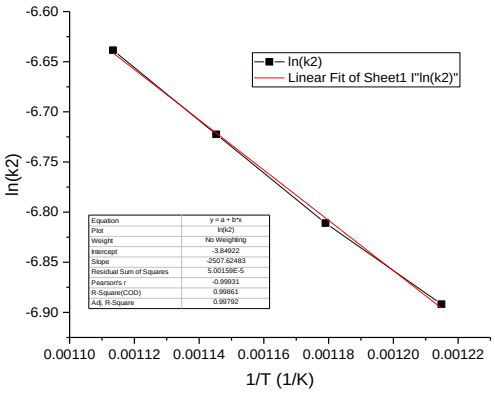

n) Ca-Sa-15%-Oct (Diffusion)

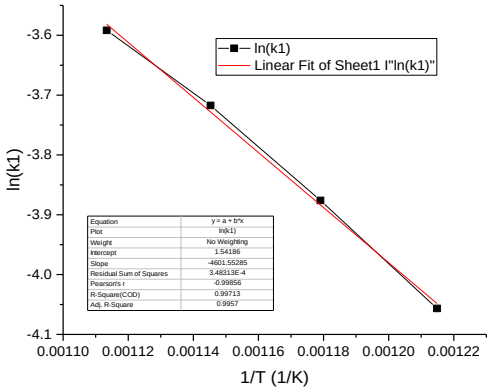

o) Ca-Sa-5%-Oct (chemical reaction)

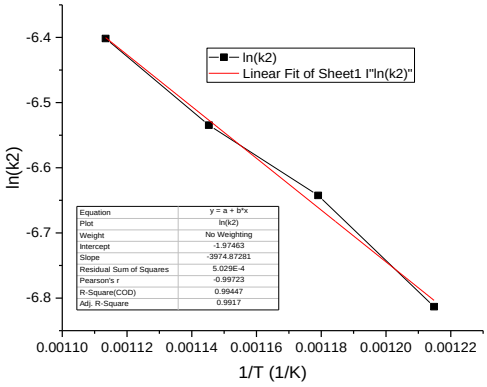

p) Ca-Sa-5%-Oct (Diffusion)

Appendix B

Decarbonation kinetics study under isothermal method

Plots associated with the decomposition process $CaCO_3 \leftrightarrow CaO + CO_2$ performed under isothermal conditions in a temperature range between 680 to 740°C. Also, this appendix includes the Arrhenius plots used for performing the estimations of the activation energies for the different families of sorbents Ca-Sa-%-WI, CaO/Sf-%-U, CaO/Sf-%-SH and CaO/Sf-%-Oct loaded with 15 and 5 wt.%.

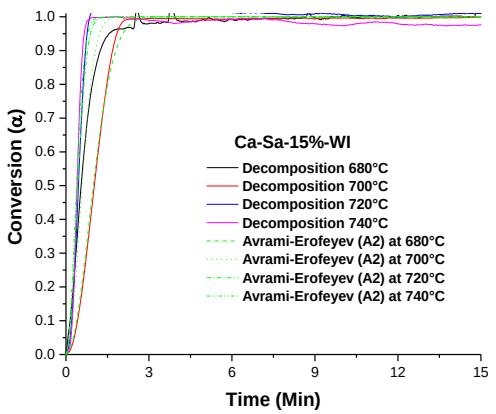

a) Ca-Sa-15%-WI

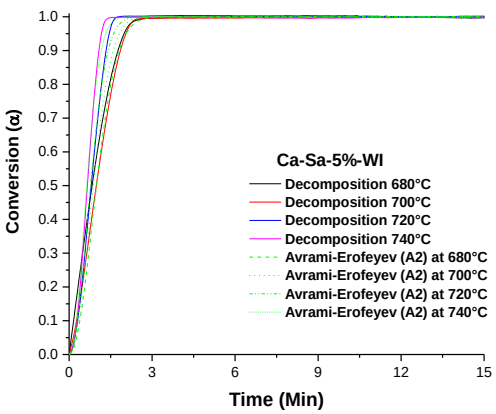

b) Ca-Sa-5%-WI

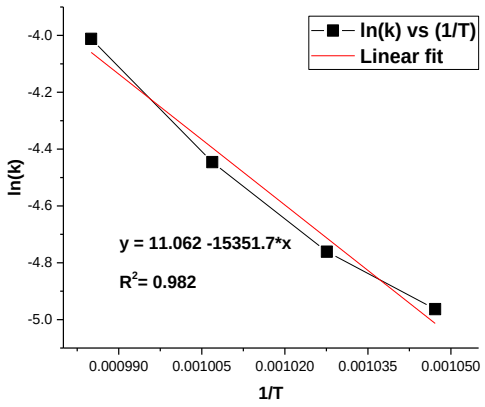

a) Ca-Sa-15%-WI (Arrhenius plot)

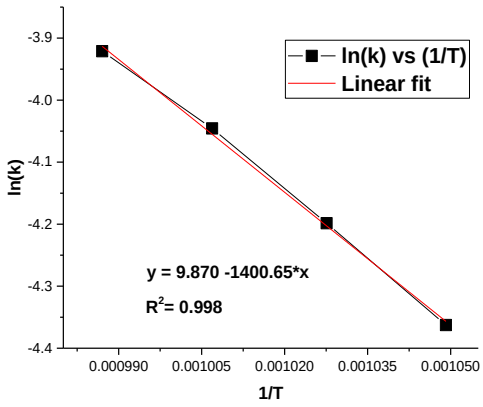

b) Ca-Sa-5%-WI (Arrhenius plot)

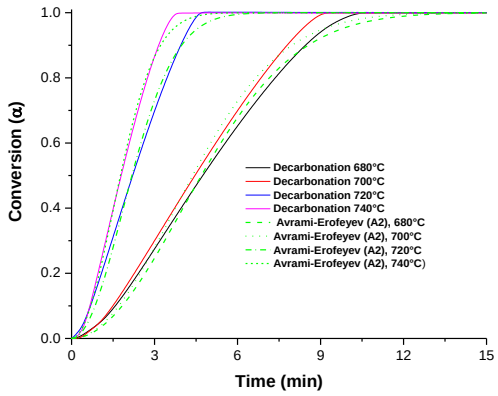

c) CaO/Sf-15%-U

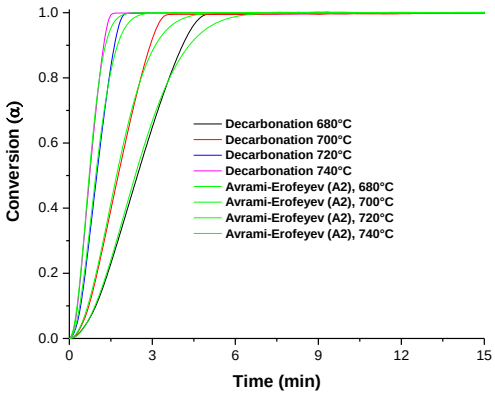

d) CaO/Sf-5%-U

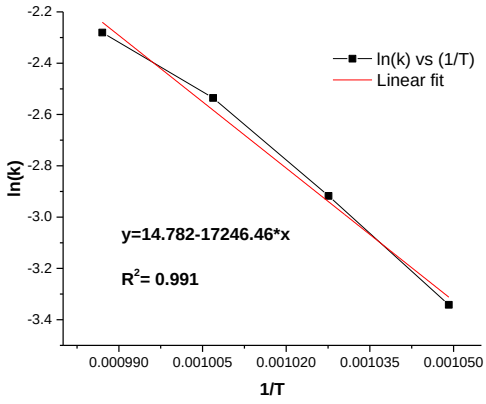

c) CaO/Sf-15%-U (Arrhenius plot)

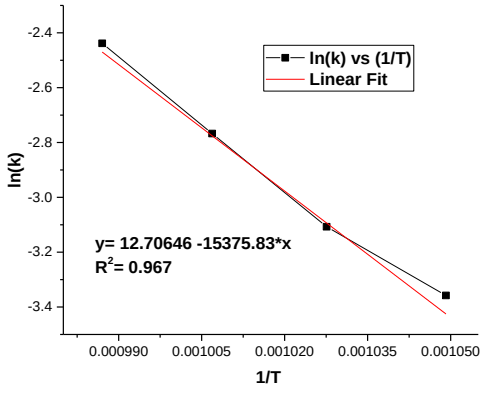

d) CaO/Sf-5%-U (Arrhenius plot)

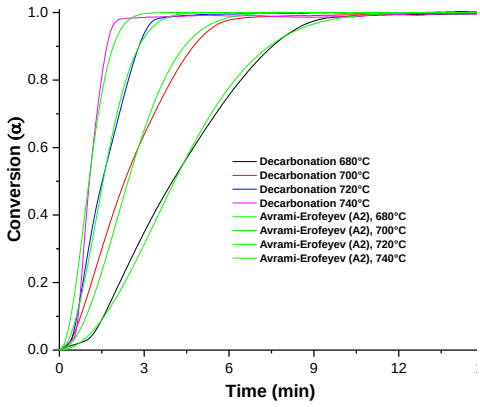

e) CaO/Sf-15%-SH

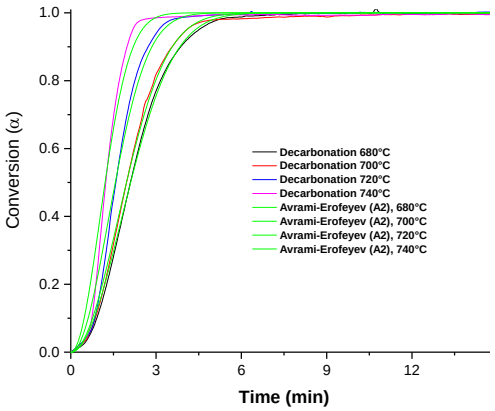

f) CaO/Sf-5%-SH

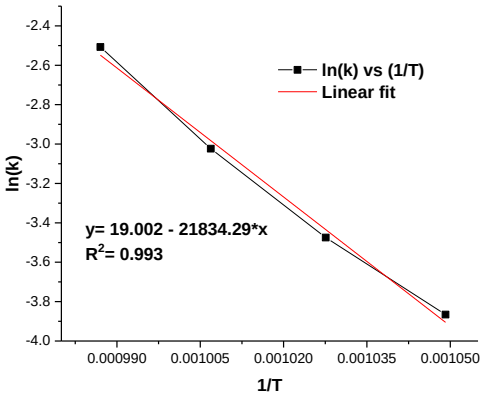

e) CaO/Sf-15%-SH (Arrhenius plot)

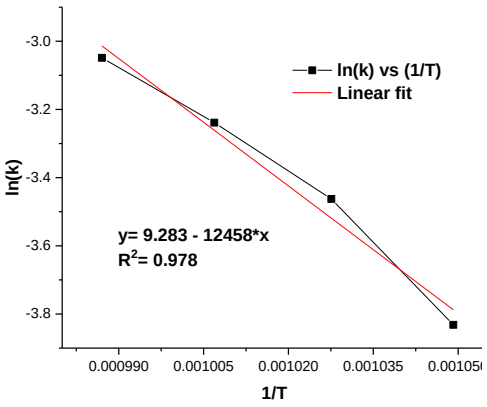

f) CaO/Sf-5%-SH (Arrhenius plot)

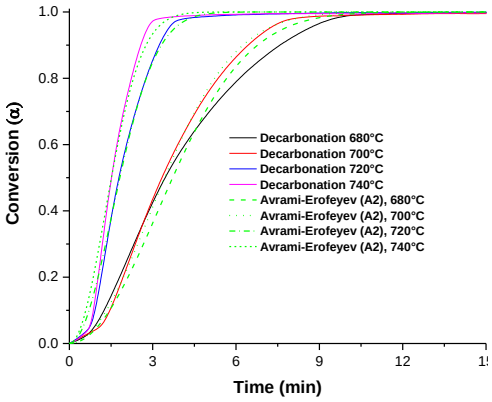

e) CaO/Sf-15%-Oct

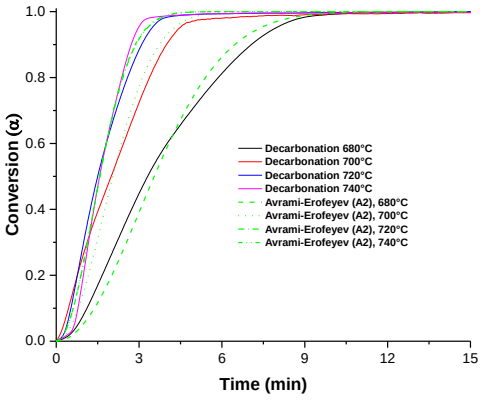

f) CaO/Sf-5%-Oct

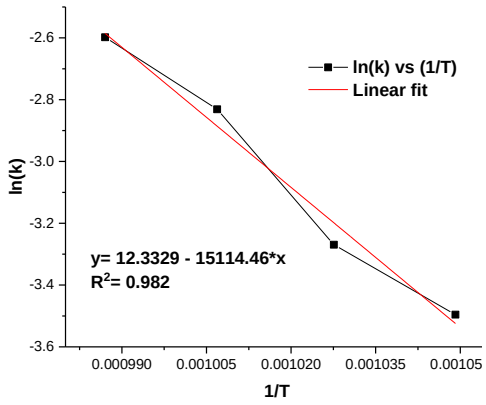

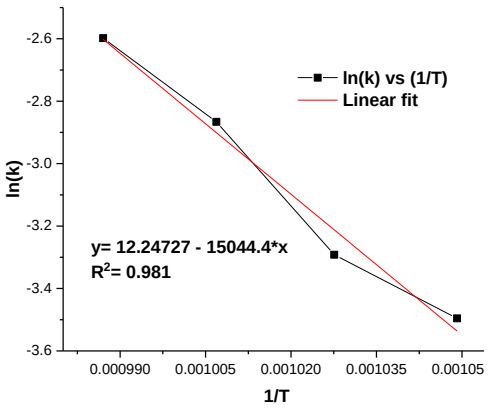

e) CaO/Sf-15%-Oct (Arrhenius plot) **f) CaO/Sf-5%-Oct (Arrhenius plot)**

Appendix C

Kinetic study carried out under non-isothermal conditions for the decarbonation reaction

The current appendix show the plots of OFW, Friedman, Kissinger and Coast-Redfern employed to evaluate the kinetics related to the decarbonation process. The kinetic parameters were elucidates by isoconversional methods using a heating rates (4, 8, 12 and 16 °C/min) in a temperature range of 680 to 740°C. The plots exhibited are those of Ca-Sa-%-WI, CaO/Sf-%-U, CaO/Sf-%-SH and CaO/Sf-%-Oct coated with 15 and 5 wt.% of CaO.

Ozawa-Flynn- Wall plots

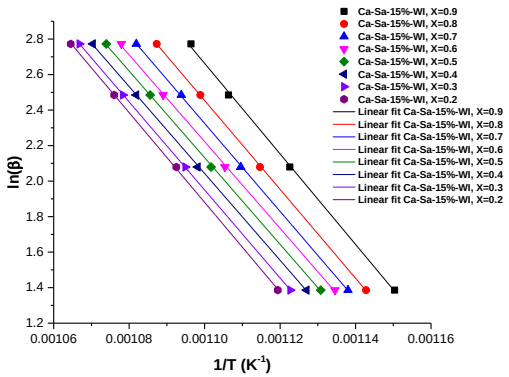

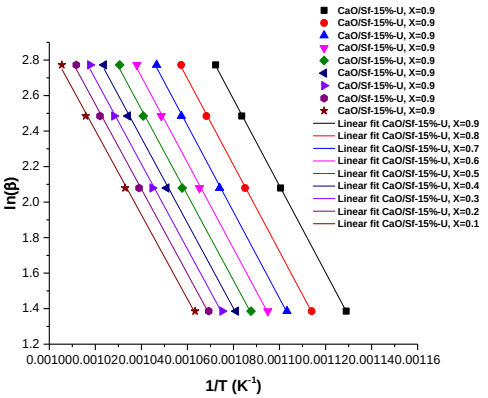

a) Ca-Sa-15%-WI (OFW) **b) CaO/Sf-15%-U (OFW)**

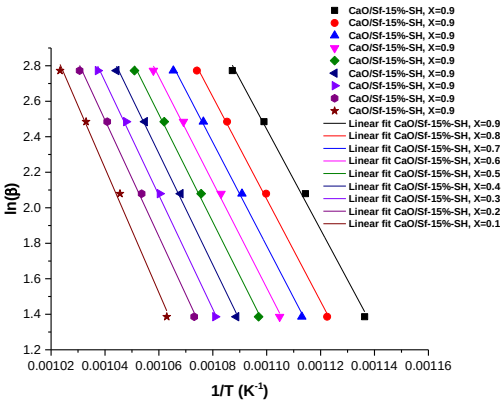

c) CaO/Sf-15%-SH (OFW)

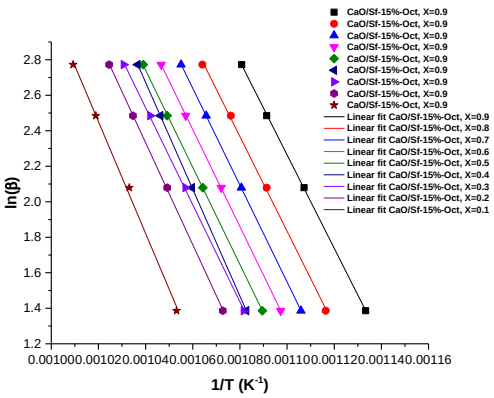

d) CaO/Sf-15%-Oct (OFW)

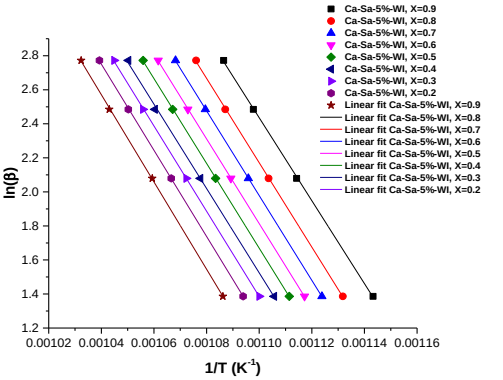

e) Ca-Sa-5%-WI

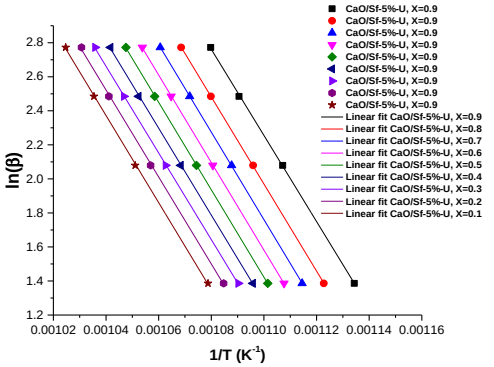

f) CaO/Sf-5%-U

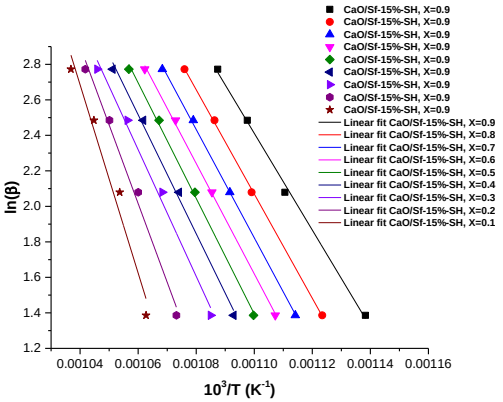

g) CaO/Sf-5%-SH

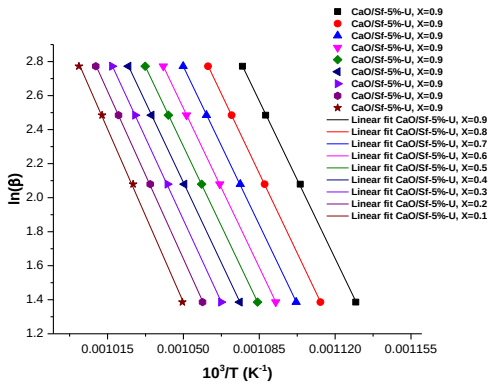

h) CaO/Sf-5%-Oct

Friedman plots

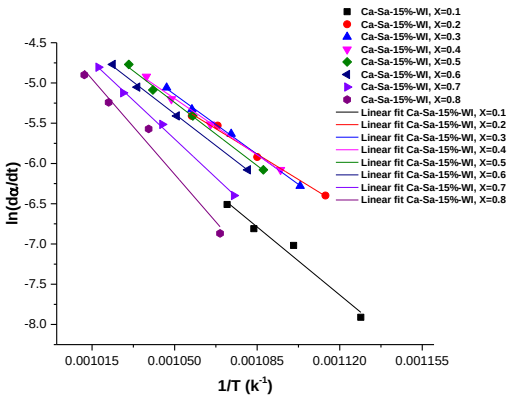

a) Ca-Sa-15%-WI

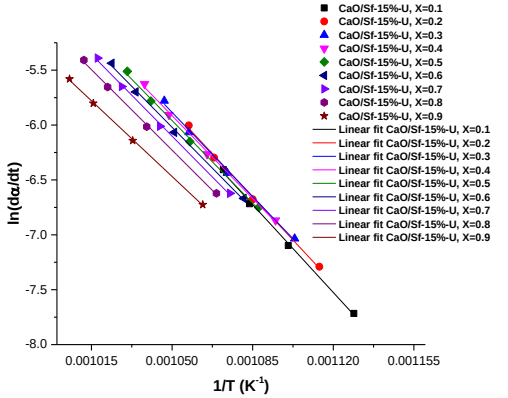

b) CaO/Sf-15%-U

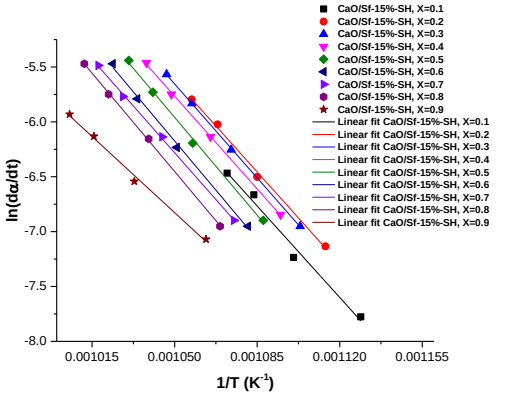

c) CaO/Sf-15%-SH

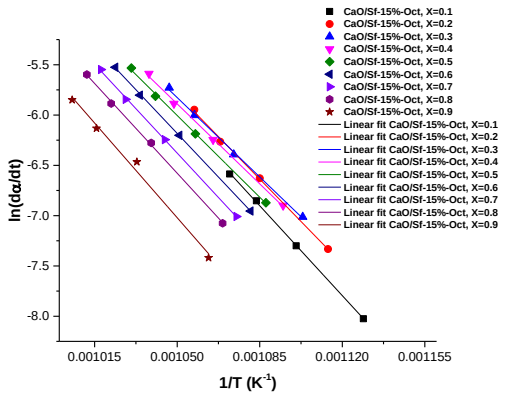

d) CaO/Sf-15%-Oct

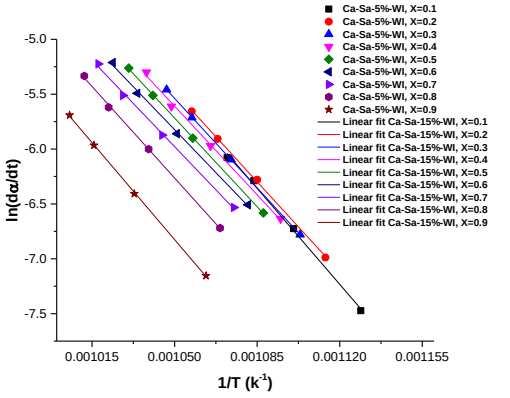

e) Ca-Sa-5%-WI

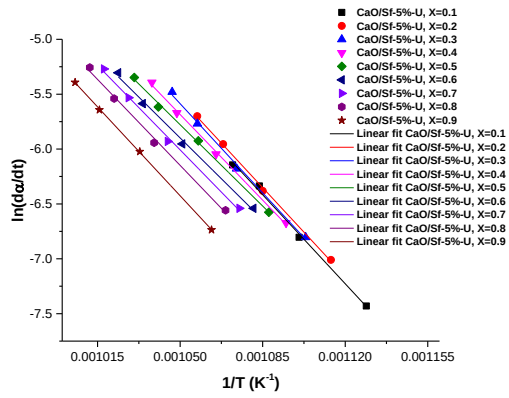

f) CaO/Sf-5%-U

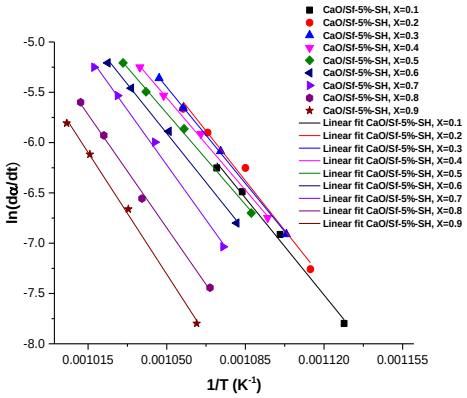

g) CaO/Sf-5%-SH

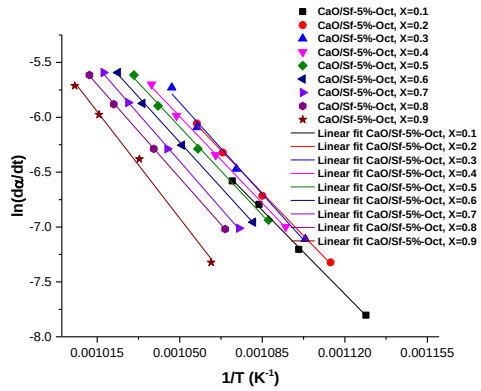

h) CaO/Sf-5%-Oct

Kissinger-Akahira-Sunose plots

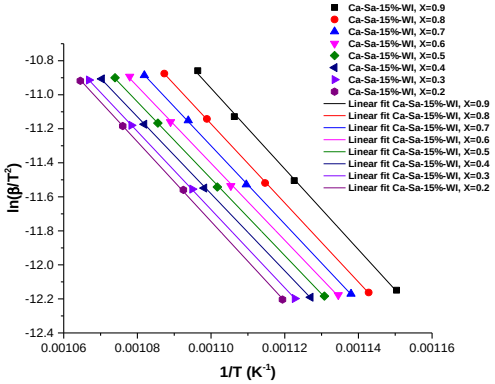

a) Ca-Sa-15%-WI

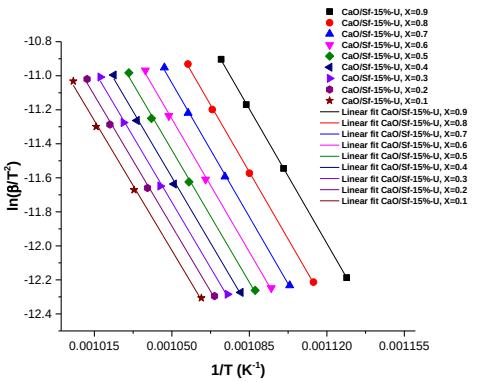

b) CaO/Sf-15%-U

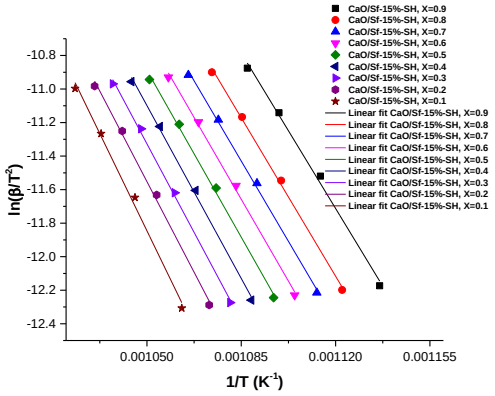

c) CaO/Sf-15%-SH

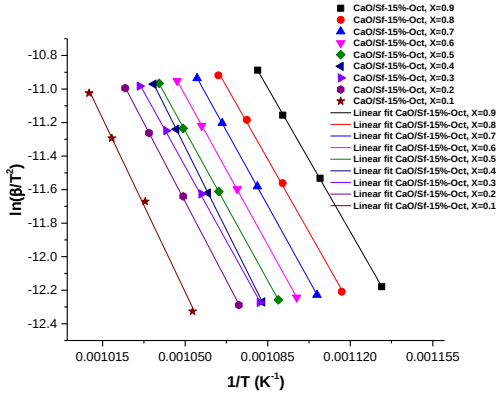

d) CaO/Sf-15%-Oct

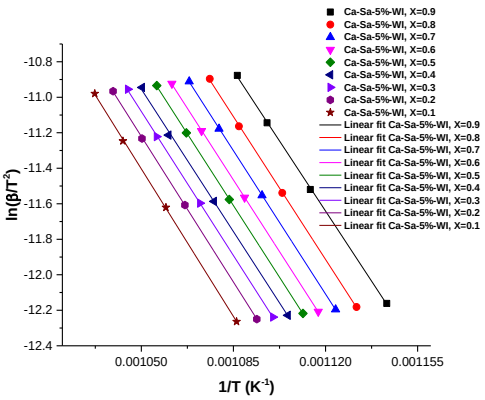

e) Ca-Sa-5%-WI

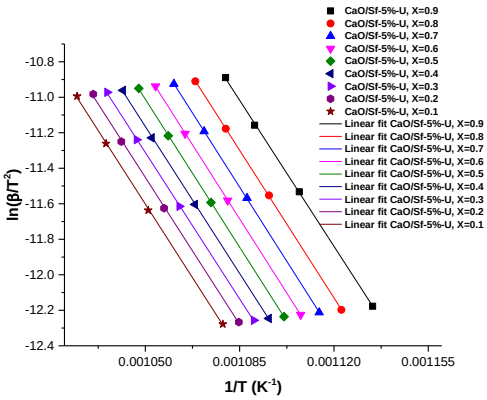

f) CaO/Sf-5%-U

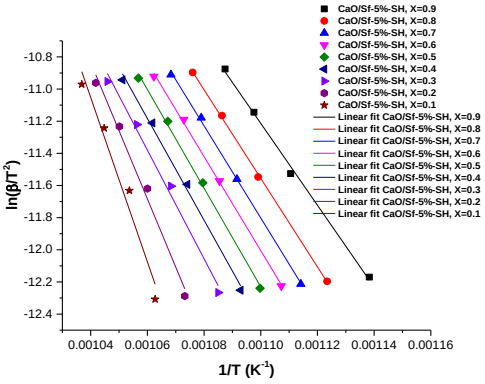

g) CaO/Sf-5%-SH

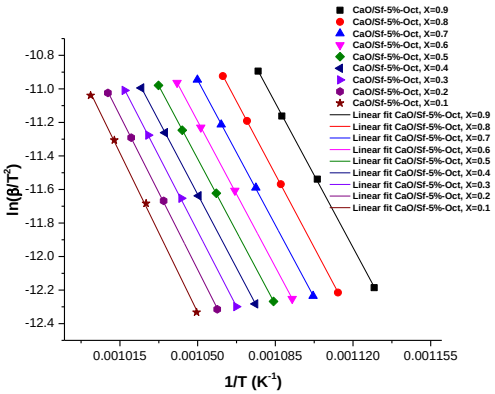

h) CaO/Sf-5%-Oct

Coast-Redfern plots

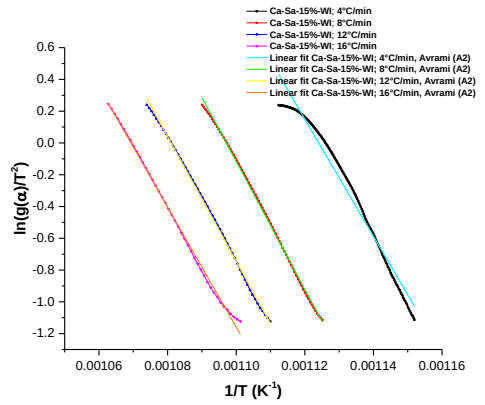

a) Ca-Sa-15%-WI

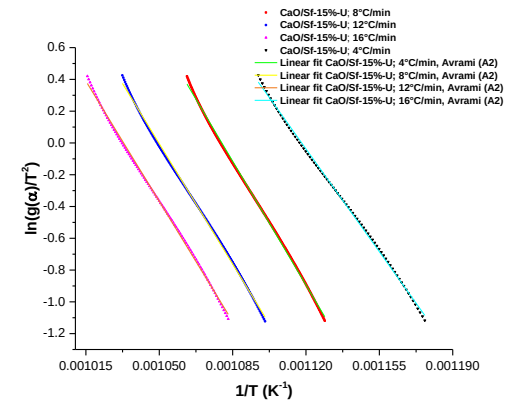

b) CaO/Sf-15%-U

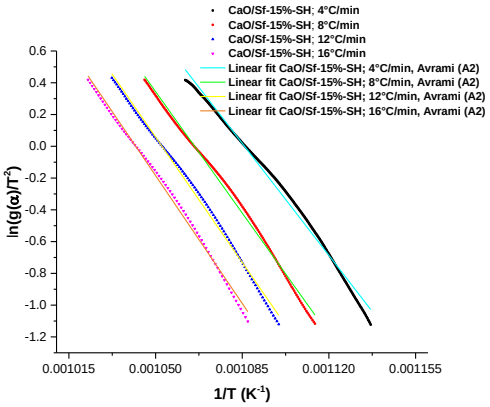

c) CaO/Sf-15%-SH

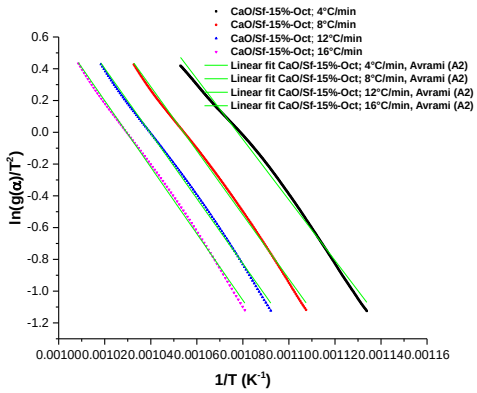

d) CaO/Sf-15%-Oct

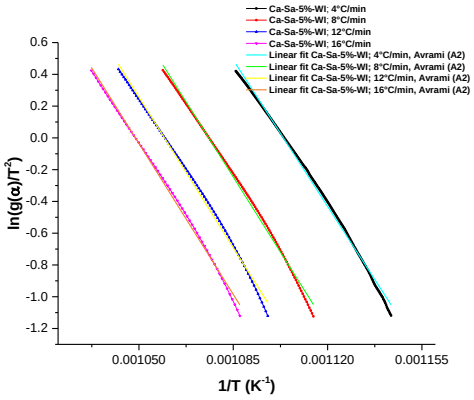

e) Ca-Sa-5%-WI

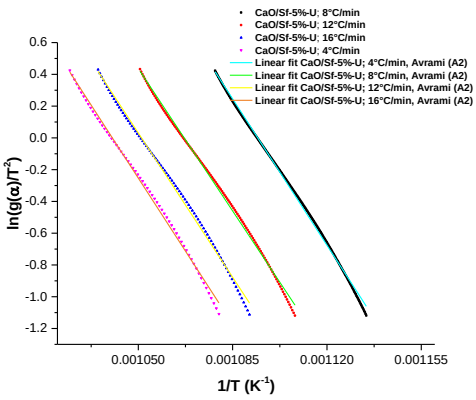

f) CaO/Sf-5%-U

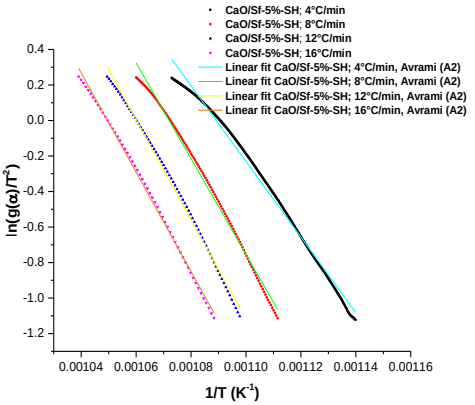

g) CaO/Sf-5%-SH

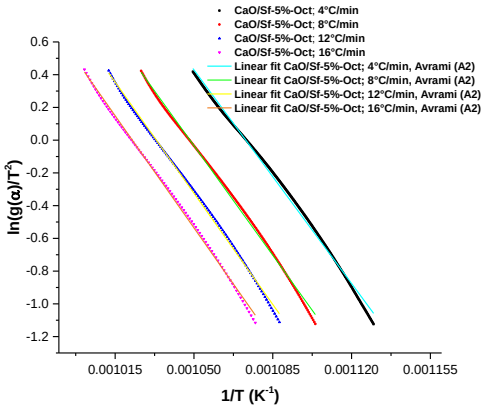

h) CaO/Sf-5%-Oct


ET
AVGE
BITVR
SCI
EN
TIA